

On the X-ray Emission of Massive Binary Stars

Dissertation
zur
Erlangung des Doktorgrades (Dr. rer. nat.)
der
Mathematisch-Naturwissenschaftlichen Fakultät
der
Rheinischen Friedrich-Wilhelms-Universität Bonn

eingereicht von
Martin Quast
aus
Osterburg

Bonn 2024

Angefertigt mit Genehmigung der Mathematisch-Naturwissenschaftlichen Fakultät der
Rheinischen Friedrich-Wilhelms-Universität Bonn

Erstgutachter: Prof. Dr. Norbert Langer

Zweitgutachter: PD. Dr. Jürgen Kerp

Tag der Promotion:

Erscheinungsjahr:

“Pleasure to me is wonder – the unexplored, the unexpected, the thing that is hidden and the changeless thing that lurks behind superficial mutability.”

Howard Phillips Lovecraft

Contents

Zusammenfassung

1	Introduction	1
1.1	How astronomy makes the unseen visible	1
1.2	Massive stars	5
1.2.1	Stellar structure	6
1.2.2	Stellar evolution	9
1.2.3	The Eddington luminosity	13
1.2.4	Stellar Winds	14
1.2.5	Wolf-Rayet stars	14
1.2.6	Core-collapse supernova	15
1.2.7	Neutron stars	15
1.2.8	Black holes	17
1.3	Aspects of binary stars	19
1.3.1	The Doppler effect and spectroscopic binaries	19
1.3.2	Mass transfer and Roche potential	20
1.3.3	Drivers of mass transfer	22
1.3.4	Stability of mass transfer	24
1.3.5	Common envelope	25
1.4	High-mass X-ray binaries	25
1.4.1	Wind Accretion	26
1.4.2	X-ray emission	28
1.4.3	Eddington accretion limit	29
1.4.4	Accretion discs	30
1.4.5	Supergiant X-ray binaries	31
1.4.6	Be X-ray binaries	33
1.4.7	Ultra-luminous X-ray sources	34
1.5	This Thesis	35
1.5.1	Mass transfer on a nuclear timescale in models of supergiant and ultra-luminous X-ray binaries	35
1.5.2	X-ray emission from massive spectroscopic binaries	35
1.5.3	Constraining the unseen companions of massive single-lined binaries by their X-ray emission	36
2	Mass transfer on a nuclear timescale in models of supergiant and ultra-luminous X-ray binaries	37

3 X-ray emission from massive spectroscopic binaries	41
3.1 Introduction	41
3.2 Black hole companions	43
3.2.1 The parameter space	43
3.2.2 X-ray detection limits	44
3.2.3 Accretion from the stellar wind	44
3.2.4 Accretion discs	45
3.2.5 Optically thin, adiabatic, spherically symmetric accretion	48
3.2.6 The Eddington limit	52
3.2.7 X-ray attenuation	52
3.2.8 Caveats	56
3.3 Neutron star companions	57
3.4 Main sequence star companions	62
3.4.1 X-ray emission from colliding stellar winds	63
3.4.2 Main sequence models	67
3.4.3 Optical flux ratio	72
3.5 Validity check	72
3.5.1 Diagnostic diagram of Cyg X-1	73
3.5.2 Diagnostic diagram of Vela X-1	76
3.6 Conclusion	78
4 Constraining the unseen companions of massive single-lined binaries by their X-ray emission	81
4.1 Introduction	81
4.2 The apparently single Wolf-Rayet stars in the SMC	83
4.3 The galactic Wolf-Rayet star WR 3	87
4.4 The galactic Wolf-Rayet star WR 6	92
4.5 The galactic Wolf-Rayet star WR 7	97
4.6 WR 124 and the galactic WN 8 stars	101
4.7 The single lined binary VFTS 243 in the LMC	105
4.8 The OB stars in 30 Dor	107
4.9 Catalogue of diagnostic diagrams	113
4.10 Conclusion	115
5 Summary and Outlook	119
Bibliography	125

A Appendix to Chapter 2	161
B Appendix to Chapter 3	185
B.1 Column density	185
B.2 Neutron star accretion	187
B.2.1 Case determination	187
B.2.2 Super-Keplerian Magnetic Inhibition	188
B.2.3 Sub-Keplerian Magnetic Inhibition	189
B.2.4 Supersonic propeller	189
B.2.5 Subsonic propeller	190
B.2.6 Direct accretion regime	191
B.3 Stellar parameters of the grid models	192
B.4 Dynamical pressure in colliding wind binaries	193
C Appendix to Chapter 4	197
C.1 Diagnostic diagrams of WR stars in the SMC	197
C.2 Diagnostic diagrams of Galactic WN 8 stars	204
C.3 Diagnostic diagrams of TMBM SB1 and uncertain SB2	217
C.4 Catalog of diagnostic diagrams	236

List of Publications

Curriculum Vitae

Danksagung

Zusammenfassung

Massereiche Sterne spielen eine zentrale Rolle für das Verständnis astrophysikalischer Prozesse wie auch für die menschliche Existenz. In ihrem Inneren werden die schweren Elemente wie Sauerstoff, Kohlenstoff oder Eisen geschmiedet, die für das Leben im Universum zwingend notwendig sind. Diese Elemente werden durch starke Sternwinde und die Supernova am Ende des Sternlebens ins All katapultiert und tragen zur Bildung neuer Sterne und Planetensysteme bei. Dadurch verändern massereiche Sterne nicht nur die chemische Zusammensetzung des interstellaren Mediums, sondern beeinflussen auch die Dynamik und Entwicklung ihrer Galaxien.

Während ihres turbulenten Lebens durchlaufen massereiche Sterne dramatische Entwicklungsphasen. So lassen sie sich beispielsweise als blaue Überriesen oder Wolf-Rayet-Sterne beobachten. Nicht weniger spektakulär ist ihr Tod in einer gewaltigen Explosion, nach der nur ein kompaktes Objekt, d.h. ein Neutronenstern oder ein Schwarzes Loch, zurückbleibt. Diese Objekte sind von zentralem Interesse für die Forschung, da sie es ermöglichen, Vorhersagen der Relativitätstheorie, der Teilchenphysik und der Plasmaphysik zu überprüfen.

Beobachtungen zeigen, dass massereiche Sterne häufig in Doppel- oder Mehrfachsystemen auftreten. Will man also ihre Entwicklung verstehen, ist die Einbeziehung der Wechselwirkung mit einem Begleitstern, beispielsweise durch einen Massentransfer, von zentraler Bedeutung. Die Entwicklung massereicher Doppelsterne mündet häufig in einem System bestehend aus zwei kompakten Objekten, die schlussendlich unter der Aussendung von Gravitationswellen verschmelzen können.

In der Regel entwickeln sich die beiden Komponenten eines Doppelsternsystems unterschiedlich schnell, sodass einer der beiden Begleiter seinen Lebenszyklus bereits beendet hat, während der andere noch aktiv Kernfusion betreibt. In dieser Entwicklungsphase besteht das System aus einem normalen Stern und einem kompakten Begleiter. Manche dieser Doppelsysteme verraten sich durch Emission von Röntgenstrahlung (Röntgendifpelsterne) oder durch ihre gravitative Wechselwirkung, die mit Hilfe spektroskopischer Messungen nachgewiesen werden kann.

Die vorliegende Arbeit widmet sich der theoretischen Untersuchung massereicher Doppelsterne bestehend aus einem normalen Stern und einem Neutronenstern oder einem Schwarzen Loch als Begleiter. Zunächst untersuchen wir dabei den Massentransfer eines bereits entwickelten Sterns auf einen kompakten Begleiter anhand numerischer Simulationen mit einem Sternentwicklungscode. Unser Ziel ist dabei den Einfluss des Wasserstoff-/Helium-Gradienten in der Hülle des massereichen Sterns zu erforschen. Wir konstruieren dazu Sternmodelle und variieren den Wasserstoff-/Helium-Gradienten sowie die Masse der wasserstofffreien Hülle. Anschließend simulieren wir ihr Verhalten bei konstantem Masseverlust und bei Massentransfer durch einen kompakten Begleiter.

Unsere Simulationen zeigen, dass das Vorhandensein eines Wasserstoff-/Helium-Gradienten in den oberflächennahen Schichten eines massereichen Sterns den Masse-Radius-Exponenten vergrößert, was zur Stabilisierung des Massentransfers führt. Wir können somit zeigen, dass ein Massentransfer auf einer nuklearen Zeitskala stabil sein kann, selbst dann, wenn das Massenverhältnis der Doppelsternkomponenten groß ist. Weiterhin demonstrieren wir, dass ein so stabilisierter Massentransfer auf eine Common-Envelope-Phase folgen kann. Um unsere Argumentation empirisch zu stützen, vergleichen wir unsere Modelle mit beobachteten Röntgendifoppelsternen und ultraleuchtkräftigen Röntgenquellen und finden eine gute Übereinstimmung zwischen Beobachtungsdaten und unseren Modellen.

In einem weiteren inhaltlichen Schwerpunkt dieser Arbeit beschäftigen wir uns mit der Detektierbarkeit von kompakten Begleitern massereicher Sterne. Unser Ziel ist es dabei, einen Methodenapparat zu entwickeln, der die Identifizierung bisher nicht detektierter Begleitsterne ermöglicht. Dazu betrachten wir für einen gegebenen massereichen Stern gleichzeitig Röntgen- und Radialgeschwindigkeitssignaturen eines potenziellen Begleiters. Dies führt zu der Konstruktion von Diagnostikdiagrammen, die leicht auf einlinige spektroskopische Doppelsterne und scheinbar einzelne massereiche Sterne angewandt werden können, um die Existenz und die Art eines Begleiters abzuleiten.

Um die Diagnostikdiagramme auf möglichst verschiedene Arten von Begleitern anwenden zu können, stellen wir verschiedene Modelle für Röntgenemission in massereichen Doppelsternen zusammen. Diese Modelle berücksichtigen die Röntgenemission kollidierender Winde zweier Sterne, die Röntgenemission eines akkretierenden Neutronensterns mit und ohne Propellereffekt und die Emission durch Akkretion eines Schwarzen Lochs. Für letzteren Fall leiten wir eine Möglichkeit her, um abzuschätzen, ob eine Akkretionsscheibe um ein Schwarzes Loch entstehen kann. Wir zeigen, dass die Röntgenemission nur bei Existenz einer solchen Scheibe stark genug ist, um detektiert zu werden.

Die so entwickelte Methodik wird anschließend auf ausgewählte massereiche Sterne angewandt. Wir konstruieren die von uns entwickelten Diagnostikdiagramme sowohl für verschiedene Wolf-Rayet-Sterne, als auch für einlinige und uneindeutig zweilinige spektroskopische Doppelsterne im Tarantelnebel. Unsere Analyse zeigt, dass mehrere der scheinbar einzelnen Wolf-Rayet-Sterne ein Schwarzes Loch als Begleiter haben könnten, das so röntgenschwach erscheint, dass es bisher noch nicht nachgewiesen werden konnte. Weiterhin können wir nachweisen, dass der einlinige Doppelstern VFTS 234 mit hoher Wahrscheinlichkeit ein solches röntgenschwaches Schwarzes Loch als Begleiter besitzt. Ähnliche Ergebnisse finden wir für die Sterne VFTS 514 und VFTS 779.

Im Rahmen unserer Untersuchungen können wir schlussfolgern, dass massereiche Sterne ein röntgenschwaches Schwarzes Loch als Begleiter besitzen können, wenn ihre Windgeschwindigkeit nur hinreichend groß ist. So könnten stellare Schwarze Löcher in massereichen Doppelsternen einer Detektion durch Röntgensatelliten entgehen, wenn die Orbitalperiode größer als ca. zehn Tage ist. Unsere Resultate stärken somit die Anhaltspunkte für eine große, bisher unentdeckte Population stellarer Schwarzer Löcher als Begleiter massereicher Sterne, wie sie von verschiedenen theoretischen Studien bereits vorhergesagt wird.

Chapter 1

Introduction

1.1 How astronomy makes the unseen visible

On January 7th, 1610, a mathematics professor in Padua pointed his self-made telescope to the sky for the first time. It was none other than Galileo Galilei who saw the moons of Jupiter that night as the first human. This discovery marked the revolution of astronomy since Ptolemaios and the final assertion of heliocentrism (though it would take a few more years to convince authorities in science and religion). The invention of the optical telescope allowed astronomers to examine even faint and apparently small objects in detail, which ultimately led to one of the greatest scientific revolutions in human history.

Several years later, in 1617, Benedetto Castelli, a student of Galileo, made another significant discovery by identifying a binary companion of the star Mizar A (Marett-Crosby 2013, p. 32). This companion, named Mizar B, marked the pioneering observation of a telescopic binary system.

Decades and centuries of significant breakthroughs followed, not only in the development of optical equipment used by astronomers but also in the astronomical theory building. For instance, Kepler's laws of celestial motion were based on accurate observations by Tycho Brahe. These laws, in turn, were generalized by Newton, leading to the laws of motion and Newton's law of gravity, describing not only the motion of celestial bodies but also the mechanical behavior of terrestrial objects with high accuracy. One of the successes of this new framework on observational astronomy was the discovery of Neptune, the outermost planet of the solar system¹. By studying the orbital motion of the planet Uranus, Alexis Bouvard found significant discrepancies between its observed and predicted position. John Adams and independently Urbain Le Verrier used Newtonian mechanics to compute the position of another as-yet-unknown planet. The existence of this planet was confirmed observationally by Johann Gottfried Galle. This example illustrates how unseen astronomical objects can indirectly be uncovered by combined consideration of observational data and theoretical approaches.

Until the last century, this observational data could only be obtained by analyzing the optical light emitted by astronomical objects and eventually captured by scientists' telescopes. Consequently, it was only possible to measure the position and brightness of the celestial bodies. This changed with the development of astronomical spectroscopy,

¹There is some evidence that Galilei saw Neptune in his telescope but mistook it for a fixed star.

i.e., the decomposition of light into its individual color or wavelengths. William Hyde Wollaston discovered absorption lines in the solar spectrum as early as 1802, which were rediscovered 12 years later by Josef Fraunhofer. The interpretation of these dark lines was initially unclear until Bunsen and Kirchhoff developed chemical spectral analysis in 1859. The dark lines are produced by the absorption of photons of certain wavelengths by ions in the solar atmosphere. Shortly afterward, this method was used by William and Margaret Huggins and Angelo Secchi to study the chemical composition of stars.

Fig. 1.1 gives an illustration of the capabilities of stellar spectroscopy. The majority of stars (e.g., Castor) show dark absorption lines in the optical spectrum. These provide information about the temperature and chemical composition of the solar atmosphere. There are also stars that show a different kind of spectrum. For instance, the Wolf-Rayet star WR 1 shows strong emission lines in the spectrum, indicating a strong stellar wind (cf. Sec. 1.2.5). Another example of an emission line star is X Per. Here, the H α emission line is attributed to the presence of the disc around the star (see Sec. 1.4.6 on BeXB for details). These are just three examples of many that show how the technique of spectroscopy enables astronomers to indirectly discover and study phenomena that are not visible, even with telescopes of maximum magnification.

However, spectroscopy proved to be an even more powerful tool. In 1887, Edward C. Pickering and Antonia C. Maury noticed a doubling of the absorption lines of Mizar A that occurred with remarkable regularity. They concluded that Mizar A itself must consist of two stars and thus found the first spectroscopic double star. This companion reveals itself by its gravitational influence on Mizar A, which can be detected in the spectrum by a Doppler shift. Consequently, Mizar A is a so-called spectroscopic binary. Once again, a new development had widened the observational window of astronomy and could be used to indirectly uncover an unseen object by studying its influences on another visible object.

The next significant expansion of the observational window occurred in the 1930s when the American radio engineer Karl Jansky found a strong radio signal while working on a 30 m antenna. This signal correlated to the sidereal time, rather than solar time (Jansky 1933). Jansky realized that he was the first human to observe the center of our galaxy in the radio regime and opened another window to the stars. The most important contribution from radio astronomy to the understanding of the evolution of stars came from Jocelyn Bell-Burnell and Antony Hewish. They found a pulsating, point-like radio source (Hewish et al. 1968). The short period of 1.3s and the point-like appearance of the radio source led Gold (1969) to the conclusion that these pulsars are, in fact, neutron stars, i.e., the dense and highly magnetic remnants of massive stars emitting radio photons in a focused beam.

The fact that visible (optical) light and radio emission interstellar sources were the first bands of the electromagnetic spectrum used for astronomical observations is not a coincidence. Electromagnetic radiation in these bands can reach the ground practically unabsorbed by the terrestrial atmosphere, while more energetic radiation like X-rays is blocked already 100 km above the ground. Hence, high-energy radiation from space cannot be detected using ground-based telescopes. Consequently, X-ray astronomy could only be developed in the space age, i.e., the 1960s, when rockets and satellites carrying X-ray telescopes became accessible.

The most promising target of early X-ray astronomy seemed to be the sun. It is sur-

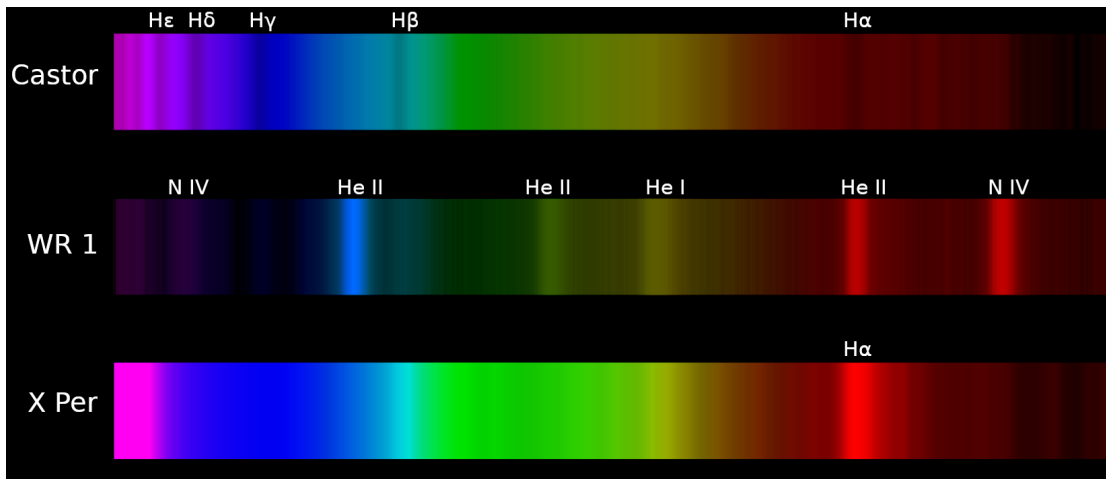


Figure 1.1.: Optical spectra of the stars Castor A, WR 1 and X-Per. This image illustrates the variety in which stellar spectra occur: Castor A shows absorption lines, as most stars do. WR 1 is a Wolf-Rayet star whose spectrum is dominated by broad emission lines caused by a strong stellar wind. X-Per is a Be-Xray binary showing a prominent hydrogen emission line due to a decretion disc. All spectra were taken by the author using a low-resolution transmission grating and a 9.25-inch telescope (Castor, X-Per) or a 24-inch telescope at the Sternwarte Kirchheim (WR 1).

Image credits: Martin Quast

rounded by a corona, i.e., an atmosphere of thin, hot gas that emits bright X-ray radiation. Another prominent X-ray source is the moon, where solar particles hitting the surface induce X-ray fluorescence. Surprisingly, while observing the latter, Giacconi et al. (1967) discovered an intense, point-like X-ray source known today as Sco X-1. This pioneering observation marks the first glimpse through the X-ray window beyond our solar system. However, the necessity of space-borne X-ray telescopes delayed the development of X-ray astronomy until the UHURU telescope was launched in 1970 and performed the first X-ray survey of the sky (Giacconi et al. 1971).

Hundreds of new X-ray objects were found in the course of this survey. It was also possible to link many objects to counterparts in the visible and radio bands, revealing their nature and enhancing the physical understanding of these targets. Now, astrophysicists could access observational data of objects that were (partly) already predicted by theory. Such objects were active galactic nuclei and hot intergalactic gas in clusters of galaxies on the large scale of the universe, as well as supernova remnants, young pulsars, and X-ray binaries on the small scale.

Figure 1.2 gives an impression of how much the use of X-ray telescopes has expanded the astrophysical view of the universe. It shows the constellation Cygnus in the optical light band from the Digitized Sky Survey and an X-ray of the same region as seen by the ASCA X-ray telescope (Sugizaki et al. 2001). The X-ray image shows multiple sources of high-energy radiation, the brightest being Cyg X-1. This X-ray source, discovered by Bowyer et al. (1965), is of most scientific importance since it provided the first evidence of a black hole (Miller-Jones et al. 2021). However, the nature of this X-ray source has been debated for years after its discovery. While the source showed variability of a very short timescale, indicating that the emitting region must be very compact (Oda et al.

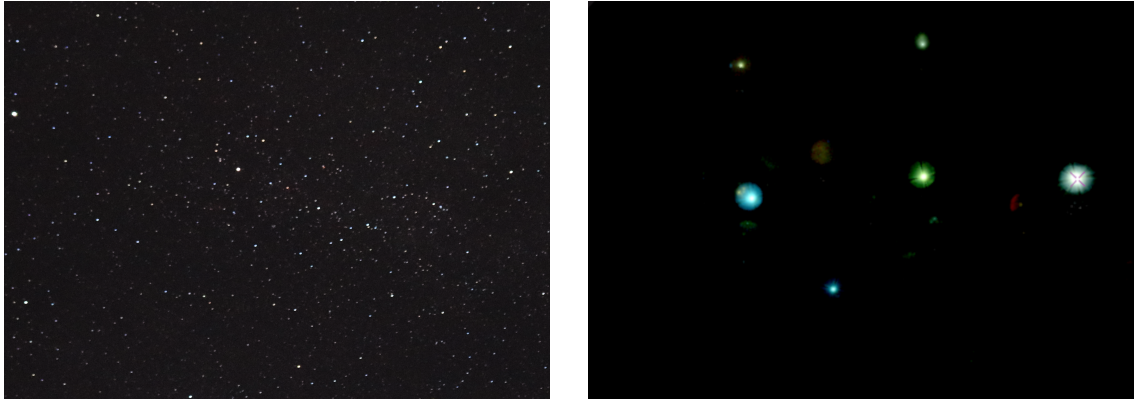


Figure 1.2.: Left: The image taken with a DSLR camera shows how the constellation Cygnus looks to the human eye when adapted to darkness. Right: The same field of view but in X-rays (0.5 to 10 keV band from the ASCA satellite). The most prominent X-ray source is Cyg X-1 (marked with a cross). Image credits Left: Martin Quast; Right: Sugizaki et al. (2001)

1971; Rappaport et al. 1971), this behavior was no proof of the existence of a black hole companion in Cyg X-1. The main problem in studying Cyg X-1 was the insufficient accuracy in determining the position of the X-ray source in the sky. Help came from radio astronomy. Braes and Miley (1971) and Hjellming and Wade (1971) discovered a variable radio source that could be associated with Cyg X-1, providing an accurate determination of the source's position, which, in turn, could be linked to a blue supergiant star visible in the optical band of electromagnetic radiation. Bolton (1972) and independently Webster and Murdin (1972) examined this star using optical spectroscopy and found a periodic Doppler shift, proving it is host to a binary companion with a mass exceeding $3 M_{\odot}$. An optical counterpart of that companion could not be found. Thus, the authors identified an optically faint object exceeding the upper limit for the stability of a neutron star. This marks the discovery of the first stellar black hole. Note that this breakthrough is the result of an interplay between X-ray and radio astronomy observing the accretion of stellar material onto the black hole, as well as optical spectroscopy, which identified Cyg X-1 as a spectroscopic binary, and theoretical astrophysics providing an interpretation of the observational data and arguments for a black hole companion based on stellar evolution.

The importance of understanding the physics of neutron stars and black holes comes from their extreme character. Understanding the structure of neutron stars or the relativistic accretion flow in the vicinity of a black hole can be used to probe fundamental theories, such as quantum physics (Li and Wang 1995; Ventura 2003) or general relativity (e.g. Done and Zycki 1999; Krawczynski 2012; Liu et al. 2019; Tripathi et al. 2020), which is impossible in terrestrial laboratories. On the other hand, neutron stars and black holes are the final products of massive star evolution. The observational understanding of their population and their interaction with a possible companion star is a good testbed for the evolution of massive stars in general and the formation and fate of interacting binaries (Tauris and van den Heuvel 2006; Marchant et al. 2017; Van den Heuvel et al. 2017; Tauris et al. 2017; Repetto et al. 2017; Shao and Li 2019).

But how do we find and study these objects? How do we investigate neutron stars, which are faint due to their small radius, and black holes that swallow light instead of

sending it to us on Earth? The key to answering these questions is to look for the effects of compact objects on their environment. We can observe the Doppler shift in the spectrum of a black hole's companion star, detect the X-rays that matter emits when it is accepted by a black hole, analyze the radio emission of charged particles captured by the magnetic field of a neutron star, and study how compact objects influence the evolution of their companion stars.

In this sense, this thesis aims to make a contribution to the understanding of neutron stars and black holes through studying their interaction with a massive companion. We will discuss how a compact companion influences the evolution of a massive star and how such a companion may be uncovered under the combined consideration of X-ray measurements and optical spectroscopy. Before we start with our study, we will lay out the most important aspects of the structure and evolution of single stars and the effects induced by a compact companion.

1.2 Massive stars

This thesis focuses on massive stars, i.e., stars that form a collapsing core at the end of their lives (Langer 2012). Initially, the mass of massive stars exceeds about $8 \dots 10 M_{\odot}$ (Heger et al. 2003). Understanding these objects holds great significance in the field of stellar astrophysics, the structure and evolution of galaxies, and astronomy in general (Langer 2012; Eldridge and Stanway 2022). Their extreme mass and resulting intense gravitational forces trigger a series of dynamic processes and energetic phenomena within them. For instance, these stars serve as cosmic engines, forging heavier elements essential for the formation of planets, other stars, and even life (Pagel 2009). Due to their high surface temperatures and luminosity, massive stars radiate copious amounts of ionizing radiation and powerful stellar winds, influencing their immediate surroundings and shaping the evolution of galaxies. In the Universe's early days, massive stars played a pivotal role in re-ionizing the interstellar medium (Haiman and Loeb 1997; Barkana and Loeb 2001).

Due to their high surface temperatures and luminosity, massive stars radiate copious amounts of ionizing radiation and powerful stellar winds, influencing their immediate surroundings and shaping the evolution of galaxies. In the Universe's early days, massive stars played a pivotal role in re-ionizing the interstellar medium (Haiman and Loeb 1997; Barkana and Loeb 2001). The dramatic life cycle of massive stars culminates in a spectacular explosion called a supernova. These energetic events also enrich the interstellar medium with crucial elements and trigger the formation of subsequent generations of stars.

The dramatic life cycle of massive stars culminates in energetic events such as a supernova or a gamma-ray burst (Smartt et al. 2009; Aguilera-Dena et al. 2018; Gal-Yam 2019). As a result of such an energetic explosion, a compact object in the form of a neutron star or black hole may remain (Bombaci 1996; Heger et al. 2003). Although these extreme objects are the final stages of massive stars, they can still appear as sources of high-energy radiation, as we shall see in this thesis.

1.2.1 Stellar structure

Stars are self-gravitating spheres of hot gas, mainly hydrogen and helium. Born in contracting molecular clouds, they refute their gravity, which tries to contract them for millions or even billions of years. Stars stabilize their selves against gravitational contraction through their internal pressure.

In the following, we will outline the basic principles underlying the theory of stellar structure. These are the conservation of mass, momentum, and energy, respectively, as well as the energy transport. Every principle yields a differential equation. This set of differential equations, together with an equation of state, the opacity of the stellar material, and a prescription of the nuclear reaction rates, has to be solved to model the structure of a star. All the concepts discussed in this section are basic principles of theoretical stellar astrophysics and are taken from the corresponding standard textbooks, e.g., Cox and Giuli (1968), Böhm-Vitense (1990), Prialnik (2009), and Kippenhahn et al. (2013).

Conservation of mass and continuity equation

Let m be the mass contained in a concentric sphere with radius r at a given instance of time. We model the stellar interior as consisting of multiple shells of radius r and width dr . The volume of a shell then is $4\pi r^2 dr$ if dr is small compared to r . Consequently, the mass dm contained in one shell is $dm = 4\pi\rho r^2 dr$, where ρ is the mass density. Rearrangement of this equation yields the first equation of stellar evolution

$$\frac{\partial r}{\partial m} = \frac{1}{4\pi\rho r^2}. \quad (1.1)$$

Here, we made a change of variables. We treat m as an independent variable and r as a function of m . The reason for using this Lagrangian mass coordinate is that the radius of a star can change by orders of magnitude during its lifetime. Also, in the course of this thesis, we will discuss the chemical profile of stars. The benefit of using the Langariang description is that the chemical composition as a function of m is independent of any expansion or contraction of the stellar radius. This would not be the case if we used r instead.

Conservation of momentum and hydrostatic equilibrium

The gravitational force pulls the stellar material toward the center. The star does not collapse under its own weight because of the gradient of the internal pressure P , which pushes the stellar material outward. In most stars, the pressure arises from the thermal movement of the gas particles (ideal gas pressure) and radiation (radiative pressure). The material of some stellar objects, namely white draws or neutron stars, receives its pressure from the degeneracy of electrons or neutrons, respectively (see section below).

If pressure force and gravity counterbalance each other, the star is said to be in hydrostatic equilibrium. If not, the resulting net force yields an acceleration, which causes a contraction or expansion of the considered mass shell. From the equilibrium of forces and Newton's second law, the corresponding differential equation can be deduced.

$$\frac{\partial P}{\partial m} = -\frac{Gm}{4\pi r^4} - \frac{1}{4\pi r^4} \frac{\partial^2 r}{\partial t^2} \quad (1.2)$$

where G is the gravitational constant. For stars in hydrostatic equilibrium, the time derivative in the second term on the right-hand side vanishes. Hydrostatic equilibrium is a reasonable assumption for most stars. This assumption is justified by the hydrostatic time scale, which measures the time the stars need to restore hydrostatic equilibrium after applying a perturbation. If the deviation from hydrostatic equilibrium is slight, the dynamical timescale is of the order of the free-fall timescale

$$\tau_{\text{hydr}} \approx \sqrt{\frac{R^3}{GM}} \quad (1.3)$$

where R is the stellar radius and M the total mass. If hydrostatic equilibrium is disturbed for any reason, the star will restore this equilibrium on this timescale. The hydrostatic timescale is of the order of minutes for stars like our sun and days for red giants. However, these stars live for millions or even billions of years. Consequently, most stars can be assumed to be in hydrostatic equilibrium during their evolution since any deviations from hydrostatic equilibrium would be restored in a time much shorter than the stellar lifetime.

There are some situations where the deviation from hydrostatic equilibrium is essential, such as the final supernova explosion of a massive star, stellar pulsations, or when mass transfer becomes dynamically unstable. The last example will become important in this thesis. However, processes on the dynamical timescale are often complicated to treat due to a lack of radial symmetry and the occurrences of turbulence. Therefore, we will rely on simplified analytical models to treat evolutionary processes on the dynamical timescale.

Conservation of energy and thermal equilibrium

Ideal gas pressure as well as radiative pressure require thermal energy. Consequently, a star is a hot object that loses energy to its surroundings via radiation. The energy loss has to be counterbalanced by some energy release process. The energy must then be transported from the interior to the stellar surface by radiative transfer and convection (see paragraph below).

Consider a spherical mass shell of radius r . Then, define l as the net energy per unit of time that passes through this sphere. This local luminosity l may change over the star's profile due to the energy release of nuclear burning or due to a change T and P . By drawing up the energy balance, one finds the differential equation for l as

$$\frac{\partial l}{\partial m} = \epsilon_n - \epsilon_\nu + c_p \frac{\partial T}{\partial t} + \frac{\delta}{\rho} \frac{\partial P}{\partial t}. \quad (1.4)$$

ϵ_n is the energy source term related to nuclear burning. The second term (ϵ_ν) accounts for the energy lost due to neutrinos that leave the star directly without interacting with the stellar matter. The third term, including the time derivative of the temperature T , is connected to the heating or cooling of the mass shell, which acts as an energy sink or source, respectively. The last term accounts for energy release or consumption due to mechanical work done via compression or expansion of the stellar material. The coefficient c_p is the heat capacity assuming constant pressure, and δ reflects the dependence of ρ on T at constant pressure (see Eq. 4.3 in Kippenhahn and Weigert 1994). Both coefficients have to be determined from the EOS.

If the mass shell does neither change temperature nor pressure, i.e., it is neither heating

nor cooling nor contracting. The energy change over the mass shell is only due to nuclear burning and neutrino cooling. The shell is then said to be in thermal equilibrium. In this case, the time derivatives in Eq. 1.4 vanish, leaving only the terms of nuclear energy release and neutrino cooling.

If thermal equilibrium is disturbed, the star can restore thermal equilibrium on a thermal timescale

$$\tau_{\text{th}} \approx \frac{GM^2}{2RL}. \quad (1.5)$$

For instance, the Sun has a thermal timescale of $\tau_{\text{th}} \sim 10^7$ years. Other stars than the Sun have a different mass, luminosity, and radius. Assuming hydrogen-burning stars, the mass-luminosity relation is approximately $L \propto M^{3.4}$ and the mass-radius relation roughly follows $R \propto M^{0.6}$ (Kippenhahn et al. 2013, p. 253). Introducing the two relations into Eq. 1.5 yields

$$\tau_{\text{th}} \approx 10^7 \text{ yr} \cdot \left(\frac{M}{M_{\odot}} \right)^{-2}. \quad (1.6)$$

Consequently, massive hydrogen-burning stars have a significantly shorter thermal timescale due to their higher luminosity.

Energy transport and temperature gradient

The differential equations for r and P are coupled via the mass density ρ . This coupling is mathematically reflected by the equation of state (EOS). In general, the EOS depends on density and temperature, e.g., in the case of an ideal gas. Consequently, an equation for the temperature profile inside the star is required to solve the system of differential equations. This equation can be found by expanding the temperature gradient using the chain rule.

$$\frac{\partial T}{\partial m} = -\frac{GmT}{4\pi r^4 P} \nabla \quad (1.7)$$

Here $\nabla := d \ln(T) / d \ln(P)$ reflects the change in temperature with pressure and has to be determined under additional assumptions on the energy transport. As an example, if the energy flux is carried via radiation within the optically thick stellar interior, the corresponding nabla is given by

$$\nabla_{\text{rad}} = \frac{3}{16\pi acG} \frac{\kappa LP}{mT^4}. \quad (1.8)$$

The opacity κ is caused by the scattering of photons on free electrons, absorption due to free-free transitions of electrons in the electric field of an ion, absorption due to bound-free transitions (separation of an electron from an atom or ion), and absorption due to bound-bound transitions (an electron is lifted into a state of higher energy). The opacity depends on temperature, density, and chemical composition and has to be read out from corresponding tables.

Besides radiative transfer, energy transport can occur in connection with the movement of matter. This phenomenon is called convection. If a portion of the stellar material is shifted in the vertical direction so fast that no heat exchange with the environment occurs, its thermal properties change adiabatically. The corresponding adiabatic temperature gradient is ∇_{ad} . For example, an ideal gas changes its temperature adiabatically with respect

to pressure according to $T \propto P^{2/5}$, and consequently, one finds $\nabla_{\text{ad}} = 2/5$ (Cox and Giuli 1968).

Scharzschild criterion for convection (Schwarzschild 1906). The energy transport in a convective layer requires treatment of the (stochastic) motion of the convective stellar material as well as the heat exchange between convection bubbles and their surroundings. One approach to model these complex physical processes is the mixing-length theory, as developed by Prandtl (1925) and applied to stars by Biermann (1932, 1942, 1948) and Siedentopf (1935).

It is assumed that convection can be modeled by blobs of gas that rise due to buoyancy and, after traveling a distance l_{ML} (the mixing length), dissolve in their surroundings. The value of the mixing length is assumed to be $l_{\text{ML}} = \alpha_{\text{ML}} \cdot H_{\text{P}}$, where $H_{\text{P}} := P/(dP/dr)$ is the pressure scale height (Kippenhahn et al. 2013). The mixing-length parameter α_{ML} is a dimensionless, free parameter and can be used to make energy transport in a stellar model artificially more or less effective. We will use this property of α_{ML} in chapter 2. A full description of the mixing-length theory, including the calculation of the temperature gradient ∇ , is beyond the scope of this introduction and can be found, e.g., in Böhm-Vitense (1958).

1.2.2 Stellar evolution

The virial theorem

The basic principle driving the evolution of stars is the virial theorem, which was already mentioned in Sec. 1.2.1. It states that for a star in hydrostatic equilibrium, gravitational binding energy E_{g} and internal energy E_{i} of the stellar material are related by

$$E_{\text{g}} = -2E_{\text{i}}. \quad (1.9)$$

Thus, the total energy of the star $E = E_{\text{g}} + E_{\text{i}}$ can be written as

$$E = \frac{1}{2}E_{\text{g}} = -E_{\text{i}}. \quad (1.10)$$

Note that the total energy has a negative value. Since the star releases energy from its surface via radiation, E declines over time. Eq. 1.10 yields that E_{g} also decreases, i.e., most of the stellar material contracts and sinks deeper into the gravitational potential of the star. At the same time E_{i} increases, meaning that the mean temperature of the stellar material also rises. Thus, stars heat up while they lose energy.

This somewhat confusing conclusion can be understood if we regard that the star has to contract during energy loss. The gravitational energy released during contraction is partly emitted via radiation and partly heats up the stellar material. This behavior of stars gives rise to the "*vicious virial circle*" (Lewin et al. 1995, p. 339): Due to radiation, the star loses energy. This energy loss increases the temperature, which forces the star to radiate even more, and so on. In the process, the star becomes denser and hotter.

At some point, the conditions in the interior are sufficient to start nuclear fusion. In this phase, the radiated energy is not balanced by the release of gravitational energy but by the transmutation of lighter into heavier elements. However, since the available fuel is

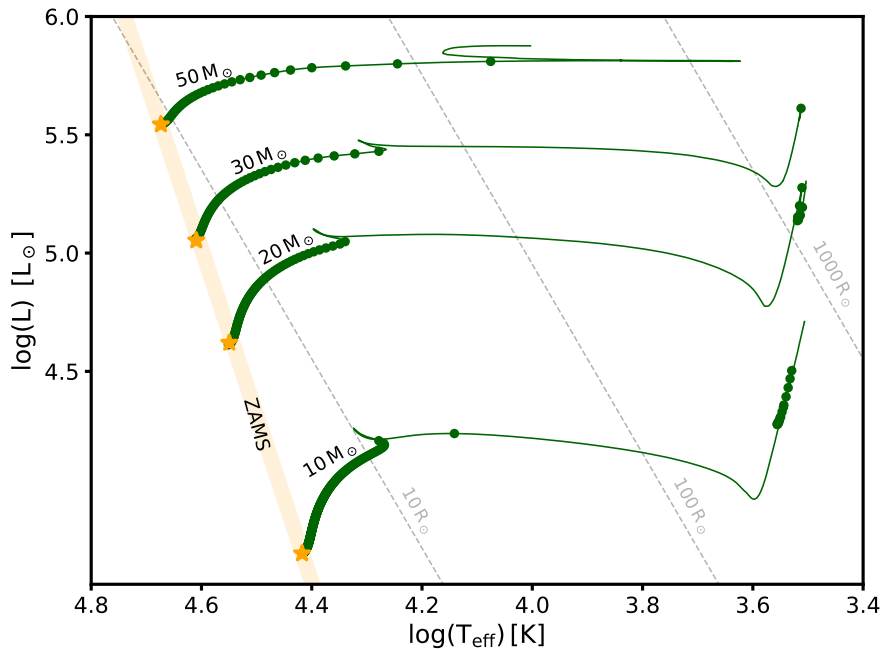


Figure 1.3.: A Hertzsprung-Russel diagram showing the evolutionary tracks of four non-rotating stellar models (green) with different initial masses and solar metallicity. The initial mass at the ZAMS is noted above the corresponding track. The big green dots along the tracks correspond to time steps of 10^5 yr. For every track, the onset of hydrogen burning is marked with a yellow star. The ZAMS is sketched yellow. The dashed lines indicate the points in the HRD where the stars have a certain radius. The evolutionary tracks were taken from Brott (2011).

limited, nuclear burning stops after some time, and the star has to contract again to release gravitational energy. This happens until the temperature and density in the stellar interior are sufficient to ignite the next burning stage. The process of contraction interrupted by temporary phases of nuclear burning happens until the material is so dense that quantum mechanical effects become important that prohibit further contraction due to radiative energy loss (e.g., in white dwarfs or neutron stars) or the star has contracted so far that it becomes a space-time singularity (a black hole).

Simply stated, stars evolve since they sink deeper into their own gravitational pit, releasing gravitational energy. This process happens on a thermal timescale and is interrupted by phases of nuclear fusion. While nuclear fusion can take millions or billions of years, it is not the driving mechanism of stellar evolution but rather a retarding momentum delaying the inevitable end of the star's life as a compact object.

Hydrogen burning

Stars are born in interstellar molecular clouds fragmentating and contracting under their own gravity (McKee and Ostriker 2007, For a review see). During this contraction, the material becomes dense and hotter, according to the virial theorem, until the conditions in the stellar center are sufficient to fuse hydrogen until helium.

The ignition of hydrogen-burning is the usual reference point from which we talk about

a zero-age main sequence (ZAMS) star. We discuss the further evolution of the star using a Hertzsprung-Russel (HR) diagram (Russell 1914), which shows the effective temperature T_{eff} and the total radiative luminosity L of a star on logarithmic scales. This diagram can be regarded as a phase space of stellar evolution. For instance, the radius R of a star can be determined directly from its position in the HR diagram using the Stefan-Boltzmann law

$$L = 4\pi\sigma RT_{\text{eff}}^4 \quad (1.11)$$

where σ is the Stefan-Boltzmann constant. Fig. 1.3 shows evolutionary tracks of four stellar models (Brott 2011) with different initial masses. We assume solar metallicity and neglect the effects of rotation. For every evolutionary track, the point where hydrogen burning starts is marked with a yellow star. These points lie on a line within the HR diagram, which is called the zero-age main sequence. The diagram shows that effective temperature and luminosity at the onset of hydrogen burning increase with initial mass.

In massive stars, hydrogen is converted into helium via the CNO cycle. This nuclear reaction cycle requires the presence of carbon, nitrogen, and oxygen isotopes, which serve as catalysts for the individual reactions of the cycle [][Chap. 18](Kippenhahn et al. 2013). Also, the energy production of the CNO cycle is very sensitive to temperature. Thus, the energy release is concentrated in the stellar center, producing a high flux at a small m . Consequently, ∇_{rad} is large in the stellar center, which causes convection in the stellar core, keeping the core material well-mixed. Thus, the central hydrogen abundance decreases with time within the entire convective region (cf. 1.4). At the same time, the core helium abundance increases. On the other hand, no nuclear reactions occur outside the convective core, and the energy is carried by radiation. In the case of hydrogen burning, the hydrogen and helium abundances of the radiative envelope stay constant over time as long as no mass is removed from this envelope.

As hydrogen burning proceeds, the star becomes more luminous while the effective temperature decreases. Consequently, its position in the HR diagram shifts to the upper right, which implies a radial expansion (cf. Eq. 1.11). This shift happens on a nuclear time scale τ_{nuc} , which is defined by the nuclear energy reservoir E_{nuc} and the luminosity of the star:

$$\tau_{\text{nuc}} = \frac{E_{\text{nuc}}}{L}. \quad (1.12)$$

We find $\tau_{\text{nuc}} \sim 10^{10}$ yr for the hydrogen burning in our sun. Since the nuclear energy reservoir depends on the amount of material that can be fused, one has $E_{\text{nuc}} \propto M$. Together with the mass-luminosity relation for hydrogen-burning stars $L \propto M^{3.4}$, we find the nuclear timescale for hydrogen burning as a function of the stellar mass:

$$\tau_{\text{nuc}} \approx 10^{10} \text{ yr} \cdot \left(\frac{M}{M_{\odot}} \right)^{-2.4}. \quad (1.13)$$

This equation shows that the time for hydrogen burning decreases significantly with stellar mass. While our sun takes 10 billion years to go through this phase, a $30 M_{\odot}$ star takes only 3 million years.

In Fig. 1.3, we marked the position after equal time steps of 10^5 yr with green dots. The density of dots along a track indicates how fast the star moves in the diagram. The

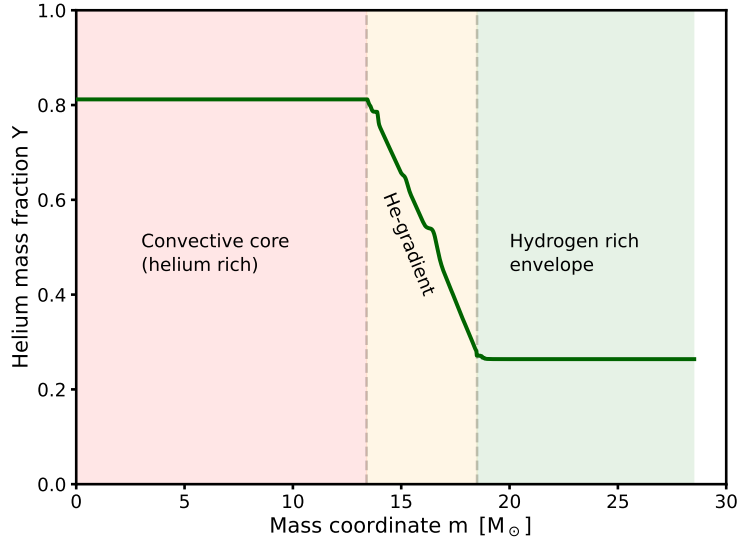


Figure 1.4.: The helium profile of an evolved massive star (core helium abundance ~ 0.8). The initial mass of the model is $30 M_{\odot}$. The convective core and the hydrogen-rich envelope are colored red and green, respectively. The transition zone with the helium-gradient is colored yellow.

stars start hydrogen burning at the ZAMS and, in the following, move slightly to the upper right in the HR diagram. During this phase, the hydrogen in the convective stellar core is converted into helium. At the same time, the mass of the convective core shrinks. This process leaves a distinct imprint on the chemical profile of the star. A transition zone above the convective core where the material becomes increasingly hydrogen-enriched outwards. Fig. 1.4 shows the helium abundance Y , i.e., the helium mass fraction, as a function of the mass coordinates for a stellar model with an initial mass of $30 M_{\odot}$ that already consumed a large fraction of its core hydrogen. In this model, only 20% of the core material is hydrogen. Consequently, the core helium abundance is $Y_C \sim 0.8$.

When the core hydrogen is wholly converted into helium, the energy generation via core hydrogen burning in the stellar center drops to zero. The star is left with a helium core surrounded by a shell where hydrogen burning continues. Without energy release in the stellar center, the central temperature gradient would vanish after a thermal timescale. However, this is not a stable situation for the core since it has to maintain a pressure gradient large enough to support itself and the stellar envelope on top against gravity. This pressure gradient can only be acquired by a temperature gradient, which in turn is related to an energy release from the core. The star's only possibility to do this is by contracting again and thereby converting gravitational energy into heat, i.e., the next round of the vicious virtual cycle. While the core contracts, the hydrogen-rich envelope expands. The stars' effective temperatures decline further, and their luminosity increases. The star moves rapidly to the upper right of the HR diagram (cf. Fig. 1.3) and is now called a red giant.

The contraction of the helium core increases its density and temperature according to the virial theorem. Eventually, the conditions in the stellar center are sufficient to ignite core helium burning. The principal reactions during this burning stage are the triple-alpha process, which converts three helium nuclei into a carbon nucleus, and a successive alpha

capture of the carbon nuclei, which leads to the generation of oxygen. After consuming the core helium, a carbon-enriched core is left surrounded by a shell where helium burning takes place. The vicious viral cycle starts round after round, producing heavier and heavier nuclei. Carbon burning produces a neon-enriched core, neon burning yields an oxygen core and oxygen burning produces a silicon core until silicon burning forms an iron core (Woosley et al. 2002). At this point, nuclear burning in the core has to end since the fusion of iron nuclei is an endothermic reaction.

At this stage, the star possesses an onionlike structure consisting of an iron core in the center surrounded by shells of elements whose cores become lighter the further out the shell lies (Kippenhahn and Weigert 1990, p. 329). Note that this is a significantly simplified picture of the late stages of massive star evolution. The nuclear processes taking place during this phase are much more complicated and require detailed modeling. However, this picture is sufficient for this thesis since we will not deal with these advanced evolutionary stages. This is justified by a timescale argument: Every of the subsequent nuclear burning stages has a shorter time scale than the one before. The reason for this is that the burning of heavier elements must take place at a higher temperature due to the increase of the repulsive Coulomb forces of the nuclei. The larger temperature increases the nuclear reaction rates and the energy loss due to neutrinos, which do not interact with the stellar material and thus do not support the star against gravity (Clayton 1968). Consequently, from the ignition of hydrogen at the ZAMS to the formation of the iron nucleus, the star spends 90 percent of its lifetime burning hydrogen and about 10 percent burning helium (Woosley et al. 2002). The higher burning stages are considerably shorter in time. Silicon burning, for example, takes only a few days or hours. For this reason, almost all stars we observe are burning hydrogen or helium in their cores.

1.2.3 The Eddington luminosity

Massive stars show large luminosities and, hence, large radiative pressure at the surface. The Eddington luminosity is defined by the balance between the outward force of radiative pressure and the inward force of gravitational attraction in a star. If the material is optically thick, the energy transport can be written as a diffusion equation (Kippenhahn and Weigert 1990), and the corresponding radiative energy flux is $f_{\text{rad}} = -\frac{c}{\kappa\rho}\frac{\partial P_{\text{rad}}}{\partial r}$ (Cox and Giuli 1968). Assuming hydrostatic equilibrium and introducing this into Eqns. 1.1 and 1.2 yields

$$f_{\text{rad}} = \frac{c}{\kappa} \cdot \frac{GM}{R^2}. \quad (1.14)$$

Note that M and R are the total mass and radius of the star since we consider the stellar surface. The corresponding luminosity can be computed by multiplying the flux with the stellar surface; this defines the Eddington luminosity

$$L_{\text{Edd}} = \frac{4\pi c G}{\kappa} M. \quad (1.15)$$

The interpretation of L_{Edd} is that a body of mass M whose constituting matter has the opacity κ can only be stable if its luminosity is smaller than L_{Edd} .

Stars with luminosities close to L_{Edd} are like to several phenomena, including enhanced mass loss (Gräfener and Hamann 2008; Gräfener 2021), envelope inflation (Sanyal et al. 2015; Gräfener 2021) and the Luminous Blue Variable phenomenon (Gräfener et al. 2012; Guzik and Lovekin 2012). In addition, the Eddington limit is a fundamental concept in accretion physics, as we will see in Sec. 1.4.2.

1.2.4 Stellar Winds

The large luminosities of massive stars also cause a strong stellar wind. The most important quantities to characterize the stellar wind are the mass-loss rate \dot{M}_W and the terminal velocity v_∞ , i.e., the wind velocity at infinity. Massive stars can exhibit mass-loss rates of more than $10^{-6} \text{ M}/\text{yr}$ (Vink et al. 2001). Thus, they can lose a significant amount of their initial mass during their time on the main sequence. Consequently, the wind mass-loss has a significant influence on the evolution of massive stars (De Loore et al. 1977; Chiosi and Maeder 1986; Brott et al. 2011).

The winds of massive main-sequences stars are radiation-driven (Lamers and Cassinelli 1999, Chap. 8). The photons in the star's atmosphere move preferentially outward, i.e., away from the photosphere. In the atmosphere, photons can be absorbed by an ion and are subsequently re-emitted. Since the re-emission happens in a random direction, the mean effect of this process is a transfer of momentum from the photon flux onto the corresponding ions in the atmosphere. The ions, in turn, are coupled to the other particles in the atmosphere via scattering and electrostatic forces. This accelerates the rest of the stellar material in the atmosphere and causes the matter outflow, known as stellar wind (Lucy and Solomon 1970; Castor et al. 1975; Kudritzki and Puls 2000; Vink 2022; Björklund et al. 2023).

1.2.5 Wolf-Rayet stars

Wolf-Rayet (WR) stars were discovered by Charles Wolf and Georges Rayet in 1867 and are phenomenologically defined as hot and luminous stars showing broad emission lines in their spectra (Underhill 1968). For instance, Fig. 1.1 shows the spectrum of the Wolf-Rayet star WR 1 with prominent emission lines of helium and nitrogen. The emission lines are the result of strong stellar winds (Beals 1929) with mass loss of 10^{-6} to $10^{-4} \text{ M}_\odot/\text{yr}$ (Gräfener and Hamann 2008). The mass loss of Wolf-Rayet stars is driven by radiation pressure (Gräfener and Hamann 2008) with photons being scattered multiple times or successive redistribution and absorption of thermalized photons.

WR stars are classified into three main subtypes based on their spectral characteristics (Adhyaqsia et al. 2020; Crowther 2007):

- WN stars are characterized by strong emission lines of ionized helium and nitrogen. They may still have some hydrogen in their outer envelopes, with some late-type WN stars having up to 50% hydrogen mass fraction (Conti et al. 1983; Gräfener and Hamann 2008; Sander et al. 2014).
- WC stars show strong emission lines of ionized helium carbon and are typically

hydrogen-deficient (Torres et al. 1986).

- WO stars are distinguished by prominent oxygen emission-line features compared to WC stars (Aadland et al. 2022).

Massive stars can evolve into WR stars as they lose their hydrogen envelopes, which can happen through intrinsic mass loss (Smith and Owocki 2006), i.e., stellar winds or eruptions, or via mass transfer in binary systems (Paczynski 1976; Schootemeijer and Langer 2018). Since WR stars are highly evolved massive stars, they are considered potential progenitors of core-collapse supernovae (Skinner et al. 2019) and may leave behind a compact object such as a neutron star or a black hole (Heger et al. 2003; Belczynski and Taam 2008; Higgins et al. 2021).

1.2.6 Core-collapse supernova

After the conversion of silicon into iron, the star cannot go on with the vicious virial cycle since the fusion of two iron nuclei is an endothermic reaction. Furthermore, the iron core becomes unstable due to electron capture and photodisintegration, leading to the collapse of the core (Janka 2012; Couch et al. 2015). At some point during the collapse, the matter in the central region consists predominantly of neutrons since the extreme central density causes the electrons to be captured by the protons. At the same time, the collapse produces a shock front that initially moves inwards but is reflected outwards when the core reaches nuclear density (Thompson et al. 2003). As a result, the outer layers of the star are expelled violently into space, producing a bright outburst of energy and light (Kotake et al. 2006).

If the core is not too massive, the only thing left is the collapsed, neutron-rich core, a neutron star. If, on the other hand, the core is massive enough, there is no stable configuration for a neutron star, and the core material collapses into a space-time singularity surrounded by an event horizon, a black hole is born. For the formation of neutron stars and black holes during the core collapse, see O’Connor and Ott (2011); Ugliano et al. (2012); Ertl et al. (2016); Sukhbold et al. (2016); Pejcha (2020).

1.2.7 Neutron stars

One of the fundamental rules of quantum physics is the Pauli principle, which states that a quantum mechanical state (defined by position and momentum) can only be occupied by one fermion (e.g., electrons, neutrons, protons, etc.). A consequence of this rule is the strange behavior of fermion gases when compressed to high densities. The compression decreases the distance between the particles, forcing them to occupy states with higher momentum and, hence, higher energy. On the macroscopic level, the additional momentum induces pressure. This so-called degeneration pressure dominates the total pressure, keeping ultradense objects like white dwarfs or neutron stars in hydrostatic equilibrium (Kippenhahn and Weigert 1990).

The pressure-balancing gravity in a white dwarf is induced by the degeneracy of electrons. It can be shown that white dwarfs become more compact as their mass increases

(Camenzind 2007). Hence, the electrons in more massive white dwarfs have a higher momentum on average and, thus, a higher mean energy. As the energy becomes comparable to the rest mass energy of the electrons, the particle behaves relativistic. This has dramatic consequences for the stability of the dwarf. A self-gravitating sphere balanced by the degeneracy pressure of completely relativistic electrons is always unstable. The maximum mass to which a white dwarf is stable is $\sim 1.4 M_{\odot}$, also known as Chandrasekhar mass (Chandrasekhar 1931). An impressive evidence of the Chandrasekhar mass limit is the observation of supernovae of type Ia, where a white dwarf accretes matter from a companion until it reaches the mass limit and explodes. White dwarfs are the end stages of stars with initial masses $\lesssim 8 M_{\odot}$ (Heger et al. 2003).

At densities comparable to the density of atomic nuclei, it becomes energetically favorable for electrons and protons to form a neutron via electron capture. This happens already during the core collapse of a massive star. Since neutrons are fermions, degeneracy may support the neutron aggregation against gravity. The result is a spherical object with a radius of 10 km and a typical mass of $1.4 M_{\odot}$, called a neutron star (NS).

The physics of NSs, involving their structure, their formation, and their fate, is only partly understood. It is known that an upper limit for their mass exists, comparable to the Chandrasekhar limit of white dwarfs. With the advent of gravitational wave astronomy and the observation of a merging NSs binary, the mass limit due to dynamical instability was estimated to be $\sim 2.2 M_{\odot}$ (Rezzolla et al. 2018; Ruiz et al. 2018; Cromartie et al. 2020).

In addition to their compactness, NSs are the most magnetic objects in the universe. The strength of the magnetic field can be of the order of 10^{12} G as observed in some X-ray pulsars (Taani et al. 2018) and even exceed 10^{14} G in magnetars (Gourgouliatos et al. 2016). Also, NSs are fast rotators, with a spin period of a few seconds down to a few milliseconds. This magnetic field, together with the fast rotation, induces the emission of radio light along the symmetry axis of the magnetic dipole. This radio beam acts like a lighthouse when hitting the earth. A terrestrial radio telescope records a pulsating point-like signal, a pulsar.

Pulsars are not the only observational manifestation of NSs. They also emerge as compact companions in X-ray binaries. The accretion and consequent X-ray emission involved make NS-hosting X-ray binaries important astrophysical laboratories to probe NS physics independently of the radio pulsar phenomenon. For instance, the plasma of the accretion flow interacts with the strong magnetic field of the NS. As a consequence, additional absorption lines in the X-ray regime can be observed (Voges et al. 1982; Wilson et al. 2008). These cyclotron absorption lines can be used to determine the magnetic field strength of NSs (Taani et al. 2018).

The plasma of the accretion flow is also captured by the field lines at high field strength, i.e., close to the NS. The region of space surrounding the NS, where the magnetic field guides the motion of the plasma, defines the magnetosphere. Following Elsner and Lamb (1977), the magnetospheric radius R_{mag} can be estimated using the Alfvén radius, which is defined as the distance from the NS where magnetic energy density and the dynamical ram pressure of the gas are equal,

$$\frac{B^2}{8\pi} = \frac{1}{2}\rho \cdot v^2, \quad (1.16)$$

where B denotes the strength of the magnetic field, ρ the mass density, and v the velocity of the accreted material. We assume spherical symmetry of the accretion flow and that the material moves with free fall velocity. Furthermore, the NS's magnetic field is assumed to be a dipole field. Then, the three quantities depend on the distance to the neutron star as

$$B \approx \frac{\mu_{\text{mag}}}{R_{\text{mag}}^3}, \quad v = \sqrt{\frac{2GM_{\text{NS}}}{R_{\text{mag}}}}, \quad \rho = \frac{\dot{M}_{\text{A}}}{4\pi R_{\text{mag}}^2}, \quad (1.17)$$

where μ_{mag} is the magnetic momentum of the neutron star. This set of equations, together with Eq. 1.16, yields the Alfvén radius (Bozzo et al. 2008)

$$R_{\text{mag}} = \left(\frac{\mu_{\text{mag}}^4}{2GM_{\text{NS}}\dot{M}_{\text{A}}} \right)^{1/7}. \quad (1.18)$$

It is important to note that the Alfvén radius is only a rough estimate for the magnetospheric radius since the magnetic field is assumed to be a dipole field. However, the plasma inside and outside the magnetosphere disturbs the magnetic field. Thus, an exact determination of the magnetospheric radius requires a full magnetohydrodynamical treatment of the accretion flow and the magnetic field, which is beyond the scope of this thesis. It is sufficient to note that numerical studies (Long et al. 2005; Bessolaz et al. 2008) suggest that R_{mag} is indeed of the order of the Alfvén radius.

Inside the magnetosphere, the plasma moves along the magnetic field lines, where it falls consequently onto the magnetic poles of the NS. Consequently, X-rays are emitted mainly from the polar regions, which act as two hot spots. This phenomenon is similar to the beamed radio emission of a (radio) pulsar and is indeed observed as a periodical X-ray pulsar as reported by Alpar et al. (1982).

1.2.8 Black holes

If the collapsing core of a dying massive star is too massive to form NS, it collapses into a black hole and represents the highest compactness that an object of a certain mass can achieve (Shapiro and Teukolsky 1986; Camenzind 2007; Misner et al. 2017). Black holes are an extreme configuration of space-time and are described by metric, which is the solution of Einstein's field equations (Einstein 1915). The collapsed material forms a singularity and is wrapped in an event horizon, which separates its interior from the surrounding space-time (Smith and Mann 2014). This means that no information from the inner part of the black hole can leave the hole. On the other hand, material and even light may pass the event horizon, falling to the singularity. The property of swallowing information makes a black hole a simple object in the sense that a small set of independent parameters describes it. According to the *no-hair theorem* (Herdeiro and Radu 2015; Misner et al. 2017), a stationary black hole is fully described by three parameters: its mass, angular momentum, and electrical charge.

In this thesis, we will focus primarily on non-rotation and electrically neutral black holes, which are described by the Schwarzschild metric (Schwarzschild 1916). In this met-

ric, the radius of the event horizon is the Schwarzschild radius

$$R_S = \frac{2GM}{c^2} \quad (1.19)$$

where c is the speed of light in vacuum.

In Newtonian physics, a test particle in the gravitational field cannot come arbitrarily close to the center of gravity if it has a non-vanishing angular momentum. The reason for this is the centrifugal barrier of Newtonian gravity, which arises from the fact that the effective potential diverges as the particle comes closer and closer to the center of gravity. Vividly said, the centrifugal force (that tries to push the particle outwards) increases faster than the gravitational force (that pulls the particle inwards) when the distance to the gravitational center becomes smaller. This means there is always an equilibrium situation possible, where centrifugal force and gravitational force cancel each other out, and the particle revolves around the center in a circular orbit.

The situation is quite different if we consider the trajectory of a test particle around a black hole on scales that are comparable to the Schwarzschild radius. In this case, the effects of general relativity have to be included. They cause the effective potential to diverge against *negative* infinity. This can be understood as the effect of higher terms of the gravitational force in the post-Newtonian treatment. These higher terms cause the gravitational force to increase faster than the centrifugal force as the particle approaches the gravitational center. Consequently, the distance from the center to the particle decreases, which makes the gravitational force even stronger than the centrifugal force. In this situation, no stable circular orbit is possible. Since higher terms of the gravitational force are only important for small distances from the singularity, particles far away from the center of gravity can still find a circular orbit. Thus, an innermost stable circular orbit (ISCO) must exist (Barack and Sago 2009). For a non-rotating black hole this ISCO is located at $R_{\text{ISCO}} = 3R_S$ (Camenzind 2007; Misner et al. 2017).

As we will see below, the existence of the ISCO has important consequences for the accretion physics of black holes. Since an accretion disc is, simply speaking, only a mass of particles moving on a circular orbit, the inner edge of the disc will never be closer to the singularity than R_{ISCO} . Every matter that passes the ISCO inwards will immediately fall into a black hole. This also means that a disc with a size smaller than R_{ISCO} will never form.

1.3 Aspects of binary stars

Until now, we have discussed the evolution of a single star, neglecting the influence of a potential companion. However, the vast majority of massive stars are born in binaries or higher multiple systems (Sana et al. 2008, 2009, 2011, 2013, 2014; Kobulnicky and Fryer 2007; Kobulnicky et al. 2014; Dunstall et al. 2015). In these systems, interactions such as mass transfer, mergers, and tidal forces significantly influence the evolution of the stars (Sana et al. 2012; de Mink et al. 2012). In addition, binarity enables us to detect compact objects via their gravitational pull on their host star or due to accretion-powered X-ray emission, as we saw in Sec.1.1. Hence, this chapter is dedicated to laying out the basic processes associated with massive binary stars.

A binary system can be modeled as a classical two-body problem. The two stellar components with masses M_1 and M_2 orbit their common center of mass with an orbital period P_{orb} and in an ellipse-shaped orbit with a semi-major axis a . The orbital period, semi-major axis, and the stellar masses are related via Kepler's third law

$$\frac{a^3}{P_{\text{orb}}^2} = \frac{G(M_1 + M_2)}{4\pi^2}. \quad (1.20)$$

We will often assume that the orbital is circular. In this case, a is equal to the distance of the two stars.

1.3.1 The Doppler effect and spectroscopic binaries

Light can be described as an electromagnetic wave. Like other waves (e.g., sound, water waves, etc.), the Doppler effect is also found with light. If a wave transmitter moves towards an observer, the wave's frequency appears larger to the observer and the wavelength smaller. If the transmitter moves away from the observer, it does not measure a lower frequency and a longer wavelength. This phenomenon is often observed in everyday life with a passing ambulance. Its tone sounds higher when it comes towards us and lower when it moves away from us. For a stellar spectrum, this effect causes a shift of spectral lines toward the blue if the star moves in our direction and a red shift if it moves away from us. Suppose a spectra line was observed at wavelength λ_0 if the star was at rest. Due to the Doppler effect, the observed wavelength of the line is shifted by an amount of $\Delta\lambda$. The Doppler shift depends on the star's radial velocity v_{rad} (RV), i.e., the velocity component along the line of sight. If $v_{\text{rad}} \ll c$, where c is the speed of light, one finds

$$\frac{\Delta\lambda}{\lambda_0} = \frac{v_{\text{rad}}}{c}. \quad (1.21)$$

If a visible star in a single-lined binary orbits the system's center of mass, it will move toward and away from us in one orbit. If we suppose the orbit to be circular, the star moves with constant orbital velocity $v_{\text{orb};1}$. Due to the orbital motion, the radial velocity of the star changes periodically between the values $\pm \sin(i) v_{\text{orb};1}$. Here, i is the orbital in-

clination, i.e., the angle between the orbital axis and the line of sight toward the observer. The period of the RV variations then corresponds to the orbital period of the binary P_{orb} . The quantity $K_1 := \sin(i) v_{\text{orb};1}$ is the semi-amplitude of the periodic variation of v_{rad} and can, in principle, be inferred from the minimum/maximum Doppler shift over one period.

From the P_{orb} and K_1 one defines the mass function f_1 of a single-lined binary as (Shore 1994)

$$f_1 = \frac{P_{\text{orb}} \cdot K_1^3}{2\pi G}. \quad (1.22)$$

Suppose the binary has a visible companion of mass M_1 and an invisible companion of mass M_2 . The mass function can then be rewritten using Kepler's third law, Eq. 1.20

$$f_1 = \frac{M_2^3 \sin^3(i)}{(M_1 + M_2)^2}. \quad (1.23)$$

We see that f_1 has the dimension of a mass, and since $\sin(i)$ is always smaller than unity, it can be used as a lower limit for the unseen companion's mass M_2 .

1.3.2 Mass transfer and Roche potential

The most crucial effect of binarity is the fact that the binary components may interact during their evolution. This happens, for instance, when one of the stars expands, and its outer layers become subject to the gravitational attraction of its companion. Consequently, mass transfer from one star (*the donor*) to the other (*the accretor*) is initiated.

A simplified picture of the mass transfer is the Roche-lobe overflow (RLOF). Assuming that the binary orbit is circular and both companions are in corotation with the orbital movement, the mass transfer can be modeled as a restricted three-body problem in a corotating frame. In this case, one can define an effective potential (Flannery 1977)

$$\Phi(\vec{r}) = -\frac{GM_1}{|\vec{r} - \vec{r}_1|} - \frac{GM_2}{|\vec{r} - \vec{r}_2|} - \frac{1}{2}|\vec{\Omega} \times \vec{r}|^2. \quad (1.24)$$

Here, indices 1 and 2 of the mass and position refer to the stellar companions, and $\vec{\Omega}$ is the angular velocity vector of the binary, directly perpendicular to the orbital plane. The first two terms in Eq. 1.24 reflect the gravitational forces on a small test particle from the two stars. The third term arises from the effect of centrifugal force in the corotating frame. As an example, Fig. 1.5 shows the effective potential of a binary system with mass ratio $q = 2$ as a function of the position in the orbital plane. It is important to note that the figure shows a two-dimensional section through the potential defined in three spatial dimensions.

The dashed lines indicate the intersection of the equipotential surfaces, i.e., surfaces of constant Φ , with the orbital plane. Close to the center of mass of each binary component, the equipotential surfaces are nearly spherical since the gravity of the corresponding star dominates the potential. With increasing distance from the center, the equipotential surfaces become more elongated towards the other star. This is the effect of the gravitational pull due to the companion star and centrifugal force.

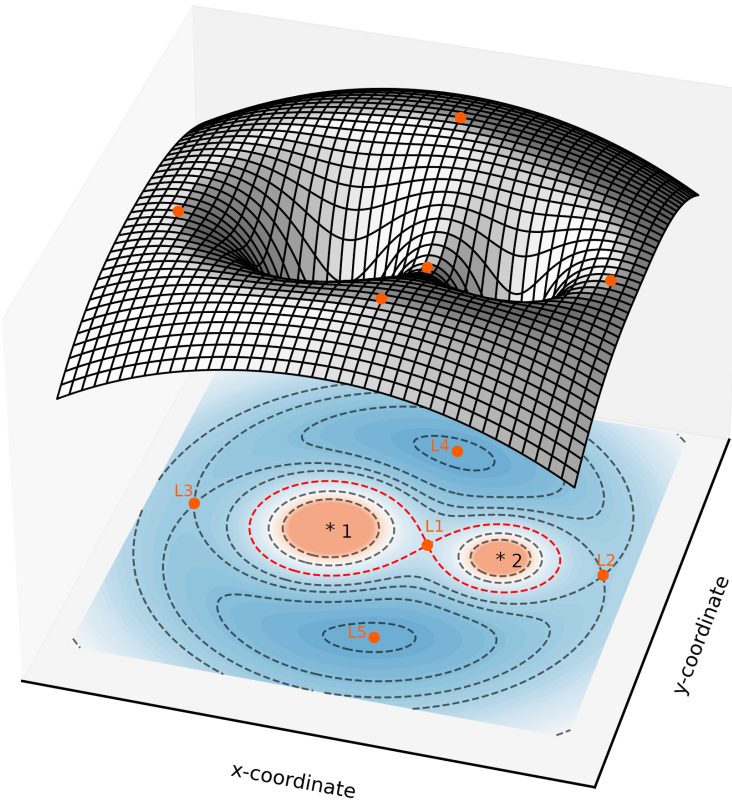


Figure 1.5.: Three-dimensional illustrations of the Roche potential for a binary with mass ratio $q = 2$. The tiled surface at the top shows the potential troughs. The contour plot at the bottom represents a projection of the Roche potential. The asterisks indicate the center of mass of each binary companion. The dashed lines indicate equipotential surfaces. The red line indicates the equipotential surface that delimits the Roche lobes. In both plots, the Lagrangian points L1 to L5 are shown as orange dots. The more massive star (1) has a larger Roche lobe than the less massive companion (2). Note the potential spout at the first Lagrangian point, which can easily be seen in the tiled surface between the potential pits of the two stars.

In Fig. 1.5, five points can be identified where the gradient of Φ vanishes. Consequently, the total force, i.e., the sum of gravitational attraction and centrifugal force acting on a mass element resting at such a point, is zero. The first of these Langragnian points lies between the two binary companions on the line connecting the centers of mass. The Langragnian points L2 and L3 are located on the same line; however, they lie on the opposite side of the companion star. L4 and L5 are of minor importance to binary evolution.

The equipotential surface highlighted in red is highly important for mass transfer processes. The two pear-shaped volumes enclosed by this critical surface are called Roche lobes. If both stars in a binary are smaller than their corresponding Roche lobe, the system is said to be detached. During its evolution, one companion may increase its radius so that it fills its Roche lobe. In this case, mass transfer from this star to the other binary companion is initiated. In this case, the system is semi-detached (Tauris and van den Heuvel 2023). If both stars fill their Roche lobes, the system is a contact binary (Qian et al. 2020).

In order to use one-dimensional stellar models, one defined the Roche-lobe radius R_L as the radius of a sphere with the same volume as the Roche lobe. Assume the mass ratio

of the binary is $q = M_1 M_2$. Using numerical calculations Eggleton (1983) found an approximation of the Roche-lobe radius of the star with mass M_1

$$R_L = \frac{0.49q^{2/3}}{0.6q^{2/3} + \ln(1 + q^{1/3})} \cdot a, \quad (1.25)$$

where a is the orbital separation. Eq. 1.25 shows that R_L is proportional to the orbital separation. Consequently, the mass transfer can be initiated if one of the stars expands or if the orbital separation decreases. In both cases, the stellar radius of the donor star matches the Roche radius at some point, i.e., the donor fills its Roche lobe. This leads to a flow of mass from the donor via the Lagrangian point L1 into the Roche lobe of the binary companion, where it can be accreted onto the star (Kolb and Ritter 1990).

Mass transfer can occur at different stages of stellar evolution. Consequently, different cases of mass transfer are categorized based on the evolutionary stage of the donor star at the onset of the mass transfer (Kippenhahn and Weigert 1967). These categories help in understanding the dynamics and outcomes of this process in a binary system.

- **Case A:** The mass transfer occurs when the donor star is still hydrogen burning (de Mink et al. 2007; Hennecou et al. 2024).
- **Case B:** If the orbital separation is large, mass transfer is not initiated during hydrogen burning. Instead, after core hydrogen depletion, the donor star expands and fills its Roche lobe in this stage (Leonard 1996; Gosnell et al. 2019).
- **Case C:** This mass-transfer case occurs when the donor star exhausts its core helium. This late-stage transfer is characterized by deep convective envelopes and significant expansion of the donor star, often leading to a common-envelope scenario (Leonard 1996; Gosnell et al. 2019).

1.3.3 Drivers of mass transfer

Mass transfer can be driven by a number of different processes. The timescale of the driving process τ approximately determines the mass transfer rate \dot{M} :

$$\dot{M} \sim \frac{M_1}{\tau}, \quad (1.26)$$

where M_1 denotes the donor's mass. The mechanisms driving the mass transfer may be divided into intrinsic and extrinsic processes. *Intrinsic* processes are determined by changes due to nuclear, thermal, or dynamical processes and occur on the corresponding timescale (Ge et al. 2010):

- **Mass transfer on a nuclear timescale:** The mass transfer is driven by the nuclear evolution on the donor star, for instance, the expansion of the donor during hydrogen burning. The corresponding mass transfer rate can be found from Eq. 1.13: $\dot{M}_{\text{nuc}} \sim 10^{-10} M_{\odot}/\text{yr} \cdot \left(\frac{M}{M_{\odot}}\right)^{3.4}$, which implies a mass-transfer rate of $10^{-5} M_{\odot}/\text{yr}$ for a $30 M_{\odot}$ main sequence donor.

- **Mass transfer on a thermal timescale:** The mass transfer is due to thermal adjustments of the donor star. The corresponding mass-transfer rate is (cf. Eq. 1.6) $\dot{M}_{\text{th}} \sim 10^{-7} M_{\odot}/\text{yr} \cdot \left(\frac{M}{M_{\odot}}\right)^3$, and $3 \cdot 10^{-3} M_{\odot}/\text{yr}$ for a $30 M_{\odot}$ main sequence donor.
- **Dynamically unstable mass transfer:** If mass transfer becomes unstable on a nuclear and thermal timescale, the process accelerates on the dynamical timescale of the donor star. This process may initiate a common envelope phase, in which the companions spiral towards each other, leading to an ejection of the envelope or to a merging of the binary.

Extrinsic driving processes are caused by the loss and/or redistribution of mass and angular momentum during the mass transfer, which is accompanied by a change of the orbital separation and a corresponding change of the Roche-lobe radius. To illustrate this, assume that the two binary components orbit their common center of mass along circular orbits. One can show that the change in the orbital separation a can be expressed in terms of the change in orbital angular momentum J and the change of the masses of the binary components (Tauris and van den Heuvel 2006)

$$\frac{\dot{a}}{a} = 2 \frac{\dot{J}}{J} - 2 \frac{\dot{M}_1}{M_1} - 2 \frac{\dot{M}_2}{M_2} + \frac{\dot{M}_1 + \dot{M}_2}{M_1 + M_2} \quad (1.27)$$

In general, one needs to consider various channels of angular momentum loss (see below). Moreover, it is important to note that angular momentum loss and mass loss are often interconnected and not mutually independent.

A simple yet important scenario arises when both the angular momentum and total mass of the binary remain conserved, i.e., $\dot{J} = 0$ and $\dot{M}_1 = -\dot{M}_2$. In this case, the first and the last term at the right-hand side of Eq. 1.27 vanish, which yields

$$\frac{\dot{a}}{a} = 2 \left(\frac{1}{M_2} - \frac{1}{M_1} \right) \dot{M}_1. \quad (1.28)$$

Assume that mass is transferred from M_1 to M_2 , i.e., $\dot{M}_1 < 0$. Eq. 1.28 shows that the orbital separation will increase if $M_1 < M_2$. Vice versa, a decreases if $M_1 > M_2$. Hence, conservative mass transfer leads to orbit expansion when matter moves from the less massive companion to the more massive one and, conversely, causes orbit contraction when the transfer is from the companion of larger mass to the less massive one.

- **Gravitational wave emission**

Angular momentum is lost due to the emission of gravitational waves (Landau and Lifschitz 1976; Peters 1964). However, the timescale of this process is large compared to the lifetime of a massive star and thus neglected in massive binary evolution (Tauris and van den Heuvel 2006).

- **Magnetic breaking**

The coupling of a magnetic field to the stellar wind efficiently drains the star's spin angular momentum, slowing down the rotation of the star (Mestel 1968; Skumanich 1972). This process is also assumed to be neglectable in massive binaries since most

massive stars do not show strong magnetic fields (Fossati et al. 2015; Grunhut et al. 2017).

- **Spin-orbit coupling**

If the donor star contracts or expands, the conservation of its spin angular momentum makes the star spin faster or slower, respectively. However, tidal forces try to keep the donor star in corotation with its binary companion. Thus, during the contraction of the donor, angular momentum is transferred from the donor star to the orbit, increasing the orbital separation (Tauris and Savonije 2001). On the other hand, if the donor expands, angular momentum has to be pumped from the orbit into the donor's corotation spin, which causes the orbit to shrink (Tauris 2001).

- **Mass loss from the system**

In general, matter that leaves the binary carries a certain amount of angular momentum. In high-mass X-ray binaries, the mass loss is due to the donor star's direct stellar wind as well as the accretion and the subsequent isotropic re-emission of mass by the accretor (Soberman et al. 1997; Tauris and van den Heuvel 2006). Massive stars have a strong stellar wind. In addition, their thermal and nuclear timescales (Eqns. 1.6 and 1.13) are significantly smaller than those of low-mass stars, which results in a correspondingly higher mass transfer rate. Consequently, the angular momentum loss is considered the dominant drive of angular momentum loss, especially if the donor star is massive (Tauris and van den Heuvel 2006, 2023).

1.3.4 Stability of mass transfer

Once the mass transfer is initiated, the further evolution of the binary depends on the mass transfer stability. Suppose the donor was in hydrostatic and thermal equilibrium before it reached its Roche lobe and began to transfer mass. Due to the loss of mass, both of these equilibria are disturbed. Consequently, the star will grow or shrink in radius to restore them. However, since the mass transfer changes the mass ratio q and the orbital separation a , the Roche-lobe radius will change (cf. Eq. 1.25). As long as the star is enclosed by the Roche lobe, mass transfer is stable.

On the other hand, if the Roche lobe shrinks faster than the stellar stellar radius, the mass transfer rate would increase further, which reinforces the decrease of the Roche lobe. In this case, the mass transfer becomes unstable. Thus, mass-transfer stability is determined by the response of the stellar radius compared to the response of the Roche-Lobe radius (Hjellming and Webbink 1987; Soberman et al. 1997). To quantify the response of the two radii, we define the mass-radius exponents (Ge et al. 2010) of the donor radius (ζ_R) and the Roche radius (ζ_L),

$$\zeta_R := \frac{d \ln(R_1)}{d \ln(M_1)} \quad \text{and} \quad \zeta_L := \frac{d \ln(R_L)}{d \ln(M_1)}. \quad (1.29)$$

For stable mass transfer, the donor radius must not shrink slower than the Roche radius.

Thus, the stability criterion for mass transfer can be written as

$$\zeta_R \geq \zeta_L. \quad (1.30)$$

Note that ζ_R and ζ_L can change during the mass transfer. Hence, an initially stable mass transfer may become unstable and vice versa (Kalogera and Webbink 1996).

The value of ζ_R depends on the stellar model and whether or not the star can maintain hydrostatic or thermal equilibrium, i.e., on the timescale of mass transfer. Considering isotropic re-emission, Tauris and Savonije (1999) derived an analytical expression for ζ_L , which yields large values for ζ_L for high mass ratios². Consequently, binaries with large mass ratios, such as NS-hosting HMXBs, are more likely to undergo unstable mass transfer. In Chap. 2, we will discuss the mass-radius exponents, their values, and their implications for mass transfer stability in more detail.

1.3.5 Common envelope

When mass transfer becomes dynamically unstable, this runaway process causes the accretor to be engulfed in the donor's envelope (Paczynski 1976). During this common envelope (CE) phase, a drag acts on the accretor, which spirals towards the donor, thereby injecting orbital angular momentum and energy into the envelope (Izzard et al. 2012). This can cause the ejection of the envelope, leaving a close binary system behind. Another possibility is the total coalescence (merging) of the binary companions to one object.

Although the CE phase is an important phase in the evolution of close binaries (Iben and Livio 1993; Taam and Sandquist 2000; Podsiadlowski 2001; Taam and Ricker 2010), the details of this process are poorly understood. A simple approach to model the outcome of a CE phase was proposed by (Webbink 1984) and de Kool (1990). Assuming that the energy necessary to unbind the envelope is provided by the release of orbital energy from the spiral-in of the binary, one can derive the change of orbital separation (see for instance Tauris and van den Heuvel 2006; Ivanova and Chaichenets 2011; Ivanova 2011).

1.4 High-mass X-ray binaries

The fact that binarity is common among massive stars leads to a crucial conclusion. Assuming one binary component ends its life and forms an NS or BH, and provided the orbit is not distributed due to a supernova kick (Tauris and Takens 1998), the massive binary enters the evolutionary stage where a compact object orbits a gaseous star. If this is the case, matter released by the gaseous companion (hereafter referred to as the donor star) may be captured by the gravitational attraction of the CO (hereafter referred to as accretor), falling into the CO's gravitational potential. This process, known as accretion, causes the emission of X-rays, as explained below.

The binary system then is a bright source in the X-ray sky, i.e., an X-ray binary (XRB). The observed X-ray luminosities of these sources range from 10^{33} erg/s to 10^{38} erg/s

²see Eqns. 25 and Fig. 1 in Appendix to Chap. 2

(Walter et al. 2015) but can exceed 10^{39} erg/s in some cases (c.f. Kaaret et al. 2017). The accretion luminosity is proportional to the amount of material captured by the accretor per unit of time, i.e., the accretion rate \dot{M}_A , and may be written as

$$L_X = \eta c^2 \dot{M}_A. \quad (1.31)$$

Where c is the speed of light, and η is the efficiency factor describing which fraction of the rest-mass energy converts into X-rays. This factor depends on the nature of the accretor. It is about 0.15 for an NS companion and, depending on the spin, between 0.06 and 0.4 for a BH accretor (c.f. Marchant et al. 2017). Assuming $\eta = 0.06$ Eq. 1.31 shows that an accretion rate of $10^{-11} M_\odot/\text{yr}$ is required to obtain an X-ray luminosity of $3 \cdot 10^{34}$ erg/s. Any physical process transferring mass from the donor to the accretor must be efficient enough to account for at least this mass-transfer rate.

The nature of the donor star has significant consequences for the evolution of the binary system, e.g., determining the mass-transfer mechanism and the timescale of evolution. Thus, it is reasonable to split X-ray binaries into Low-mass X-ray binaries (LMXB) and High-mass X-ray binaries (HMXB), depending on the donor's mass. Since this thesis focuses on binaries with a massive donor star, we are mostly interested in HMXBs.

In these systems, the accretion can be caused by three processes:

- **Mass transfer via Roche-lobe overflow** from the donor to the accretor, as shown in Fig. 1.7 and described in Sec. 1.3.2.
- **Wind accretion**, i.e., the capture of material from the stellar wind of the donor, which we will discuss in Sec. 1.4.1.
- Accretion of material from a **circumstellar disc**, which is observed in Be X-ray binaries (see Sec. 1.4.6).

1.4.1 Wind Accretion

The X-ray emission in X-ray binaries is powered by accretion, i.e., the capture of matter by the CO. One way the material is transported to the CO mass transfer is via RLOF (Sec. 1.3.2). Fig. 1.7 gives an impression of how RLOF from the massive star to the CO leads to the release of X-rays. However, RLOF is not the only process that can be used to power accretion. For instance, if the donor launches a stellar wind, the material can be captured by the accretor. This process is called wind accretion (Negueruela 2010; Shakura et al. 2014).

An approach to model wind accretion was provided by Bondi and Hoyle (1944). It is assumed that the mass flow is supersonic. This is a reasonable assumption for winds of massive stars since the speed of sound is of order 10 km/s and the wind velocity is about 1000 km/s and above (Vink et al. 2001). Then, the fluid particles can be regarded as following Keplerian trajectories in the gravitational field of the companion.

The principle situation is sketched in Fig. 1.6. The streamlines are asymptotically parallel to the left side and focus due to the gravitational attraction of the accretor. The upper and the lower streams meet in the vicinity of the line of the center, where they

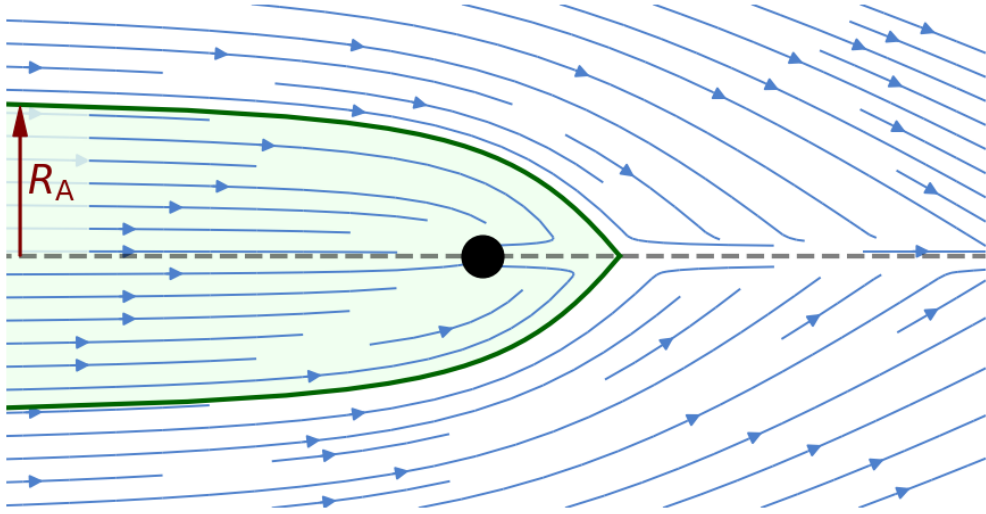


Figure 1.6.: Streamlines (blue) of the accretion flow in the Bondi-Hoyle accretion model. Streamlines in the green area are accreted onto the companion (black circle). The impact factor of the threshold (thick green line) defines the accretion radius R_A .

collide inelastically. In this collision, kinetic energy is converted into heat. Depending on the remaining kinetic energy, the material can either escape the gravitational field (flow to the right) or be accreted onto the companion. This yields a critical accretion radius R_A , which is given by

$$R_A = \frac{2GM_2}{v_{\text{rel}}^2}, \quad (1.32)$$

where M_2 is the mass of the accretor and v_{rel} is the relative velocity of the wind with respect to the accretor. Note that the relative velocity is a superposition of the wind velocity \vec{v}_W and the orbital velocity of the accretor $\vec{v}_{\text{orb};2}$, i.e., $\vec{v}_{\text{rel}} = \vec{v}_W + \vec{v}_{\text{orb};2}$.

Matter moving along the streamlines with an impact factor smaller than R_A is accreted onto the companion (green area in Fig. 1.6). Thus, the geometrical cross-section for wind accretion is πR_A^2 . Assuming an isotropic stellar wind, this yields an accretion rate of

$$\dot{M}_A = \frac{G^2 M_2^2}{v_{\text{rel}}^4 a^2} \cdot \dot{M}_W \quad (1.33)$$

where \dot{M}_W is the mass-loss rate of the donor star. For instance, a $10 M_\odot$ BH accretor in a binary with $100 R_\odot$ orbital separation and a relative wind velocity of 1000 km/s would accrete a fraction of 3×10^{-4} from the donor's wind. Assuming a mass loss rate of $10^{-6} M_\odot/\text{yr}$ and an accretion efficiency of 0.06, this would produce an luminosity accretion luminosity of $\sim 10^{36}$ erg/s. If the accretor is a BH, this presupposes, however, that the matter has time to radiate the released gravitational energy before it passes the event horizon, e.g., in an accretion disc. In the case of a NS the matter will eventually hit the surface of the accretor and radiate the released gravitational energy anyway.

To form such a disc, the accreted material needs angular momentum. Naively, based on the symmetry of the flow with respect to the accretor (cf. Fig 1.6), one would expect

the angular momentum to vanish. However, Shapiro and Lightman (1976) showed that the superposition of the orbital motion of the accretor and radial symmetric motion of the stellar wind induce angular momentum of the accreted matter with respect to the accretor. The specific angular momentum j is given by

$$j \approx \frac{v_{\text{orb},2} R_{\text{A}}^2}{a}. \quad (1.34)$$

Note that the accreted angular momentum is proportional to R_{A}^2 and thus proportional to v_{rel}^{-4} (cf. Eq 1.32). Hence, the angular momentum is significantly larger if the relative velocity between wind and accretor is smaller. This has important consequences for the formation of accretion discs, as we will see in the course of this thesis.

1.4.2 X-ray emission

Accretion is a process in which the gravitational energy of the accreted material is released efficiently and converted into kinetic energy of the free fall. In general, the free fall velocity is large, implying a large Reynold number and, consequently, turbulences, which convert the kinetic energy of the directed movement into heat. As a consequence, the accreted material starts radiating its energy into space.

Assuming a spherical accretor, we may estimate the amount of energy that is released per unity time (i.e., the luminosity), assuming that the released gravitational energy is converted into radiation. This yields an accretion luminosity of

$$L_{\text{acc}} = G \frac{\dot{M}_{\text{A}} M_{\text{A}}}{R}, \quad (1.35)$$

\dot{M}_{A} is the accretion rate, M_{A} the mass of the accretor, and R its radius. This equation shows that the luminosity is not only proportional to the amount of accreted matter but also to the compactness of the accretor $\frac{M_{\text{A}}}{R}$. Hence, it is not surprising that the most efficient radiation sources powered by accretion are ultra-dense and exotic astrophysical objects, like neutron stars and black holes. It is important to note that neutron stars have a solid surface. The horizon of a black hole, on the other hand, is rather a boundary in space-time, marking the point of no return for matter falling into the black hole. This implies an important difference in the accretion physics for black holes: While matter falling *onto* a neutron is always stopped and radiates its energy away, material falling *into* a black hole can drag its heat over the horizon and into the black hole, where it can not escape anymore. It is, hence, possible that a black hole, while the most compact object in nature, has a much fainter accretion luminosity than a neutron star.

As most stellar radiation sources shine due to their internal heat, accreting NSs and BHs may be modeled as black bodies for a rough estimate. Equating Eqns. 1.11 and 1.35 yields the effective temperature of the accreting body

$$T_{\text{eff}} = \sqrt[4]{\frac{G}{4\pi\sigma} \frac{\dot{M}_{\text{A}} M_{\text{A}}}{R^3}}. \quad (1.36)$$

We then can apply Wien's displacement law for black-body radiation

$$\lambda_{\max} = \frac{2.9 \times 10^6 \text{ \AA K}}{T_{\text{eff}}}, \quad (1.37)$$

where λ_{\max} is the wavelength where most of the energy is released. Using Eq. 1.36 we may express this in the more convenient way as

$$\lambda_{\max} = 8.8 \text{ \AA} \left(\frac{R}{\text{km}} \right)^{3/4} \left(\frac{\dot{M}_A}{10^{-14} M_{\odot}/\text{yr}} \right)^{-1/4} \left(\frac{M_A}{M_{\odot}} \right)^{-1/4}. \quad (1.38)$$

This equation shows that a typical neutron star accretor ($R \sim 10 \text{ km}$, $M_A \sim 1.4 M_{\odot}$) emits mainly in the wavelength regime of 45 \AA when accreting $10^{-14} M_{\odot}/\text{yr}$. This wavelength corresponds to a photon energy of 27 keV , i.e. energetic X-ray photons.

As mentioned above, a BH has no definite surface from where it can emit black-body radiation. However, hot plasma that orbits the BH in an accretion disc may spend enough time in the vicinity of the ISCO to release a large fraction of its thermal energy as radiation. A rough estimate for a $3 M_{\odot}$ black hole yields a typical wavelength of 80 \AA . While it is still in the X-ray regime, the corresponding photons are less energetic than the X-ray photons emitted by a neutron star. Consequently, the wavelength where most of the energy is emitted is larger for a BH than for a NS. This can be understood with Eq. 1.38. Since $R_{\text{ISCO}} \propto M_A$ we find $\lambda_{\max} \propto M_A^{1/2}$.

1.4.3 Eddington accretion limit

The importance of the Eddington limit for accretion physics arises from the fact that the accretion process itself releases energy in the form of radiation. This means that if the accretion rate is so large that the released radiative energy per time exceeds L_{Edd} , the radiative force will push the accreted material outwards. Following this picture, the accretion luminosity L_X is limited by L_{Edd} and, since we assume $L_X \propto \dot{M}_{\text{acc}}$, so is the accretion rate. Equating Eqns. 1.15 and 1.31 yields an accretion rate of

$$\dot{M}_{\text{Edd}} = \frac{4\pi G}{\eta \kappa c} M_A \quad (1.39)$$

for an accretor at the Eddington limit (Bu and Yang 2019). Assuming electron scattering opacity of $\kappa = 0.3 \text{ cm}^2/\text{g}$ and a $10 M_{\odot}$ BH accretor with $\eta = 0.06$, we find an Eddington accretion rate of $\sim 3 \times 10^{17} \text{ g/s}$ corresponding to an accretion luminosity $\sim 2 \times 10^{37} \text{ erg/s}$. This accretion rate is a theoretical limit for the rate at which mass can be accreted by a $10 M_{\odot}$ BH without ejecting incoming material away due to the radiation pressure exceeding the gravitational pull.

1.4.4 Accretion discs

Accretion discs are present on many scales in astrophysics, from mass transfer in stellar binaries to accreting supermassive black holes. Hence, it is not surprising that the theory of disc accretion onto compact objects has been a major research field in astrophysics for half a century (Lynden-Bell 1969; Shakura 1973; Shakura and Sunyaev 1973; Novikov and Thorne 1973). To model an accretion disc, suppose that a gas element with a certain negligible mass m orbits the black hole with mass M on a circular, stationary orbit with radius R_D and velocity v . In this case, the centrifugal force balances the gravitational attraction. Equating these two forces yields

$$R_D = \frac{GM}{v^2} \quad (1.40)$$

which can be re-written as

$$R_D = \frac{j^2}{GM}, \quad (1.41)$$

where j denotes the angular momentum per unit mass. If we assume that this specific angular momentum is equally distributed over the whole material in the accretion disc, it follows from Eq. 1.41 that the material would form a ring with radius R_D .

This ring would have a finite thickness, which may be very small compared to R_D but not zero. From Eq. 1.40, we deduce that $v^2 \propto R_D^{-1}$, i.e., the inner gas elements of the ring move faster. This causes a shear and, hence, friction between the inner and the outer parts of the ring. This generates torque, transferring angular momentum from the inner border of the ring to the outer edge. As a consequence, the outer part moves outward, and the inner part moves inward, as implied by Eq. 1.41. Hence, the ring expands and spreads to a disc (see Fig. 1.7).

The physical nature of the angular momentum transport is not yet completely understood. While the thermal movement of the molecules and atoms produces the shear torque in most terrestrial flows, this process is too inefficient to fit the observations of astrophysical accretion discs. It is discussed that angular momentum transport in accretion discs is mostly due to micro-turbulence (Shapiro and Teukolsky 1986; Lipunov 1992) as well as by the interaction of the accretion flow with magnetic fields, creating magnetohydrodynamical turbulence (Balbus and Hawley 1998).

The discussion above implies that accretion discs would spread from the compact object to infinity. This is, of course, not true since the density of the disc declines outward. At a certain point, the disc is so thin that emission is inefficient, and the disc is virtually invisible. In addition, the disc size is limited by the Roche lobe of the accretor. It may be surprising that the inner edge of the disc is not determined by the surface of the compact accretor (i.e., the surface of the neutron star or the horizon of the black hole). In the case of a neutron star, the inner disc radius is of the order of the Alfvén radius (Sec. 1.2.7). The inner edge for a black hole accretor is determined by the innermost stable circular orbit (c.f. Sec. 1.2.8).

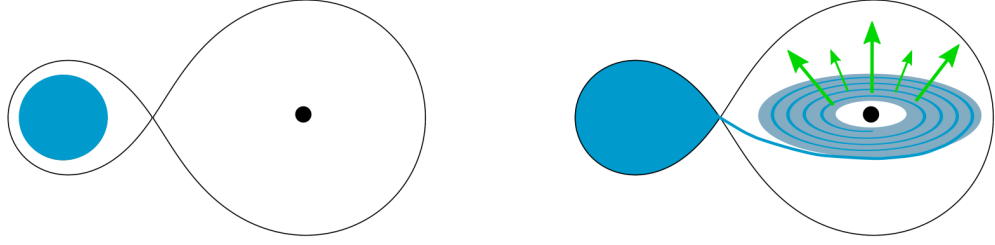


Figure 1.7.: Roche-lobe overflow in an HMXB. A massive star (blue) hosts a compact companion (black). The Roche lobes are indicated by black lines, which intersect at the first Lagrangian point. The star initially under-fills its Roche lobe (left). During its evolution, it expands and eventually fills the Roche lobe and transfers matter via the first Lagrangian point to the Roche lobe of its companion (right). The material accumulates and orbits the CO in an accretion disc. Angular momentum transport by turbulent viscosity and dragged magnetic field lines causes the matter to spiral down. The gained gravitational energy heats the material and leads to the emission of X-rays (green rays).

1.4.5 Supergiant X-ray binaries

The majority of HMXBs fall into one of two subclasses depending on the nature of the donor star: supergiant X-ray binaries or Be X-ray binaries (Coleiro et al. 2013; Walter et al. 2015).

Supergiant X-ray binaries (SGXBs) involve a supergiant star as donor and a CO accretor. These systems are mostly persistent X-ray emitters with stable luminosity, occasionally exhibiting flares (Walter and Zurita Heras 2007). These flares are thought to be caused by the interaction of the neutron star with clumps in the accreted material (Oskinova et al. 2012).

The X-ray emission can be due to the accretion from the stellar wind of the supergiant donor (Shakura et al. 2014; Giménez-García et al. 2016) or due to mass transfer via RLOF (Savonije 1978). However, RLOF would lead to a rapid shrinking of the orbit due to the large mass ratio between the donor star and the accretor, possibly leading to a common envelope phase. Van den Heuvel et al. (2017) proposed that mass transfer would be unstable when the mass ratio $q = M_1/M_2$ exceeds 3.5. Hence, RLOF in a SGXB consisting of an O star donor, and an NS accretor would likely be unstable. Thus, RLOF is often dismissed as the cause of the X-ray emission in the majority of observed SGXBs (Tauris and van den Heuvel 2006). We will discuss this problem in more detail in Chapter 2.

To illustrate the importance of the SGXB phase for the evolution of massive binaries, we will now briefly discuss the role of SGXBs in massive binary evolution. We will follow an evolutionary scenario proposed by De Loore and De Greve (1975) illustrated in Fig. 1.8. Note that this scenario is by no means to be generalized. The evolution of massive binaries depends on the initial parameters of the system and may lead to completely different evolutionary paths (Marchant et al. 2016, 2017; Kruckow 2018).

- (a) The initial binary consists of two ZAMS stars, star A and star B, orbiting each other.

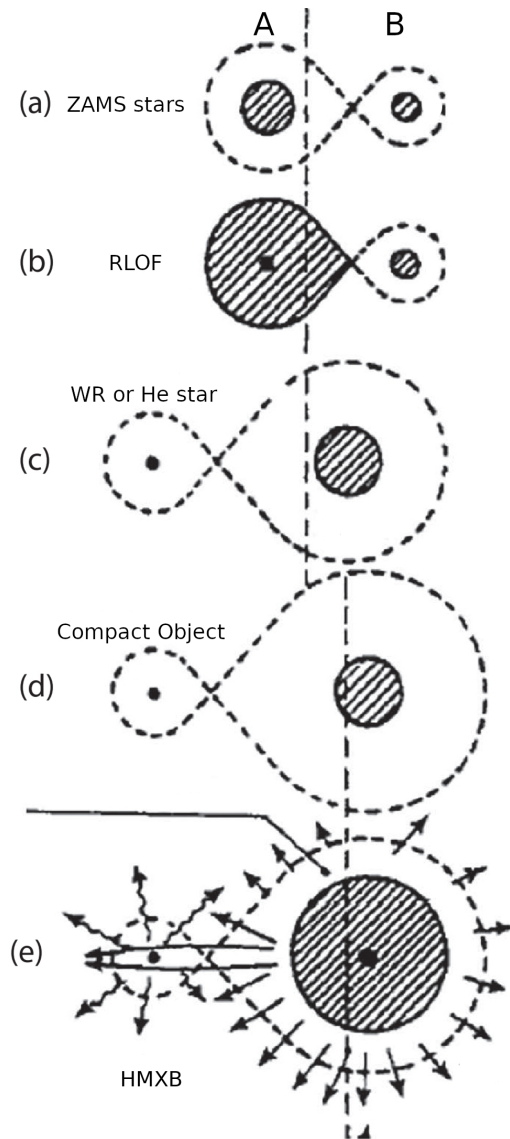


Figure 1.8.: Evolutionary scenario for the formation of a HMXB adopted from (De Loore and De Greve 1975). Image descriptions were included by the author.

- (b) The more massive star A evolves faster than its companion. After core hydrogen exhaustion, A expands and eventually fills its Roche lobe. Consequently, a phase of Case B mass transfer via RLOF is initiated.
- (c) Due to the mass transfer, star A has lost its hydrogen-rich envelope and has become a helium-enriched star. Star B has gained mass. Due to the mass transfer, the orbital separation has increased. The reason for this is that this first mass transfer is assumed to be conservative (De Loore and De Greve 1975). However, this does not have to be the case in reality. The proportion of mass lost from the system depends on complex processes within the system and is not easy to determine (Soberman et al. 1997).
- (d) At the end of its life, star A finally explodes in a supernova. The binary now consists of a compact object (A) and a massive star (B).

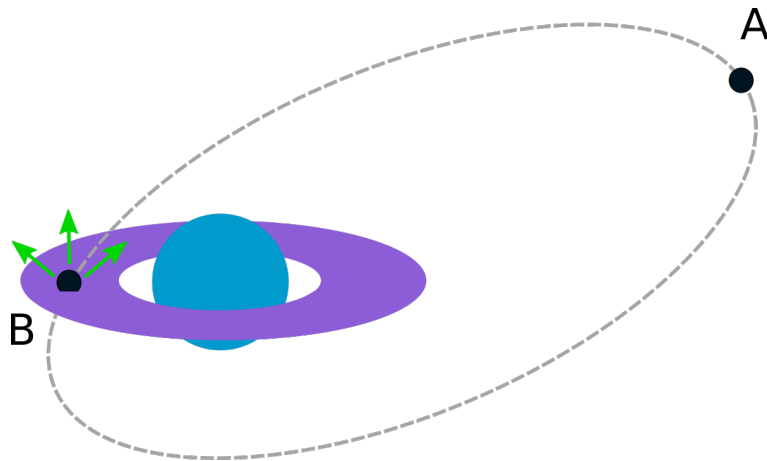


Figure 1.9.: Accretion in BeXBs. A CO orbits a Be star hosting a circumstellar decretion disc. The CO moves in a wide and eccentric orbit. Close to the apastron (A), the CO is too far from the disc to be an efficient accretor, and the system is X-ray faint. As the CO approaches the Be star on its orbit, perhaps penetrating the disc, the system becomes X-ray bright due to an enhanced accretion rate (B).

- (e) The stellar wind from star B is accreted by the compact companion powering the X-ray emission. This may happen directly after the supernova of star A or due to evolutionary changes of star B. As star B continues to evolve, it can fill its Roche lobe so that another mass transfer phase takes place. Both wind accretion and mass transfer make the system emerge as a HMXB.

The further evolution of the binary depends on the stability of the second mass transfer from B to A. This mass transfer can involve a common envelope evolution, which may lead to a merger of the two companions or a close binary. In the latter case, this leads to a binary of two compact objects when B ends its life in a supernova. These close binaries with compact components are progenitors of gravitational wave mergers (de Kool 1990; Pavlovskii et al. 2017; Tauris et al. 2017; Van den Heuvel et al. 2017; Kruckow et al. 2018).

1.4.6 Be X-ray binaries

The most numerous type of HMXBs involves a Be star, i.e., a fast-rotating early-type star displaying spectral line emission, noted by "e" in their spectral type (Rivinius et al. 2013; Porter and Rivinius 2003; Balona 2000; Struve 1931). Typically, emission lines from the Balmer series are observed alongside helium and iron lines in some cases (Hanuschik 1996). The presence of emission lines indicates the presence of a circumstellar decretion disc formed by equatorial mass outflow induced by rapid rotation and centrifugal force (Struve 1931). For illustration, we show the optical spectrum of Per X-1. in Fig. 1.1. The H α line is clearly visible in the spectrum and is a hint for the presence of a circumstellar disc.

Packet (1981) and Pols et al. (1991) demonstrated that fast rotational velocity in stars could result from spin-up via mass transfer from a companion star and subsequent angular

momentum transfer. This aligns with Be stars commonly serving as donors in HMXBs. According to this scenario, Be X-ray binaries (BeXBs) naturally emerge from binary systems, where one companion evolves faster, undergoes mass transfer via RLOF, and explodes in a supernova, leaving a CO remnant. However, it's important to note that not all Be stars are necessarily in binary systems; Hastings et al. (2020) indicated that a significant portion of Be stars may also form through a single-star pathway.

BeXBs have observed orbital periods ranging between 20 and 300 days as well as moderate eccentricities of $e \sim 0.3$ (Reig 2011). This means that BeXBs are long-period systems (compared to SGXBs). It is assumed that the wide orbital separation and the eccentricity are footprints of a supernova kick during the birth of the neutron star (van den Heuvel 1994; Tauris and van den Heuvel 2023). BeXBs typically show transient X-ray activity that correlates with the orbital period, peaking when the CO interacts with the Be star'scretion disc (Kurfürst et al. 2018). The CO accretes matter from the disc during periastron, its closest approach to the Be star. In some cases, it may even penetrate the disc. During this active accretion phase, the binary becomes a luminous X-ray source. Fig. 1.9 illustrates the two phases of X-ray faintness (A) and brightness (B) in BeXBs.

It has to be noted that the accretion mechanism, as described above, only provides a basic picture of the physics working in BeXBs. The observed X-ray behavior of these sources is far more complex and diverse. For instance, while the accretion mechanism, as depicted above, suggests that BeXBs should always be transient X-ray sources, Reig and Roche (1999) showed that (although a minority) persistent BeXBs exist. Also, transient BeXBs may undergo dramatic outbursts that occur rather spontaneously and seem to be unrelated to the orbital phase (Wilson et al. 2008; Reig 2011). These outbursts may reach the Eddington accretion rate and lead to the total disruption of the disc, as can be seen from the vanishing of the emission lines.

1.4.7 Ultra-luminous X-ray sources

It seems, indeed, that the majority of the observed X-ray binaries are not brighter than the Eddington luminosity of a $10 M_{\odot}$ BH (Walter et al. 2015). However, there is a subclass of stellar X-ray sources that are significantly brighter than the Eddington limit of a BH. These sources are called Ultraluminous X-ray sources (ULX). These sources are found in nearby galaxies and are not associated with the central nucleus (King 2001; Kaaret et al. 2017; Fabrika et al. 2021). ULXs are thought to be X-ray binaries, which include either a neutron star or a black hole accreting from a companion star at rates above the Eddington limit (Erkut and Ekş 2019).

However, the nature of the CO in ULXs is not yet fully clarified; some are stellar-mass black holes possibly accreting at super-Eddington rates (Poutanen et al. 2007; Motch et al. 2014), while others could be intermediate-mass black holes (Farrell et al. 2011), i.e., BHs with masses above $100 M_{\odot}$ (Colbert and Mushotzky 1999). At the same time, some ULXs have been identified as NS hosting, which is indicated by the detection of X-ray pulsations (Bachetti et al. 2014; Ekş 2015; Israel et al. 2017; Maitra et al. 2018). The nature of ULX, as well as their role in massive binary evolution, is not yet understood and is an ongoing subject of research (Marchant et al. 2017; Pavlovskii et al. 2017; Misra et al. 2020; Fabrika et al. 2021).

1.5 This Thesis

The general aim of this thesis is to study and analyze the processes in binary stars consisting of a massive star and a NS or BH companion from a theoretical point of view. We use the Binary Evolution Code (BEC) (Braun and Langer 1993) to compute models of single stars and binaries and apply the models for mass transfer, wind accretion, and angular momentum loss to study the X-ray luminosity and the evolution of the binary orbit.

1.5.1 Mass transfer on a nuclear timescale in models of supergiant and ultra-luminous X-ray binaries

In Chapter 2, we explore the impact of the proximity of supergiant donor stars to the Eddington limit and their advanced evolutionary stage on the behavior of mass transfer in supergiant and ultra-luminous X-ray binaries. We construct models for massive stars by varying internal gradients of hydrogen and helium as well as the masses of hydrogen-rich envelopes. These models undergo gradual mass loss to investigate the response of the stellar radius. Additionally, we used our detailed binary stellar evolution code to calculate the associated evolution of mass transfer through Roche-lobe overflow.

We observe that the presence of a hydrogen/helium gradient in the layers beneath the surface, a characteristic likely found in extensively studied donor stars of observed SGXBs, has the potential to facilitate mass transfer in SGXBs and ULXs on a nuclear timescale with a black hole or neutron star accretor, even in systems with high mass ratio. We study the change of the orbital separation and the orbital period and find our models closely correspond with observed X-ray binaries. We argue that the SGXB phase might be heralded by a preceding common-envelope evolution, which may help to dig out the hydrogen/helium gradient and lead to a phase of stable mass transfer. Consequently, we refute the long-standing argument that accretion in SGXBs must be due to wind accretion. Our findings perhaps open a new perspective for understanding that SGXBs are numerous in our Galaxy and are almost completely absent in the Small Magellanic Cloud. Since ULXs are unlikely powered by wind accretion but rather RLOF, our results may also offer a way to understand these systems and their role in massive binary.

1.5.2 X-ray emission from massive spectroscopic binaries

The aim of Chapter 3 is to develop a method for analyzing single-line massive binaries and seemingly single massive stars for a compact binary companion. As we saw above, these companions of massive stars reveal themselves through two processes. On the one hand, X-ray emission due to the accretion of material from the stellar wind and RLOF. On the other hand, the compact object induces RV variations on its binary companion.

We combine these two detection approaches by constructing a diagnostic diagram. For a given massive star with known stellar parameters, this diagram shows the expected X-ray luminosity of a putative compact companion as a function of the putative orbital period and semi-amplitude of the RV variations.

We discuss the X-ray emission of a BH fed by wind accretion and give a criterion for the formation of an accretion disc based on the accreted angular momentum. By developing a model for spherically symmetric accretion, we show that the X-ray detectability of these companions depends significantly on the formation of an accretion disc. Only if the BH forms an accretion disc, does the material have enough time to emit a detectable amount of X-rays. Otherwise, the released gravitational energy of the accreted matter is dragged into BH. The consequence of this result is that BHs can accrete a significant amount of matter but still be X-ray faint.

To distinguish between a faint main sequence and a compact companion, we develop a similar diagnostic diagram considering the ratio of the optical fluxes of the two companions and the X-ray emission that would be emitted due to the colliding winds of the two binary partners. Furthermore, we develop a diagnostic diagram to predict the X-ray emission of a putative NS companion. This diagram takes different modes of the propeller effect into account, i.e., the inhibition of accretion due to the coupling of the accretion flow to the NS's magnetic field.

1.5.3 Constraining the unseen companions of massive single-lined binaries by their X-ray emission

In Chapter 4, we examine selected massive stars for an unseen compact companion using the methods developed in the previous chapter. We construct the diagnostic diagrams for the seemingly single WR stars in the Small Magellanic Cloud, three Galactic WR stars, and the Galactic WN 8 stars, all suspected of possessing an unseen companion. We discuss a subset of eight of these stars in more detail.

We find that the seemingly single WR star SMC AB11 is a potential host to a companion. This is also observed in the Galactic WR stars WR 3, WR 6, and WR 7. For WR 124, our analysis suggests the existence of a low main-sequence companion. Our research demonstrates that the single-lined binary system VFTS 234 contains an X-ray faint BH companion. We find analogous outcomes for the single-lined binaries VFTS 514 and VFTS 779.

Additionally, we offer a catalog of diagnostic diagrams for massive stars, showcasing various effective temperatures and surface gravities. These diagrams can assist in identifying stars with the potential to host an undetected companion.

Our results demonstrate the capacity to identify the companion type in single-lined binaries by utilizing stellar parameters of the primary star, radial velocity data, and X-ray observations. We identify three critical factors that facilitate the identification of a companion using our diagnostic diagram: A small terminal velocity of the donor's wind, a large X-ray luminosity, and a small lower-mass limit of the putative companion. Consequently, our findings suggest that O stars may host X-ray quiet BH companions due to their high wind velocity. This is especially true when the orbital period of the putative companion surpasses approximately 10 days. This provides increasing evidence for the presence of an as-yet-undetected population of O+BH binaries.

Chapter 2

Mass transfer on a nuclear timescale in models of supergiant and ultra-luminous X-ray binaries

M. Quast, N. Langer^{1,2} & T. M. Tauris^{3,4}

Astronomy & Astrophysics, 2019, 628, A19, DOI: 10.1051/0004-6361/201935453

Author contributions: M.Q. constructed the single-star models, performed the numerical experiments with these models, computed the binary evolution models, reduced and analyzed the data from the numerical experiments with the single-star models, and the binary evolution models, produced the plots, interpreted the results, wrote the first draft of this article. N.L. and T.T. reviewed the first version of the draft.

Summary: Supergiant X-ray binaries (SGXBs) and ultra-luminous X-ray sources (ULXs), may offer insights into the physics of massive binary stars, the physical mechanisms associated with mass transfer, and the formation of merging BHs and NSs, connecting directly to gravitational-wave signals detected by observatories like LIGO and Virgo. Despite their essential role in astrophysics, more needs to be understood regarding the genesis and quantity of Galactic SGXBs. These systems comprise an evolved massive star with either a neutron star or a black hole companion. The emission of X-rays is believed to stem from the accretion of the supergiant's material onto the compact companion.

The transfer of material in SGXBs is believed to occur through either wind accretion or RLOF. However, in SGXBs, RLOF may lead to rapid orbit shrinkage due to the high mass ratio between the donor star and the accretor, potentially triggering a common envelope (CE) phase. Systems with a mass ratio above a certain threshold are suggested to inevitably undergo unstable RLOF mass transfer, limiting the X-ray lifetime of such systems to the thermal timescale of the donor star, i.e., $\sim 10^4$ yr. Consequently, many astronomers dismiss the notion of mass transfer via Roche-lobe overflow in the observed SGXBs due to the short X-ray lifetime implied by the mass transfer instability. However, the observed number of Galactic SGXBs and the characteristics of numerous ultraluminous X-ray binaries (ULXs) challenge this perspective. In this chapter, we explore the potential impact of supergiant donor stars nearing the Eddington limit and their progressed evolutionary phase on the evolution of massive and ultra-luminous X-ray binaries.

To investigate the influence of a massive donor's chemical composition profile on mass transfer stability, we artificially constructed models of massive stars varying in internal hydrogen and helium gradients and differing hydrogen-rich envelope masses. We performed numerical experiments in which the models underwent gradual mass loss to investigate how the stellar radius would respond. Furthermore, using our comprehensive binary stellar evolution code, we simulated the corresponding evolution of mass transfer, treating the compact objects as point masses. We assume different approaches to model the wind mass-loss rate of the donor star and investigate the influence of isotropic re-emission versus conservative mass transfer on our binary models.

This chapter's key result is that a hydrogen/helium gradient in the surface layers of a massive donor star makes the donor's radius much more sensitive to mass loss, resulting in a large value of the donor's mass-radius exponent ζ_R . We show that this sensitivity is related to the strength of the gradient: a high gradient means a strong shrinkage of the stellar radius during mass loss. We also find that the radius of more evolved models and more luminous stellar models is more sensitive to mass loss than the radius of less evolved models.

We demonstrate the implications of this insight in our binary simulations, which reveal that mass transfer from a massive donor to a less massive accretor can be stable on a nuclear time scale, even at mass ratios as high as ~ 20 . This is due to the large value of ζ_R in accordance with the discussion in Sec. 1.3.4. Our models suggest X-ray lifetimes exceeding 6×10^5 yr and accretion rates that could account for overluminous X-ray sources. We conclude that an H/He gradient close to the surface of an evolved massive star facilitates RLOF over a nuclear timescale, even if the companion mass is small resp. the mass ratio is large. Consequently, we refute the long-standing belief that mass transfer in binary systems with a high mass ratio is always unstable and lasts only a short duration. Instead, we find in our binary evolution models that the donor stars rapidly decrease their thermal equilibrium radius and can, therefore, cope with the inevitably strong orbital contraction imposed by the high mass ratio.

A drawback of the stabilizing mechanism that we propose is a fine-tuning problem. Since mass transfer is only stable if the H/He gradient is close to the surface, this requires a precise alignment of conditions. Specifically, the expansion of the OB star must catch up with the increasing Roche radius exactly when the H/He gradient appears near the stellar surface. On the other hand, a large value of the H/He gradient means that the gradient only extends over a small fraction of the envelope. We approach this fine-tuning problem by proposing that the SGXBs and ULXs may have formed through an initially unstable mass transfer followed by a CE evolution. During this phase, the donor star loses its hydrogen-rich envelope. When the H/He is close to the surface, the thermal equilibrium radius of the donor shrinks significantly, which ends the CE phase and initiates a phase of stable nuclear timescale mass transfer. Thus, the CE phase helps to remove the fine-tuning problem by facilitating the loss of the H-rich envelope.

We argue that different phenomena observed in SGXB and ULXs may be interpreted as empirical evidence for mass transfer stabilized by a H/He gradient and a preceding CE phase. Firstly, the observed orbital decay rates, i.e., the time derivative of the orbital period \dot{P}/P , of supergiant X-ray binaries (SGXBs) can agree with the orbital change due to isotropic re-emission, as long as the mass transfer occurs on the nuclear timescale.

Both highly non-conservative and conservative mass transfer show similar orbital decay rates for high mass ratios, implying that SGXBs and ULXS should exhibit similar values of \dot{P}/P .

Furthermore, enhanced surface helium abundance has been observed in several SGXBs, such as 4U 1700-377, GX301-2, and Vela X-1. This suggests that the chemically homogeneous part of the hydrogen-rich envelope has been removed, supporting our model's predictions.

Also, observations show that the donor stars in SGXBs do not match single-star tracks of the corresponding mass, as they tend to be more luminous than their stellar mass would suggest. This may indicate that the donor stars have lost a significant portion of their hydrogen envelope, consistent with the model's assumptions

Another observational support comes from the detection of ULXs with supergiant donor stars and NS accretors: As super-Eddington accretion luminosities can hardly be achieved by wind accretion, the discovery of ULXs with supergiant donor stars and NS accretors, such as NGC 7793 P13, challenges the traditional view that high mass ratios lead to unstable mass transfer. Our models show that stable RLOF can occur on a nuclear timescale even with high mass ratios, which aligns with the observed properties of these ULXs.

We further argue that the recently discovered obscured SGXBs, which may have circumstellar material producing obscuration, could be explained by the CE scenario for pre-SGXB evolution.

Our findings reveal a new perspective, about the mass transfer mechanisms, the number frequency and the formation of SGXBs. Additionally, our results provide a potential method to identify more ULX systems and detect mass transfer on nuclear timescales in ULX systems with neutron star accretors.

Chapter 3

X-ray emission from massive spectroscopic binaries

3.1 Introduction

Massive stars play a crucial role in astrophysics due to their immense influence on the cosmos. These stars exhibit intense gravitational forces and high-energy processes that give rise to high-energetic phenomena, which profoundly shape the dynamics and evolution of galaxies (Eldridge and Stanway 2022). During their life cycle, massive stars forge heavy elements in their centers, which drives the chemical evolution of their surroundings. At the end of their life, massive stars explode in a core-collapse supernova (Heger et al. 2003), leaving behind a neutron star (NS) or a black hole (BH) remnant. The high luminosity of massive stars gives rise to a strong stellar wind. These winds, as well as the explosive deaths of massive stars, are important mechanisms for transporting mechanical energy and momentum into the interstellar medium, triggering the formation of new stars (Roberts 1969; Mac Low et al. 2005).

The majority of massive stars are formed within multiple stellar systems (Sana et al. 2008, 2009, 2011, 2013, 2014; Kobulnicky and Fryer 2007; Kobulnicky et al. 2014; Dunstall et al. 2015). Interaction between the stellar companions can influence and complicate the system's evolution. For instance, mass transfer between the two components of a binary system changes the orbital period and separation, the stars' masses, and the whole system's mass and has a significant impact on the binary's fate (van den Heuvel 1994; Tauris and van den Heuvel 2006; Menon et al. 2021). Modeling the evolution of an interacting binary requires detailed knowledge of the physical processes that take place during the interaction phase. Consequently, massive binaries serve as pivotal laboratories for probing not only the evolution of massive stars in a broader context but also the physics of mass transfer and accretion, the terminal phases of massive star lifecycles, and the formation of compact remnants. The last aspect is of particular interest since massive binaries are progenitors of merging stellar black holes or neutron stars and hence give us insights into the population of potential sources of gravitational waves (Marchant et al. 2016; Tauris et al. 2017), which have been detected for the first time a few years ago (Abbott et al. 2016, 2017).

A common way to study binaries observational is via spectroscopy: In a binary system,

two stars orbit around their common center of mass. As they do so, they periodically approach and recede from Earth. This motion results in a regular change in their radial velocity (RV), causing their optical spectra to show a periodic shift towards the blue and red ends of the spectrum. Systems that display these periodic Doppler shifts are known as spectroscopic binaries. Among them, we have the double-lined spectroscopic binary (SB2), where we can observe spectral lines from both stars. In contrast, the single-lined binary (SB1) is a type of spectroscopic binary where only one of the stars is visible in the spectrum because it is significantly brighter than its binary companion. Although only one set of spectral lines is apparent in SB1 systems, studying the orbital motion of the brighter, observable star still provides valuable information. By analyzing the observable star's RV over a more extended period of time, a lower limit of the unseen star's mass can be derived (Shore 1994). Together with other data, e.g., from X-ray telescopes, RV measurements help to uncover the nature of the unseen companion, as we will see in the course of this paper.

The theory of stellar evolution shows that the more massive stars are, the faster they evolve. If one of the two companions has already reached the end of its life and exploded in a supernova, a system can remain that consists of a massive star and a compact object, i.e., a NS or a BH. Due to its very nature, the compact companion does not impart any significant optical flux. Consequently, the sole contributor to the visual spectrum emanates from the non-compact star, rendering the system discernible as a SB1. Hence, SB1s stand as promising candidates for the quest to find NSs and BHs, and discerning the concealed companion is a pivotal task in unraveling the population of compact objects within the Milky Way and its neighboring galaxies.

Compact companions, though not significant contributors to the optical flux of a binary, possess the capacity to accrete matter and emit X-rays, which can be observed through space-based X-ray telescopes. This process powers X-ray binaries (XRBs), consisting of an ordinary, i.e., gaseous donor star and a compact companion. In these binary systems, the material is released from the donor and partly captured and accreted by the compact companion (Verbunt 1992; Tauris and van den Heuvel 2006). During this accretion process, gravitational energy converts into heat and is subsequently emitted as X-rays (Shklovsky 1967; Frank et al. 1985). Combining RV variations and the detection of X-rays from a putative binary system can help uncover the unseen companion's nature. Pioneering this approach, Bolton (1972) initially demonstrated that the X-ray source Cyg X-1 represents a SB1 and argued that an accreting BH companion causes the X-ray emission.

Accretion is not the only mechanism that causes the emission of X-rays in a binary system. First of all, single stars themselves can be prominent X-ray sources (Nazé et al. 2021; Rauw and Nazé 2016; Bergheuer et al. 1996; Seward et al. 1979). This intrinsic X-ray emission is caused by the generation of shocks within the stellar wind of the massive star (Feldmeier et al. 1997). If a non-compact binary companion is present, the stellar wind of one star will collide either with the companion's wind or directly on the companion's surface (Prilutskii and Usov 1976). The generated shock in these colliding wind binaries is another important X-ray source.

The X-ray emission from accretion, intrinsic emission, and colliding wind produces different amounts of X-ray flux. This can be used to narrow down the possibilities for the

nature of an unseen companion. This method becomes even more efficient when including RV data. In this study, we further develop the idea outlined by Bolton (1972). Our objective is to devise a technique that integrates radial velocity data with X-ray observations to enhance our ability to discern the potential existence and the nature of hidden companions in SB1s and apparently single stars. The structure of this paper is as follows:

In Sec. 3.2, we discuss the X-ray emission assuming a wind-fed BH accretor. We deduce a criterion for the existence of an accretion disk and provide a scheme for estimating the X-ray luminosity of an accreting black hole with and without an accretion disk. In Sec. 3.3, we present a recipe to estimate the accretion luminosity of a wind-fed NS companion, including the effects of the NS spin and magnetic field on the accretion stream. In Sec. 3.4, we discuss the observable effects of an MS companion. We develop a method to estimate the X-ray luminosity of colliding winds and compare the computed X-ray luminosities with observations of known colliding wind binaries. Also, we discuss how we compare the optical fluxes of two MS companions. This is important to predict whether a binary of two MS stars would be detected as a SB1 or a SB2. Using this diagram, we investigate the well-known X-ray binaries Cyg X-1 and Vela X-1 in Sec. 3.5 and show that our approach identifies the companion correctly as a BH and a NS, respectively. We draw the conclusion of our investigation in Sec. 3.6.

3.2 Black hole companions

3.2.1 The parameter space

To describe the properties of a stellar wind's velocity and density, we use models that express these quantities as functions of a spatial coordinate. Since we are interested in the wind velocity and density close to the accretor, we use the orbital separation. It is intuitive that the gravitational mass of the accretor influences the accretion rate and, hence the luminosity. Thus, given the properties of the donor star, such as mass, radius, mass-loss rate, and terminal velocity, we can compute the X-ray luminosity of an assumed accretor by knowing its orbital separation a and its mass M_2 .

However, in general, neither a nor M_2 are directly accessible from observations. In order to constrain observational limits, we transform the a and M_2 to the orbital period P_{orb} and the orbital velocity $v_{\text{orb};\text{D}}$ of the donor star. To compute the first, we use Kepler's third law

$$P_{\text{orb}} = \sqrt{\frac{4\pi^2}{G(M_1 + M_2)} a^3}, \quad (3.1)$$

while for the latter, we use

$$v_{\text{orb};\text{D}} = \frac{2\pi a}{(1 + M_1/M_2)P}. \quad (3.2)$$

Thus, we are able to compare detection thresholds of compact companions from spectroscopy and thresholds from X-ray photometry by computing the X-ray luminosity at a given point in the $(P_{\text{orb}}, v_{\text{orb};\text{D}})$ -parameter space.

3.2.2 X-ray detection limits

To discuss the possibility of detecting X-ray sources, we need to compare our estimated X-ray luminosities to the detection limit of current X-ray observatories. The two most important X-ray satellites today are *Chandra* and *XMM-Newton*. Most of the X-ray studies of stellar X-ray sources were performed with the first one. We will thus assume that an X-ray source is detectable if the *Chandra* observatory is able to detect it. *Chandra* is equipped with a Wolter telescope to focus X-rays, which are subsequently detected by the Advanced CCD Imaging Spectrometer (*ACIS*). The *ACIS* broad band window is located between 0.5 and 7 keV. The effective area reaches a maximum value of 600 cm^2 at about 1.5 keV, where quantum efficiency exceeds 80%. This together results in a point source detection limit for the X-ray flux of $4 \times 10^{-15} \text{ erg cm}^{-2}\text{s}^{-1}$ at an integration time of 10 ks. Neglecting interstellar absorption and assuming an isotropically radiating point source, this translates into a limiting X-ray luminosity of

$$L_{\text{X; limit}} = 4.8 \times 10^{29} \text{ erg/s} \left(\frac{d}{\text{kpc}} \right)^2 \quad (3.3)$$

where d is the distance from the source to Earth.

As summarized by Walter et al. (2015), galactic HMXBs typically have a distance of a few kpc up to about 10 kpc. Hence, we adopted 10^{30} erg/s as the detection threshold for the Milky Way. We note that this is a lower limit for the detection threshold since we assume that the point source is the only X-ray or at least the dominating X-ray source in its vicinity. However, the fast wind of a WR star may emit intrinsic X-rays, e.g., when the wind collides with the surrounding ISM that may be dense in the vicinity of massive stars. This will increase the detection threshold for X-rays emitted from the accretor.

The Large and the Small Magellanic Cloud have distance modulus of 18.5 mag (Pietrzyński et al. 2013) and 18.9 mag (Graczyk et al. 2013) respectively. The corresponding distances of 50 kpc for the LMC and 60 kpc suggest a detection threshold of about 10^{33} erg/s for both galaxies.

3.2.3 Accretion from the stellar wind

To compute the rate at which material is captured by the CO and accreted, we assume that the velocity profile of the donor wind obeys a β law (Castor et al. 1975), that takes the form

$$v_w(a) = v_\infty \left(1 - \frac{R_1}{a} \right)^\beta, \quad (3.4)$$

where v_∞ is the terminal velocity of the stellar wind and R_1 is the donor's radius. β is a parameter that is found to be of the order unity (Puls et al. 1996).

Using the continuity equation

$$\dot{M}_w = 4\pi a^2 \rho_w v_w, \quad (3.5)$$

we find the wind density profile (Heger and Langer 1996)

$$\rho_w(a) = \frac{\dot{M}_w}{4\pi v_\infty \left(1 - \frac{R_1}{a}\right)^\beta a^2} \quad (3.6)$$

or, if we assume $\beta = 1$

$$\rho_w(a) = \frac{\dot{M}_w}{4\pi v_\infty (a^2 - R_1 a)} \quad (3.7)$$

Following Bondi and Hoyle (1944) the accretion radius R_A of the CO is given by comparing the kinetic energy of the wind material with respect to the accretor and gravitational energy, which yields (Frank et al. 2002)

$$R_A = \frac{2GM_2}{v_{\text{rel}}^2}, \quad (3.8)$$

where v_{rel} is the relative velocity between the CO and the wind it accretes from. Assuming that the wind flows spherically outwards, the direction of the wind flow is perpendicular to the orbital velocity of the accretor $v_{\text{orb A}}$ (Tauris et al. 2017). Pythagoras theorem then yields

$$v_{\text{rel}}^2 = v_w^2 + v_{\text{orb A}}^2 \quad (3.9)$$

or, introducing $\xi = \left(\frac{v_{\text{orb A}}}{v_w}\right)^2 + 1$

$$v_{\text{rel}} = \xi v_\infty \left(1 - \frac{R_1}{a}\right)^\beta. \quad (3.10)$$

The accretion rate from the capture of a fraction of the stellar wind is given as

$$\dot{M}_A = \frac{G^2 M_A^2}{\xi^3 v_\infty^4} \frac{\dot{M}_w}{\left(1 - \frac{R_1}{a}\right)^{4\beta} a^2}. \quad (3.11)$$

3.2.4 Accretion discs

In the last section, we computed the accretion rate of a wind-fed accretor. However, this is not sufficient to calculate the accretion luminosity. We also need information about the accretion flow, i.e., the accretion geometry and the thermal properties of the gas. Accretion flows may show extreme behaviors: On the one hand, the matter may fall directly onto the CO, which implies a spherically symmetric flow. On the other hand, material may orbit the CO in an accretion disc if it has enough angular momentum. In the following, we will discuss both cases, starting with the latter.

If the wind flow was plane parallel and homogeneous, no accretion of net angular momentum is possible due to the symmetry of the flow geometry. However, since the wind flow is spherically symmetric, it has a spherical density gradient. Also, the so-called accretion cylinder of the CO is not precisely aligned with the wind velocity since the relative velocity between the CO and the wind flow is the vectorial sum of wind velocity and or-

bital velocity. The result is a tilt of the accretion cylinder that "breaks" the symmetry and allows for the accretion of non-vanishing net angular momentum (Shapiro and Lightman 1976; Wang 1981; Livio et al. 1986).

Matter captured from the stellar wind has a certain amount of specific angular momentum j with respect to the accretor. The value of j for each amount of material depends on the impact parameter but is equally distributed over the whole accreted matter within the accretion radius.

The mean accreted angular momentum per unity mass was computed by Shapiro and Lightman (1976) and expressed as

$$j = \frac{\sigma}{2} \frac{v_{\text{orb;A}} R_{\text{A}}^2}{a}. \quad (3.12)$$

The efficiency factor σ considers our ignorance of the exact flow structure. In the study of Shapiro and Lightman (1976) it is assumed that $\sigma \simeq 1$ if $v_{\text{orb;A}} \ll v_{\text{W}}$, which would be the case if the donor stars was a $30 M_{\odot}$ star with a wind velocity of 2000 km/s and compact companion on a 0.3 d orbit or further away. Wang (1981) argued that rather

$$\sigma = 1 + \frac{7}{2} \frac{\beta}{a/R_1 - 1} \quad (3.13)$$

also takes the gradient of the wind velocity into account. This yields an accretion efficiency of $\sigma \simeq 4.5$ if the orbit is very compact, i.e., $a = 2R_1$.

We note that the efficiency is much larger if the wind speed is slower, i.e., the order of the sound speed. In this case, σ may be much higher, as found in numerical studies of Matsuda et al. (1987). The reason for this is that in slow winds, the force from the internal pressure gradient cannot be neglected. Since flow velocities in radiation-driven winds are much larger than the sound speed, the pressure gradient of the gas can be neglected in our study and the ballistic approach by Shapiro and Lightman (1976) and Wang (1981) is applicable.

Also, if the primary is close to filling its Roche-lobe, tidal forces from the secondary change the shape of the primary and alter its surface gravitational potential. Both effects influence the primary's stellar wind. As a result, the wind becomes increasingly anisotropic and slower. This increases the efficiency of angular momentum accretion and makes the formation of an accretion disc more likely. The influence of tidal forces on angular momentum accretion has been investigated by Hirai and Mandel (2021). They discovered that this can increase the accreted angular momentum by a factor of 10. However, the impact of tidal forces becomes significant only when the radius of the primary has expanded to 80% of the critical Roche radius. In most cases discussed below, the assumed orbital separation is assumed to be wide. Hence, the primary radius is assumed to be well below the Roche radius.

We can use Eq.3.12 to predict where a possible disc should form. Suppose we neglect angular momentum transport by shear within the accreted matter. In that case, we can assume that all the material will cumulate at the disc radius R_{D} , which is the separation of a circular Keplerian orbit, where the centrifugal force of a body with specific angular momentum j balances the gravitational force. The disk radius can thus be expressed as

(Frank et al. 2002)

$$R_D = \frac{j^2}{GM_2}. \quad (3.14)$$

In this assumption, the material would instead form a ring-like structure around the black hole. However, the large Reynolds number induces instability against turbulences. These turbulences efficiently transfer angular momentum from the inner parts (closer to the accretor) to the outer, causing the disc to spread out (Frank et al. 2002). The material at the inner disc edge will thus lose angular momentum and decrease its distance to the black hole's event horizon.

Eventually, the material is so close to the black hole that the gravitational attraction can no longer be expressed Newtonian, but higher orders of the gravitational force have to be taken into account. In this post-Newtonian regime, the material does not necessarily find a stable circular orbit (ISCO) since the gravitational force increases faster than the centrifugal force if angular momentum is conserved. Instead, the matter will spiral in rapidly. One can thus define an innermost stable circular orbit with an orbital separation R_{ISCO} (Misner et al. 2017). For a non rotation black hole R_{ISCO} can be expressed as

$$R_{\text{ISCO}} = \frac{6GM_2}{c^2}. \quad (3.15)$$

If $R_{\text{ISCO}} < R_D$, the ISCO defines the inner edge of the accretion disc. If, however, $R_{\text{ISCO}} > R_D$, we would not expect that an accretion disc can form since the material can not cumulate inside R_{ISCO} . Combining Eqns. 3.8, 3.12, 3.14 and 3.15, we express the condition for the existence of an accretion disc as

$$P_{\text{orb}} < \sqrt{\frac{8}{3}} \pi \sigma G c \frac{M_2}{v_{\text{rel}}^4}, \quad (3.16)$$

which can be rearranged to

$$\frac{2}{3} \frac{\sigma}{(1+q)^2} \left(\frac{v_{\text{orb}}}{c} \right)^{-2} \left(1 + \frac{v_w^2}{v_{\text{orb}}^2} \right)^{-4} > 1. \quad (3.17)$$

Eq. 3.17 is similar to the disk condition given by Sen et al. (2021). The difference is that we do not investigate the effects of BH spin. This corresponds to a factor of $\gamma_{\pm} = 1$ in Eq. 10 of Sen et al. (2021).

Eq. 3.16 shows that the threshold for the existence of an accretion disc is sensitive to the relative velocity of the BH and the stellar wind. Doubling the relative velocity yields an upper limit for the orbital period that is 16 times smaller. Since v_{rel} is dominated by the wind velocity v_w , it is rather unlikely that an accretion disc forms if a BH on a wide orbit captures material from a fast radiation-driven wind.

Figure 3.1 shows the threshold line in the $v_{\text{orb}}-P_{\text{orb}}$ -diagram where the equality sign in Eq. 3.16 applies. This line was plotted for different values of v_{∞} , assuming a $30 M_{\odot}$ donor star. This means that according to the disk criterion in Eq. 3.16, we would not expect an accretion disk around a black hole if it would orbit the star in such a way that the corresponding point was right and below the line determined by the donor's wind velocity.

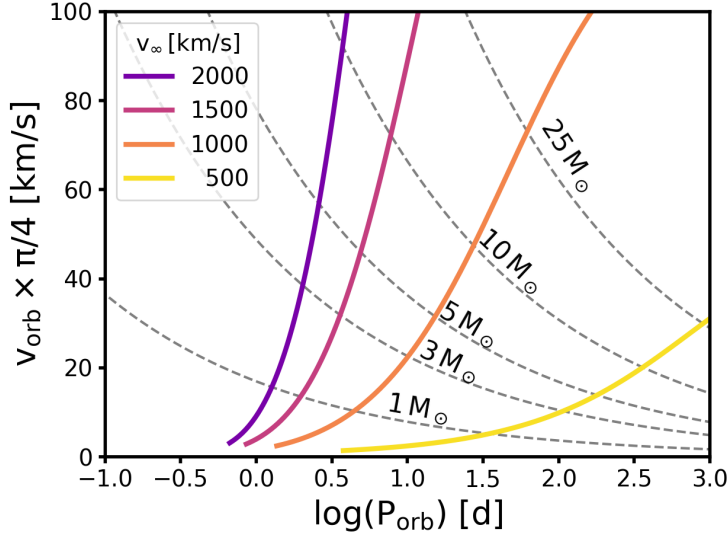


Figure 3.1.: Disc condition for a $30 M_{\odot}$ star hosting a compact object. Every line corresponds to a certain terminal velocity of the donor wind. The lines are defined by equating the specific accreted angular momentum to the specific angular momentum corresponding to the ISCO. For a given terminal velocity, we expect the formation of an accretion disc for every point above the line. Below the line, the accreted angular momentum is so small that the disc radius is smaller than the ISCO. Hence, we assume that no accretion disc forms in this regime. In this plot, we adopt a wind-acceleration parameter of $\beta = 1$.

As can be seen in Figure 3.1, we do not expect an accretion disk around a $10 M_{\odot}$ black hole orbiting the $30 M_{\odot}$ donor with an orbital period of 30 days, if the terminal velocity of the donor's wind exceeds 1000 km/s. Note that this value is roughly the escape velocity of a $30 M_{\odot}$ with a $10 R_{\odot}$ radius.

However, since $v_{\infty} \approx 2.3 v_{\text{esc}}$ (Vink et al. 2001), we can assume that the wind velocity is at least twice that high. A wind velocity of 2000 km/s would leave a large fraction of the parameter space where we would not expect the existence of an accretion disk.

If an accretion disc is present, the X-ray luminosity can be computed from the rest-mass energy of the captured matter as (Shapiro and Teukolsky 1986)

$$L_X = \eta \dot{M}_A c^2 \quad (3.18)$$

assuming stationary accretion. For an accretion neutron star, the efficiency factor is $\eta = 0.15$ and $\eta = 0.06$ for an accreting black hole with the disc. The efficiency of an accreting BH without a disc has to be deduced from another emission model.

3.2.5 Optically thin, adiabatic, spherically symmetric accretion

In this section, we derive a prescription for the X-ray luminosity of an accreting BH without accretion disc. Suppose that a BH accretes with an accretion rate \dot{M}_A . Furthermore, suppose that the material falls radially into the BH. Let the free fall time be short enough so that energy transport and cooling are negligible, i.e., that the process can be treated as

adiabatically. The accretion rate is connected to the flow velocity and the density of the material

$$\dot{M}_A = 4\pi r^2 \rho(r) v(r), \quad (3.19)$$

where r is the distance to the CO. Assuming that the velocity matches the free fall velocity

$$v_{\text{ff}}(r) = \sqrt{\frac{2GM_2}{r}}, \quad (3.20)$$

we can write the density as a function of r

$$\rho(r) = \frac{\dot{M}_A}{\sqrt{32\pi^2 GM_2 r^3}}. \quad (3.21)$$

Using the adiabatic relation for ideal gas

$$T \propto \rho^{2/3} \quad (3.22)$$

we write the temperature profile as

$$T(r) = T_0 \left(\frac{\dot{M}_A}{\sqrt{32\pi^2 GM_2 r^3 \rho_0}} \right)^{2/3}, \quad (3.23)$$

where T_0 and ρ_0 correspond to a point far away from the CO. We assume that they match the donor's wind temperature and density at the orbital separation a , i.e., $\rho_0 = \rho_w(a)$. We assume further that the wind expands isothermally starting at the photosphere, i.e., $T_0 = T_{\text{eff}}$. We note that this assumption gives a highly uncertain value for the temperature. However, as we will see above, the wind's temperature has only a small influence on the X-ray luminosity. Thus, the assumption seems justified in order to estimate the accretion luminosity.

If the material is optically thin and fully ionized, the spectrum of emitted radiation is no longer given by Planck's formula. Instead, emission by thermal bremsstrahlung dominates the X-ray radiation. For thermal bremsstrahlung the integrated X-ray emissivity (i.e., energy per unit volume and unit time) is given by (Courvoisier 2013)

$$\epsilon_{\text{ff}} = C g_B Z^2 n_e n_i T^{1/2} \quad (3.24)$$

where n_e and n_i are the particle density of electrons and ions, respectively, Z is the mean charge number of an ion, and g_B the integrated gaunt factor, with a value between 1.1 and 1.5. Assuming $g_B = 1.2$ leads to an uncertainty of about 20% (Shapiro and Teukolsky 1986; Frank et al. 2002; Courvoisier 2013). The constant C is given as

$$C = \left(\frac{2048\pi^3}{27} \right)^{1/2} \frac{e^6 k_B^{1/2}}{m_e^{3/2} c^3 h} \approx 1.4 \times 10^{-27} \text{ erg cm}^3 \text{ s}^{-1} \text{ K}^{-1/2}. \quad (3.25)$$

As mentioned above, we assume a fully ionized gas. In addition, we suppose that the gas from a stellar wind will consist mainly of hydrogen, with mass fraction X , and helium,

with mass fraction $Y \approx 1 - X$. Thus, the electron and ion density may be written as

$$n_e = \frac{X+1}{2} \frac{\rho}{m_p} \quad (3.26)$$

and

$$n_i = \frac{3X+1}{4} \frac{\rho}{m_p} \quad (3.27)$$

where m_p is the mass of a proton. The mean charge number is given as

$$Z = \frac{2X+2}{3X+1}. \quad (3.28)$$

Inserting this, as well as Eq. 3.23 into Eq. 3.24 we find

$$\epsilon_{\text{ff}} = C \frac{g_B}{2m_p^2} \frac{(X+1)^3}{3X+1} \frac{T_0^{1/2}}{\rho_0^{1/3}} \left(\frac{\dot{M}_A}{\sqrt{32\pi^2 G M_2}} \right)^{7/3} r^{-7/2}. \quad (3.29)$$

The X-ray luminosity can be computed from Eq. 3.29 under the assumption of radial symmetry by integration from the Schwarzschild radius R_S to the accretion radius:

$$L_X = 4\pi \int_{R_S}^{R_A} \epsilon_{\text{ff}} r^2 dr. \quad (3.30)$$

This yields

$$L_X = 4\pi C \frac{g_B}{m_p^2} \frac{(X+1)^3}{3X+1} \frac{T_0^{1/2}}{\rho_0^{1/3}} \left(\frac{\dot{M}_A}{\sqrt{32\pi^2 G M_2}} \right)^{7/3} R_S^{-1/2}, \quad (3.31)$$

where we made use of the fact that $R_A \gg R_S$.

Using the same approach, Shapiro and Teukolsky (1986) and Frank et al. (2002) derived a similar formula for the X-ray emission from a BH accreting from the interstellar medium (ISM). Their results show that stellar mass BHs are basically undetectable in X-rays if they accrete from the ISM. Only supermassive BHs may emit sufficient energy to be detected by X-ray telescopes.

While wind density and velocity of the stellar wind are different from the conditions in the ISM, Our approach suggests that wind-accreting BHs with spherical accretion flows are also very faint in X-rays and may even be undetectable. To illustrate the dependence of the accretion luminosity on the orbital separation, involving the formation criterion of the accretion disk and the approach for spherically symmetric accretion, we define an exemplary binary that consists of a $30 M_\odot$ donor star hosting a $10 M_\odot$ BH companion star. The mass-loss rate is arbitrarily set to $10^{-6} M_\odot/\text{yr}$ and the terminal wind velocity to 2000 km/s. Note that this setting does not represent a physical binary model but is only for illustration.

Figure 3.2 shows the accretion luminosity of our exemplary binary setting for different orbital periods. For narrow orbits, with a period of less than seven days, we expect the formation of an accretion disc since Eq. 3.16 applies (red solid line). Thus, the X-ray

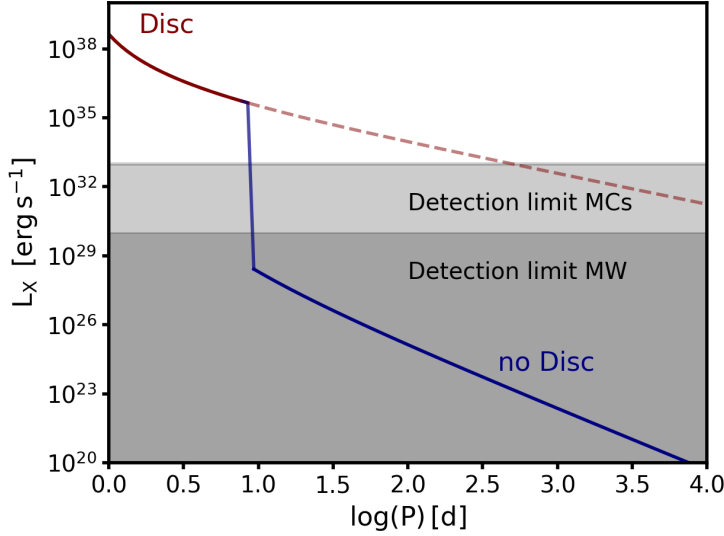


Figure 3.2.: Accretion luminosity of a $10 M_{\odot}$ BH orbiting a $30 M_{\odot}$ donor star. The mass-loss rate is $10^{-6} M_{\odot}/\text{yr}$ and $v_{\infty} = 2000 \text{ km/s}$. The red solid line shows the range of orbital periods where the formation of an accretion desk is expected, and the blue solid line shows the period range where we do not expect an accretion disk and assume spherically symmetric accretion. The dashed red line is the extrapolation of the X-ray luminosity from a disk for illustration purposes. The grey regions show the luminosity range that cannot be detected, assuming the source is in the Milky Way or the Magellanic Clouds, respectively.

luminosity is computed using Eq. 3.18, which gives a high luminosity up to 10^{38} erg/s . As the orbit widens, the accreted angular momentum is no longer sufficient to form an accretion disc. Here, we use Eq. 3.31 to compute the total luminosity (blue solid line). This gives a discontinuity, and the luminosity decreases roughly ten orders of magnitude. We note that Eq. 3.31 might not apply close to the transition between disc formation and spherically symmetric accretion. Thus, the luminosity values close to the discontinuity must be considered cautiously. If the orbital separation is, however, much larger than the value where the discontinuity occurs, i.e., an orbital period of a few hundred days and more in Fig. 3.2, Eq. 3.31 may be a good estimate.

We also displayed the detection limits of the Milky Way and the Magellanic clouds as well as the X-ray luminosity that would be achieved if an accretion would always be formed (red dashed line). Fig. illustrates that the formation of an accretion disk is crucial for detecting a wind accreting BH: Assuming that an accretion disk forms, regardless of the orbital separation, leads to the conclusion that galactic accreting BHs should be detectable even at $P_{\text{orb}} \sim 10^4 \text{ d}$ and still at orbital periods of $\sim 300 \text{ d}$. However, taking into account the disk condition derived above and the luminosity for spherical accretion, we may expect that accreting black holes are below the current detection limits if the orbital period exceeds a few tens of days. This was also pointed out by Vanbeveren et al. (2020).

In the following, we check the self-consistency of our spherical accretion model. To do this, we compute the optical depth τ of the inner edge of the accretion flow, i.e., the Schwarzschild-radius. The mass column density of the Schwarzschild radius $\Sigma_{\text{acc}} := \int \rho ds$

can be immediately computed using Eq. 3.21 and reads

$$\Sigma_{\text{acc}} = \frac{c\dot{M}_A}{4\pi GM_2}. \quad (3.32)$$

For an optically thin flow, the optical depth $\tau = \kappa\dot{M}_A$ has to be smaller than unity. Eq. 3.32 can be inverted and yields for $\tau = 1$

$$\dot{M}_A = \frac{4\pi GM_2}{c\kappa}. \quad (3.33)$$

This is the accretion rate of the spherically symmetric flow that yields a certain optical depth at R_S . Thus, in order to apply thermal bremsstrahlung as the emission mechanism, the actual accretion rate has to be smaller than the value given by Eq. 3.33. If we assume that the opacity arises from electron scattering, the accretion flow is optically thin if the accretion rate is below 10^{18} g/s in the case of a $10 M_\odot$ BH. This is the case for all regarded donor stars if the orbital period is above ten days. Thus, the condition of optically thin accretion flow is, in general, fulfilled.

3.2.6 The Eddington limit

The X-ray flux of an accreting CO generates radiative pressure onto the in-falling material. Assuming spherically symmetric accretion of matter and spherically symmetric emission of radiation, the force from radiative feedback balances gravitational attraction at the Eddington luminosity (Heinzeller and Duschl 2007)

$$L_{\text{Edd}} = 1.3 \times 10^{38} \left(\frac{M_2}{M_\odot} \right) \text{erg/s}. \quad (3.34)$$

We assume this is the maximum X-ray luminosity for all COs (BH and NSs). This means if the computed luminosity of Eqn. 3.18 and 3.31 exceeds L_{Edd} , we use the value of L_{Edd} . It is important to note that some X-ray binaries, called ultraluminous X-ray sources, exceed the Eddington luminosity by a factor of 10 or more (Swartz et al. 2004). The reason for violating the Eddington limit may be a non-spherical accretion geometry and instabilities of the accretion flow (Kaaret et al. 2017).

3.2.7 X-ray attenuation

In the case of wind accretion, the companion is embedded in a more or less dense medium, depending on the mass-loss rate and wind velocity of the donor. X-ray photons will be scattered and absorbed if the wind is dense enough. This reduces the flux in the observation band, making an accreting CO companion harder to detect.

In this approach, the fraction $\exp(-\tau)$ is not scattered but can be detected by an observer. Here, the optical depth is $\tau = \int \kappa \rho ds$, where, in general, the opacity κ depends on the photon energy. Introducing the mass column density $\Sigma := \int \rho ds$ the optical depth can

be expresses as

$$\tau = \kappa \Sigma \quad (3.35)$$

under the assumption that κ is constant everywhere.

Assuming a coordinate system whose origin coincides with the position of the accretor, we can write the hydrogen column density as

$$\Sigma = \int_0^\infty \rho ds \quad (3.36)$$

where ds is the path differential along the line of sight to the observer at infinity. Using the wind profile of the mass density (Eq. 3.6), we rewrite the column density as

$$\Sigma = \frac{\dot{M}_w}{4\pi v_\infty} \int_0^\infty \frac{1}{\left(1 - \frac{R_1}{r}\right)^\beta r^2} ds, \quad (3.37)$$

where r is the distance to the donor star. The solution of the integral depends on the orbital inclination as well as the orbital phase and thus is time-dependent in general. For simplicity, we will assume two extreme cases of orbital inclination of 90° and the accretor aligned along the line of sight and an orbital inclination of 0° . In the first case, $s = r - a$, and thus

$$\Sigma = \frac{\dot{M}_w}{4\pi v_\infty} \int_a^\infty \frac{1}{\left(1 - \frac{R_1}{r}\right)^\beta r^2} dr, \quad (3.38)$$

which integrates to

$$\Sigma = \frac{\dot{M}_w}{4\pi v_\infty R_1} \times \begin{cases} -\ln(1 - R_1/a) & : \beta = 1 \\ \frac{1 - (1 - R_1/a)^{1-\beta}}{1-\beta} & : \text{else} \end{cases} \quad (3.39)$$

This is the column density derived by Leutenegger et al. (2010) corrected by a factor that accounts for the fact that the wind is accelerated.

Eq. 3.39 sets a lower limit for the mass column density of an accretor with orbital separation of a . As shown in Appendix B.1, the value of Σ may be larger by a factor of about 1.6, depending on the inclination angle. We also note that our calculation holds for a homogeneous and isotropic wind. The real column density may be affected by inhomogeneities on small (wind clumping) and large scales (e.g., by gravitational wind-focusing of the accretor). It will also be time-dependent since the binary changes, and the donor star may undergo phases of strong mass ejection.

To estimate the attenuation of X-rays by the stellar wind material, a prescription of the opacity κ is needed. In general, this wind medium will be highly ionized due to the donor's intrinsic luminosity and the energetic X-rays from a potential accretor, i.e., the wind consists of ions and free electrons that scatter incoming photons. Typically, the photon energies do not exceed a few ten keV, which is less than the rest of the mass energy of an electron. Thus, electron scattering can be modeled as Thompson scattering.

This gives a wavelength-independent contribution to the overall opacity. Under the assumption that the whole material consists purely of hydrogen with mass fraction X and helium with mass fraction $1 - X$, the electron scattering opacity can be computed using

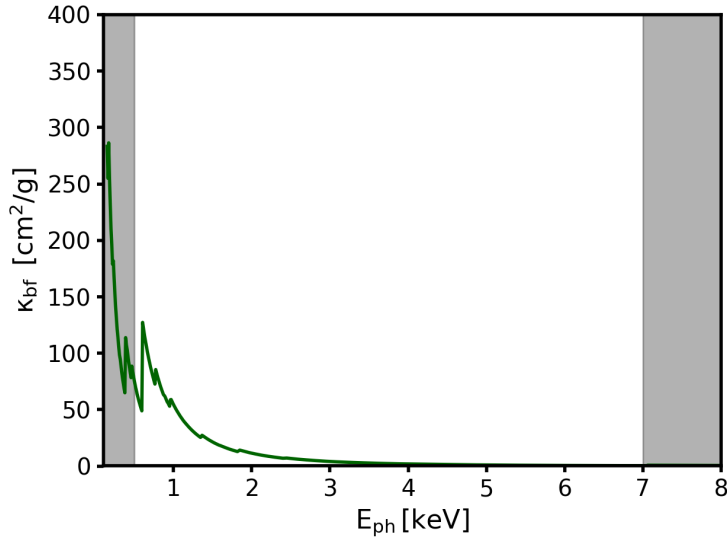


Figure 3.3.: Energy dependent opacity of a partially ionized stellar wind from Leutenegger et al. (2010). Hydrogen and helium are supposed to be completely ionized. The absorption edges arise mainly from Fe and the CNO elements. The white area indicates the *Chandra* broadband.

the formula given by Cox and Giuli (1968) (see also Kippenhahn and Weigert 1990)

$$\kappa_{\text{sc}} = 0.2(1 + X) \text{ cm}^2/\text{g} . \quad (3.40)$$

Another important contribution to the opacity comes from the interaction of X-ray photons with the innermost electrons of the metal ions that are not completely ionized. To account for this so-called K-shell or bound-free absorption, we use the opacities κ_{bf} computed by Leutenegger et al. (2010) based on the cross-sections of Verner and Yakovlev (1995) to calculate the broadband X-ray absorption by stellar winds of O stars. The opacities were calculated assuming solar abundances and neglecting the effect of the absorption edges of hydrogen and helium since these elements are completely ionized. Figure 3.3 shows the energy dependence of the resulting opacity.

The most significant contribution to the X-ray opacity comes from the K-shell absorption edges of Fe and C, N, and O due to their high abundance. An important contribution also comes from Ne, Mg, and Si. As noted by Pauldrach (1987) and Hillier et al. (1993), absorption by partially ionized helium has to be regarded if the stellar wind cools and helium can partially recombine. However, we do not expect this to happen near the donor star or the accretor since their powerful radiation will inhibit the recombination of helium. Recombination processes may become important far away from the system. This, however, implies a low mass density, which makes the absorption due to partially ionized helium unimportant.

Since K-shell absorption makes the opacity wavelength dependent, we need a specific X-ray spectrum to predict the overall X-ray absorption. For the purpose, we used the *Xspec* version 12.1, an X-ray spectral fitting code (Schafer 1991; Arnaud 1996). We synthesized X-ray spectra using the emission model *grad* for an accretion disc around a Schwarzschild black hole (Hanawa 1989; Ebisawa et al. 1991). The inclination was fixed to 0 degrees,

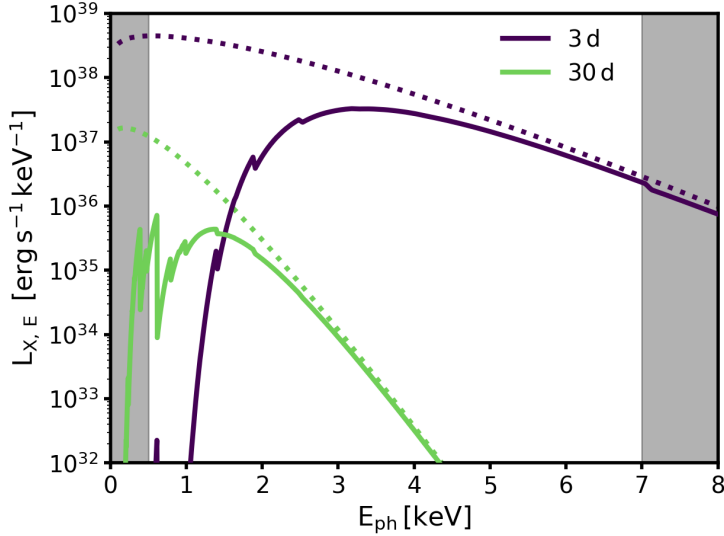


Figure 3.4.: Synthetic X-ray spectra of accretion discs around a $10 M_{\odot}$ BH that orbits a $30 M_{\odot}$ donor star with a terminal velocity of 1000 km/s and a mass-loss rate of $10^{-5} M_{\odot}/\text{yr}$. The color indicates different orbital periods. The solid lines show the spectrum with absorption from the stellar wind material. The dashed lines indicate the unabsorbed spectrum. The *Chandra* broadband is indicated as a white area.

the spectral hardening factor was set to 1.7 as suggested by Shimura and Takahara (1995), and relativistic effects were included. Thus, the only parameters left were the accretor mass and the accretion rate. The latter is assumed to be the Bondi-Hoyle accretion rate as given by Eq. 3.11.

We computed a grid spectra for BH masses ranging between 3 and $100 M_{\odot}$ and accretion rates of between 10^{10} g/s and 10^{20} g/s . The upper limit of the accretion rates corresponds roughly to the Eddington accretion rate of a $10 M_{\odot}$ BH. Hence, *Xspec* does not allow higher values for the accretion rate. In our study, we did not encounter the case that a wind-accreting black hole exceeded the

We can now compute an accretion disc spectrum for given donor star parameters and a given mass of the BH accretor as a function of the orbital period. Assume for instance a $30 M_{\odot}$ donor star with a terminal velocity of 2000 km/s . According to Figure 3.2, a $10 M_{\odot}$ BH companion would form an accretion disc if the orbital period is shorter than about 10 days. Further assume that the mass-loss rate is $10^{-5} M_{\odot}/\text{yr}$. Based on this, we can compute the accretion rate and the accretion spectrum as described above. Consequently we multiply the spectrum with the absorption factor $\exp(-\kappa\Sigma)$, where $\kappa = \kappa_{\text{sc}} + \kappa_{\text{bf}}$. Figure 3.4 shows the results for two orbital periods. Comparing the two spectra in Figure 3.4, we see that the absorbed spectrum of the accretion disc is harder if the orbit is more compact. This has two reasons: On the one hand, the accretion rate of a BH is higher if the orbital separation is small. This gives rise to hotter accretion flows in the disc (Frank et al. 1985). Consequently, the unabsorbed spectrum (dashed lines in Fig. 3.4) has to be harder. In addition, the column density of the BH increases. Thus, X-ray absorption is more important for an orbital period of 3 days than for 30 days. Since the opacity increases with decreasing photon energy (Fig. 3.3), absorption tends to make the spectrum harder.

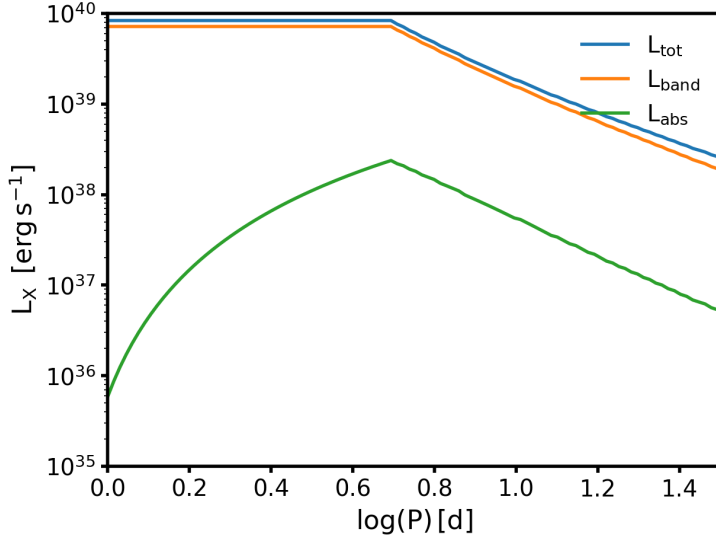


Figure 3.5.: Total luminosity L_{tot} , luminosity in the *Chandra* broadband without absorption L_{band} and with L_{abs} .

To infer the total luminosity, we integrate the spectrum over the *Chandra* broadband, i.e., from 0.5 keV to 7 keV. As shown in Fig. 3.4, the soft part of the accretion disc spectrum is not in the *Chandra* band. This means, even if we do not take absorption due to the stellar wind into account, we can only detect the X-ray luminosity L_{band} in the *Chandra* broadband, which is only a fraction of the total luminosity L_{tot} . However, an even smaller fraction of the luminosity L_{abs} is detectable if we include absorption.

3.2.8 Caveats

We assume a non-rotation BH, i.e., a spin parameter of 0. For spin parameters close to 1, the ISCO is close to the event horizon, assuming the accreted matter rotates prograde in the equatorial plane of the BH. In this case, R_{ISCO} is smaller for a rotating BH than for a non-rotating BH. Consequently, the threshold period up to which a disc can form increases. Also, the accretion efficiency can increase up to a factor of 7 (Shapiro and Teukolsky 1986). However, incorporating the effects of the BH spin parameter requires knowledge of its spin evolution, including the BH formation and the supernova explosion, as well as the angular momentum accretion of the BH in the post-SN binary. Keeping track of the BH spin evolution and the modeling of accretion discs around spinning BHs is a more complicated task (cf. Medvedev and Murray 2002; Sadowski et al. 2011; Cencini et al. 2021) and is beyond the scope of this study.

We also note that we use thermal bremsstrahlung only in the case of spherically symmetric accretion. Consequently, we neglected other non-thermal emission mechanisms, such as synchrotron emission and inverse Compton scattering (Sen et al. 2024). The interaction of relativistic electrons with a magnetic field results in synchrotron radiation, which can dominate at low mass accretion rates. This emission is influenced by the magnetic field strength and can peak in hard X-rays. A problem with modeling synchrotron

radiation arises from our ignorance of the magnetic field strength in the accretion flow. Hence, we do not regard synchrotron emission in this study. Inverse Compton scattering, on the other hand, is expected to scatter the X-ray photons up, thereby hardening the X-ray spectrum (Sridhar et al. 2021). However, this emission mode is expected to be negligible at low accretion rates (Esin et al. 1997). Thus, the X-ray luminosity for radially symmetric infalls can only be regarded as a lower limit for the expected value.

In the absence of a disc, we assume a radial symmetric accretion flow. The disc and the radial symmetric accretion have to be regarded as extreme cases. The treatment of the threshold region is difficult due to the marginal stability of the accretion flow. Shapiro and Lightman (1976) showed that an accretion flow near this threshold can spontaneously form a disc due to the inhomogeneous stellar wind. This marginal stability makes an analytic model for the accretion in the threshold regime implausible. Consequently, this regime has to be regarded cautiously.

Disc models for advection-dominated accretion flows (ADAF) exist. However, analytical ADAF models presume a stationary accretion disc, where the cooling rate is small compared to the viscous heating (Yuan and Narayan 2014). An interesting feature of the ADAF solutions is that they decrease the accretion efficiency by a factor of 10 to 1000, depending on the accretion rate and the advection parameter. However, the effects ADAF become only crucial if the accretion rate is 10^{-4} of the Eddington accretion rate and below (Esin et al. 1997). For the binaries discussed in this study, this would make the predicted X-ray luminosity slightly fainter in the disc regime.

3.3 Neutron star companions

Accretion onto a NS differs from accretion onto a BH. The surface of a BH is the event horizon, i.e., a threshold determined by the configuration of space-time. Hence, a large amount of accreted material's energy may be dragged into the BH before it is radiated away. In contrast, the surface of a NS is solid. This means that a large fraction of the gravitational energy is converted into heat and consequently radiated in X-rays, even without an accretion disk. Thus the formalism developed in section 3.2.5 cannot be applied.

On the other hand, NSs possess a strong magnetic field of the order of $B_{\text{NS}} \sim 10^{12}$ G and rotate quickly around their axis with a spin period P_{NS} of a few to a few hundred seconds in XRBs (Bhattacharya 1995). Table 3.1 shows magnetic field strengths, inferred from cyclotron lines by Taani et al. (2018), and spin periods of XRBs where X-ray pulsation have been discovered.

This section briefly discusses how the magnetic field and the spin of the NS influence the accretion flow. Different accretion modes have to be considered depending on the accretion rate, the strength of the magnetic field B_{NS} , and the spin period P_s of the NS. Here, we outline the principal picture of the different accretion modes that we adopted from Bozzo et al. (2008). Appendix B.2 describes how we computed the X-ray luminosity in every accretion regime.

The different accretion modes of a NS are determined by the accretion radius as defined in Eq. 3.8, the radius of co-rotation R_{co} and the radius of the magnetosphere R_{mag} . R_{co} is defined as the radius of an orbit around the NS with an orbital period that matches the

NS's spin period.

$$R_{\text{co}} = \left(\frac{GM_2 P_s^2}{4\pi^2} \right)^{1/3} = 1.5 \times 10^8 \text{ cm} \left(\frac{P_s}{\text{s}} \right)^{2/3} \left(\frac{M_2}{\text{M}_\odot} \right)^{1/3}. \quad (3.41)$$

Within the magnetosphere, the accreted material, which consists of highly ionized plasma, couples to the magnetic field and flows along the field lines. The outer boundary of the magnetosphere is called the magnetopause. R_{mag} is the radius of the magnetosphere and can be estimated by the Alfvén radius, i.e., the distance from the NS where the ram pressure of the gas is comparable to the magnetic pressure. If the wind velocity dominates the velocity of the gas flow, the magnetopause is well outside of the accretion radius, equating the magnetic pressure and the ram pressure yields

$$R_{\text{mag}} = \left(\frac{\mu^2 a^2}{2\dot{M}_W v_{\text{rel}}} \right)^{1/6}. \quad (3.42)$$

If the magnetopause is inside the accretion radius, the flow velocity is comparable to the free fall velocity of the gravitational potential. The radius of the magnetosphere then read (Elsner and Lamb 1977)

$$R_{\text{mag}} = \left(\frac{\mu^4}{GM_2 \dot{M}_A^2} \right)^{1/7} \quad (3.43)$$

or, more convenient,

$$R_{\text{mag}} = 3.2 \times 10^8 \text{ cm} \left(\frac{\mu}{10^{30} \text{ G cm}^3} \right)^{4/7} \left(\frac{\dot{M}_A}{10^{17} \text{ g/s}} \right)^{-2/7} \left(\frac{M_2}{\text{M}_\odot} \right)^{-1/7}, \quad (3.44)$$

where $\mu \sim B_{\text{NS}} R_{\text{NS}}^3$ is the magnetic dipole moment of the NS.

The difference between Eq. 3.42 and Eq. 3.43 arises from the fact that in the second equation, it is assumed that the gravitational field of the NS captures the plasma. This leads to an acceleration and compression of the plasma, both increasing the gas pressure. However, if the accretion radius is smaller than the magnetospheric radius, the influence of the gravitation field on the gas can be neglected. Hence, the ram pressure $\rho_W v_{\text{rel}}^2$ results solely from the stellar wind velocity.

Outside the wind acceleration zone, the ram pressure decreases with distance from the donor star since the velocity reaches v_∞ and the density decreases. Consequently, R_{mag} for a NS companion increases with orbital separation (cf. Eq.3.42). If $R_{\text{mag}} > R_A$, the NS accretes via the Magnetic Inhibition mode. The stellar wind material couples to the magnetic field outside the accretion radius. A shock front forms at the magnetopause and is heated by the conversion of the kinetic energy of the wind material. This shock front contributes to the X-ray luminosity in this accretion mode.

From Eqns. 3.8 and 3.42 one finds that magnetic inhibition applies if

$$a > \sqrt{\frac{128\dot{M}_W}{v_\infty^{11}} \frac{G^3 M_2^3}{\mu}}, \quad (3.45)$$

Here, we assume that the wind has reached terminal velocity, i.e., $v_{\text{rel}} \approx v_{\infty}$. For a donor star with a mass-loss rate of $10^{-6} M_{\odot}/\text{yr}$ and a terminal velocity of 2000 km/s, a typical NS of $1.4 M_{\odot}$ and with $\mu = 10^{30} \text{ G cm}^3$ would be in the Magnetic Inhibition accretion mode if its orbital separation exceeds $1800 R_{\odot}$. This corresponds to an orbital period of 2000 d of the donor has a mass of $20 M_{\odot}$. We can conclude that the Magnetic Inhibition mode does not play a dominant role in regarding the parameters space in this study. It may become, however, important for donor stars that show a large terminal velocity, such as the Wolf-Rayet star WR 3 (see below).

If, in addition, $R_{\text{mag}} > R_{\text{co}}$, the coupling of the shocked matter to the rotating field lines induces a centrifugal barrier that prevents the matter from flowing into the gravitational potential of the NS. The accretion mode is called the super-Keplerian Magnetic Inhibition mode. One can show that the magnetosphere rotates supersonically. Consequently, coupling the supersonic magnetosphere to the plasma results in the dissipation of rotational energy of the NS. The released energy adds to the X-ray luminosity of the shock front. We use the upper limit provided by Eq. 6 of Bozzo et al. (2008) for our computations.

If $R_{\text{mag}} < R_{\text{co}}$ the centrifugal force at the magnetopause is not sufficient to prevent the accreted matter from penetrating the magnetosphere. This is the Sub-Keplerian Magnetic Inhibition mode. The shear between the material captured by the magnetic field and the shocked material induces Kelvin-Helmholtz instabilities, resulting in an accretion rate onto the NS surface (cf. Harding and Leventhal 1992; Burnard et al. 1983). The resulting accretion luminosity is computed as outlined in Appendix B.2.3 and adds to the shock luminosity.

For the rest of this section, we suppose that $R_{\text{mag}} < R_{\text{A}}$, i.e., the accretion flow is gravitationally accelerated towards the NS. Consequently, the magnetospheric radius is estimated with Eq. 3.43. At R_{mag} , the coupling of the plasma flow to the magnetic field lines takes place. We assume that the material rotates with the NS's spin frequency as soon as it couples to the magnetic field. The faster rotation induces a centrifugal force, which balances the gravitational attraction and hinders efficient accretion. This happens if $R_{\text{mag}} > R_{\text{co}}$ (Frank et al. 2002). This accretion inhibition caused by this centrifugal barrier is known as the propeller effect (Stella et al. 1986).

As the magnetic field couples to the accreted material, it induces a torque in the plasma that increases the angular momentum until equilibrium between gravitational and centrifugal force is reached. The torque can be computed assuming that the accreted material has negligible angular momentum initially and the specific angular momentum is $j = \sqrt{2GM_2R_{\text{mag}}}$ at the magnetopause. Consequently, the torque acting on the plasma is $N \simeq \dot{M}_{\text{A}}j$ (Tauris 2012). The angular momentum needed to accelerate the plasma is gained from the NS. We assume that the NS can be modeled as a sphere of homogeneous density. Consequently, its moment of inertia is $I_{\text{NS}} = \frac{2}{5}M_2R_{\text{NS}}^2$. The NS's total angular momentum $J_{\text{NS}} = \frac{2\pi I_{\text{NS}}}{P_{\text{ps}}}$.

The timescale of the propeller accretion state can be computed as the time needed to transfer the NS's angular momentum to the entire plasma, i.e., $\tau_{\text{prop}} = J_{\text{NS}}/N$. This can be expressed by combining the above formulas as

$$\tau_{\text{prop}} = 5.5 \times 10^4 \text{ yr} \left(\frac{P_{\text{ps}}}{\text{s}} \right)^{-1} \left(\frac{\dot{M}_{\text{A}}}{10^{-10} M_{\odot}/\text{yr}} \right)^{-6/7} \left(\frac{M_2}{M_{\odot}} \right)^{4/7} \left(\frac{\mu_{\text{NS}}}{10^{30} \text{ G cm}^3} \right)^{-2/7}. \quad (3.46)$$

If then $R_{\text{co}} < R_{\text{mag}}$, the wind material will be first captured gravitationally as described above but can not pass the magnetopause. This results in an accumulation of shocked matter forming an "atmosphere" between R_{mag} and R_{A} . Material that falls in from further outside is braked quickly. The pressure at R_{mag} , i.e., at the bottom of the atmosphere, can then be approximated by the ram pressure of the infalling plasma.

In this case, the spin velocity of the magnetosphere is larger than the adiabatic sound speed of the gas. This leads to the dissipation of the NSs rotational energy at R_{mag} as in the super-Keplerian accretion mode. The rotational energy of the NS is converted into the kinetic energy of the plasma. It is transported to the upper parts of the atmosphere by turbulence, which is also induced by the supersonic rotation of the magnetosphere. Subsequently, the energy is released as X-ray emission. This so-called Supersonic Propeller mode was considered by Davies et al. (1979) and Davies and Pringle (1981), who also computed the X-ray luminosity in this regime assuming an adiabatic atmosphere.

The supersonic propeller effectively converts the NS's rotational energy into X-ray radiation. Consequently, the NS slows down until the material can be directly accreted again or until the subsonic propeller (see below) is initiated. The time scale for the NS to slow down can be estimated from the rational energy of a homogeneous sphere and the released X-ray luminosity. We yield

$$\tau_{\text{supers}} = 5 \times 10^5 \text{ yr} \left(\frac{P_{\text{ps}}}{\text{s}} \right)^{-2} \left(\frac{M_2}{M_{\odot}} \right) \left(\frac{L_X}{10^{33} \text{ erg/s}} \right)^{-1}. \quad (3.47)$$

If $R_{\text{co}} > R_{\text{mag}}$, the centrifugal barrier does not operate, and the rotation of the magnetosphere is no longer supersonic. However, dissipation (less efficient than in the supersonic propeller) still occurs and heats the material. As noted by Davies and Pringle (1981), the material has to cool sufficiently to be accreted onto the NS surface. This prohibits efficient accretion if the accretion rat is larger than a critical value(Ikhsanov et al. 2001). We use the critical accretion rate defined in Eq. 23 of Bozzo et al. (2008). Only a fraction of the material that falls inward through Bohm diffusion and Kelvin-Helmholtz instabilities contributes to the X-ray luminosity. This accretion state is called the Subsonic Propeller mode.

To compute the X-ray luminosity in the supersonic and subsonic propeller regimes, we rely on the work of Bozzo et al. (2008), who applied the investigations of Davies et al. (1979) and Davies and Pringle (1981) to wind fed supergiant X-ray binaries. If the accretion rate is lower than the critical value of the subsonic propeller, the direct accretion mode takes place, releasing an X-ray luminosity as estimated by Eq. 3.18.

In their paper Bozzo et al. (2008) express the X-ray luminosities in the five accretion modes discussed above as a function of accretion rate, spin period, and magnetic momentum of the NS, fixing its mass to $1.4 M_{\odot}$. While the first parameter can be calculated from the position in the $v_{\text{orb};\text{D}}-P_{\text{orb}}$ -diagram, P_{NS} and μ_{NS} have to be considered.

Table 3.1 shows that the magnetic field of observed X-ray pulsars is about 10^{12} G, which corresponds to a magnetic momentum of 10^{30} G cm³, under the assumption that the NS has a radius of 10 km. That scatter of the magnetic field is quite low. Consequently, we fix $\mu = 10^{30}$ G cm³. The detected spin periods, however, vary over several orders of magnitude. If we fix the NS mass to $1.4 M_{\odot}$ the orbital separation and the donor star's orbital velocity become unique functions during the orbital period. We thus lose one free

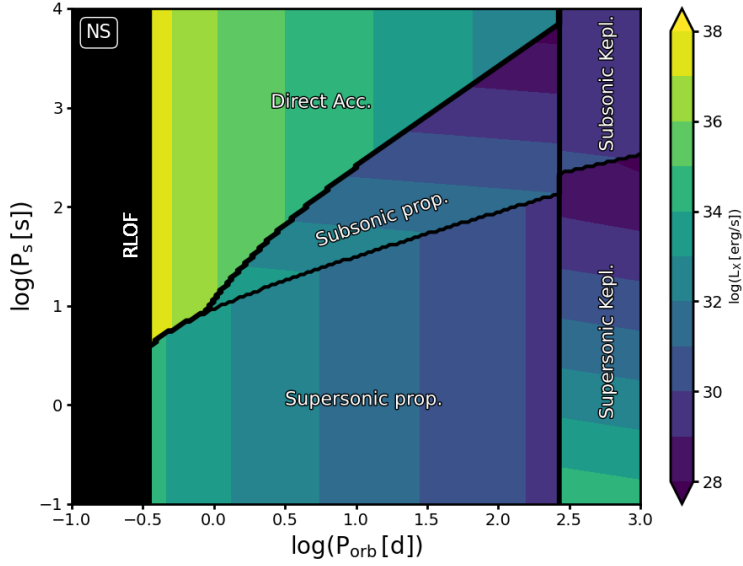


Figure 3.6.: X-Ray luminosity of an accreting neutron star depending on the orbital period and spin period, according to Bozzo et al. (2008). The black lines distinguish the different accretion modes. $M_1 = 30 M_\odot$, $R_1 = 10 R_\odot$, $\dot{M}_W = 10^{-6} M_\odot/\text{yr}$ and $v_\infty = 2500 \text{ km/s}$.

parameter, which can be replaced by the spin period of the NS in the diagnostic diagram.

For illustration purposes, we show a diagnostic diagram for a NS in Fig. 3.6. Every point in the diagram corresponds to a certain orbital period and spin period of the NS companion. For given parameters of the donor star, we compute the orbital separation, local wind velocity, and accretion rate as outlined in the previous sections. We compute R_A , R_{mag} and R_{co} using Eqns. 3.8, 3.41, 3.42 and 3.43 to distinguish between the different accretion modes. Consequently, we compute the X-ray luminosity for every accretion mode relying on the recipes provided by Bozzo et al. (2008) and outlined in Appendix B.2 for alle accretion regimes discussed above.

Fig. 3.6 shows the result of our analysis. The stellar parameters of the donor star are given in the caption. As in the previous section, we marked the parameter space where RLOF is initiated in black. In the upper middle of the diagnostic diagram, the NS companion accretes in the direct accretion mode. The NS does not spin fast enough. Consequently, the propeller effect can not work in this regime. Since the accretion is not inhibited, the X-ray emission reaches its maximum in the direct accretion regime for the most minor orbital periods.

At the bottom of the diagnostic diagram, the NS accretes in the supersonic accretion regime. By comparing the X-ray luminosity 3.6 of an NS with spin period 10^4 s (direct accretion) and 1 s (supersonic accretion) at the same orbital period, we find that the supersonic propeller reduces the X-ray luminosity by a factor of 1000.

The subsonic propeller regime becomes important for NSs with spin periods above a few seconds and orbital periods above a few days. Hence, it is located in the middle of the diagnostic diagram. The X-ray luminosity in the regime is comparable to the supersonic propeller.

The sub- and super-Keplerian inhibition regimens are at the diagnostic diagrams' right.

As discussed above, they become essential when the terminal wind velocity of the donor star becomes large. If the NS spins with a period of 10 s or more, the resulting X-ray luminosity in this regime is low, i.e., less than 10^{30} erg/s. However, if the NS spins faster, the X-ray luminosity increases in the super-Keplerian accretion mode. As described above, the increase of X-ray emission with a decreasing spin period results from the dissipation of rotational energy into heat. We will see below that for most of our analyzed stars, the Keplerian inhibition modes are not expected to be initiated at orbital periods below 1000 d. Since we restrict ourselves to an orbital period smaller than this, we will not cover the Keplerian accretion modes for these stars. These accretion modes become important only for a few stars with large terminal velocities.

We can hence conclude that a NS in the direct accretion regime is expected to show the largest X-ray emission compared to the other accretion regimes. If the NS spins fast enough or revolves in an orbit of a few days or more, its X-ray luminosity is too dim to be detected.

Table 3.1.: Magnetic field strengths (Taani et al. 2018) and spin periods (Walter et al. 2015) of X-ray pulsars.

Name	$B_{\text{NS}}[10^{12} \text{ G}]$	$P_{\text{NS}}[\text{s}]$
LMC X-4	11.2	13.5
Cen X-3	3.4	4.82
J16393	3.3	912
4U1538	2.4	530
J18027	2.6	140
J16493	3.7	1093
4U1907	2.1	4.4
Vela X-1	6	8.96
OaO1657	4	38.2
2S0114	2.5	9700

3.4 Main sequence star companions

It is also possible that the companion of a massive star is a main-sequence (MS) star instead of a CO. A MS companion differs from a CO companion in three ways. On the one hand, a MS star is extended. Thus, the gravitational potential on its surface is much lower compared to a CO, and in addition to RLOF from the primary to the MS secondary, RLOF from the secondary to the primary may occur. On the other hand, a MS companion has an intrinsic luminosity, which could be comparable to the primary's luminosity. At last, a main sequence companion may also launch a strong stellar wind. Especially if the companion is luminous, mass-loss rates comparable to the primary's mass-loss rate may be achieved. The shock front of two colliding winds is the source of energetic X-ray emission due to thermal bremsstrahlung.

3.4.1 X-ray emission from colliding stellar winds

If the MS companion is a massive star, it will have a mass-loss rate comparable to the primary's wind. Consequently, the interaction of the two wind flows will lead to a shock of the wind material, which can heat the gas to temperatures of 10^7 K and above. For a review on these colliding-wind binaries, see Rauw and Nazé (2016). The hot gas emits X-rays with a luminosity up to 10^{33} erg/s if both companions are O stars (Pittard and Dawson 2018). In WR+O binaries, the X-ray luminosity can reach up to 10^{35} erg/s as in the case of WR 25 (Gagné et al. 2012). Other WR+O binary systems are too dim to be identified in the X-ray band. This is illustrated by Nazé et al. (2021), who propose that the faintness of these systems could result from significant X-ray absorption due to the dense WR wind. They also consider the likelihood that WR+O binaries may exist without a noticeable X-ray bright wind collision zone.

Consequently, determining whether a WR+O binary produces intense X-rays is not straightforward. The complicated flow structures within these colliding-wind binaries contribute to the complexity of addressing this question. Thus, a full treatment to reproduce the X-ray luminosity as a function of the stellar parameters, such as the mass-loss rate or terminal velocity, requires full 3D numerical simulations. Since this is beyond the scope of this study, we developed a much simpler approach to estimate the X-ray luminosities from colliding stellar wind.

Assuming radial symmetry the dynamic pressure $p_{\text{dyn}} = \frac{1}{2}\rho v$ of the stellar wind reads

$$p_{\text{dyn}} = \frac{\dot{M}}{8\pi} \frac{v(r)}{r^2}. \quad (3.48)$$

Regarding the connecting line of the two binary components, the shock front is located at the point where the dynamic pressure of the wind from the primary equals the pressure of the secondary's wind (Stevens et al. 1992; Usov 1992). Equating the dynamic pressures leads to

$$\frac{(1 - R_1/r_1)^\beta r_2^2}{(1 - R_2/r_2)^\beta r_1^2} = \xi, \quad (3.49)$$

which defines the location of the equilibrium of forces, i.e., a fixed point. Here, $\xi := \frac{\dot{M}_2 v_{\infty;2}}{\dot{M}_1 v_{\infty;1}}$ is the ratio of the wind momentum at infinity. From here, we assume the same β -value for both companion winds. Note that r_1 and r_2 are the distances of the shock front from the corresponding binary companion, i.e., $r_1 + r_2 = a$.

We define the radius of the shock front as $r_{\text{shock}} := \min(r_1, r_2)$. Suppose that r_1 and r_2 are large compared to the stellar radii or that the wind is launched fast, i.e., $\beta = 0$. In this case, Eq. 3.49 may be solved analytically and yields

$$r_{\text{shock}} = \frac{\sqrt{\xi}}{1 - \sqrt{\xi}} a. \quad (3.50)$$

In the following investigation, we assume $\beta = 1$, and the shock radius may be of the same order as the stellar radii. In this case, a numerical solution has to be computed. We use Newton's method to solve Eq. 3.49.

In the case of a non-vanishing β value, Eq. 3.49 has multiple solutions in general. While every one of these points is a fixed point, since force equilibrium holds, they are not all stable against perturbations. This can be seen from a brief analysis: assume a small amount of matter at a distance r from the primary's center of mass. The matter is subject to forces from the dynamic pressure of the stellar wind from the primary and the secondary star. The total force is proportional to the difference of the dynamic pressures

$$\Delta p(r) = p_1(r) - p_2(r). \quad (3.51)$$

If Δp is positive, the matter is pushed away from the primary towards the secondary. On the other hand, if Δp is negative, the matter is pushed away from the secondary. At a fixed point r_{fix} , we have $\Delta p(r_{\text{fix}}) = 0$ per definition, and the matter experiences no total force. Now assume that the matter is close to a fixed point. A Taylor expansion then yields

$$\Delta p(r) \approx \Delta p'(r_{\text{fix}})(r - r_{\text{fix}}). \quad (3.52)$$

Here, the dash denotes the derivative with respect to r . Since $\Delta p'(r_{\text{fix}}) = p'_1(r_{\text{fix}}) - p'_2(r_{\text{fix}})$, we can conclude that the pressure difference grows with r if p_1 grows faster than p_2 , i.e., $p'_1(r_{\text{fix}}) > p'_2(r_{\text{fix}})$.

This means a small perturbation that pushes matter from a fixed point toward the secondary would lead to a positive pressure difference and a subsequent force toward the secondary. This would increase the perturbation even more. Vice versa, a perturbation that shifts the matter closer to the primary would lead to a negative pressure difference, which means that the secondary's wind would overcome the primary's wind, pushing the matter closer to the primary until the primary's surface is reached. At this point, the dynamical wind pressure of the primary vanishes since the wind velocity vanishes at the photosphere. However, the gas pressure at the primary's photosphere now balances the secondary's wind pressure. This leads to an equilibrium where the shock radius equals the primary radius. We can conclude the discussion with the result that fixed points where $p'_1(r_{\text{fix}}) > p'_2(r_{\text{fix}})$ are unstable against perturbations, while fixed points are stable $p'_1(r_{\text{fix}}) < p'_2(r_{\text{fix}})$.

A shock front can only exist at stable fixed points. The algebraic analysis of Eq. 3.49 shows that either one or three fixed points exist. Regard the fixed point that is closest to the primary. We find $\Delta p < 0$ at the primary's photosphere since the primary's wind has vanishing velocity. At the fixed point $\Delta p = 0$, which means the pressure difference changes from negative to positive, i.e., $\Delta' p > 0$. Thus, the fixed point that is closest to the primary must be unstable. The argument holds vice versa for the fixed point that is closest to the secondary. If three fixed points exist, the point in the middle must be stable since Δp is a continuous function.

As an illustration, we show the dynamical wind pressure in the colliding wind binary HD 93161A in Fig. 3.7. The stellar parameters are inferred from the discussion below. The radial extensions of the two binary components are visible as shaded areas, where the primary is blue and the secondary is orange. The lines show the dynamic wind pressure. The fixed points are the points where the two lines intersect (red and green dots). We find three of these points in Fig. 3.7. The discussion above shows that the two red dots must be unstable since they are the closest fixed point to the primary and the secondary,

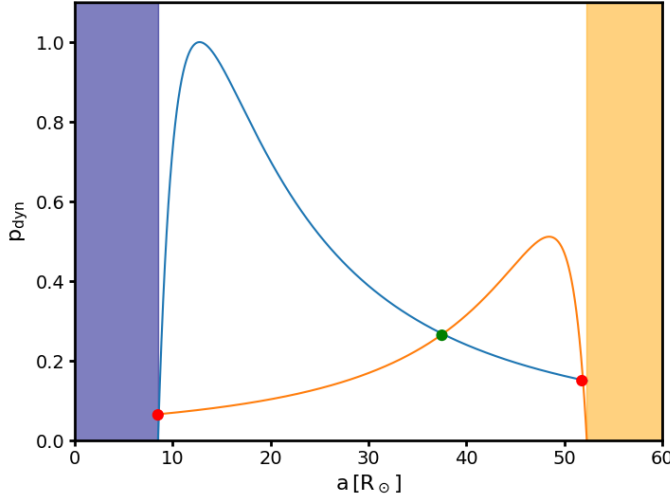


Figure 3.7.: Dynamical wind pressure as a function of the distance from the primary in the colliding wind binary HD 93161A. The orbital separation of the binary is $60 R_{\odot}$. The shaded areas show the radial extension of the primary (blue) and the secondary (orange). The lines show the dynamic pressure of the corresponding stellar wind normalized to the maximum. The colored dots mark the points where the dynamical pressure is equal, i.e., fixed points. Red dots mark unstable fixed points, while green dots mark the stable fixed point, i.e., the shock front.

respectively. The green dot in the middle marks the stable fixed point, which we assume is the shock's location. Thus, the shock $r_{\text{shock}} = 22.4 R_{\odot}$, which is the distance from the secondary's center of mass.

Two examples where no stable fixed point exists are shown in Fig. 3.8. The top panel shows the dynamic pressure in HD 215835. The orbital separation of the binary is relatively small and comparable to the size of the wind acceleration zone. This leads to the situation that only one fixed point exists, which is the closest fixed point to the primary and the secondary and, hence, unstable. We call binaries having only one unstable fixed point due to a small orbit separation *compact unstable*.

The bottom panel of Fig. 3.8 shows the dynamical pressure in QZ Car. The orbital separation of this binary is larger than the wind acceleration zone. After computing the shock radius, we compute the shocked wind material's X-ray emissivity ϵ . If a stable fixed point exists, we do this for the primary's and secondary's wind and add the inferred emissivities. If no stable solution exists, we only compute the emissivity of the stronger wind.

We first compute wind density and the wind velocity at the location of the shock front using Eqs. 3.4 and 3.6, where we use the distance to the shock front for a . The density and temperature of the shocked material are inferred from using the Rakine-Hugoniot jump condition for an ideal gas with adiabatic exponent $\gamma = 5/3$ (Regev et al. 2016). These conditions imply that the density of the shocked wind material is

$$\rho_{\text{shock}} = \frac{(\gamma + 1)\mathcal{M}^2}{(\gamma + 1) + (\gamma - 1)(\mathcal{M}^2 - 1)} \rho_{\text{w}}, \quad (3.53)$$

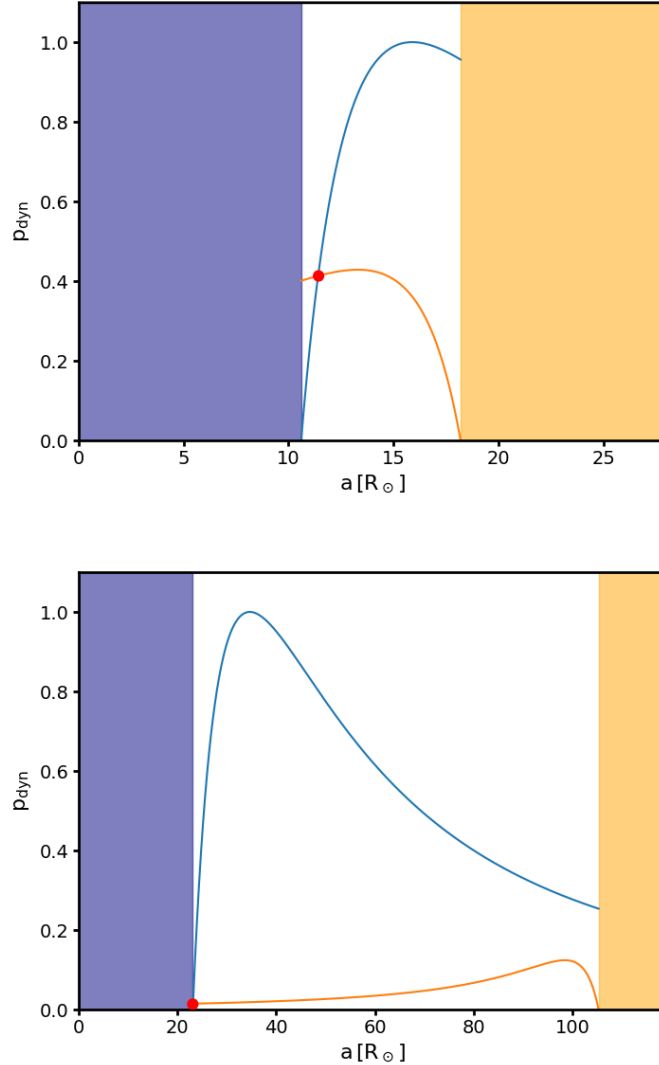


Figure 3.8.: Similar to Fig. 3.7 for the colliding wind binaries HD 215835 (top) and QZ Car. Both binaries have an unstable fixed point. In the first case, the unstable fixed point arises from the small orbital separation, and the fixed point is the wind acceleration zone. In the second case, the primary's wind is much stronger than the secondary's wind. Since the only fixed point is unstable in both cases, the shock radius is chosen to be the radius of the wind-weaker star (orange).

where $\mathcal{M} := v_{\text{W}}/c_s$ is the Mach-number of the un-shocked wind material and v_{W} is the wind velocity at r_{shock} . Since the flows that we regard are highly supersonic, we compute the limit of Eq. 3.53 for $\mathcal{M} \gg 1$ and find

$$\rho_{\text{shock}} = 4\rho_{\text{W}}, \quad (3.54)$$

which we use in our calculations. The thermal pressure of the shocked gas can be expressed as

$$p_{\text{shock}} = \frac{(\gamma + 1) + 2\gamma(\mathcal{M}^2 - 1)}{(\gamma + 1)} p_{\text{W}}. \quad (3.55)$$

Note that p_W denotes the thermal gas pressure of the unshocked wind material. Taking again the limit for $\mathcal{M} \gg 1$ we simplify this equation and obtain

$$p_{\text{shock}} = \frac{5}{4} \mathcal{M}^2 p_W. \quad (3.56)$$

Since we assume an ideal gas, we have $T \propto p \rho^{-1}$, which yields

$$T_{\text{shock}} = \frac{5}{16} \mathcal{M}^2 T_W. \quad (3.57)$$

This can further be simplified using the formula for the sound speed of an ideal gas $c_s^2 = \gamma \frac{R}{\mu} T_W$, R is the universal gas constant (Kippenhahn and Weigert 1990) and μ the mean molecular weight. Using this relation, we find

$$T_{\text{shock}} = \frac{3}{16} \frac{\mu}{R} v_W^2. \quad (3.58)$$

Using ρ_{shock} and T_{shock} , we can compute the emissivity under the assumption of thermal bremsstrahlung as the dominant radiation mechanism. The emissivity is computed using Eq. 3.24 together with Eq. 3.26 to 3.28, which yields

$$\epsilon_{\text{shock}} = \sqrt{12 \frac{\mu}{R}} \times \frac{C g_B}{m_p^2} \times \frac{(X+1)^3}{3X+1} \times \rho_W^2 v_W \quad (3.59)$$

Neglecting metals, the mean molecular weight is $\mu = 0.62$ for a hydrogen abundance of $X = 0.7$ (Kippenhahn and Weigert 1990). Assuming these value for μ and X the emissivity simplifies to

$$\epsilon_{\text{shock}} = 2.85 \times 10^{17} \text{ erg cm}^2 \text{ g}^{-2} \times \rho_W^2 v_W. \quad (3.60)$$

As written above, we compute and add the emissivities of both shocked winds. The stable fix-point of the colliding winds defines the shock-front and consequently r_{shock} . The total luminosity is then inferred by multiplication with the volume occupied by the shocked material. To estimate this volume, we use the radius of the shock-front as a characteristic scale length and consequently r_{shock}^3 as a characteristic volume. This estimate was suggested and applied by Stevens et al. (1992) and Usov (1992). However, numerical studies (Pittard and Dawson 2018) suggest that emission volume is rather the product of a characteristic surface r_{shock}^2 and a length scale (thickness of the shock-front) that is independent of the wind parameters. While we could also follow this approach, we decided to use the first since we cannot give a reasonable assumption for the universal length scale. In addition, our X-ray luminosity predictions are insufficient to prove which of the two mentioned approaches to derive the shock volume yields better results.

3.4.2 Main sequence models

To estimate the X-ray emission for the case of a main-sequence companion, we need the stellar parameters and wind properties as a function of the stellar mass. We used the grid of detailed evolutionary models computed by Brott et al. (2011) using the stellar evolution

code BEC (e.g. Yoon et al. 2010) to infer the stellar radius R_2 and the luminosity L_2 as a function of the total companion mass M_2 . Both parameters were taken at the ZAMS, i.e., the onset of hydrogen burning. Hence, we assume the companion is not in an evolved stage, i.e., late main-sequence, hydrogen shell burning, or helium burning.

We use a cubic spline to interpolate R_2 and $\log(L_2)$. The interpolation enables us to compute the effective temperature $T_{\text{eff},2}$ and the escape velocity $v_{\text{esc},2}$ of the companion. The terminal wind velocity is computed as a multiple of the escape velocity using the scaling formula provided by Kudritzki and Puls (2000), where

$$v_{\infty}/v_{\text{esc}} = \begin{cases} 2.65 & : T_{\text{eff}} \geq 21 \text{ kK} \\ 1.4 & : 10 \text{ kK} < T_{\text{eff}} < 21 \text{ kK} \\ 1.0 & : T_{\text{eff}} < 10 \text{ kK} \end{cases} . \quad (3.61)$$

The mass-loss rate as a function of stellar mass, luminosity, effective temperature, and terminal velocity is inferred using the prescription of (Vink et al. 2001). The mass-loss rate at the bi-stability jump between 22.5 and 27.5 kK is computed by linear interpolation of $\log(\dot{M})$ between the two threshold temperatures.

We used the list of colliding wind binaries compiled by Gagné et al. (2012), who list spectral types, periods, distances, and X-ray luminosities of multiple colliding wind binaries. We selected 13 O+O binaries where the spectral type and luminosity class are known sufficiently well. In addition, we selected 3 WR+O binaries where the spectral type of the O star is known and Hamann et al. (2019) provided stellar parameters of the Wolf-Rayet star.

The listed X-ray luminosities were corrected for the *Gaia* distances d (Salgado et al. 2017; Luri et al. 2018) by re-scaling the luminosity according to

$$L_X = L_{X,0} \left(\frac{d}{d_0} \right)^2 , \quad (3.62)$$

where the subscript 0 refers to the X-ray luminosity and distance listed by Gagné et al. (2012). In the following analysis, we use the corrected luminosity L_X for comparison with our theory. The corrected X-ray luminosities are listed in Table 3.2.

The stellar parameters of the O stars were inferred by Muijres et al. (2012), who lists the stellar mass and radius, based on calibration of Martins et al. (2005), as well as wind mass-loss rates based on the prescription provided by Vink et al. (2001). The terminal velocity of the stellar wind is assumed to be 2.6 times the escape velocity of the star (Muijres et al. 2012). The stellar parameters and wind parameters of the WR stars are adopted from Hamann et al. (2019).

Once the stellar masses are known, we compute the orbital separation under the assumption of circular orbits. Using the mass-loss rates and terminal velocities, we can determine the location of the shock front as described above. For this, we assume a wind acceleration parameter of $\beta = 1$. We further discriminate between cases where the shock-front is a stable fixed point and binaries where the fix-point is compactly unstable or widely unstable. Finally, we compute the density and temperature to infer the emissivity of the shocked material and, consequently, the X-ray luminosity as described above. The assumed stellar parameters and the predicted X-ray luminosities are listed in Tab. 3.2.

The top panel of Fig. 3.9 shows the X-ray luminosity predicted by our model against the observed X-ray luminosity for the 16 colliding wind binaries. For comparison, we included a dashed line to indicate where the theoretical model matches the observation. We find that our model predicts the order of magnitude of the X-ray luminosity fairly well in most cases, independently of the stability of the fix-point. For comparison, we present a similar plot using the model proposed by Usov (1992) in the bottom panel of Fig. 3.9. We find a similar agreement between theory and observations as with our model. Consequently, we will use our model in the further course of this study.

We note that WR 3 shows the largest deviation from our model. Based on the parameters in Tab. 3.2, our model predicts an X-ray luminosity of $\sim 10^{35}$ erg/s; however, the observed X-ray luminosity is three orders of magnitude smaller. Using the model provided by Usov (1992), we find an even bigger deviation between theory and observation. This raises the question if WR 3 is an actual colliding wind binary. In Sec. 4.3, we discuss the possibility of an MS, BH, and NS companion of WR 3 in more detail.

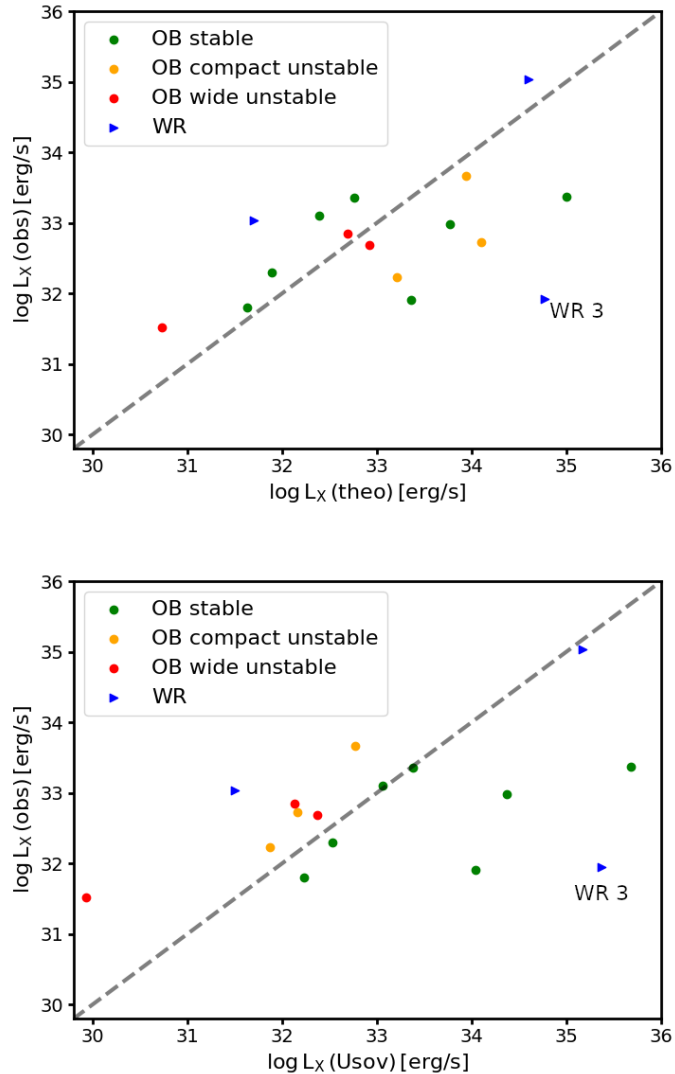


Figure 3.9.: Top panel: Observed X-ray luminosity and X-ray luminosity as predicted from our theoretical model. Every point indicates a colliding wind binary from Table 3.2. This color indicates the stability of the fix-point and the nature of the primary (OB or WR). The dashed line indicates the point in the diagram where the theoretically predicted luminosity matches the observation. Bottom panel: The same as the top panel, but using the theoretical model provided by Usov (1992).

Table 3.2: Parameters of the 16 colliding wind binaries analyzed in this study. The spectral type (SpType), orbital period, and the observed X-ray luminosity ($\log(L_X)$ obs.) – corrected for Gaia distances – are adopted from Gagné et al. (2012). The stellar parameters, the O stars are adopted from Muijres et al. (2012). The parameters of the WR stars are from Hamann et al. (2019). We also list orbital separation (a), the shock radius (r_{shock}), and the X-ray luminosity as predicted by our prescription ($\log(L_X)$ theo.). In the last column, we indicate if a stable fixpoint for the shock-front exists (stb.) or if the fix-points are compactly unstable (cu) or wide unstable (wu).

Name	Sp 1	Sp 2	P [d]	M_1 [M_\odot]	M_2 [M_\odot]	R_1 [R_\odot]	R_2 [R_\odot]	$v_{\infty;1}$ [km/s]	$v_{\infty;2}$ [km/s]	$\log(\dot{M}_1)$ [M_\odot/yr]	$\log(\dot{M}_2)$ [M_\odot/yr]	a [R_\odot]	r_{shock} [R_\odot]	$\log L_{X,\text{th}}$ [erg/s]	$\log L_{X,\text{obs}}$ [erg/s]	stability
HD 165052	06.5V	06.5V	6.14	29.0	29.0	9.8	9.8	2810	2810	-6.43	-6.43	55	27.5	33.77	32.98	stb
HD 47129	06I	07.5I	14.40	45.8	39.2	20.3	21.7	2460	2200	-5.44	-5.78	109	72.1	35.00	33.37	stb
HD 101131	06.5V	08.5V	9.65	29.0	19.8	9.8	8.1	2810	2560	-6.43	-7.17	70	52.6	32.39	33.10	stb
HD 101436	06.5V	07V	37.37	29.0	26.5	9.8	9.4	2810	2750	-6.43	-6.62	179	100.6	32.76	33.36	stb
HD 93161A	08 V	09V	8.57	22.0	18.0	8.5	7.7	2630	2500	-7.02	-7.37	60	37.6	31.89	32.29	stb
HD 93343	08 V	08V	44.15	22.0	22.0	8.1	8.1	2700	2700	-7.17	-7.17	185	92.5	31.63	31.80	stb
QZ Car	09.5I	09III	20.72	30.4	23.1	23.1	13.7	1880	2120	-6.15	-6.56	119	48.1	33.36	31.91	stb
HD 100213	07 V	08V	1.39	26.5	22.0	9.4	8.5	2750	2630	-6.62	-7.02	19	8.5	34.10	32.73	cu
HD 1337	09 III	09III	3.52	23.1	23.1	13.7	13.7	2120	2120	-6.56	-6.56	35	13.7	33.21	32.23	cu
HD 215835	05.5V	06.5V	2.11	34.2	29.0	10.6	9.8	2940	2810	-6.01	-6.43	28	9.8	33.94	33.66	cu
HD 101190	04 V	07.5V	6.05	46.2	24.2	12.3	8.9	3170	2690	-5.57	-6.82	58	8.9	32.69	32.85	wu
TR 16-34	08 V	09.5V	3.00	22.0	16.5	8.1	7.4	2700	2450	-7.17	-7.59	30	7.4	30.73	31.52	wu
HD 93205	03 V	08V	6.08	58.3	22.0	13.8	8.5	3360	2630	-5.38	-7.02	60	8.5	32.92	32.69	wu
WR 3	WN3h	O4 V(?)	46.85	17.0	46.0	2.5	12.3	2700	3160	-5.40	-5.57	217	117.2	34.77	31.97	stb
WR 22	WN7h	09 V	80.34	49.0	18.0	22.7	7.7	1785	2500	-4.40	-7.37	318	7.7	31.70	33.03	wu
WR 25	WN6h	04V	207.80	58.0	46.0	20.2	12.3	2480	3160	-4.60	-5.57	694	508.7	34.60	35.03	stb

3.4.3 Optical flux ratio

Since we are mainly interested in the investigation of single-lined binaries, it is necessary to predict if the absorption lines of the companion are detectable in the optical spectrum of the binary. Since hot stars release most of their energy in the UV range, it is not sufficient to compare the bolometric luminosities of the two binary companions. Instead, we use the visual magnitude M_V to measure the visual band's flux. The visual magnitude can be computed from the stellar luminosity and effective temperature with

$$M_V = M_{\text{bol};\odot} - 2.5 \log(L/L_\odot) - BC(T_{\text{eff}}) \quad (3.63)$$

where $M_{\text{bol};\odot}$ is the bolometric luminosity of the sun and BC the bolometric correction. We adopt $M_{\text{bol};\odot} = 4.72$ mag (Gray 2005; Torres 2010). The bolometric correction as a function of effective temperature is adopted from the empirical fit relation of Flower (1996), which was rectified by Torres (2010). The analyzed data set included stars of all luminosity classes from I to V. The fit relation is a sixth-order polynomial of $\log(T_{\text{eff}})$ that reproduces the BC in the temperature range between 5 and 50 kK with an uncertainty of about 0.1 mag.

Below this range, the accuracy of the fit suffers from a lack of measurements. Thus, the BC is less reliable and unusable for M stars. However, the absolute value of the BC in the cool temperature regime hardly exceeds 3.5 mag (Ridgway et al. 1980), i.e., a factor of 25 in linear flux. This means that main-sequence stars with effective below 5000 K are always undetectable if their binary companion is a massive star. Consequently, we do not have to consider the cool range where the fit relation of Flower (1996) is inapplicable.

At the hot threshold, at 50 000 K, the fit polynomial swings up. This behavior results from the high polynomial order. As shown in Fig. 3.10, the fit relation suggests the absolute value of the BC decreases with increasing temperature (dashed line). Since this is un-physical, we extrapolate the BC linearly as a function of $\log(T_{\text{eff}})$.

In the following investigation, we will exclude the regime of the parameter space where the difference of absolute visual brightness between the two companions exceeds 2.5 mag. This corresponds to a flux difference of 10% in the optical spectra of the two stars, which observers would detect. We also mark the regime where the difference of the visual magnitudes is 5 mag. This corresponds to the case where the companion's optical spectrum has only 1 % of the primary spectrum's flux. Stars less massive than this second threshold are assumed to be utterly undetectable due to their faintness.

3.5 Validity check

This section discusses the three cases of Cyg X-1 and Vela X-1. We do this to illustrate our method on well-studied objects and to compare them with observations. The first two can be regarded as archetypal examples of wind-fed X-ray binaries hosting a BH and a NS, respectively (Bolton 1972; Ziolkowski 2014). The latter is known to be a colliding wind binary.

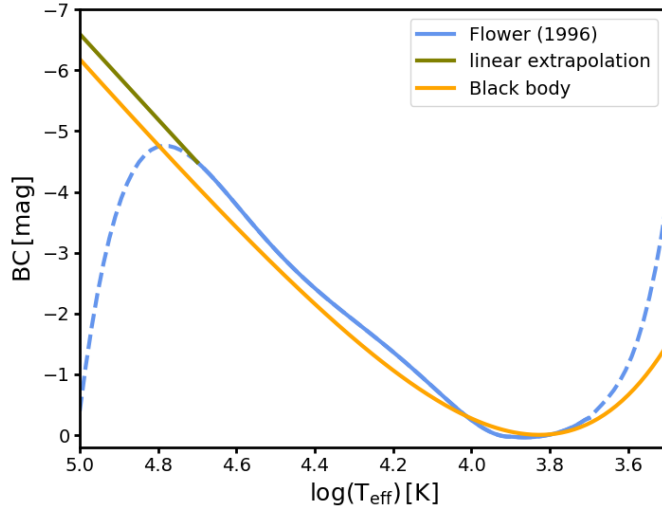


Figure 3.10.: Bolometric correction as inferred from observations by Flower (1996) and rectified by Torres (2010). The blue line shows the fit relation proposed in the cited studies. The fit relation reproduces the observations between 5 and 50 kK (solid blue). Above this range, the polynomial fit relation starts to oscillate up (dashed). We apply a linear extrapolation instead. Stars with temperatures below this range are not considered in this study.

3.5.1 Diagnostic diagram of Cyg X-1

Cyg X-1 was the first HMXB recognized to host a BH (Bolton 1972). The HMXB is one of the brightest X-ray sources in the sky and one of the best-studied stellar X-ray sources. Assuming a distance of 2.5 kpc, Schulz et al. (2002) derived an X-ray luminosity of the accretion disc of 5.3×10^{36} erg/s and a total luminosity of 1.6×10^{37} erg/s. Correcting for the *Gaia* distance of 2.25 kpc we find a disk luminosity of 4.3×10^{36} erg/s and a total X-ray luminosity of 1.3×10^{37} erg/s.

The BH orbits an O type supergiant with a period of 5.6 d (Brocksopp et al. 1999; Walter et al. 2015). The mass of the donor and the accretor was estimated to be $27 M_{\odot}$ and $16 M_{\odot}$ respectively by Ziolkowski (2014) using evolutionary models. Recent studies by Miller-Jones et al. (2021) suggest significantly higher masses of $41 M_{\odot}$ for the donor star and $21 M_{\odot}$ for the BH accretor, based on radio interferometry. The system has a distance of 2.2 kpc and is inclined by 27° to the line of sight (Orosz et al. 2011; Miller-Jones et al. 2021).

Based on mass-luminosity relation Miller-Jones et al. (2021) also derived $\log(L/L_{\odot}) = 5.63$ and $T_{\text{eff}} = 31.1$ kK for the donor star, which implies a stellar radius of $22 R_{\odot}$. The binary interaction, as well as the fact that the system is almost Roche-lobe filling, makes a reliable determination of the wind parameters v_{∞} , \dot{M}_W and β difficult. Kudritzki and Puls (2000) inferr a terminal velocity of 1430 km/s⁽³⁾. However, given the parameters in Tab. 3.3, this value yields $v_{\infty}/v_{\text{esc}} = 1.7$, which is significantly below the value of 2.65 that is expected according to Kudritzki and Puls (2000) (cf. Eq. 3.61). Davis and Hartmann (1983) infer a larger value for the terminal velocity of 2300 km/s. This is in better

Table 3.3.: Adopted parameters for Cyg X-1. References: 1 Miller-Jones et al. (2021), 2 Brockopp et al. (1999), 3 Vrtilek et al. (2008)

M_1	$41 M_{\odot}^{(1)}$
R_1	$22 R_{\odot}^{(1)}$
T_{eff}	$31 \text{ kK}^{(1)}$
M_2	$21 M_{\odot}^{(1)}$
$\log(L_1/L_{\odot})$	$5.63^{(1)}$
P	$5.6 \text{ d}^{(2)}$
β	$0.75^{(3)}$
i	$27 \text{ deg}^{(1)}$
$\log(\dot{M}/M_{\odot} \text{ yr}^{-1})$	$-5.3^{(3)}$
v_{∞}	2234 km/s

agreement with what would be expected from Eq. 3.61. However, the simplified picture of an isotropic wind is insufficient to describe this binary system's flow. As a result, the wind parameters may not be deduced uniquely, as pointed out by Gies and Bolton (1986). Using a model for the focused stellar wind, we estimated a value between 1650 km/s and 2540 km/s, depending on the Roche-lobe filling factor and the direction in which the wind is launched.

Since a determination of the wind velocity is beyond the scope of this study, we will use $v_{\infty} = 2234 \text{ km/s}$, i.e., $2.65 \times v_{\text{esc}}$.

The wind mass-loss rate is also subject to uncertainties. Values for $\log(\dot{M}_w)$ reach from -5.9 (Gies and Bolton 1986) to -5.6 (Gies et al. 2003) and -5.3 (Vrtilek et al. 2008). However, these values agree with the receipt of (Vink et al. 2001) which implies $\log(\dot{M}_w) = -5.6$. We shall adopt this value in our calculations.

An additional constraint for the wind parameters comes from the measurement of the hydrogen column density. Schulz et al. (2002) derived a column density of $N_{\text{H}} = 6.2 \times 10^{21} \text{ cm}^{-2}$. Together with a hydrogen mass fraction of $X = 0.7$ (Miller-Jones et al. 2021) the column mass density can be computed using

$$\Sigma = \frac{m_p}{X} N_{\text{H}}. \quad (3.64)$$

We thus find the mass column density $\Sigma = 0.015 \text{ g/cm}^2$, which is in good agreement with a value of 0.019 g/cm^2 that is derived by Eq. (3.39). The Bondi-Hoyle accretion model yields an accretion rate following Eq. (3.11) of $\dot{M}_A = 2.8 \times 10^{-9} M_{\odot} \text{ yr}^{-1}$.

Figure 3.11 shows the X-ray luminosity of a hypothetical CO orbiting the donor stars of Cyg X-1. White dashed lines correspond to the CO's mass. For comparison, we marked the observed BH in Cyg X-1 using the observed orbital period and the inferred mass of the BH. The parameter space, where $R_L < R_1$ is marked black. If the orbital parameters were close to the edge of this area, Roche-lobe overflow would power the accretion. The luminosity would be comparable to the Eddington limit, and the binary would be a bright X-ray source.

All companions less massive than $3 M_{\odot}$ are treated as neutron stars. In this plot, we assume a direct accretion onto the NS. A more detailed analysis of NS accretion is demon-

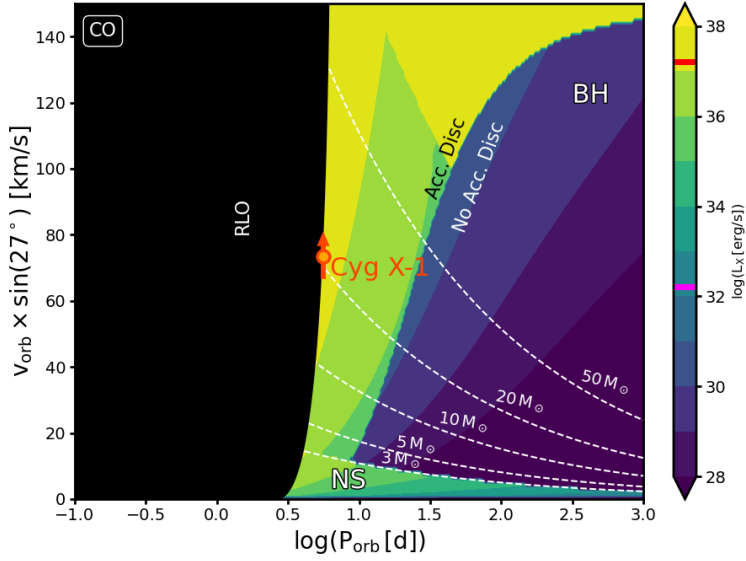


Figure 3.11.: Expected X-ray luminosity of a hypothetical CO in Cyg X-1 as a function of orbital period and projected orbital velocity of the donor star. The white dashed lines mark the mass of the companion star. A companion less massive than $3 M_{\odot}$ is assumed to be a neutron star (NS). A more massive companion is treated as a black hole (BH). The BH regime is subdivided into a part where an accretion disc is formed around the BH and a part where no disc is expected to form. In the accretion disc regime, the BH emits a large amount of X-rays (green, yellow area in the BH regime). We apply the spherically symmetric accretion model in a regime where no disc is expected. This leads to the prediction of faint X-rays from the BH companion (blue area). The black area marks the regime of Roche-lobe overflow (RLOF). The orange dot shows the observed orbital parameters of Cyg X-1. The error bars correspond to the error of the companion mass provided by Miller-Jones et al. (2021). We marked the observed X-ray luminosity (red) and the expected intrinsic X-ray luminosity from the stellar wind of the primary (pink).

strated in the next section. More massive companions are treated as black holes. The BH regime in two areas: An X-ray bright area ($\log(P_{\text{orb}}) = 0.6 \dots 1$) where the angular momentum of the accreted material is sufficient to support an accretion disc according to Eq. 3.16 and an area where we assume that the matter falls spherically symmetric into the black hole. In the first case, the X-ray luminosity is computed using Eq. 3.18; we use Eq. 3.31 for the spherically symmetric in-fall regime. While the plot suggests a sharp threshold between these two regimes, we note that this results from simplification. In our model, we do not treat the transition between the accretion disc area and the area of spherically symmetric in-fall. Thus, the computed X-ray luminosities in the vicinity of this threshold are very uncertain.

According to Fig. 3.11 the X-ray luminosity of Cyg X-1 exceeds 10^{36} erg/s. This is in fairly good agreement with observations as we model the X-rays from the accretion disc. Following the dashed line of a $20 M_{\odot}$ BH, our model predicts a transition from the accretion disc regime to spherically symmetric in-fall at an orbital period of about ten days. According to our model, the X-ray luminosity drops below 10^{30} erg/s at an orbital period of 20 days. This means that the X-ray emission of Cyg X-1 would be undetectable with current telescopes if its orbital period were only four times larger than its actual

value.

3.5.2 Diagnostic diagram of Vela X-1

Here, we discuss the diagnostic diagram of a NS companion using the example of Vela X-1. Vela X-1 is one of the best-studied NS-hosting HMXBs. It has a persistent X-ray luminosity of 4×10^{36} erg/s (Nagase et al. 1986), but shows some variability on short time scale (Kreykenbohm et al. 2008). The variability is believed to arise from changes in the donor star's wind and clumping of the wind matter (Haberl and White 1990; Odaka et al. 2013). These two effects and their influence on the accretion rate are poorly understood. Hence, we investigate the persistent X-ray luminosity only. The neutron star has a mass of $1.8 M_{\odot}$ (Rawls et al. 2011). It possesses a strong magnetic field of 2.6×10^{12} G (Kreykenbohm et al. 2002). Assuming that its radius is 10 km and that the magnetic field is a dipole field, it implies a magnetic moment of 1.3×10^{30} erg/G. The orbital separation of the binary is $55 R_{\odot}$. Eq. 3.4 yields a wind velocity 743 km/s at the position of the NS, which results in a relative velocity of 797 km/s between the wind material and the NS. The corresponding accretion radius (Eq. 3.8) is $R_A = 1.2 R_{\odot}$ and the Bondi-Hoyle accretion rate (Eq. 3.11) is $2 \times 10^{-10} M_{\odot}/\text{yr}$.

From the NSs spin and mass, we find the value of the co-rotation radius (Eq. 3.41) $R_{\text{co}} = 0.12 R_{\odot}$. According to Eq. 3.44, the radius of the magnetosphere is below $0.01 R_{\odot}$. Since $R_{\text{mag}} < R_{\text{co}} < R_A$, the accretion flow is not inhibited by the propeller effect. The relatively small wind speed of the donor star and the compact orbit of Vela X-1 result in a high accretion rate. This, in turn, leads to a high gas pressure of the in-falling material. As a result, the magnetosphere is small, and the centrifugal force at the magneto-pause is not strong enough to push the accreted matter outwards. Hence, the NS in Vela X-1 accretes directly from the stellar wind. In this cases Eq. 3.18 yields an X-ray luminosity of 1.7×10^{36} erg/s. This agrees with observations already pointed out by Sako et al. (1999) and Watanabe et al. (2006).

Table 3.4.: Adopted parameters for Vela X-1. References: 1 Falanga et al. (2015), 2 Watanabe et al. (2006), 3 Prinja et al. (1990)

M_1	$26 M_{\odot}^{(1)}$
R_1	$30 R_{\odot}^{(1)}$
M_2	$2 M_{\odot}^{(1)}$
P	$8.96 \text{ d}^{(1)}$
β	0.50
i	$73 \text{ deg}^{(1)}$
$\log(\dot{M}/M_{\odot} \text{ yr}^{-1})$	-5.8 ⁽²⁾
v_{∞}	1100 km/s ⁽³⁾

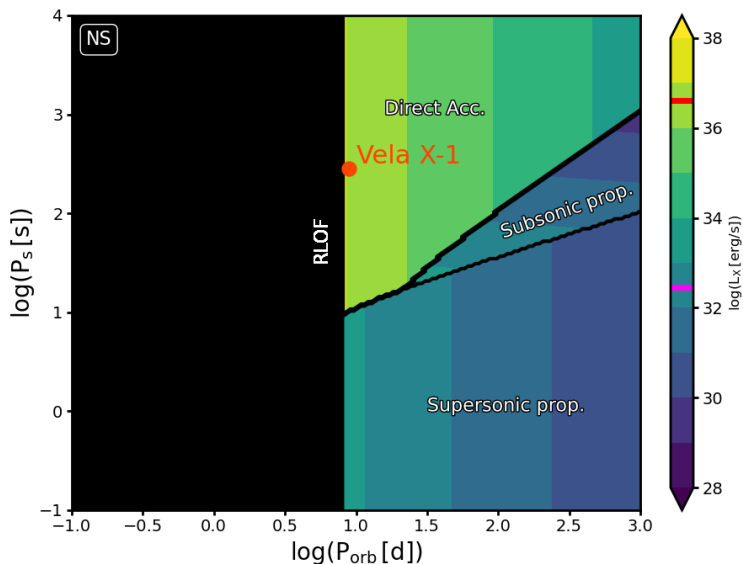


Figure 3.12.: Expected X-ray luminosity of a neutron star in Vela X-1 as a function of the orbital and spin periods. As in Fig. 3.11, the black area marks the parameter space where the system undergoes RLOF. The remaining parameter space is subdivided into three regions. In the bottom section, the supersonic propeller effect inhibits the accretion onto the NS. In the midsection, the accretion inhibition is due to the subsonic propeller effect. In the upper section, the accreted matter falls directly onto the NS. The orbital and spin periods of the NS in Vela X-1 are marked with an orange dot. The observed X-ray luminosity is marked in the color bar with a red line. The expected X-ray luminosity from the stellar wind is marked with a pink line.

3.6 Conclusion

The theory of stellar evolution predicts a significant number of OB+BH binaries (Langer et al. 2020; Sen et al. 2024). At the same time, only a few massive binaries that host a BH have been discovered by X-ray observatories (Walter et al. 2015). To understand this gap between prediction and observation, we have to investigate the mechanisms that cause the emission of X-rays in OB+BH binaries. In addition, understanding the cause of X-ray emission from massive binaries with NS or MS companions may help us to uncover the existence and the nature of the companion of single-lined spectroscopic binaries and apparently single stars.

In this chapter, we provided recipes to predict the X-ray emission from a binary considering a BH, NS, or MS companion, respectively. We note that our approaches are basic in the sense that they provide only an order-of-magnitude estimate of the X-ray emission.

In Sec. 3.2.4, we derived a criterion for the formation of an accretion disc of the BH. By assuming radial symmetric infall of the accreted material into the BH we derive a lower limit for the X-ray luminosity of an accreting BH without disc. Subsequently, we show that the X-ray luminosity of an accreting BH without a disc can be orders of magnitude smaller compared to a BH with an accretion disc. We demonstrate that the X-ray luminosity may drop below the detection limit in the absence of an accretion disc.

We also found that the formation of an accretion disc depends significantly on the wind velocity of the host star and the orbital separation of the binary. The larger the wind velocity, the less likely it is that an accretion disc can form, as the matter accreted by BH carries less angular momentum. If the host star has a wind velocity of 2000 km/s a BH companion would have an accretion disc with an orbital period of less than 10 d. At the same time, we expect that many OB+BH binaries have orbital periods above 10 d (Langer et al. 2020; Sen et al. 2024). Thus, the lack of observed X-ray bright, massive binaries with BH companion could be caused by the absence of an accretion disc due to the fast wind of the OB star. This hypothesis is strengthened by the detection of an X-ray quiet BH companion in the single-lined binary VFTS 243 in the Large Magellanic Cloud (Shenar et al. 2022). We will discuss this binary in the next chapter in more detail and show that our approach indeed predicts an X-ray faint BH as the companion of VFTS 243.

The next central result of this chapter is the development of the diagnostic diagram. This diagram can be created given known stellar parameters (mass, mass-loss rate, terminal velocity, etc.) of a host star. The diagnostic diagram serves as a phase diagram and shows the expected X-ray luminosity as a function of the binary’s orbital period and the expected value of RV variations as independent variables. In this way, we combine RV signatures of massive binaries with the X-ray detection from these systems. This enables us to draw conclusions about detected or putative BH companions of massive stars. We see this in the case of Cyg X-1, where the diagnostic diagram predicts the right order of magnitude of the observed X-ray luminosity from this X-ray binary. However, the diagnostic diagram of Cyg X-1 also shows that a BH companion can be X-ray faint within a large fraction of the phase space. Hence, these diagrams can predict whether a BH companion would be bright or quiet, given that the stellar parameters of the host star and the RV data are known.

To enhance our method and draw a better conclusion about the existence and nature of a putative binary companion, we also investigate the emission from accreting NS companions and X-ray emission from the collision of the primary's stellar wind with the wind of a MS companion. The goal of this analysis is to distinguish between BH, NS, and MS companions by the amount of detected X-rays.

For a NS companion, we distinguish between different accretion regimes depending on the strength of the NS's magnetic field and its spin period. We use recipes for the X-ray luminosity provided by (Bozzo et al. 2008). The corresponding diagnostic diagram shows the X-ray luminosity as a function of the orbital period and the NS spin period. By constructing this diagram for the X-ray binary Vela X-1 we find that the detected amount of X-rays and the orbital period of this system correspond to a NS companion that accretes directly, i.e., not inhibited by the propeller effect.

For MS companions, we develop a prescription to estimate the X-ray luminosity from colliding stellar winds based on the stability of the collision point. Our estimate shows a reasonably good agreement with the magnitude of the observed X-ray luminosity in colliding wind binaries.

The diagnostic diagrams of these three companions types, i.e., BH, NS, and MS companion, can be constructed and analyzed simultaneously to narrow down the phase space and draw a conclusion about the existence and the nature of a putative companion of a single-lined spectroscopic binary or an apparently single star. We will apply this methodology to different stars in the next chapter.

Chapter 4

Constraining the unseen companions of massive single-lined binaries by their X-ray emission

4.1 Introduction

The detection of gravitational waves has introduced a new observational avenue in astronomy (Abbott et al. 2016, 2017). To advance our understanding of the origins of stellar gravitational wave sources, we need to explore the evolutionary pathways of massive binary stars. However, in many binary systems, only the brighter star can be studied through optical spectroscopy, leaving the companion often undetected. Investigating the presence and nature of these unseen companions provides crucial tests for the predictions of massive binary evolution models.

The advent of X-ray astronomy in the last century opened a new observational window, especially for the detection and investigation of binary stars. Thus, even when the companion is too faint in the optical range to be detected, various effects within the binary system can result in X-ray emission. These effects include accretion from the stellar wind of the host star onto a compact companion in X-ray binaries (van den Heuvel and De Loore 1973; Hanawa 1989; King 1995; Negueruela 2010; Tauris and van den Heuvel 2023) as well as X-ray emission due to the collision of the host star's and the companion's stellar winds in cooling wind binaries (Portegies Zwart et al. 2002; Gagné et al. 2012; Zhekov 2012; Pittard and Dawson 2018).

Depending on the donor mass, X-ray binaries are divided into low-mass- (LMXBs) and high-mass X-ray binaries (HMXBs). HMXBs are divided in two main subclasses (Corbet 1984, 1986; Bildsten et al. 1997; Walter et al. 2015). The more numerous subclass contains Be type donor stars that are orbited by a NS on a wide and eccentric orbit (Reig 2011). The donor star is surrounded by a decretion disk (Lamers and Waters 1987; Waters et al. 1988; Rivinius et al. 2013). Accretion occurs every time the NS penetrates the decretion disk and captures some of the disk material (Apparao 1985).

The second subclass contains X-ray binaries with an OB type supergiant donor star. The mass-transfer mode operating in these supergiant X-ray binaries (SGXBs) is uncertain, and no general consensus has yet been reached. While RLO provides the high mass-transfer rates that are necessary to produce X-ray luminosity observed in some SGXBs, it

is believed that the X-ray emission in most SGXBs is due to wind accretion (Chaty et al. 2019). This accretion mode occurs as the compact companion captures a fraction of the wind material ejected by the massive donor Bondi and Hoyle (1944). The observed X-ray luminosities of SGXBs often agree with the accretion rates provided by accretion from an OB supergiant’s stellar wind (Shakura et al. 2014; Bozzo et al. 2016). We note, however, that many studies suggest mechanisms that could lead to a long-term stable RLO (Pratt and Strittmatter 1976; Basko et al. 1977; Pavlovskii and Ivanova 2015; Pavlovskii et al. 2017; Quast et al. 2019).

Since the majority of massive stars are formed within multiple stellar systems (Sana et al. 2008, 2009, 2011, 2013, 2014; Kobulnicky and Fryer 2007; Kobulnicky et al. 2014; Dunstall et al. 2015), one can expect that a significant number of massive stars hosts a BH companion (Langer et al. 2020). However, it is not always true that a BH is X-ray bright if it orbits a massive star (Shapiro and Lightman 1976; Sen et al. 2021, 2024, and Chap. 3 of this thesis). Binaries with X-ray faint black hole companions may appear as single-lined spectroscopic binaries (SB1). It is thus crucial to investigate these SB1s for the presence of a X-ray faint companion in order to better understand the BH population and to probe the models of binary evolution.

In addition to massive SB1s, Wolf-Rayet (WR) stars may also potentially harbor a BH companion. As massive stars with initial masses of $\gtrsim 20M_{\odot}$ evolve, they may strip their hydrogen-rich envelope and enter the WR phase (Crowther 2007). The hot and luminous WR stars are evolved stages of massive stars. Their high luminosity of the WR stars causes an intense radiative pressure, which launches a dense stellar wind, leading to the formation of broad emission lines predominantly of nitrogen and helium (WN-stars) or carbon (WC-stars) (Lamers 1991). With wind mass-loss rates up to a hundred times that of an OB star, it is natural to expect that Wolf-Rayet X-ray binaries (WRXBs) should be easily detected (Tutukov and Yungelson 1973). However, the only known WRXB in the Milky Way is Cyg X-3 (Giacconi et al. 1967; van den Heuvel and De Loore 1973), while about 40 SGXBs and over a hundred HMXBs in total are known in our galaxy (Walter et al. 2015). This raises the question of whether some of the apparently single WR stars have a companion that is not visible by RV variations or by emission of X-rays.

In this chapter, we explore various stars for the possibility of a binary companion. Our selected targets are chosen such that indications of a binary companion in the literature have been reported. These include SB1s, stars exhibiting unusual light curve behavior, or those suspected to be part of a binary system based on arguments from binary evolution models. We use the diagnostic diagrams developed in Chap. 3. This chapter is dedicated to applying this method to investigate the selected massive stars for the presence of an unseen compact companion. We create diagnostic diagrams for seemingly single WR stars in the Small Magellanic Cloud (Sec. 4.2), as well as three Galactic WR stars (Sec. 4.3 to 4.5), the Galactic WN 8 stars (Sec. 4.6), and the single-lined and uncertain double-line spectroscopic binaries from the Tarantula Massive Binary Monitoring (Sec. 4.7 and 4.8), all of which could harbor an unseen companion. Additionally, we provide a catalog of diagnostic diagrams for massive stars, illustrating various effective temperatures and surface gravities (Sec. 4.9). These diagrams assist in identifying stars that could harbor an unseen companion and help refine the potential nature of the suspected companion. We conclude our investigation in Sec. 4.10.

4.2 The apparently single Wolf-Rayet stars in the SMC

Investigating the evolution of massive stars at low metallicity is of particular importance if we want to understand the sources of gravitational waves as detected by the LIGO/Virgo observatories (Giacobbo et al. 2018). In order to comprehend the formation of black holes in low-metallicity environments, it is crucial to understand how massive stars shed their hydrogen-rich envelopes. This loss can occur either through the stellar wind or through interactions with a binary companion (Yusof et al. 2013; Szécsi et al. 2015; Pauli et al. 2022). With a metallicity approximately one-fifth that of the Sun (Venn 1999), the Small Magellanic Cloud (SMC) offers an ideal testing ground for studying binary evolution models in low-metallicity environments, as it is close enough to allow for detailed investigation of individual stars. Thereby, WR stars and their potential binary companions are of particular interest, as they represent advanced stages of massive binary evolution.

In a spectroscopic campaign, Foellmi et al. (2003) studied the binarity of eleven Wolf-Rayet stars in the SMC by searching for periodic radial velocity variations. Their results suggest a binary companion for the five WR stars AB 3, AB 5, AB 6, AB 7, and AB 8. No radial velocity variation above the detection limit of 30 km/s could be found for the other WR stars. A recent spectroscopic study by Schootemeijer et al. (2024) on these seemingly single WR stars found no evidence of binarity, with a mean RV standard deviation of 5 km/s. The authors showed that the probability for any of the apparently single WR stars to have a companion more massive than $5 M_{\odot}$ with an orbital period of less than a year is below 5%.

In this section, we discuss the possibility of the apparently single WR stars in the SMC by combining constraints of X-ray emission, which we developed in the previous chapter, and the detection limits of RV variations by Schootemeijer et al. (2024). Table 4.1 gives the parameters of the apparently single WR stars in the SMC adopted to construct the diagnostic diagrams. Stellar masses were taken from Schootemeijer and Langer (2018), while all other parameters were derived by Hainich et al. (2015).

A survey conducted by Guerrero and Chu (2008) for X-rays from the WR stars in the Magellanic Clouds did not detect any X-ray flux. The findings indicated an upper limit of approximately 5×10^{-5} counts per second. Assuming a mean photon energy of 1 keV, an effective area of 600 cm^2 for the Chandra telescope and an distance of 60 kpc to the SMC, the upper limit of the count rate corresponds to an upper limit of $6 \times 10^{32} \text{ erg/s}$ for the X-ray luminosity of the SMC WR stars. This value agrees with the detection limit discussed in Sec. 3.2.2, and we will use it as the upper limit of the X-ray luminosity for all SMC WR stars in the following discussion.

In the following, we discuss the possibility of a compact companion for some promising SMC WR stars. We discuss SMC AB 11 in more detail, the WR star with the fastest wind velocity among the considered stars. Figure 4.1 shows the diagnostic diagrams as developed above and applied to AB 11. We indicated the detection limit of RV variations by Schootemeijer and Langer (2018) with an orange dashed line in the top and mid panel.

The expected X-ray emission for a main-sequence (MS) companion is illustrated in the top panel of Fig. 4.1. This diagnostic diagram displays the anticipated X-ray luminosity as a function of the orbital period and the expected value of the radial velocity (RV)

semi-amplitude of the WR star. Additionally, the parameter space where a hypothetical MS companion would be less than 2.5, mag fainter than the WR star is highlighted (red hatched area), along with the region where it would be 5, mag fainter (red dotted line). These magnitude differences correspond to flux ratios of 10% and 1%, respectively. A MS companion contributing 10% to the total optical flux would likely have been detected by its signature in the spectrum. For companions with a flux ratio between 1% and 10%, i.e., those situated between the red dotted line and the red hatched area, detection in the optical spectrum is still possible, though it cannot be entirely ruled out that such a companion has evaded detection thus far.

This diagram indicates that a MS companion, more massive than $7M_{\odot}$, would be visible in the optical spectrum since its absolute magnitude exceeds the magnitude of the WR star (red area). Even if the companion was a $2.8 M_{\odot}$ star, detection of the binary partner would be possible (red line). In addition, a MS of $2.8 M_{\odot}$ or more would have been detected by Schootemeijer et al. (2024) if its period was smaller than about ~ 1 yr.

For such a low-mass MS companion, the X-rays would be produced mainly due to the direct collision of the WR wind onto the companion's surface since the companion does not possess a stellar wind strong enough to produce a stable shock front. In the area of the parameter space, where the orbital velocity of the WR star is below the detection limit of RV variations, the X-ray emission does not exceed 10^{33} erg/s for periods larger than a fraction of a day. Since this is of the order of the X-ray detection limit of the SMC, we conclude that a MS companion of AB 11 would be basically undetectable in X-rays.

The mid panel of Fig. 4.1 shows the X-ray emission expected from a compact object (CO) companion of AB 11. The figure shows that BHs accreting with an accretion disc (bright area on the left) are above the detection threshold of Schootemeijer et al. (2024) for most of the parameter space that corresponds to a black hole companion, spherically symmetric accretion takes place. The X-ray luminosity does not exceed 10^{32} erg/s in this accretion regime and, thus, does not exceed the detection limit. Consequently, detection of a putative BH companion by X-ray telescopes would only be possible for small orbital periods, e.g., three days for a $10 M_{\odot}$ BH. However, such short periods contradict the limit of RV variations of Schootemeijer et al. (2024). If the period exceeds a few years, the RV variations were small enough to fall below the detection limit of 5 km/s. Another possibility could be a small inclination reducing the RV semi-amplitude. Supposing a $10 M_{\odot}$ BH companion with an orbital period of 100 days would induce a RV semi-amplitude of the WR star of less than 5 km/s if the inclination was smaller than 7° .

Given a random orientation of the orbital axis, the probability that the inclination i is smaller than a particular value x is defined by the probability distribution function $P(i < x) = 1 - \cos(x)$. For the cases under consideration, the likelihood of the orbital inclination being less than 7° is 0.7%. Consequently, it is unlikely that AB 11 possesses an X-ray faint BH companion that avoided detection spectroscopically.

The expectation for the case of a NS companion is shown in the bottom panel of Fig. 4.1. This panel illustrates that X-rays are detectable if the NS companion accretes directly from the stellar wind, i.e., the orbital period of a putative NS is below 100 days and the spin period is above 1000 s. A NS companion would accrete in the subsonic accretion regime for orbital periods between 3 days and about 1000 days and spin periods between 10 and 1000 seconds (depending on the orbital period). In this stage, the NS would not

Table 4.1.: Assumed parameters of the SMC WR-stars without a detected companion. Stellar masses are from Schootemeijer and Langer (2018), all other parameters from Hainich et al. (2015).

SMC AB	v_∞ [km/s]	R_1 [R_\odot]	M_V [mag]	$\log \dot{M}$ [M_\odot/yr]	M_1 [M_\odot]
1	1700	5.7	-4.57	-5.58	32
2	900	9.1	-4.96	-5.75	18
4	1000	13.0	-5.85	-5.18	22
9	1800	3.5	-3.94	-5.65	30
10	2000	2.2	-3.38	-5.64	20
11	2200	3.5	-3.69	-5.56	26
12	1800	2.4	-3.34	-5.79	28

exceed an X-ray luminosity of a few 10^{33}erg/s . The Bondi-Hoyle accretion rate of the NS would be roughly $3 \times 10^{14}M_\odot/\text{yr}$ at 10 days orbital period and $5 \times 10^{11}M_\odot/\text{yr}$ and at 1000 days. This gives a lifetime of the propeller accretion state of 2×10^4 yr and 4×10^6 yr according to Eq. 3.46 and assuming a spin period of 100 s.

A NS with a spin period smaller than 10 s would accrete in the supersonic accretion regime and would also emit X-rays that were too faint to be detected. Since the spin period of the supersonic accretion regime is at least one order of magnitude smaller compared to the spin period of the subsonic accretion regime, Eq. 3.46 implies that the time scale of the supersonic propeller regime is longer than 10^5 yr at an orbital period of 10 d and longer than 10^7 yr at 1000 d. Thus, a NS accreting in the supersonic propeller state could last in this phase as long as the WR star lives. Additionally, a $1M_\odot$ NS companion would induce a RV semi-amplitude of less than 5 km/s if its orbital period were greater than 30 days. For a $1.4M_\odot$ neutron star, the orbital period would need to exceed 140 days for the same effect. Consequently, we cannot rule out a fast-spinning NS companion of AB 11 based on the limits of RV observations and our X-ray emission constraints.

We conclude that in the case of AB 11 a MS companion would be undetectable as long it is less massive than a few solar masses. Signatures of a BH companion will be undetectable if the orbital period is above 100 d. However, the mass range of BH's with masses exceeding $5M_\odot$ makes the existence of such a companion very unlikely due to the large RV variations induced on the WR star. Third, a NS would be undetectable if its spin period were smaller than roughly 100 s and its orbital period exceeds tens of days since the subsonic and supersonic prohibit an efficient X-ray emission.

Constructing similar diagrams for the other apparently single SMC WR stars yields comparable results (see Appendix C.1). We conclude that BH and massive MS companions are highly unlikely for these apparently single WR stars. However, it cannot be entirely ruled out that these stars might have a low-mass MS companion or a NS companion. Schootemeijer et al. (2024) argued that a NS companion seems unlikely because the progenitor of a compact companion would initially need to be more massive than AB 11, which would typically result in a black hole rather than a neutron star.

Taking this into account, we can conclude that our analysis supports the conclusion of Schootemeijer et al. (2024) that the apparently single WR stars in the SMC are likely truly single stars.

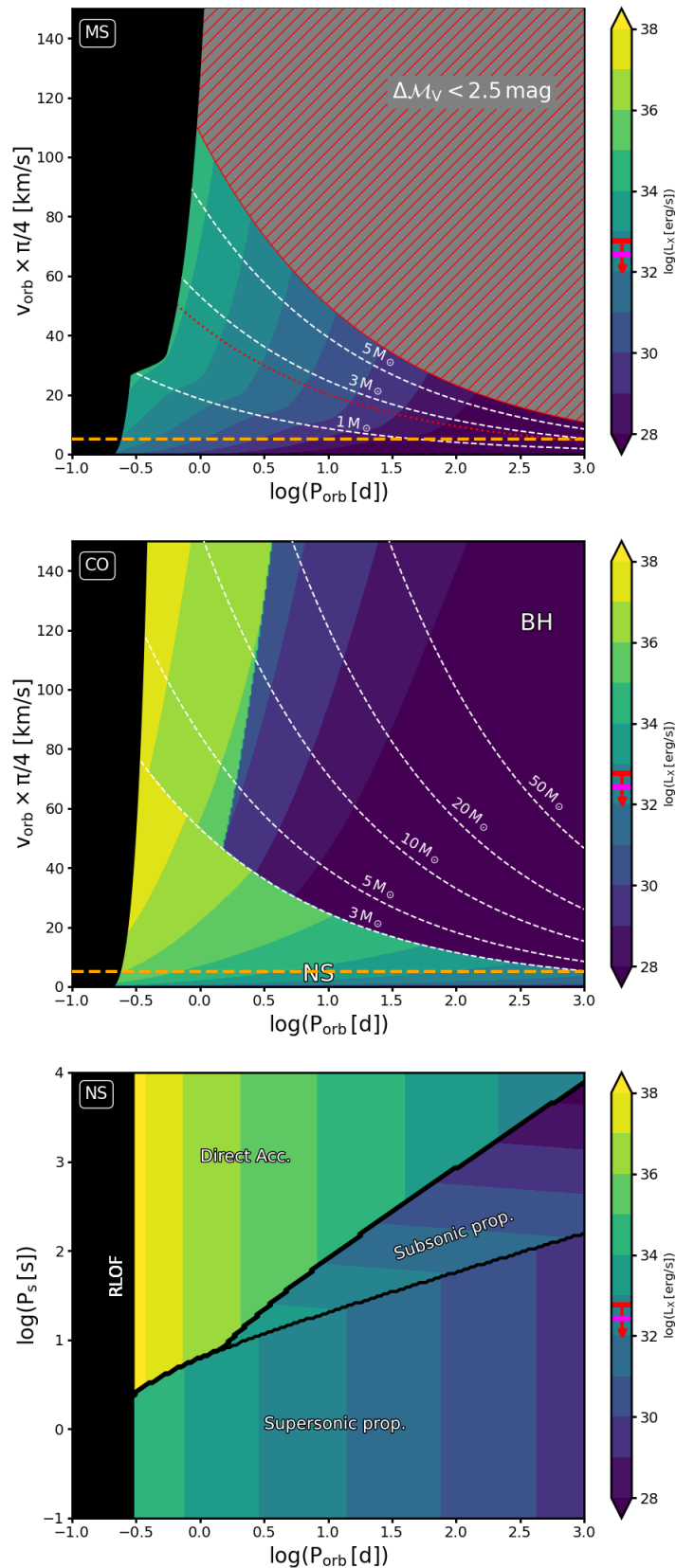


Figure 4.1.: Diagnostic diagram for SMC AB 11. The dashed orange line represents the mean standard deviation of RV by Schootemeijer et al. (2024).

4.3 The galactic Wolf-Rayet star WR 3

WR 3 is a galactic hydrogen-rich Wolf-Rayet star of spectral type WN3h (Hamann et al. 2019). The binary nature of the star is debated in the literature (Massey and Conti 1981; Marchenko et al. 2004; Dsilva et al. 2022). While the WR catalog (van der Hucht 2001) classifies the star as WN3+O4 binary, Hamann et al. (2006) did not find contamination of the spectrum by an OB companion. A spectroscopic study by Moffat et al. (1986) suggested the existence of radial velocity variations with an amplitude of 33 km/s and a period of 46.85 d. Moffat et al. (1986) argued that WR 3 may host an undetected binary companion of at least $5 M_{\odot}$. A re-investigation by Marchenko et al. (2004) did not reveal any radial velocity variations down to a lower limit of 8 km/s. A more recent study by (Dsilva et al. 2022) could not find radial velocity variation down to an upper limit of 5 km/s within a time span of 120 d.

The detection of X-rays with a luminosity of 8×10^{31} erg/s (Ignace et al. 2000) was interpreted as intrinsic X-ray emission by Ignace et al. (2000) and as emission from colliding stellar wind by Gagné et al. (2012).

To shed new light on the possible existence of a companion hosted by WR 3, we used the stellar parameters provided by Hamann et al. (2019) and listed in Table 4.2. Fig. 4.2 shows the corresponding diagnostic diagrams.

Table 4.2.: Parameters for WR 3 adopted from Hamann et al. (2019).

M_1	$17 M_{\odot}$
R_1	$2.5 R_{\odot}$
$\log(L_1/L_{\odot})$	5.56
$\log(\dot{M}/M_{\odot} \text{ yr}^{-1})$	-5.4
v_{∞}	2700 km/s
M_V	-3.13 mag

The top panel illustrates the expected X-ray emission of the binary system assuming a main sequence (MS) companion. The vertical orange line represents the lower limit of the orbital period, set at 120 days. Similarly, the horizontal orange line represents the upper limit of RV variations, measured at 5 km/s according to Dsilva et al. (2022).

This plot shows that a MS companion more massive than $5 M_{\odot}$ would contribute more than 10% to the total optical flux of the supposed binary. The existence of such a highly luminous binary companion would lead to noticeable characteristics in the optical spectrum. Consequently, the parameter space indicated by the hatched area can be ruled out through observations. Thus, an early O star companion does not seem plausible as it would be clearly visible in the spectrum and most likely be brighter than the WR star itself (Martins et al. 2005). Similarly, the red dashed line indicates $2 M_{\odot}$ MS companion, which would be 5 mag fainter than the Wolf-Rayet star and consequently, contribute 1% to the total flux in the optical band. Below such a flux ratio, the companion could potentially go undetected in the optical spectrum.

We can use the X-ray luminosity to narrow down the possible parameter space. Suppose that the observed X-ray emission is due to the interaction of the companion with the

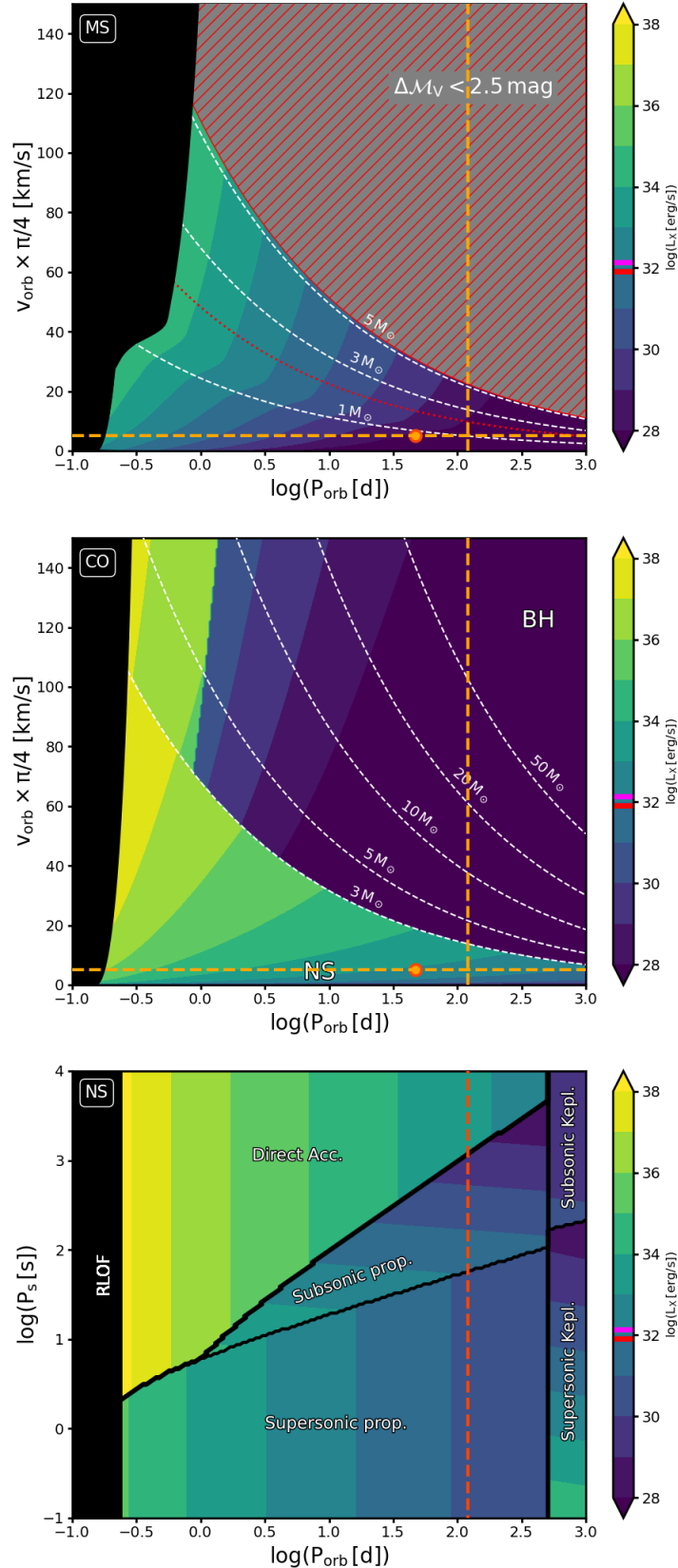


Figure 4.2.: Diagnostic diagrams for WR 3. The vertical and horizontal orange lines correspond to the lower limit of the orbital period and the upper limit of the RV variations, respectively. Both limits are provided by Dsilva et al. (2022). The red-orange dot in the top and mid panel corresponds to the period of RV claimed by Moffat et al. (1986) and the upper limit of RV semi-amplitude by Dsilva et al. (2022).

WR wind. Our model of colliding wind emission predicts that a $2 M_{\odot}$ MS companion will produce 8×10^{31} erg/s, i.e., the observed amount of X-rays if its orbital period is about 3 days.

In this configuration, the WR star would have an orbital velocity of 41 km/s, and the expected value of the amplitude of the RV would be 33 km/s, which would have been observed in previous studies. However, if the orbital inclination is less than 7 degrees, the observed RV would be less than 5 km/s, i.e., the detection limit of Dsilva et al. (2022). Assuming a random distribution of the orientation of the orbital axis, the probability that the orbital inclination is less than 7° is 0.7%. It is, therefore, unlikely that a $2 M_{\odot}$ MS companion could be close enough to the WR star to produce the observed amount of X-rays and at the same time not be detected by the RV of the WR star.

The situation is somewhat relaxed if we assume a less massive binary companion. In the case of a $1 M_{\odot}$ MS companion, a similar discussion shows that the orbital period is about 2 days to reproduce the observed X-ray emission. Consequently, the orbital inclination must be less than 11° to avoid detection by RV. The probability that i is below that value is roughly 2%.

We can conclude that the X-ray emission of WR 3 is not likely to come from a colliding wind process with a MS companion. Massive MS companions are too bright and would be visible in the spectrum. Low-mass MS companions must be close to the WR star to produce enough X-rays to match observations. This requires a low orbital inclination to avoid detection by RV, which is unlikely. At the same time, WR 3 may have a low-mass MS companion that avoids detection due to a large orbital period.

We note that a putative MS with an orbital period of 46.85 d as proposed by Moffat et al. (1986) my exists if it is less massive than $1 M_{\odot}$. In this case, the X-ray emission from the colliding WR wind is more than three orders of magnitude fainter than the expected intrinsic emission of the WR star. A similar argument holds if the putative MS companion had a period of 120 d or above, i.e., the lower limit given by Dsilva et al. (2022). A companion in this area of the diagnostic diagram could be as massive as $2 M_{\odot}$ due to the exclusion of companions that contribute more than 1% to the optical flux. Our estimate shows, however, that the expected X-ray luminosity from colling winds is still four orders of magnitude below the observed value. We may conclude that the X-ray emission is unlikely to stem from the interaction of the WR star with the surface or the wind of a MS companion.

The mid panel of Fig. 4.2 shows the diagnostic diagram of a CO companion. If the orbital period is smaller than 1 d, the condition for building an accretion disc applies. We expect X-ray luminosities of 10^{34} erg/s and above. This is two orders of magnitude above the observed X-ray emission. In addition, as the BH companion must be close to the WR star it should induce observable RV of the host star. Assuming a $5 M_{\odot}$ in a 1 d, we find the expected value of RV to be ~ 100 km/s. To be below the detection limit of ~ 5 km/s, an orbital inclination of $i < 2^{\circ}$ or below is required. The probability for this is $P(i < 2^{\circ}) \approx 0,06\%$. We see that a BH hosting an accretion disc would be too X-ray bright to be compatible with observations and requires an improbability small orbital inclination to avoid detection via RV. Hence, a BH with an accretion disc can be ruled out as the source of X-ray radiation from WR 3.

We now discuss a putative BH companion without an accretion disc. Our model pre-

dicts that a BH is practically undetectable in the X-ray band if the orbital period is above ~ 1 d. In this case, the accretion luminosity is expected to be smaller than 10^{31} erg/s, assuming an orbital period of more than one 1d. At the period suggested by Moffat, the X-ray luminosity is below 10^{28} erg/s and, hence, at least four orders of magnitude below the observed value. The same holds for the lower period limit suggested by Dsilva et al. (2022). In this case, the X-ray radiation due to the intrinsic emission of the WR star is expected to be at least four orders of magnitude above the X-ray luminosity expected from the spherically symmetric accretion flow into the BH. Consequently, in this case, the observed X-ray flux would be due to intrinsic X-ray emission.

Supposing a $5 M_{\odot}$ BH companion with an orbital period proposed by Moffat, we find an expected value of RV of ~ 30 km/s. With a putative inclination of 8° and below the observable RV drops below the detection limit of Dsilva et al. (2022). However, the probability of the system having orbital inclination below 8° is $\sim 1\%$. Assuming a more massive BH companion, this probability is even smaller. Also, in the case of a putative $3 M_{\odot}$, the probability of the orbital inclination not detecting it via RV is $\sim 2\%$. Hence, given the orbital period provided by Moffat, it is unlikely that an X-ray quite BH companion would avoid spectroscopic detection.

The diagnostic diagram shows that the observations cannot exclude BH companions with orbital periods above 120 d. Their expected X-ray brightness is more than four orders of magnitude below the expected intrinsic X-ray emission of the WR star. Since observational data for RV variations are lacking beyond the 120 d limit provided by Dsilva et al. (2022) and an X-ray quiet BH is consistent with the observations, such a companion cannot be ruled out.

For companion masses below $3 M_{\odot}$, i.e., a putative NS companion, the mid panel in Fig. 4.2 shows that we expect a brighter accretion luminosity. In more detail, the expected value of a Chandrasekhar mass NS companion with orbital, as proposed by Moffat would be ~ 9 km/s. If the orbital inclination of this system were below 25° the RV would drop below the ~ 5 km/s limit. The X-ray emission from wind capture and direct accretion would be $\sim 10^{32}$ erg/s.

The bottom panel of Fig. 4.2 shows a diagnostic diagram of a putative NS companion in more detail. The Bondi-Hoyle accretion rate of a NS in a 120 d orbit is about $8 \times 10^{-14} M_{\odot}/\text{yr}$. For this orbital period, the direct accretion regime applies for spin periods larger than 1000 s (area top left). The X-ray luminosity in the direct accretion regime would be about 10^{33} erg/s and thus above the observed value. The subsonic accretion regime applies for spin periods between 25 and 1000 s. We predict an X-ray luminosity less than 10^{32} erg/s. The same holds true for the supersonic accretion regime below 25 s spin period.

Assuming 100 s spin period for the subsonic propeller regime and 1 s in the supersonic regime, as well as a mass accretion rate of $8 \times 10^{-14} M_{\odot}/\text{yr}$, Eq. 3.46 implies that the lifetime of the subsonic state is about 3×10^5 yr, and 3×10^7 yr in the supersonic regime. Consequently, an accreting NS in the subsonic propeller state is possible since the timescale of this state is comparable to the lifetime of a Wolf-Rayet star. Also, the supersonic accretion state can not be ruled out since the time scale is much longer than the lifetime of the Wolf-Rayet star.

Considering the discussion above, we draw the following conclusions for a putative

companion: WR 3 may possess a low mass MS companion, a BH companion with an orbital period above ~ 100 d or a NS companion. In the case of an undetected MS or BH companion, the observed X-ray radiation is intrinsic to the WR star itself. An accreting NS companion may be X-ray luminous enough to be compatible with observations.

Interestingly, WR 3 has a radial velocity of ~ 100 km/s (Duflot et al. 1995; Kharchenko et al. 2007). The radial velocity may result from a previous supernova (Blaauw 1961; Tauris and Takens 1998). If this was the case, the question arises if WR 3 is still in a binary system or broke up during the supernova. Neither of these two possibilities can be ruled out based on our discussion. A long-term observation of the RV and an investigation of possible evolutionary scenarios that could lead to a similar system are necessary to clarify the nature of WR 3.

4.4 The galactic Wolf-Rayet star WR 6

WR 6 is a nitrogen-rich WR star of spectral type WN 4 (Hamann et al. 2019) exhibiting an X-ray luminosity of 8×10^{32} erg/s (Oskinova et al. 2012). The binary status of this WR star is still unclear. WR shows remarkable photometric (Marchenko et al. 1998) and spectral (Morel et al. 1997; Flores et al. 2007) variations of which occur with a period of ~ 3.77 d.

Interestingly, the period of the lightcurve variability changes over timescales of about two weeks (Drissen et al. 1989; Robert et al. 1992). By analyzing the times of minima in the photometric lightcurve, Schmutz and Koenigsberger (2019) found that this lack of coherence can be explained if one supposes WR 6 to be a binary with an orbital period of 3.6 d and an apsidal motion with a period of 100 km/s. Schmutz and Koenigsberger (2019) speculate that WR 6 is part of a hierarchical triple system where the WR star and its inner companion form a close binary that is orbited by a third body with an orbital period of 22 d or above.

The Galactic Catalogue of WR stars (van der Hucht 2001) designates WR 6 as a possible SB1. Firmani et al. (1980) detected a periodic RV variation with a period of 3.76 d and a semi-amplitude of 36.1 km/s. Assuming a WR mass of $10 M_{\odot}$ and an orbital inclination of 71° McLean (1980) concluded that WR 6 possesses a companion with a mass of $1.3 M_{\odot}$ and argued that this companion may be a NS. In another scenario proposed by Skinner et al. (2002), the WR star hosts a non-degenerate low-mass star. The observed X-rays can then be explained by the direct impact of the WR wind onto the companion's surface. In a recent spectroscopic survey, Dsilva et al. (2022) found the RV of WR 6 varies between -108 and $+62$ km/s, i.e., a difference of RV of $\Delta RV = 170$ km/s. However, they could not deduce any periodicity in the RV variations.

In the following analysis, we will discuss multiple putative companions: An inner companion corresponding to an orbital period of 3.6 d and RV semi-amplitude of 36 km/s as deduced by Firmani et al. (1980). We also discuss a putative outer companion for which we assume an orbital period of 22 d and above. In addition, we investigate the possibility that the ΔRV detected by Dsilva et al. (2022) is induced by a binary companion. Under this assumption, the corresponding semi-amplitude of RV is $\Delta RV/2 = 85$ km/s.

Table 4.3.: Parameters for WR 6 adopted from Hamann et al. (2019).

M_1	$23 M_{\odot}$
R_1	$3.25 R_{\odot}$
$\log(L_1/L_{\odot})$	5.79
$\log(\dot{M}/M_{\odot} \text{ yr}^{-1})$	-4.2
v_{∞}	1700 km/s
M_V	-5.33 mag

Using the stellar parameters provided by Hamann et al. (2019) (cf. Tab. 4.3), we construct the diagnostic diagrams for WR 6. First, we discuss putative MS companions of WR 6. In the diagnostic diagrams (Fig. 4.3), the red-orange dot marks the period and RV semi-amplitude induced by a possible inner companion. The dotted vertical orange line

marks the minimum orbital period of a putative outer companion estimated by Schmutz and Koenigsberger (2019). The dotted horizontal orange line marks the half value of ΔRV reported by Dsilva et al. (2022).

Given the RV, the period, and the semi-amplitude of RV, we deduce a mass to a $\sim 3 M_{\odot}$ companion with an orbital separation of $\sim 30 R_{\odot}$. The difference to McLean (1980) comes from the fact that we use a different mass of the WR star. Assuming that the inner companion is a MS star, we see from the diagnostic diagram that the contribution of the putative companion to the optical flux is less than 1%. Hence, such a MS companion would not be detectable in the optical spectrum of WR 6. Also, the stellar wind of such a companion would be smaller compared to the WR star's wind. This would lead to a direct impact of the WR wind onto the surface of the MS companion. The X-ray luminosity released in this process would be $\sim 10^{35}$ erg/s. This is two orders of magnitude above the observed value. Given the orbital separation of $30 R_{\odot}$ and the wind parameter of the WR star the mass column density of the MS in the WR wind would be $\Sigma \approx 1 \text{ g/cm}^2$ (Eq. 3.39). Assuming that the WR wind is hydrogen deficient, the electron scattering opacity is $\kappa_{\text{el}} \approx 0.2 \text{ cm}^2/\text{g}$. This yields an optical depth of $\tau \approx 0.2$, which would reduce the X-ray flux by only 18%. Thus, the observed X-ray flux is not significantly smaller than the value we expected from our model. Consequently, it seems unlikely that WR 6 possesses an inner MS companion.

We can estimate the radius of the companion that produces the observed amount of X-rays via a direct impact of the WR wind on the companion surface: Assuming an orbital separation of $\sim 30 R_{\odot}$, we can deduce the wind velocity and wind density. With equation 3.60, we find the emissivity of the shocked material to be $\epsilon_{\text{shock}} \sim 10 \text{ erg}/(\text{cm}^3 \text{s})$. Assuming that the characteristic volume is defined by the shock radius as r_{shock}^3 , we find

$$r_{\text{shock}} = \left(\frac{L_X}{\epsilon_{\text{shock}}} \right)^{1/3}. \quad (4.1)$$

Given the emissivity, we find that the observed X-ray luminosity of 8×10^{32} erg/s is consistent with a shock radius of $0.6 R_{\odot}$. Interestingly, this is roughly the radius of a $\sim 3 M_{\odot}$ He star. A detailed analysis of He star companions is beyond the scope of this study. However, answering the question if WR 6 possesses a He star companion is an interesting task for future research.

For an outer companion, we find that it can remain undetected in the optical band as long as it has a mass of less than $5 M_{\odot}$. The expected X-ray luminosity of such a companion is 10^{33} for an orbital period of 22 d or below for wider orbits. Suppose a $5 M_{\odot}$ MS with orbital period of 100 d. The expected X-ray luminosity would be 10^{30} erg/s and thus three orders of magnitude below the observed value. Thus such an outer companion could have avoided detection in the optical and the X-ray band.

The vertical dotted line shows that the RV variations detected by Dsilva et al. (2022) are unlikely to be caused by a MS companion: Given the RV semi-amplitude of 85 km/s, the orbital period of the MS companion cannot be smaller than ~ 1 d. Otherwise, RLOF from the MS companion to the WR star would be initiated (black area). For orbital periods between 1 and ~ 15 d along the horizontal line, we find that the expected X-ray luminosity ranges between 10^{37} and 10^{34} erg/s. This is at least one order of magnitude above the

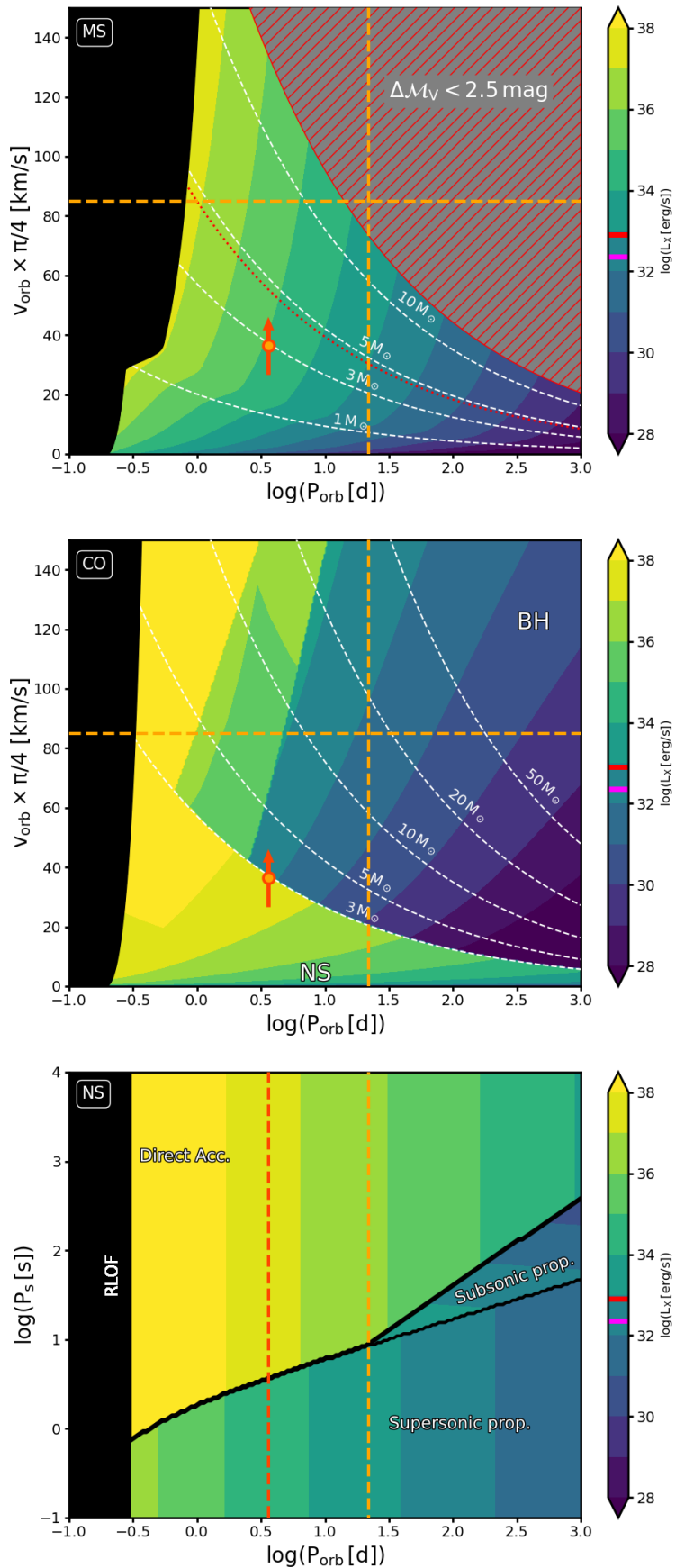


Figure 4.3.: Diagnostic diagrams for WR 6 with stellar parameters from Tab. 4.3.

observed value. In addition, the MS companion would contribute a significant fraction of the optical flux. For orbital periods above ~ 15 d, the MS would contribute more than 10% to the total optical flux, which should make it detectable in the spectrum. Consequently, MS companion that induces a RV of ± 85 km/s is not compatible with the observed X-ray flux and the optical spectra.

Next, we explore the potential presence of a compact companion for WR 6. As illustrated in the middle panel of Fig. 4.3, our analysis suggests that the RV data could correspond to either a massive NS or a BH as an inner companion. We discuss a NS companion further below. The results of this analysis must be viewed with caution: If WR 6 is a triple system, the inner companion will disturb the flow of the WR wind. Thus, the wind velocity field can not be assumed to be radially symmetric at the position of the outer companion. In this case, the analytical estimates provided by (Shapiro and Lightman 1976) break down. To make reliable predictions for the formation of a wind-fed accretion disc, more sophisticated methods are needed. Nevertheless, we apply our model to a hypothetical outer companion to make a first guess if it could be undetectable in X-rays.

Assuming the inner companion of WR 6 is a black hole, we find from our analysis that we don't expect the formation of an accretion disc. Interestingly, the model for radial symmetric infall would predict an X-ray luminosity of $\sim 10^{32}$ erg/s, i.e., of the same order as the X-rays observed. Hence, we cannot rule out the possibility that the inner companion of WR 6 is an X-ray quiet BH.

A putative outer companion of WR 6 could be a BH as well. At orbital periods above 22 d, we do not expect the formation of an accretion disc for all BH masses investigated. Consequently, the X-ray luminosity does not exceed the observed luminosity. For instance a $10 M_{\odot}$ BH with orbital period of 100 d is expected to emit $\sim 10^{29}$ erg/s. Such a faint X-ray source would be difficult to detect, even if it were not outshone by the intrinsic X-ray emission of the WR star.

A companion that would induce RV with semi-amplitude of 85 km/s would form an accretion disc at an orbital period of 4 d or less. This would correspond to a $8 M_{\odot}$ BH. For larger orbital periods at the same RV variations, the expected BH mass increases. Interestingly, at an orbital period of 22 d would correspond to a $18 M_{\odot}$. Since we do not expect the formation of an accretion disc for such a companion, the X-ray luminosity from the spherically symmetric infall $\sim 10^{32}$ erg/s is slightly smaller but of the same order of magnitude as the observed value. Hence, the hypothesis that the RV variations detected by Dsilva et al. (2022) are induced by a BH companion with an orbital period of ~ 22 d is not in contradiction with observations. Such a companion could be the reason for the observed X-ray flux and cause the apsidal motion of the (hypothetical) inner companion. Furthermore, it can not be ruled out that a BH companion with a wider orbit exists at WR 6. Such a companion could also cause the apsidal motion. However, we expect its X-ray flux to be significantly fainter and the RV variations induced to WR star smaller. Thus, in this case, the X-rays emission may be an intrinsic emission by the WR wind and the RV variations may be caused by clumps in the wind.

The lower panel in Fig. 4.3 presents the diagnostic diagram of a hypothetical NS companion. As mentioned earlier, the mass of a hypothetical inner companion would be large for a NS. In addition, the Bondi-Hoyle accretion rate for the NS would be approximately $2 \times 10^{-9}, M_{\odot}/\text{yr}$. The NS would accrete the material directly if the spin period of the

neutron star exceeds ~ 3 s. In this case, the predicted X-ray luminosity would be around $\sim 2 \times 10^{37}$ erg/s, surpassing the observed value. If the NS spins faster, the supersonic propeller will reduce the X-ray luminosity to $\sim 3 \times 10^{34}$ erg/s, which is still two orders of magnitude above the detected luminosity. Thus, the assumption that the inner companion of WR 6 is a NS is not compatible with the detected X-ray flux. This result is in agreement with Stevens and Willis (1988) and Pollock (1989).

A hypothetical outer companion would still have an X-ray luminosity that is larger than the observed value if it accretes directly. However, for an orbital period above 20 d, the supersonic and the subsonic propeller apply if the spin period is smaller than 10 s at $P_{\text{orb}} = 20$ d orbital period and ~ 200 s at $P_{\text{orb}} = 1000$ d. In the case of supersonic or subsonic propeller accretion, the X-ray luminosity is reduced to a value between $\sim 10^{30}$ erg/s and $\sim 10^{33}$ erg/s. Thus, the expected X-ray emission is of the same order of magnitude or below the detected X-ray flux. However, the timescale for converting the neutron star's rotational energy into X-ray radiation (as indicated by Eq. 3.47) is of the order of a few Myr and hence, comparable to the lifetime of the WR star. Consequently, a hypothetical outer companion could be a NS with undergoing propeller-inhibited accretion. If we assume that the mass of this outer NS companion is $1.4 M_{\odot}$, the expected value for the RV semi-amplitude is 10 km/s for an orbital period of 22 d and even smaller for larger orbital period and low inclination. Hence, it cannot be ruled out that WR 6 possesses an outer NS companion that avoided detection in the X-ray band and via spectroscopic studies.

We conclude that the inner companion, if it exists, is unlikely to be a MS star since we would expect brighter X-ray emission from the collision of the WR wind onto the MS star's surface. An inner BH companion cannot be excluded. However, it would be close to forming an accretion disc, which makes the scenario rather unlikely. A NS companion does not seem plausible since we expected a significantly larger X-ray luminosity even if we included propeller-inhibited accretion. In addition, the mass of the inner companion would suggest a very massive NS. For the hypothetical outer companion, we find that a MS with a mass below $\sim 3 M_{\odot}$ is possible. Also, an outer BH companion or a fast-spinning NS cannot be ruled out.

4.5 The galactic Wolf-Rayet star WR 7

WR 7 is another galactic Wolf-Rayet star. It shows an X-Rayet luminosity of 2×10^{33} erg/s (Toalá et al. 2015) in the soft X-ray band. The luminosity is consistent with the self-shocking mechanism in Wolf-Rayet stars as described by Oskinova (2015).

Interestingly, Toalá et al. (2022) found a variability of the light curve with a dominant period of 2.64 d. However, theoretical work by Grassitelli et al. (2016) suggests that WR stars in the mass range of WR 7 show pulsations of the order of minutes. Thus, pulsation seems to be unlikely as the origin of the variability. Instead, Toalá et al. (2022) addresses whether WR 7 has an unseen companion. They did not find a signature of binarity in their spectroscopic analysis. They conclude that a possible companion must be a main sequence star not earlier than B5 V. On the other hand, they point out that WR 7 could host a CO.

We assume a terminal velocity of 1600 km/s a BH more massive than $5 M_{\odot}$ would host an accretion disc and produce a significant amount of X-rays. However, if we assume that the period of light-curve variability corresponds to the orbital period of a putative BH companion of $5 M_{\odot}$, the system would be close to the threshold between the disc formation regime (i.e., X-ray bright) and accretion regime without disc formation (see Fig. 4.2). To investigate the existence of a BH companion of WR 7, more reliably, a more sophisticated model is needed that treats the transition from the accretion disc regime to the regime of spherically symmetric in-fall. At last, a directly accreting NS can be ruled out due to its X-ray brightness. A NS companion whose accretion is inhibited by the supersonic propeller seems possible. This would imply a spin period of the NS of a few seconds or less.

Table 4.4.: Parameters for WR 7 adopted from Hamann et al. (2019).

M_1	$13 M_{\odot}$
R_1	$1.26 R_{\odot}$
$\log(\dot{M}/M_{\odot} \text{ yr}^{-1})$	-4.8
v_{∞}	1600 km/s
M_V	-3.62 mag

Using the stellar parameters provided by Hamann et al. (2019) (cf. Tab. 4.4), we computed the diagnostic diagrams for WR 7. The orange line marks the detected period of the light-curve variability. If we assume a MS companion, we find that a companion more massive than $\sim 6 M_{\odot}$ would be optically detectable since the brightness difference between the two companions is less than 2.5 mag. This matches the results of Toalá et al. (2022). If we assume that a spectroscopic detection was possible down to a magnitude difference of 5 mag, we may rule out companions more massive than roughly $3 M_{\odot}$.

In addition, the wind of the WR star should produce significant amounts of X-rays, as can be seen from the top panel in Fig. 4.4. If we assume the detected period as orbital period, a $3 M_{\odot}$ companion would yield an X-ray luminosity above 10^{34} erg/s which could be detected. Toalá et al. (2022) argue that the orbital period may be twice the period of

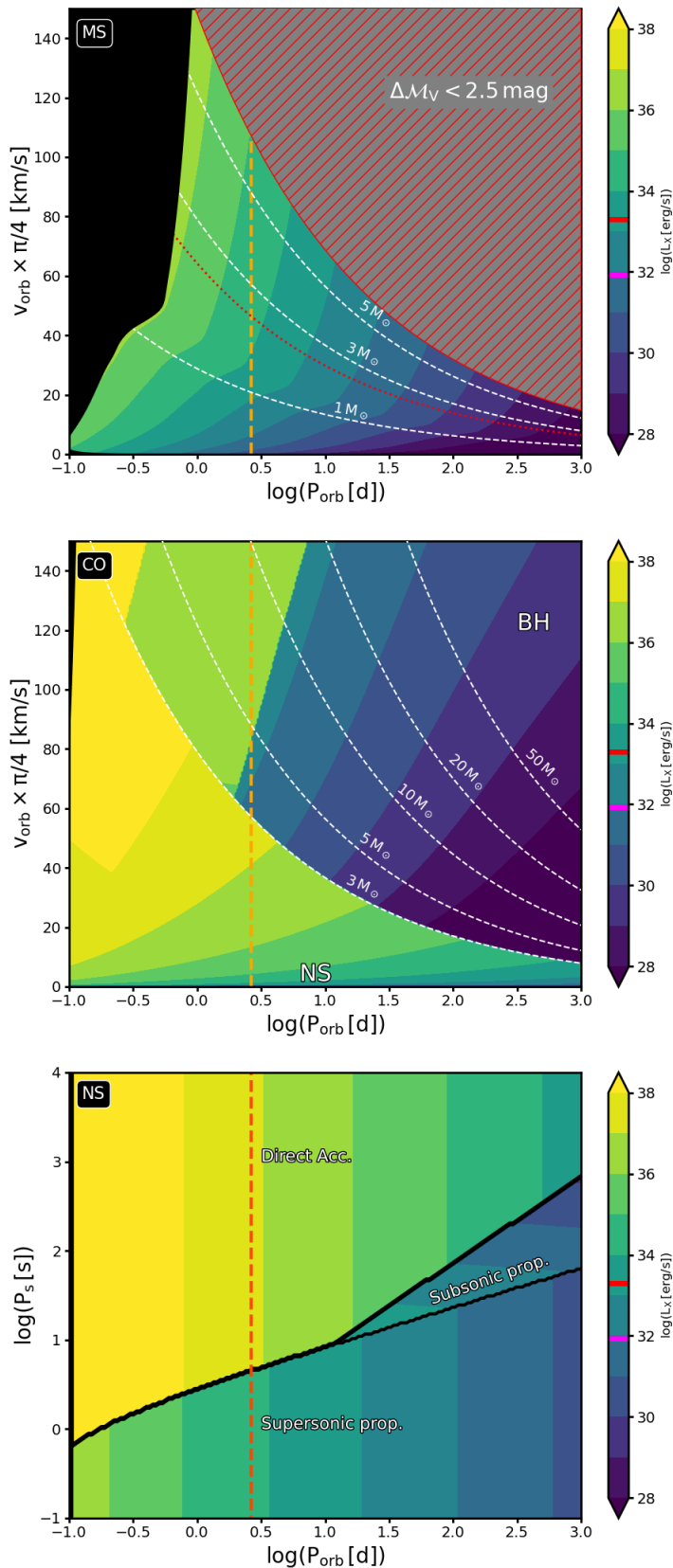


Figure 4.4.: Diagnostic diagrams for WR 7 with stellar parameters from Tab. 4.4. The orange line indicates the period of the variable light curve. For further explanation see Fig. 4.1.

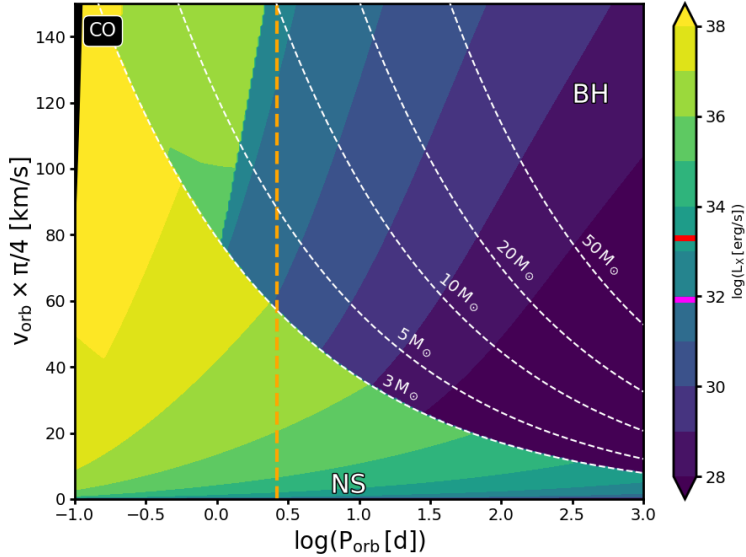


Figure 4.5.: Same as mid panel in Fig. 4.4 but with terminal wind velocity of 2000 km/s.

variability. In this case, our prediction of the X-ray luminosity would be one order of magnitude smaller and thus comparable to the observed X-ray luminosity of WR 7.

If we increase the terminal wind velocity to 2000 km/s, we find that the range of possible undetected BH companions increases significantly. This is shown in Fig. 4.5. For the larger wind velocity, we find that a BH companion could not be detected in the X-ray regime as our model does not predict the formation of an accretion disc. The resulting X-ray luminosities for an orbital period of 2.6 d do not exceed 10^{33} erg/s in the investigated parameter space. A detection is even more unlikely if an orbital period of 5 d is assumed. We conclude that a BH companion may not be directly detectable if the wind velocity is larger than suggested by the study of Hamann et al. (2019).

A NS companion (cf. bottom panel in Fig. 4.4) should be X-ray bright if it spins slower than ~ 3 s the material would be accreted directly on the NS's surface. In this case the luminosity would exceed 10^{37} erg/s at 2.6 d and is still larger than 10^{36} erg/s even at 10 d. Consequently, a slow-rotating NS can be ruled out as it would be a prominent X-ray source.

The supersonic propeller effect would inhibit the accretion if the NS spins slower. In this case, an essential amount of the radiated energy stems from converting the NS's rotational energy into X-rays (see Sec. 3.3). We predict an X-ray luminosity of 2×10^{34} erg/s for a $1.4 M_{\odot}$ NS companion with 2.6 d orbital period.

If we suppose that the orbital period of the NS was twice the period of the light-curve variability, the predicted X-ray luminosity would be about 8×10^{33} erg/s. This is still larger than the observed X-ray luminosity. However, we note that our NS accretion model does not include absorption effects. We compute the mass column density to estimate how strongly the absorption may affect (Eq. 3.32). We find a value of 0.4 g/cm^2 . Assuming a mean opacity of $\kappa \approx 1 \text{ cm}^2/\text{g}$, we find that the NS would have an optical depth of $\tau \approx 0.4$, corresponding to a loss of roughly 30%. In addition, the time scale to convert the NS's rotational energy into X-ray radiation (Eq. 3.47) is about 70000 yr assuming a

spin period of 1 s. This is about 15% of the life lifetime of a Wolf-Rayet star as predicted from evolutionary models (Woosley 2019). If the spin period were a factor of 10 smaller, the timescale of the supersonic propeller would increase by a factor of 100. Since this is much longer than the lifetime of WR 7, a NS companion in the supersonic propeller regime can not be ruled out regarding the expected X-ray luminosity and the timescale of the accretion state.

We conclude that WR 7 is unlikely to have a main-sequence companion since its presence should be visible either in the optical spectrum of the star or as a bright X-ray source due to the colliding Wolf-Rayet wind. We assume a terminal velocity of 1600 km/s a BH more massive than $5 M_{\odot}$ would host an accretion disc and produce a significant amount of X-rays. However, if we assume that the period of light-curve variability corresponds to the orbital period of a putative BH companion of $5 M_{\odot}$, the system would be close to the threshold between the disc formation regime (i.e., X-ray bright) and accretion regime without disc formation (see Fig. 4.2). To investigate the existence of a BH companion of WR 7, more reliably, a more sophisticated model is needed that treats the transition from the accretion disc regime to the regime of spherically symmetric in-fall. At last, a directly accreting NS can be ruled out due to its X-ray brightness. A NS companion whose accretion is inhibited by the supersonic propeller seems possible. This would imply a spin period of the NS of a few seconds or less.

Table 4.5.: Stellar parameters of the galactic WN8 stars adopted from Hamann et al. (2019).

WR ID	SpType	T_{eff} [kK]	$\log L_1$ [L_{\odot}]	M_1 [M_{\odot}]	R_1 [R_{\odot}]	v_{∞} [km/s]	M_V [mag]	$\log \dot{M}$ [M_{\odot}/yr]	X_H
12	WN8h + OB	44.7	5.98	31	16	1200	-6.7	-4.3	0.27
16	WN8h	44.7	5.72	21	12	650	-6.1	-4.6	0.25
40	WN8h	44.7	5.91	28	15	650	-6.9	-4.2	0.70
66	WN8(h)	44.7	6.15	41	20	1500	-7.2	-3.9	0.05
89	WN8h	39.8	6.33	53	31	1600	-7.6	-4.4	0.20
107	WN8	50.1	6.20	44	17	1200	-7.2	-4.0	0.00
116	WN8h	39.8	5.44	14	11	800	-5.8	-4.4	0.10
123	WN8 (WNE-w)	44.7	5.28	12	7	970	-5.3	-4.6	0.00
124	WN8h	46.0	5.75	22	12	710	-6.6	-4.3	0.13
130	WN8(h)	44.7	6.25	47	22	1000	-7.2	-4.2	0.12
147	WN8(h) + B0.5V	39.8	6.30	51	30	1000	-7.2	-3.8	0.05
148	WN8(h)+B3IV/BH	39.8	6.20	44	27	1000	-7.2	-4.5	0.15
156	WN8h	39.8	6.01	32	21	660	-7.0	-4.6	0.27

4.6 WR 124 and the galactic WN 8 stars

WR stars that display strong lines of nitrogen in the optical spectrum of their stellar winds are classified as WN stars. Most of the cooler (later) WNL stars contain hydrogen in their atmospheres. This distinguishes them from the hotter (earlier) hydrogen-free WNE stars (Hamann et al. 2006). Among the WNL stars, the subclass of WN 8 stars are considered peculiar compared to other WNL stars (Moffat et al. 1986; Antokhin et al. 1995). These WR stars are variable (Chené et al. 2011) and show a suspiciously small binary fraction. Furthermore, many stars of this class are runaway stars with high galactic latitudes. The last property is a hint of a past supernova kick that catapulted the star out of the galactic disk (Blaauw 1961; De Donder et al. 1997; Marchenko et al. 1998). Consequently, it is speculated that some of the WN 8 stars are binaries with an unseen compact companion or Thorne-Zytkow-Objects (TZO) (Foellmi and Moffat 2002).

We analyzed 13 galactic WN stars classified as WN 8 by Hamann et al. (2006) and estimated the expected X-ray emission for possible MS, BH, and NS companions. For our investigation, we used the stellar parameters provided by Hamann et al. (2019) as cited in Tab. 4.5. We discuss WR 124 below in more detail. The diagnostic diagrams of all other WN 8 stars are provided in Appendix C.2 (see. Figs. C.8 to C.19).

WR 124 is an example of a WN8 star showing a light-curve variability with a period of 2.4 d (Moffat et al. 1986). A dense nebula surrounds the star. The bipolar nebula morphology is interpreted as another hint of a binary companion (Chu and Treffers 1981). An X-ray observation of WR 124 has been performed by Toalá et al. (2018) revealing hard X-ray radiation of the order of 10^{31} erg/s. Taking the wind parameters and the bipolar nebula into account, the authors come to the conclusion that WR 124 is either an advanced

evolutionary stage of a TZO or a WR+NS binary.

We provide diagnostic diagrams for WR 124 in Fig. 4.6. We marked the 2.4 d period of the light-curve variability as a possible orbital period of a putative companion. From the top panel of the figure, it can be seen that a MS companion of about $3 M_{\odot}$ with an orbital period of 2.4 d would result in the WR star filling its Roche-lobe leading to a mass transfer from the WR star to the MS companion. If the MS companion were less massive, the WR wind would directly collide with the companion's surface. This process would produce X-rays of the order of 10^{33} erg/s, which is two orders of magnitude above the observed value. Consequently, a MS companion in a 2.4 d orbit would either be X-ray bright or would have initiated a mass transfer from the WR star to the companion. In the second case, the high mass ratio of the binary companions would make the mass-transfer unstable, leading to a common envelope, if no stabilizing effects, such as a helium gradient, are taken into account (Tauris and van den Heuvel 2006; Quast et al. 2019). From the top panel of Fig. 4.6, we see that a putative MS companion less massive than $7 M_{\odot}$ would be at least 5 mag fainter in the \mathcal{V} band than the WR star. Supposing an orbital period above 30 d, we expect that such a companion would be detectable neither in the optical nor in the X-ray band of the electromagnetic spectrum. Thus, a MS companion cannot be completely ruled out. However, the companion seems unlikely to have an orbital period corresponding to the light-curve variations period. Also, a helium star companion is possible. In both cases, the nature of WR 124 as a runaway star cannot be explained from a SN kick. A possible mechanism is the dynamical ejection of the binary system from an open cluster as discussed by Poveda et al. (1967) and proposed for the runaway star WR 148 by Munoz et al. (2017).

A BH companion seems unlikely, as shown in the mid panel of Fig. 4.6. We would expect that a BH in an orbit of 2.4 d would lead to a RLO. Assuming a $10 M_{\odot}$ BH companion, the WR star would fill its Roche-lobe if the orbital period was 2.9 d. In this configuration, the mass column density of the BH would be (Eq. 3.32) $\Sigma \approx 2.5 \text{ g/cm}^2$. If we suppose an opacity of $\kappa \approx 1 \text{ cm}^2/\text{g}$ we find an optical depth of $\tau \approx 2.55$. This means that the X-ray flux is reduced by a factor of 12. In the case of mass transfer, we expect that the BH accretes at the Eddington limit. This implies a luminosity of $\sim 10^{39}$ erg/s (Eqn. 3.34). Consequently, we expect a luminosity of $\sim 10^{38}$ erg/s taking the absorption into account. Hence, the WR wind's X-ray attenuation is insufficient to hide a BH accreting with Eddington accretion rate.

While we assume $\beta = 1$ in the upper discussion, we can also assume that the stellar wind is launched slower, i.e., $\beta = 3$. In this case, the X-ray flux would be reduced by a factor of 150. Although absorption decreases the luminosity by more than two orders of magnitude, it is not sufficient to reduce the 10^{39} erg/s (Eddington luminosity) down to the observed value 10^{31} erg/s. A putative $10 M_{\odot}$ BH orbiting WR 124 with a period of more than 120 d would not form an accretion disc. As can be seen in Fig. 4.6, the spherically symmetric accretion model predicts an X-ray luminosity of 10^{32} erg/s for a 120 d orbital period. This is of the same order of magnitude as the X-ray intrinsic X-ray luminosity from the WR star (violet mark at the color bar). Consequently, we conclude that observations can not rule out a BH companion in a sufficiently wide orbit.

The last possibility investigated here is a NS companion. The X-ray attenuation can be computed as shown for the BH case. We find the X-ray flux is reduced by a factor of 20

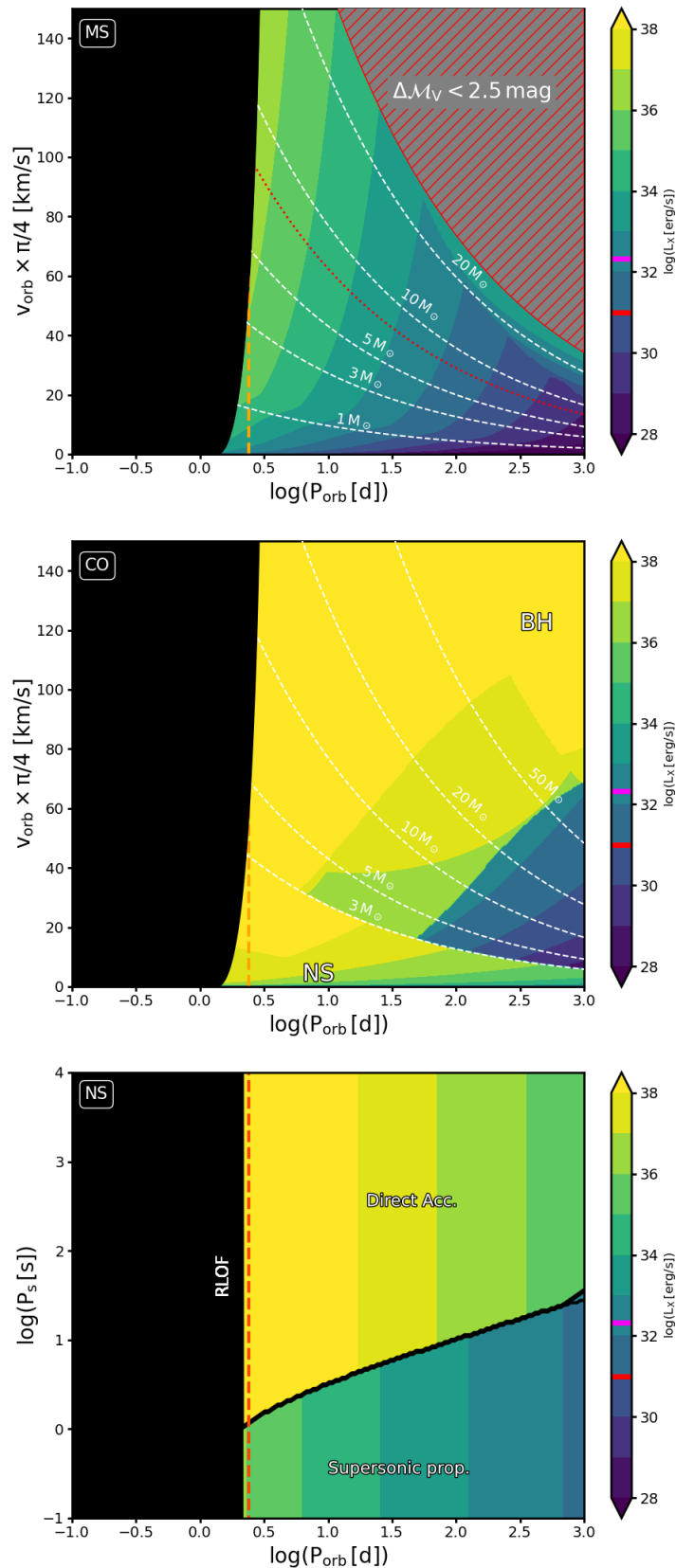


Figure 4.6.: Diagnostic diagrams of WR 124. The 2.4 d period is indicated with an orange dashed line. For further explanation see Fig. 4.1.

assuming $\beta = 1$ and by a factor of 8 000 assuming $\beta = 3$. A directly accreting NS should still be detectable since its X-ray luminosity would still exceed 10^{34} erg/s.

However, a NS with an orbital period of 2.4 d in the supersonic propeller accretion regime would emit $\sim 10^{35}$ erg/s as shown in the lower panel of Fig. 4.6. Supposing a slow wind acceleration ($\beta = 3$), the wind absorption could reduce the X-ray flux sufficiently to make the NS companion undetectable. Assuming a spin period of 0.1 s of a newly born NS and an X-ray luminosity of 5×10^{35} erg/s, we find a timescale of the supersonic propeller accretion (Eq. 3.47) of $\sim 10^5$ yr. This is larger than the dynamical time scale of the nebula, which is $\sim 10^4$ yr (Marchenko et al. 2010). Hence a rapidly rotating NS would be faint enough to be ruled out from the observed X-ray flux and would stay in this accretion regime long enough to provide for the creation of the observed nebula.

As outlined in the method section, we only discuss wind accretion in the Bondi-Hoyle model. As shown in the lower panel of Fig. 4.6, the WR star would be close to Roche-lobe filling if we assume a 2.4 d period for the NS companion. In this case, the mass transfer rate would exceed the Eddington limit of the NS. Consequently, this would result in an X-ray luminosity of the order of $\sim 10^{39}$ erg/s (Eqn. 3.34). As shown in the paragraphs, this would also yield a detectable amount of X-rays even if attenuation by the wind is regarded. If, on the other hand, the NS has initially been spun up by the mass-transfer (Tauris and van den Heuvel 2006), accretion in the current phase may be prohibited by the propeller effect. As in the case of a MS companion, a mass transfer on a long time scale seems unlikely since the mass ratio of the putative WR+NS binary is large. This would lead to a coalescence of the binary faster than the thermal timescale (~ 1000 yr), which is in contradiction to the nebula's dynamical age.

Quast et al. (2019) showed that a mass transfer could be stable for more than 100 000 yr even if the donor was a $30 M_\odot$ star and the accretion a NS. However, this requires a steep He-gradient in the donor's chemical profile and fine-tuning regarding the orbital separation at the beginning of the mass transfer. In the context of mass transfer stabilized by a He-gradient, it is interesting to note that the NS could dig out the He-gradient in a common envelope phase, which would then initialize the stable mass transfer. From this perspective, the hydrogen abundance of 13% (Hamann et al. 2019) could be interpreted as evidence for the He-gradient at the surface. Suppose that the gradient is of the order of $0.4 M_\odot^{-1}$, which is the highest value assumed in the calculations of Quast et al. (2019). In the NS configuration, their models yielded a mass-transfer rate between 10^{-6} and $10^{-5} M_\odot/\text{yr}$. Consequently, the remaining time of the stable mass transfer would be 30 000 to 300 000 yr. This first value is of the same order of magnitude as the dynamical age of the nebula, which could be evidence for the stable mass transfer. We note, however, that the discussion in this paragraph is highly speculative.

Our analysis shows that a companion more massive than $\sim 1 M_\odot$ with an orbital period that corresponds to the period of the light-curve variations seems to be unlikely. This rules out a BH companion in a compact orbit as well as a massive MS companion. Our model predicts a low-mass MS companion or a fast-spinning NS to be in agreement with the observed X-ray flux.

4.7 The single lined binary VFTS 243 in the LMC

The star VFTS 243 is a massive star in the LMC and one of 51 O-type single-lined spectroscopic binaries investigated by the Tarantula Massive Binary Monitoring (Almeida et al. 2017). A detailed spectral analysis by Shenar et al. (2022) found an orbital period of 10.4 d and a companion mass of at least $9 M_{\odot}$ with a median value of $10 M_{\odot}$.

The authors argue that the companion has to be a BH since a non-compact companion should leave detectable signatures in the spectrum. Observations with Chandra show no detectable X-rays from the system above a lower limit of 7×10^{31} ergs/s (Crowther et al. 2022). This makes VFTS 242 one of the few known X-ray quiet O + BH binaries. We investigate the binary system using our diagnostic diagrams (see Fig. 4.7). We marked the detected companion mass and orbital period in our plots for the following discussion. The error bars correspond to the 1σ error provided by Crowther et al. (2022). The upper error bar is an arrow to indicate that the companion mass may be much larger if the system has a low orbital inclination. Table 4.6 shows the adopted stellar parameters of VFTS 243.

Table 4.6.: Parameters for VFTS243 adopted from Shenar et al. (2022).

M_1	$26.2 M_{\odot}$
R_1	$10.3 R_{\odot}$
T_{eff}	36 kK
$\log(L_1/L_{\odot})$	5.2
$\log(\dot{M}/M_{\odot} \text{ yr}^{-1})$	-6.3
v_{∞}	2100 km/s

The top panel in Fig. 4.7 shows that a MS companion is inconsistent with the fact that no spectral signature of a non-compact companion has been found. If the companion was a MS star, the brightness difference of the two stars would be at least 2.5 mag. This means that roughly 10% of the flux would come from the companion star. Thus, a MS companion can clearly be ruled out as concluded by Shenar et al. (2022). This even holds for stars down to $4 M_{\odot}$, since all stars more massive than this contribute more than 1% to the total flux (red dashed line in Fig. 4.7).

From the lower panel in Fig. 4.7, we see that a $10 M_{\odot}$ BH companion should be X-ray faint. The fast wind velocity yields a narrow accretion cylinder and a low amount of specific orbital angular momentum. Consequently, Eqs. 3.14 and 3.15 yield a disc radius of $R_D \approx 4$ km and an innermost stable orbit of $R_{\text{ISCO}} \approx 90$ km. Hence, we do not expect the formation of an accretion disc around the BH companion. Assuming spherically symmetric in-fall (Eq. 3.31) we obtain an X-ray luminosity of $\sim 10^{27}$ erg/s. This is 5 to 6 orders below the current detection limit for X-ray sources in the LMC, hence undetectable. This was already pointed out by Shenar et al. (2022).

VFTS 243 is one of 11 SB1 identified by Shenar et al. (2022) (see next section). A BH hosting binary is not unexpected since Langer et al. (2020) predict a probability of up to 8% of finding a BH companion in a randomly chosen O star. Thus, in a sample of 11 massive SB1, we would expect about 1 BH hosting binary. If we include the 12

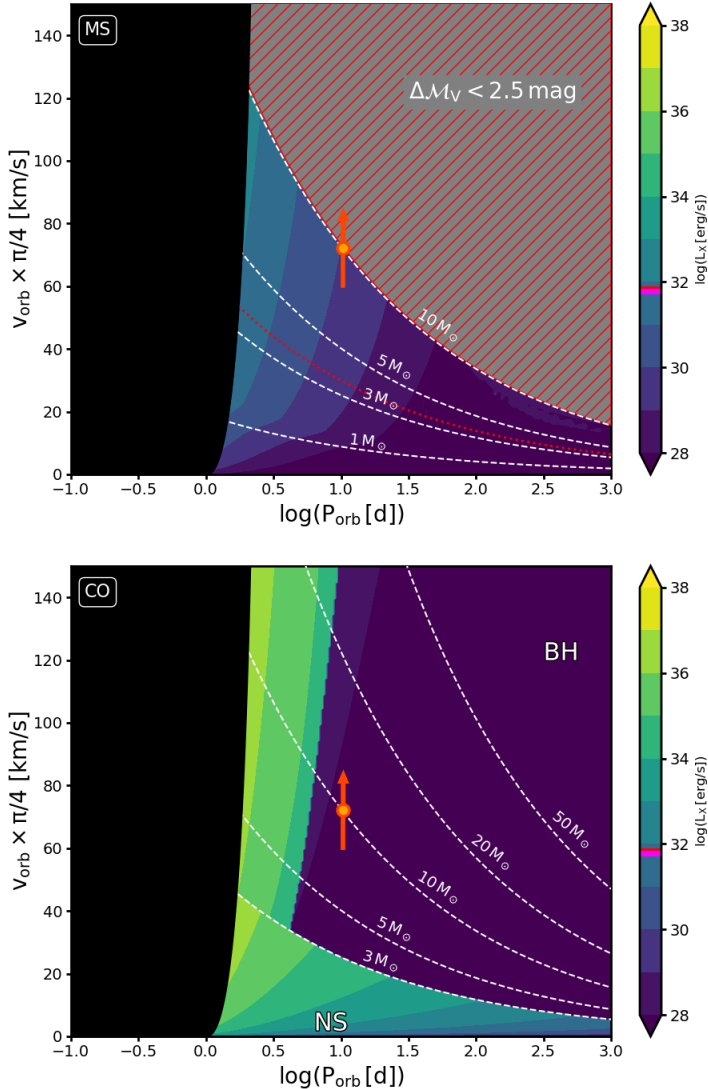


Figure 4.7.: Diagnostic diagrams for VFTS 234 with stellar parameters from Tab. 4.6. The orange dot indicates the companion mass and the orbital period detected by Shenar et al. (2022). For further explanation see Fig. 4.1.

systems identified as uncertain SB2, we expect about two X-ray quiet OB+BH systems. We discuss this question in the next section.

In its further evolution, the primary of VFTS 243 will expand. This will lead to a slower terminal velocity of the stellar wind. As the stellar radius of the star doubles, the terminal wind velocity decreases to 1500 km/s assuming that $v_\infty \propto v_{\text{esc}} \propto \sqrt{R_1}^{-1}$. In this case, the disc radius would increase to $300 R_\odot$, implying the formation of an accretion disc. We note that the ISCO does not change. Thus, VFTS 243 will become a wind-capturing high-mass X-ray binary, similar to Cyg X-1. After a wind-capturing phase, a mass transfer would be initiated due to further expansion of the primary if we assume the current mass ratio of $q \sim 2.6$. As shown by Quast et al. (2019), the mass transfer may be stable on a nuclear timescale emitting large amounts of X-rays close, or even above the Eddington

limit (see also (Tauris and van den Heuvel 2006)).

4.8 The OB stars in 30 Dor

The VLT FLAMES-Tarantula survey (VFTS) obtained multi-epoch spectroscopy of over 800 massive OB and WR stars in the 30 Doradus region (Evans et al. 2011). In the Tarantula Massive Binary Monitoring, Almeida et al. (2017) studied 102 massive binaries and obtained orbital solutions of 51 single-lined (SB1) and 31 double-lined (SB2) spectroscopic binaries.

A detailed analysis of the seemingly 51 SB1s has been performed by Shenar et al. (2022) showing that a large fraction of them was either SB2 systems, eclipsing binaries or multiple systems, and therefore hosting at least one non-compact companion. They found 11 SB1 systems, including VFT 243 (see Tab. 4.7). However, the spectral classification as SB1 is uncertain for 3 of these systems, namely VFTS 619, VFTS 827, and VFTS 829. Furthermore, 12 systems are classified as uncertain SB2s (see Tab. 4.8).

To obtain the stellar parameters necessary for our analysis, we relied on the effective temperature, luminosity, and stellar provided by Shenar et al. (2022). We also used the orbital periods and the supposed companion mass as well as the 1σ error bars from this study. We note, however, that the upper limit of the companion mass is not strict since a low inclination would make the mass of the binary companion substantially larger. We then computed the terminal velocity (Eq. 3.61 and the mass-loss rate (Vink et al. 2001). The visual brightness was obtained as described in Sec. 3.4.2. We discuss two stars in more detail below. The diagnostic diagrams of all other analyzed stars are provided in Appendix C.3.

Besides VFT 243, there are two other promising candidates for an X-ray quiet BH companion: VFTS 514 and VFTS 779, both hosting a companion with an assumed mass of $5 M_{\odot}$ with an orbital period of 185 d and 60 d respectively. Because the mass rules out an NS star as a binary companion, we only discuss the case of a main-sequence companion and a BH companion in this study.

The analysis of VFT 514 is shown in Fig. 4.8. The diagram for an MS companion (top) shows that the companion is close to the optical detection threshold, i.e., the visual brightness difference between the two stars would be close to 2.5 mag. The reason for this is the low luminosity of the host star. As shown in Tab. 4.7, VFTS 514 is the faintest star in the SB1 sample. Consequently, an MS sequence companion should provide a non-negligible amount of light flux in the optical band. Hence, it would have been likely identified by the analysis of Shenar et al. (2022). We note that a strict upper limit on the companion mass cannot be inferred solely from the Doppler shift. Consequently, an MS companion more massive $5 M_{\odot}$ would contribute even more to the total flux of the system, making it very likely to be detected. Hence, a more massive MS companion can be ruled out.

Fig. 4.8 also shows that the lower mass limit is well above the 5 mag threshold (red dashed line). Shenar et al. (2022) rule out a companion contribution of more than 5% to total flux, which corresponds to a magnitude difference of 3.3 mag. Thus, a companion fainter than 0 mag would be the lower limit for spectral detection. This brightness

Table 4.7: Single-lined binaries in the TMBM. Parameters marked with (1) are adopted from Shenar et al. (2022). VFTS 243 is not included since it is discussed in a separate section. The SB1 classification of VFTS 619, VFTS 827, and VFTS 829 is uncertain.

VFTS ID	SpType ⁽¹⁾	$T_{\text{eff}}^{(1)}$ [kK]	$\log L^{(1)}$ [L_{\odot}]	$M_1^{(1)}$ [M_{\odot}]	R_1 [R_{\odot}]	v_{∞} [km/s]	M_{v} [mag]	$\log \dot{M}$ [M_{\odot}/yr]	$P_{\text{orb}}^{(1)}$ [d]	$M_2^{(1)}$ [M_{\odot}]
225	B0.7 III	24.50	4.53	15	10.2	1720	-4.2	-7.81	8.2	2.2
514	O9.7V	32.50	4.44	19	5.2	2700	-3.3	-8.17	184.9	5.3
619	O8: V	36.90	4.86	23	6.6	2650	-3.8	-7.23	14.5	4.4
631	O9.7 V	32.50	4.75	19	7.5	2260	-4.0	-7.49	5.4	3.6
645	O9.5 V	32.90	4.68	20	6.7	2450	-3.8	-7.66	12.5	3.2
743	O9.5 V ((n))	32.90	4.72	20	7.1	2390	-3.9	-7.57	14.9	2.5
769	O9.7 V	32.50	4.74	19	7.4	2270	-4.0	-7.51	2.4	2.2
779	B1 II-III	23.50	4.73	14	14.0	1420	-4.8	-7.24	59.9	4.8
827	B1.5 III	21.00	5.03	13	24.8	1030	-5.9	-6.47	43.2	3.1
829	B1.5 III	20.50	4.78	13	19.5	1160	-5.3	-6.68	202.9	2.5

Table 4.8: Uncertain double-lined binaries in the TMBM. Parameters marked with (1) are adopted from Shenar et al. (2022).

VFTS ID	SpT	Type ⁽¹⁾	$T_{\text{eff}}^{(1)}$ [kK]	$\log L^{(1)}$ [L_{\odot}]	$M_1^{(1)}$ [M_{\odot}]	R_1 [R_{\odot}]	v_{∞} [km/s]	M_V [mag]	$\log \dot{M}$ [M_{\odot}/yr]	$P_{\text{orb}}^{(1)}$ [d]	$M_2^{(1)}$ [M_{\odot}]
73	09.5	IV + B:	31.85	5.00	19	10.4	1920	-4.7	-6.97	150.6	6.8
171	08.5	III:(f) + B1.5:V	34.25	5.43	21	14.8	1690	-5.6	-5.99	677.0	4.1
184	06.5	V n + OB:	38.90	4.91	30	6.3	3100	-3.8	-7.24	32.1	2.1
256	07.5	V: + OB:	36.90	4.98	25	7.6	2580	-4.2	-7.01	246.0	4.8
332	09	III + 09.2 V	31.80	5.19	20	13.0	1760	-5.2	-6.58	1025.0	11.4
409	03.5:	V:((f)) + B:	47.00	5.94	45	14.1	2540	-5.8	-5.18	22.2	9.3
479	04.5	V ((fc))z +B:	42.90	5.14	39	6.7	3420	-4.1	-6.85	14.7	12.9
603	04	III:(fc) + OB:	42.20	5.98	61	18.3	2590	-6.3	-5.27	1.8	1.1
657	07	II:(f) + OB:	35.30	5.52	35	15.4	2140	-5.7	-6.06	63.5	9.3
736	09.5	V + B:	32.90	4.70	20	6.9	2420	-3.9	-7.61	68.8	4.7
750	09.5	V + B:	32.90	4.64	20	6.4	2500	-3.7	-7.74	417.0	6.5
812	04	V((fc))	43.90	5.48	40	9.5	2910	-4.9	-6.12	17.3	6.4

translates into a stellar mass of $4 M_{\odot}$ and a spectral type of B 8 to 9, assuming a MS star.

If we assume a BH companion, the lower panel in Fig. 4.8 shows that no detectable amount of X-rays would be expected from the system. The reasons for this are the wide orbit of the binary and the low mass-loss rate predicted from Vink et al. (2001). Since $5 M_{\odot}$ is a lower limit for the BH, we see that even more massive BH companions are possible if the binary has low orbital inclination. In agreement with Shenar et al. (2022), we conclude that VFTS 514 has a high probability of being an X-ray-quiet OB+BH binary.

The analysis of VFTS 779 is shown in Fig. 4.9. While the companion is supposed to have a similar mass as VFTS 514, the orbit is more compact, and the primary star is brighter by 1.5 mag. The top panel of Fig. 4.9 reveals that a low-mass MS companion could have been undetected in the spectrum if the real companion mass is at the lower limit provided by the error bars. A mass higher than $4 M_{\odot}$ would yield a brightness difference of 5 mag, which should be visible in the optical spectrum. MS stars more massive than $10 M_{\odot}$ can be ruled out due to their brightness. As Fig. 4.9 suggests, we do not expect a significant amount of X-rays from the presence of an MS companion. The reason for this is the low mass-loss rate of the O star compared to a WR star. We conclude that a MS companion of VFTS 779 can escape detection if its mass is in the lower range of the confidence interval provided by Shenar et al. (2022).

The lower panel of Fig. 4.9 shows that a BH companion is also undetectable in X-rays. The assumption of a BH companion is supported by the analysis of Shenar et al. (2022). However, they note that a stripped helium star companion cannot be ruled out.

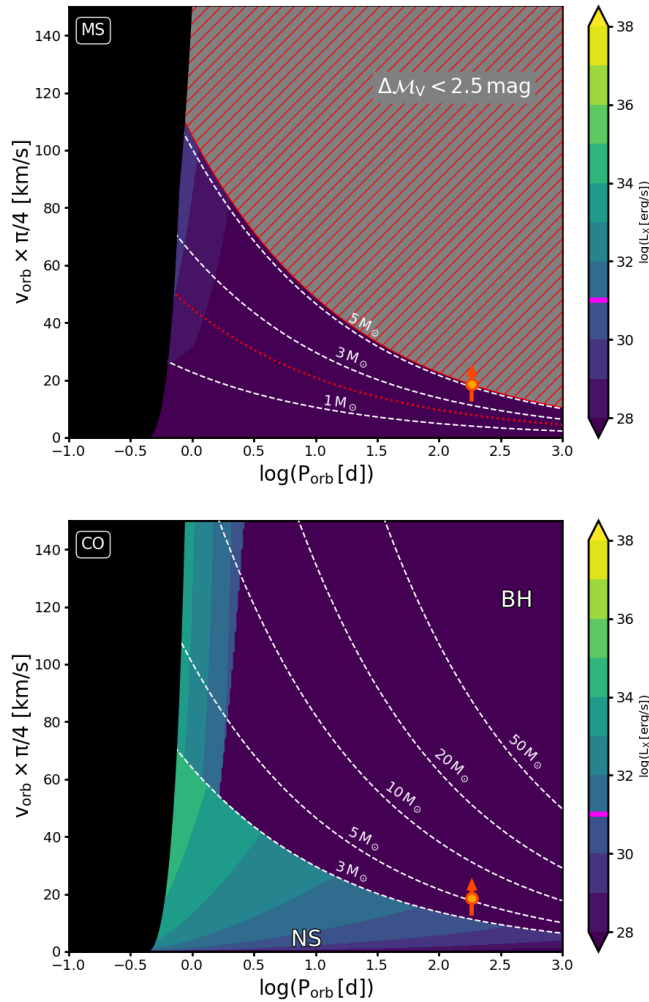


Figure 4.8.: Diagnostic diagrams for VFTS 514 with stellar parameters from Tab. 4.6. The red dot indicates the companion mass and the orbital period detected by Shenar et al. (2022). For further explanation see Fig. 4.1.

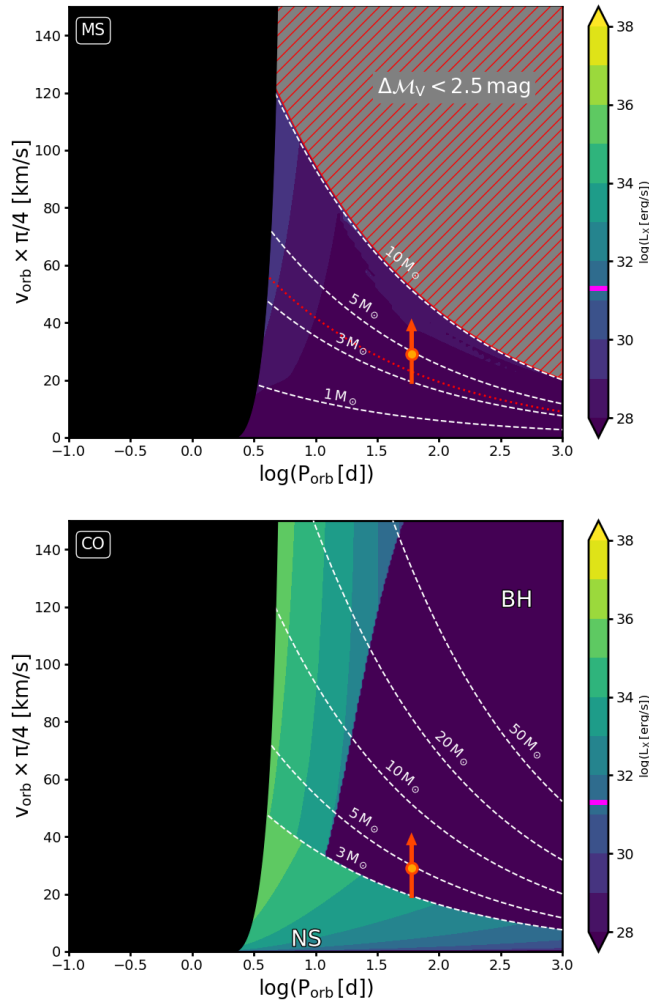


Figure 4.9.: Diagnostic diagrams for VFTS 779 with stellar parameters from Tab. 4.6. The red dot indicates the companion mass and the orbital period detected by Shenar et al. (2022). For further explanation see Fig. 4.1.

4.9 Catalogue of diagnostic diagrams

The aim of this section is to provide a catalog of diagnostic diagrams based on the spectroscopically derived properties of the primary star in SB1 systems. This enables the reader to investigate the expected X-ray flux due to the presence of a compact or main-sequence companion. We chose effective temperature T_{eff} and surface gravity g as parameters for our catalog.

We used these values to infer the stellar mass and luminosity from the *BONNSAI* code (Schneider et al. 2014), a Bayesian statistical method that predicts stellar parameters based on a set of observables. We use a parameter grid of $T_{\text{eff}} = 15 \dots 45 \text{ kK}$ and $\log\left(\frac{g}{\text{cm s}^{-2}}\right) = 3.0 \dots 3.8$. We assumed an uncertainty of 1 kK for the effective temperature and 0.1 dex of $\log(g/(\text{cm s}^{-2}))$. The values of effective temperatures and their corresponding uncertainties provided us with a value of the most likely stellar mass and luminosity.

Note that the quantity $\mathcal{L} := T_{\text{eff}}^4/g$ (Langer and Kudritzki 2014) cannot be arbitrarily large since large temperature and small gravity would imply a large L/M . For sufficiently large temperatures and small surface gravity, the star would exceed its Eddington limit, which means that the force implied by radiation pressure exceeds the star’s gravitational force. Consequently, no hydrostatic configuration of the star is possible (Sanyal et al. 2015). This limit occurs at $\log(\mathcal{L}/\mathcal{L}_\odot) \simeq 4.6$ (Langer and Kudritzki 2014). Since stellar models that exceed the Eddington limit do not exist, *BONNSAI* does not provide stellar parameters for corresponding values of T_{eff} and $\log(g)$. Consequently we excluded the parameter pairs $\log(g/(\text{cm s}^{-2})) = 3.4$ and $T_{\text{eff}} = 45 \text{ kK}$, as well as $\log(g/(\text{cm s}^{-2})) = 3.0$ and $T_{\text{eff}} > 35 \text{ kK}$ from the catalog.

We used these values to compute the terminal velocity and the mass-loss rate described above. The computed values are listed in Table 4.9. Based on the inferred values, we provide diagnostic diagrams in Appendix C.4.

T_{eff} [kK]	$\log(g)$ [cm/s ²]	M_1 [M _⊕]	$\log(L_1)$ [L _⊕]	v_{∞} [km/s]	$\log(\dot{M})$ [M _⊕ /yr]	Figure
15	3.8	4.8	2.89	931	-12.17	C.39
20	3.8	7.8	3.62	1040	-10.71	C.40
25	3.8	11.8	4.19	2180	-10.30	C.41
30	3.8	17.0	4.67	2382	-9.53	C.42
35	3.8	24.2	5.11	2573	-8.57	C.43
40	3.8	36.4	5.53	2832	-5.79	C.44
45	3.8	58.4	5.91	3243	-5.21	C.45
15	3.4	6.0	3.39	781	-11.20	C.46
20	3.4	9.8	4.15	859	-9.67	C.47
25	3.4	15.0	4.70	1832	-9.32	C.48
30	3.4	23.2	5.22	2027	-6.50	C.49
35	3.4	37.2	5.77	2182	-5.37	C.50
40	3.4	72.0	6.15	2788	-4.82	C.51
15	3.0	7.4	3.76	701	-10.50	C.52
20	3.0	13.4	4.60	775	-8.85	C.53
25	3.0	22.8	5.28	1618	-6.28	C.54
30	3.0	53.6	5.90	2083	-5.49	C.55
35	3.0	49.8	6.18	1994	-4.64	C.56

Table 4.9.: Stellar parameters as function of T_{eff} and $\log(g)$. Masses and luminosities are inferred from *BONNSAI* (Schneider et al. 2014). Terminal velocities and mass-loss rates are computed based on Kudritzki and Puls (2000) and Vink et al. (2001). The last column gives the figure number of the corresponding diagnostic diagrams.

4.10 Conclusion

The majority of spectroscopic binaries identified in various observational campaigns are categorized as SB1s. For instance, the B-type binaries characterization (BBC) program (Villaseñor et al. 2021) classified 70 out of 84 systems as SB1. The Tarantula Massive Binary Monitoring (Almeida et al. 2017) lists 51 SB1 systems out of 82 identified binaries.

We combined these approaches to investigate the nature of unseen companions based on spectroscopic and X-ray data as well as measurements of the primary's stellar parameters. We used models for X-ray emission of a putative MS, BH, or NS companion to construct the diagnostic diagrams. These diagrams can be used to compare data from RV measurements with X-ray observations and narrow down the possibilities for the companion's nature. This method is particularly useful for excluding one or more companion types.

We saw this in the example of WR 124, where we could show that the RV period is not compatible with the existence of a BH companion or a slowly spinning NS companion. Furthermore, our diagnostic diagram reveals that the unseen companion in the X-ray-quiet SB1s VFTS 234, VFTS 514, and VFTS 779 is likely to be a BH. It is important to note that the diagrams depend exclusively on the current stellar parameters of the primary. Hence, the diagnostic diagrams are independent of the stellar and binary evolution and the associated uncertainties.

However, we also saw that our model cannot always clearly identify a putative companion's existence or its nature. We found that the following factors facilitate the identification of a putative companion with our diagnostic diagrams:

1. A small terminal velocity of the primary wind: A wind velocity of about 1000 km/s and below makes the existence of an accretion disc more likely. Consequently, a putative BH would be X-ray bright in a larger fraction of the parameter space and may be ruled out based on the non-observation of the X-ray luminosity.
2. A large observed X-ray luminosity: The X-ray emission from an accretion disc or an accreting NS tends to be more X-ray luminous than from colliding stellar winds. Hence, if an SB1 system is observed as an X-ray source, a comparison between the diagnostic diagrams provides evidence of a MS, BH, or NS companion, respectively.
3. Large minimum mass of the unseen companion. If the RV of an SB1 implies a minimum companion mass of a few solar masses and above, we find that a MS companion can often be ruled out due to the optical flux ratio, as seen, i.e., in the cases of VFTS 234, VFTS 514 and VFTS 779. Also, a NS companion can be ruled out if the minimum mass is above $2 M_{\odot}$. In this case, it is a reasonable assumption that the companion is an X-ray-quiet BH.

If the primary star does not show these characteristics, it is harder to identify a putative companion based on the diagnostics diagrams. An example shown in this study is WR 3. The large terminal velocity of this WR star's wind makes it difficult to exclude the exis-

tence of a BH. In addition, no definitive companion identification could be made based on X-ray or RV measurements.

An interesting extension of our model would be the inclusion of decretion discs around the primary. Including a model that estimates the X-ray luminosity emitted from a CO that captures material from a circumstellar disc of its host star could extend our model so that it is applicable to Be stars as well. Hastings et al. (2020) showed that Be stars can be formed via a single star path. Therefore, the existence of a decretion disc around a star is no proof of a binary companion. With the interference of the diagnostic diagrams developed here, the question of whether a particular Be star has a companion may be addressed. Modeling the expected X-ray luminosity in BeXRBs requires knowledge of the decretion disc's structure, and the orbital geometry of the binary is necessary to predict the accretion rate of a putative companion and the X-ray luminosity. Models of decretion discs have been vividly investigated in the past, as well as the formation of Be stars (Lee et al. 1991; McGill et al. 2013; Cochetti et al. 2019; Hastings et al. 2021; Curé et al. 2022).

Also, since diagnostics diagrams depend on the stellar parameters of the primary star, the diagrams of a given primary star would change throughout the primary's evolution. Assuming BH companions, such a study of the time dependence of accretion has been performed by Sen et al. (2021) to investigate the future of observed OB+WR binaries. Our approach can be used to extend this idea to colliding wind binaries and OB/WR+CO binaries, including NS companions.

In those cases where our diagram is inconclusive, the possibilities of identifying a companion could be improved by including other characteristics of the primary. One way to do that is to apply our models of X-ray emission to a synthesized population of binaries. This would provide a probability distribution of periods and RV variations for a given primary. Using our diagnostic diagrams, we could narrow down these distributions to the area of the parameter space that agrees with observations. This approach could not only identify putative companions but would also provide an estimate of the likelihood for the companion in question to exist. Also, applying our diagnostic diagrams could give insights into the question of the missing BH companions. The disadvantage of including population synthesis is that the uncertainties of stellar and binary evolution are introduced into the model.

Nevertheless, we briefly illustrate here how the diagnostic diagrams can be combined with population synthesis to gain new insights into the population of O+Co binaries: For instance, a population synthesis performed by Shao and Li (2020) suggests that the period distribution of OB+BH binaries peaks between 7 and 10 d. From the O stars analyzed in the previous sections, we see that in some cases, a $10 M_{\odot}$ BH companion with a 10 d would be X-ray quiet. The question arises: How many X-ray-quiet BH companions would be predicted?

Langer et al. (2020) used a grid of binary evolution models to estimate the population of OB+BH binaries, which emerge after mass transfer. They found that most OB+BH binaries originate from Case B mass transfer. The periods of the Case B systems distribute between 10 and 1000 d with a maximum of ~ 180 days. OB+BH binaries that emerge after Case A mass transfer occur less frequently and have smaller orbital periods between 3 and 20 d with a distribution peak at ~ 6 d. We can use this distribution of orbital periods to discuss the observability of these systems in the X-ray regime.

To accomplish this task, we construct diagnostic diagrams for two OB stars, contingent on assuming specific stellar parameters for the primary star. As indicated by Langer et al. (2020), the likelihood of a star in a binary system having a black hole companion is highest when the OB star's mass falls within the range of 15 to 22, M_{\odot} . In constructing the diagrams, we rely on the stellar parameters outlined in Tab.4.9. We adopt a primary with $T_{\text{eff}} = 30,000$ K and $\log(g/(\text{cm s}^{-2})) = 3.8$, referred to as the first primary. Additionally, we consider a primary with $T_{\text{eff}} = 25,000$ K and $\log(g/(\text{cm s}^{-2})) = 3.0$, referred to as the second primary. These parameter values correspond to stars with masses of 17 and 22.8, M_{\odot} , respectively (cf. Tab.4.9). We intentionally opted for these parameters to represent extreme cases of surface gravity.

Fig. 4.10 shows the diagnostic diagrams of the two primary stars. In both diagrams, we included the range of orbital period and BH mass predicted by the population synthesis of Langer et al. (2020). We distinguished between the systems originating from Case A and Case B mass transfer, respectively. The dot marks the orbital period and BH mass, where the corresponding frequency distribution peaks. The diagrams show that all synthesized systems are predicted to be X-ray quiet if we assume the stellar parameters of the first primary.

The reason for this is simply the small mass-loss rate of such a star (cf. Tab.4.9). However, if we consider the second primary, we find that most O+BH systems that originate from Case A mass transfer are X-ray bright. Interestingly, the Case A systems show pronounced RV variations of 50 km/s and above. Consequently, these systems would be identified as SB1 in spectroscopic surveys. The systems from Case B mass transfer have significantly larger orbital periods, which also leads to smaller RV variations. Both the large orbital period and the smaller RV variations make it less likely that such a system is identified as an SB1.

Regarding the diagnostic diagram of the second primary, we find that effectively all systems from Case A mass transfer undergo RLFO or are wind-accreting systems with an accretion disc. Consequently, we predict these systems to be X-ray bright with X-ray luminosities of 10^{34} erg/s and above. Most of the Case B originating systems are predicted to be still X-ray quiet. Only the systems with periods smaller than ~ 20 d are expected to form an accretion disc. We find that the majority of the O+BH from Case B mass transfer is expected to be X-ray quiet, as shown by the red dot in Fig. 4.10 and since most of the O+BH binaries in the population synthesis by Langer et al. (2020) originate from Case B mass transfer, we have to come to the conclusion that most of the O+BH are X-ray faint. Again, we point out that this conclusion also depends on the models used to perform the population synthesis. Applying our scheme to construct the diagnostic diagrams to a population synthesis with a different methodology could show how robust this result is.

Our approach helps clarify the nature of the invisible companion in SB1s, providing new insights into the evolution of binaries. For instance, the diagnostic diagrams may help uncover the undetected population of O+BH binaries predicted by Langer et al. (2020) so far. Identifying this population not only holds substantial promise in mitigating uncertainties within models of massive binary evolution. Also, by finding and studying X-ray faint O+BH binaries, like VFTS 234, we may improve our understanding of the accretion processes of wind-fed BHs.

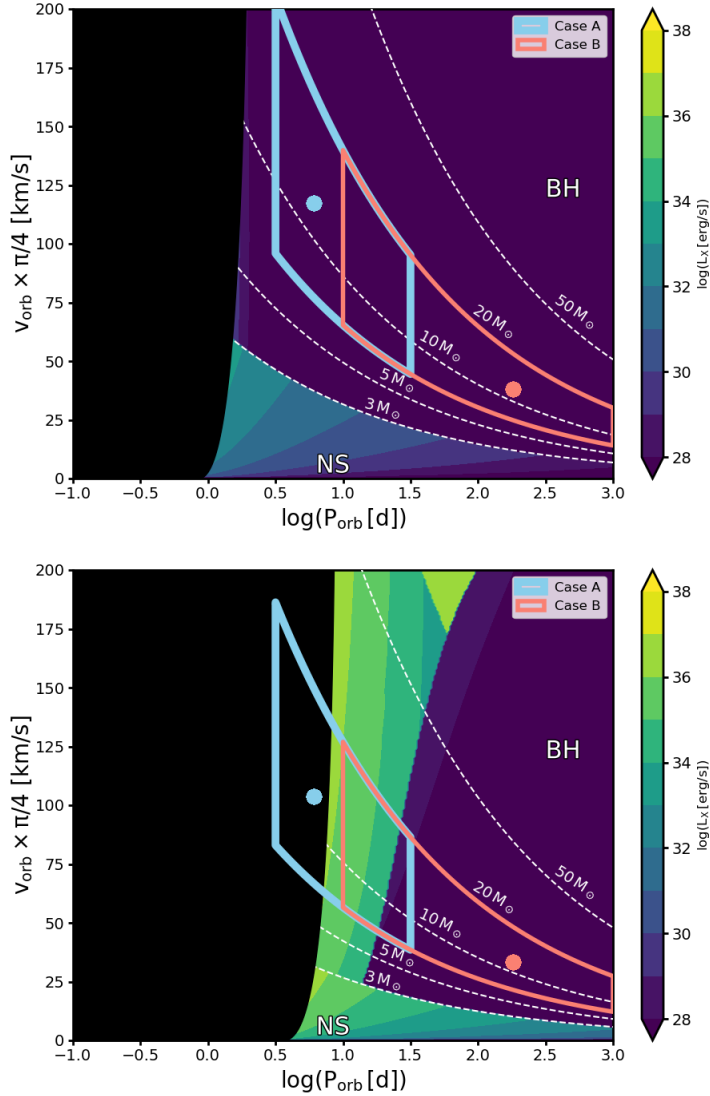


Figure 4.10.: Top: Diagnostic diagram for a CO companion hosted by a primary star with $T_{\text{eff}} = 30 \text{ kK}$ and $\log(g/(\text{cm s}^{-2})) = 3.8$. Mass, luminosity, terminal velocity, and mass-loss rate of the primary are listed in Tab. 4.9. Bottom: Similar to top panel, but primary has $T_{\text{eff}} = 25 \text{ kK}$ and $\log(g/(\text{cm s}^{-2})) = 3.0$.

The blue and red lines outline the regimes of the BH mass and orbital period of the OB+BH binaries synthesized by Langer et al. (2020). The dots mark the orbital period and the BH mass where the corresponding distribution reaches a maximum.

Chapter 5

Summary and Outlook

Massive binaries are linked to a variety of astrophysical phenomena, such as WR stars (Paczynski 1976; Schootemeijer and Langer 2018), supernovae (Dessart et al. 2020), X-ray binaries (Marchant et al. 2017), gamma-ray bursts (Fryer and Heger 2005), or the emission of gravitational waves (Marchant et al. 2016). Consequently, understanding the intrinsic processes and the evolution of these systems is of high significance for astrophysics. As massive stars can end their life as a NS or a BH, the stage where the binary consists of a massive normal star and a compact companion emerges naturally. This thesis aimed to investigate and analyze the processes responsible for the emission of X-rays in binary systems consisting of a massive star and a companion, either a neutron star (NS) or a black hole (BH). Our investigation focused on the interaction between the binary components, including mass transfer from the normal star to the compact companion and accretion of the compact companion from the massive star's wind. We investigated how these processes influence the evolution of the binary and how they enable us to determine the nature of the companion in seemingly single stars and single-lined binaries. This is important when we want to understand the evolution of massive binaries and compare theoretical results with observational evidence.

Chapter 2 was dedicated to studying mass transfer via RLOF from a massive star to a compact companion to understand the mechanisms powering the X-ray emission in SGXBs and ULXs. The key finding of this chapter was that the presence of a hydrogen/helium gradient at the surface of a massive star increases the mass-radius exponents of the thermal equilibrium radius. This constitutes the possibility of stable mass transfer on a nuclear timescale, challenging the conventional belief that mass transfer in binary systems with a large mass ratio is unstable and short-lived. We showed this by constructing detailed binary evolution models featuring an evolved massive star with a hydrogen/helium gradient as the donor and a NS or BH companion as the accretor. Our models defy the anticipated instability of mass transfer despite the considerable orbital contraction of the binary. During the mass transfer, the donor stars undergo significant radius reduction, transitioning from hydrogen- to helium-enriched stars. While our models are hypothetical constructions and not directly derived from previous binary evolution phases, their central premise finds support in observations, particularly regarding the helium-rich and overluminous nature of SGXB donors.

Moreover, our models offer insights into various observational phenomena connected to SGXBs and ULXs. Firstly, they may help to understand the abundance of SGXBs in the Milky Way, since the number frequency of observable X-ray sources is proportional

to the duration of their X-ray phase, which our models significantly extend. Secondly, they may elucidate the presence of ULXs featuring supergiant donors and NS accretors. We showed that a binary consisting of a $\sim 30 M_{\odot}$ star and a $2 M_{\odot}$ NS accretor can undergo a stable mass transfer, leading to an X-ray lifetime of a few hundred thousand years (see for instance Model d2ns0 cons. in Chap. 2). We found, however, that the stabilizing effect relies on a large value of the hydrogen/helium gradient. Consequently, H and He abundances change significantly over a small mass fraction of the envelope. This imposes a fine-tuning problem, which we addressed by proposing that SGXBs, and potentially ULXs with NS accretors, may have formed through a CE evolution phase facilitated by the loss of the H-rich envelope of the donor star that is initially unstable as the H/He gradient is zero in the outer part of the envelope. Similar results were for instance found by Marchant et al. (2021), Vigna-Gómez et al. (2022), Klencki et al. (2022) and Misra et al. (2024).

Enhancing observational constraints on the CE evolution of massive binaries could provide further validation and insights into these phenomena. For instance, recent X-ray observations by Belfiore et al. (2024) of the ultraluminous X-ray pulsar NGC 5907 ULX-1 indicate a binary period of 5.7 d. Depending on the donor radius, which is currently unknown, this may be evidence that the system undergoes RLOF. Moreover, Belfiore et al. (2020) detected an expanding nebula powered by the wind of NGC 5907 ULX-1 with a dynamical age of 7×10^4 yr. If the formation of this nebula is connected to a mass transfer or a CE phase at the beginning of the mass transfer, NGC 5907 ULX-1 may currently undergo nuclear timescale RLOF stabilized by a hydrogen/helium gradient. This would be a direct observation of the stabilizing effect proposed in Chapter 2. In particular, a long-term observation of the orbital period to determine the orbital decay rate \dot{P}_{orb} would be interesting. A match with our predicted values would provide further evidence to support our models. Additional observational support for RLOF stabilized by a hydrogen/helium gradient comes from observations of Zhou et al. (2023) showing that the donor star of the ultraluminous X-ray source NGC 247 ULX-1 is helium-enriched. If the ULX originates from a CE phase, a stripped and thus helium-enriched donor star is precisely what one would expect.

In Chapter 3, we combined models for X-ray emission and RV variations, aiming to clarify the nature of the unseen companion. These processes included X-ray emission mechanisms such as X-rays from accretion, intrinsic emission from the massive star, and colliding stellar winds. We compiled approaches from the literature to estimate the emitted amount of X-rays and developed a technique that integrates radial velocity data with X-ray observations to discern the potential existence and the nature of hidden companions in single-lined massive binaries and apparently single stars.

The central benefit of this chapter was the development of diagnostic diagrams as a tool to study binaries. These diagrams link RV data (RV variation and orbital period) to expected X-ray emission and thus enable us to combine X-ray and RV data to clarify the existence and/or the nature of a putative binary companion. They can be constructed depending on the stellar parameters of the primary star only without assumption about the evolution of the primary star or the binary system. This makes them useful tools for understanding observed RV and X-ray data of a putative binary system.

We showed this in Chapter 4, where we investigated different apparently single stars

Table 5.1.: Summary of the results of the detailed discussed stars in Chapter 4. For each star under investigation, it is indicated whether a MS companion, BH companion, or NS companion is compatible with the observed X-ray data and RV variations. If not, the corresponding type of companion is categorized as unlikely. See the corresponding section in Chapter 4 for discussion and details.

Name	MS	BH	NS
SMC AB 11	compatible if low-mass	unlikely	unlikely
WR 3	low mass only	compatible	compatible
WR 6	unlikely	compatible	compatible
WR 7	unlikely	compatible	compatible
WR 124	compatible	unlikely	unlikely
VFTS 234	unlikely	compatible	unlikely
VFTS 514	unlikely	compatible	unlikely
VFTS 779	unlikely	compatible	unlikely

and SB1s. We discussed a subset of eight of these stars in more detail. The corresponding results of this discussion are summarized in Tab. 5.1, where we indicated for every star if a certain companion type is compatible with observations based on the analysis using our diagnostic diagrams or not.

Furthermore, we provided a catalog of diagnostic diagrams for massive stars with different effective temperatures and surface gravities. These can be used to identify stars that have the potential to host an undetected companion. In addition, we demonstrated that a large fraction of the O+BH binary population predicted by Langer et al. (2020) is potentially X-ray quiet and thus has avoided detection until today. In particular, we were able to refute the paradigm that a BH companion of a massive star with strong stellar wind is always X-ray bright. Instead, we argued that the X-ray brightness of a BH depends on the parameters of the stellar wind, especially the terminal velocity, whereby a high wind results in a low X-ray brightness.

These findings, in turn, generate a series of new questions, which we will briefly discuss three of them in the following paragraphs:

What is the exact number of undetected BHs in massive binary systems?
 We saw in Chap. 3 and 4 that it is possible for an OB star to host an X-ray with a quiet BH companion. On the other hand it is expected that most massive stars are part of a multiple system (Sana et al. 2008, 2009, 2011, 2013, 2014; Kobulnicky and Fryer 2007; Kobulnicky et al. 2014; Dunstall et al. 2015). This leads to the assumption that a significant fraction of the OB+BH binaries may be X-ray quiet due to the inability to form an accretion disc. A similar result was found by Sen et al. (2021) and Hirai and Mandel (2021). Since X-ray observation is the main way to detect BHs, our results led to the conclusion that our sample of observed stellar BHs is most likely incomplete. Indeed, evidence for a large as-yet undetected population of stellar BHs is growing over the past years (Timmes et al. 1996; Breivik et al. 2017; Langer et al. 2020; Chawla et al. 2022; Sen et al. 2024).

Where are the X-ray bright WR+BH binaries?

During the evolution of a massive binary, one would expect that the phase where one companion is a WR star and the other a BH should also arise naturally. However, the only WR+BH candidate we know in the Milky Way is Cyg X-3 (Belczynski et al. 2013; Zdziarski et al. 2013; van den Heuvel 2019). In Chap. 4 of this thesis, we demonstrated that there are WR stars that could host an unseen BH companion (for instance, WR 3 and WR 7). In these cases, increased monitoring of RV variations and X-ray observations would be interesting to deduce if these WR stars have companion stars and, if so, of which nature are these companions. On the other hand, we found multiple examples (for instance, WR 124) where a BH companion is very unlikely due to the expected, but not observed, X-ray brightness that such a companion should induce. For these stars, the question remains if they are indeed single stars or if these stars were born as binaries. In the second case, a possible explanation of the missing BH companion may be found in Chap. 2 of this thesis, where we showed that an unstable mass transfer can result in a CE phase that unbinds large fractions of the hydrogen-rich envelope. This may be followed by a phase of stable mass transfer due to a large H/He at the surface. After this phase, a second CE may follow the stable mass transfer, ultimately leading to the merger of the two companions. A similar scenario has also been described by (Van den Heuvel et al. 2017), but more theoretical and observational research needs to be done to clarify the seeming lack of BH companions in WR binaries.

How can we find X-ray quiet BHs in binaries?

In the introduction of this thesis, we argued that BHs can reveal themselves by interacting with a stellar companion. One such interaction is the gravitational pull of the BH, causing a Doppler shift of the normal companion's spectrum. A binary with an X-ray quiet BH companion may thus be classified as an SB1. Several of these SB1s were discovered in the past years (Almeida et al. 2017; Villaseñor et al. 2021; Shenar et al. 2022). The number of these systems is expected to grow significantly in the next decades as the first light of the world's largest optical and near-infrared telescope, the European Extremely Large Telescope, is expected in 2028. With an aperture diameter of nearly 40 meters, it will be able to collect 16 to 25 times more light than the largest current telescopes (Padovani and Cirasuolo 2023), thereby increasing the limiting distance of observable objects by a factor of 4 to 5 and the observable volume of the universe by a factor between 64 and 125. In particular, we will be able to study significantly more apparently single stars and single-lined binaries. By introducing the diagnostic diagrams, this thesis provided an approach that can help to characterize unseen companions. This would provide a good sample to test our predictions about the detectability of different types of companions in massive binary stars.

Besides improvements in optical astronomy, we expect refined X-ray considerations (Sen et al. 2024) and the possibility of better X-ray observations for the next generation of X-ray observatories, including the space observatories eROSITA (Predehl et al. 2021), LYNX (Gaskin et al. 2019), and Athena (Barcons et al. 2017). With improved sensitivities in addition to long exposure observations, these new X-ray telescopes might be able to detect X-rays from BH companions as well as isolated BHs that are too faint to be found yet. The diagnostic diagrams developed in this thesis may be useful tools for estimating what X-ray flux is expected from a putative companion of a certain star, thereby improving

the target scheduling of X-ray observatories. On the other hand, long exposure observations and detailed X-ray analysis of known X-ray quiet BH in massive binaries (such as in VFTS 243) may help to improve the X-ray estimations for our diagnostic diagrams, especially at the faint X-ray regimes of the parameter space.

Besides optical and X-ray observations, we expect an enormous increase in observational data from the new generation of gravitational wave observatories. Since the first detection of gravitational waves from merging compact objects (Abbott et al. 2016, 2017), LIGO and VIRGO have detected almost 100 merger events (Benjamin 2022). The next generation of gravitational waves observatories, including the Einstein Observatories and Cosmic Explorer, will be equipped with larger interferometer arms and enhanced isolation from external noise, resulting in an increased sensitivity for gravitational wave detection and an increased detection frequency of merging compact objects (Chassande-Mottin et al. 2011; Bertocco et al. 2024). These observations provide another way to deduce the parameters of the massive binary population, particularly the birth rates, the masses, and the number frequency of these systems. This provides an independent way to probe our conclusions concerning the X-ray quiet BHs in massive binaries.

In addition to the three methods of uncovering unseen companions, other techniques have shown their potential: Compact companions can be found via gravitational lensing (Sahu et al. 2022) or precise astrometric measurements (Gaia Collaboration et al. 2024). All the detection methods outlined above have been developed and improved over the last decades. Considering the results of this thesis and the variety of theoretical and observational work cited above, we expect the next years and decades to be very fruitful for the research of compact objects in massive binaries. The recent advancements in observational astronomy and theoretical astrophysics have broadened our understanding of the universe, allowing us to detect faint black holes and gain deeper insights into the past and future of massive binary stars. By uncovering the unseen, we unravel the secrets of the universe step by step, just like astronomers have done since Galileo in 1610.

Bibliography

Aadland, E., P. Massey, D. J. Hillier, N. I. Morrell, K. F. Neugent, and J. J. Eldridge (2022, June). WO-type Wolf-Rayet Stars: The Last Hurrah of Massive Star Evolution. *ApJ* 931(2), 157.

Abbott, B. P., R. Abbott, T. D. Abbott, M. R. Abernathy, F. Acernese, K. Ackley, C. Adams, T. Adams, P. Addesso, R. X. Adhikari, and et al. (2016, February). Observation of Gravitational Waves from a Binary Black Hole Merger. *Physical Review Letters* 116(6), 061102.

Abbott, B. P., R. Abbott, T. D. Abbott, F. Acernese, K. Ackley, C. Adams, T. Adams, P. Addesso, R. X. Adhikari, V. B. Adya, and et al. (2017, October). Multi-messenger Observations of a Binary Neutron Star Merger. *ApJ* 848, L12.

Adhyaqsaa, A., H. L. Malasan, Aprilia, and L. Puspitarini (2020, April). Spectroscopic Observation of Wolf-Rayet Stars: Study of Expansion Velocity and Mass Loss as Contributors of Interstellar Matter Enrichment. In *Journal of Physics Conference Series*, Volume 1523 of *Journal of Physics Conference Series*, pp. 012001. IOP.

Aguilera-Dena, D. R., N. Langer, T. J. Moriya, and A. Schootemeijer (2018, May). Related Progenitor Models for Long-duration Gamma-Ray Bursts and Type Ic Superluminous Supernovae. *ApJ* 858(2), 115.

Almeida, L. A., H. Sana, W. Taylor, R. Barbá, A. Z. Bonanos, P. Crowther, A. Damineli, A. de Koter, S. E. de Mink, C. J. Evans, M. Gieles, N. J. Grin, V. Hénault-Brunet, N. Langer, D. Lennon, S. Lockwood, J. Maíz Apellániz, A. F. J. Moffat, C. Neijssel, C. Norman, O. H. Ramírez-Agudelo, N. D. Richardson, A. Schootemeijer, T. Shenar, I. Soszyński, F. Tramper, and J. S. Vink (2017, February). The Tarantula Massive Binary Monitoring. I. Observational campaign and OB-type spectroscopic binaries. *A&A* 598, A84.

Alpar, M. A., A. F. Cheng, M. A. Ruderman, and J. Shaham (1982, December). A new class of radio pulsars. *Nature* 300(5894), 728–730.

Antokhin, I., J.-F. Bertrand, R. Lamontagne, A. F. J. Moffat, and J. Matthews (1995, February). The Enigmatic WN8 Stars: Intensive Photometry of Four Southern Stars on Time Scales from 30 Min to 3 Months. *AJ* 109, 817.

Apparao, K. M. V. (1985, May). X-ray emission from Be star binaries. *ApJ* 292, 257–259.

Arnaud, K. A. (1996). XSPEC: The First Ten Years. In G. H. Jacoby and J. Barnes (Eds.), *Astronomical Data Analysis Software and Systems V*, Volume 101 of *Astronomical Society of the Pacific Conference Series*, pp. 17.

Bachetti, M., F. A. Harrison, D. J. Walton, B. W. Grefenstette, D. Chakrabarty, F. Fürst, D. Barret, A. Beloborodov, S. E. Boggs, F. E. Christensen, W. W. Craig, A. C. Fabian, C. J. Hailey, A. Hornschemeier, V. Kaspi, S. R. Kulkarni, T. Maccarone, J. M. Miller, V. Rana, D. Stern, S. P. Tendulkar, J. Tomsick, N. A. Webb, and W. W. Zhang (2014, October). An ultraluminous X-ray source powered by an accreting neutron star. *Nature* 514, 202–204.

Balbus, S. A. and J. F. Hawley (1998, January). Instability, turbulence, and enhanced transport in accretion disks. *Reviews of Modern Physics* 70(1), 1–53.

Balona, L. A. (2000). *The Be Phenomenon*¹, Volume 214 of *Astronomical Society of the Pacific Conference Series*, pp. 1.

Barack, L. and N. Sago (2009, May). Gravitational Self-Force Correction to the Innermost Stable Circular Orbit of a Schwarzschild Black Hole. *Phys. Rev. Lett.* 102(19), 191101.

Barcons, X., D. Barret, A. Decourchelle, J. W. den Herder, A. C. Fabian, H. Matsumoto, D. Lumb, K. Nandra, L. Piro, R. K. Smith, and R. Willingale (2017, March). Athena: ESA’s X-ray observatory for the late 2020s. *Astronomische Nachrichten* 338(153), 153–158.

Barkana, R. and A. Loeb (2001, July). In the beginning: the first sources of light and the reionization of the universe. *Phys. Rep.* 349(2), 125–238.

Basko, M. M., R. A. Sunyaev, S. Hatchett, and R. McCray (1977, July). Evaporative winds in X-ray binaries. *ApJ* 215, 276–284.

Beals, C. S. (1929, December). On the nature of Wolf-Rayet emission. *MNRAS* 90, 202–212.

Begelman, M. C. (2002, April). Super-Eddington Fluxes from Thin Accretion Disks? *ApJ* 568, L97–L100.

Belczynski, K., T. Bulik, I. Mandel, B. S. Sathyaprakash, A. A. Zdziarski, and J. Mikołajewska (2013, February). Cyg X-3: A Galactic Double Black Hole or Black-hole-Neutron-star Progenitor. *ApJ* 764(1), 96.

Belczynski, K. and R. E. Taam (2008, September). The Most Massive Progenitors of Neutron Stars: CXO J164710.2-455216. *ApJ* 685(1), 400–405.

Belfiore, A., P. Esposito, F. Pintore, G. Novara, R. Salvaterra, A. De Luca, A. Tiengo, P. Caraveo, F. Fürst, G. L. Israel, D. Magistrali, M. Marelli, S. Mereghetti, A. Papitto, G. A. Rodríguez Castillo, C. Salvaggio, L. Stella, D. J. Walton, A. Wolter, and L. Zampieri (2020, February). Diffuse X-ray emission around an ultraluminous X-ray pulsar. *Nature Astronomy* 4, 147–152.

Belfiore, A., R. Salvaterra, L. Sidoli, G. L. Israel, L. Stella, A. De Luca, S. Mereghetti, P. Esposito, F. Pintore, A. D'Aì, G. Rodríguez Castillo, D. J. Walton, F. Fürst, D. Magistrali, A. Wolter, and M. Imbrogno (2024, April). The Orbit of NGC 5907 ULX-1. *ApJ* 965(1), 78.

Benjamin, K. (2022). Third-generation gravitational-wave detectors. *Einstein Online Band 14, 1002*.

Berghofer, T. W., J. H. M. M. Schmitt, and J. P. Cassinelli (1996, September). The ROSAT all-sky survey catalogue of optically bright OB-type stars. *A&AS* 118, 481–494.

Bertocco, A., M. Bruno, R. De Rosa, L. Di Fiore, D. D'Urso, F. Frasconi, A. Gennai, L. Lucchesi, M. Refat, F. Pilo, D. Rozza, P. Ruggi, V. Sipala, I. Tosta e Melo, and L. Trozzo (2024, June). New Generation of Superattenuator for Einstein Telescope: preliminary studies. *Classical and Quantum Gravity* 41(11), 117004.

Bessolaz, N., C. Zanni, J. Ferreira, R. Keppens, and J. Bouvier (2008, January). Accretion funnels onto weakly magnetized young stars. *A&A* 478(1), 155–162.

Bhattacharya, D. (1995, June). The Evolution of the Magnetic Fields of Neutron Stars. *Journal of Astrophysics and Astronomy* 16, 217.

Biermann, L. (1932, January). Untersuchungen über den inneren Aufbau der Sterne. IV. Konvektionszonen im Innern der Sterne. (Veröffentlichungen der Universitäts-Sternwarte Göttingen, Nr. 27.) Mit 5 Abbildungen. *ZAp* 5, 117.

Biermann, L. (1942, January). Über das Ionisationsgleichgewicht und den Aufbau der Wasserstoffkonvektionszone. Mit 2 Abbildungen. *ZAp* 21, 320.

Biermann, L. (1948, January). Konvektion in rotierenden Sternen. *ZAp* 25, 135.

Bildsten, L., D. Chakrabarty, J. Chiu, M. H. Finger, D. T. Koh, R. W. Nelson, T. A. Prince, B. C. Rubin, D. M. Scott, M. Stollberg, B. A. Vaughan, C. A. Wilson, and R. B. Wilson (1997, December). Observations of Accreting Pulsars. *ApJS* 113, 367–408.

Bird, A. J., A. Bazzano, L. Bassani, F. Capitanio, M. Fiocchi, A. B. Hill, A. Malizia, V. A. McBride, S. Scaringi, V. Sguera, J. B. Stephen, P. Ubertini, A. J. Dean, F. Lebrun, R. Terrier, M. Renaud, F. Mattana, D. Götz, J. Rodriguez, G. Belanger, R. Walter, and C. Winkler (2010, January). The Fourth IBIS/ISGRI Soft Gamma-ray Survey Catalog. *ApJS* 186, 1–9.

Bird, A. J., A. Malizia, A. Bazzano, E. J. Barlow, L. Bassani, A. B. Hill, G. Belanger, F. Capitanio, D. J. Clark, A. J. Dean, M. Fiocchi, D. Gotz, F. Lebrun, M. Molina, N. Produit, M. Renaud, V. Sguera, J. B. Stephen, R. Terrier, P. Ubertini, R. Walter, C. Winkler, and J. Zurita (2007, October). VizieR Online Data Catalog: Third IBIS/ISGRI soft gamma-ray survey catalog (Bird+, 2007). *VizieR Online Data Catalog* 217.

Björklund, R., J. O. Sundqvist, S. M. Singh, J. Puls, and F. Najarro (2023, August). New predictions for radiation-driven, steady-state mass-loss and wind-momentum from hot, massive stars. III. Updated mass-loss rates for stellar evolution. *A&A* 676, A109.

Blaauw, A. (1961, May). On the origin of the O- and B-type stars with high velocities (the “run-away” stars), and some related problems. *Bull. Astron. Inst. Netherlands* 15, 265.

Blondin, J. M. and M. P. Owen (1997). Wind Accretion VS Roche Lobe Overflow in HMXBs. In D. T. Wickramasinghe, G. V. Bicknell, and L. Ferrario (Eds.), *IAU Colloq. 163: Accretion Phenomena and Related Outflows*, Volume 121 of *Astronomical Society of the Pacific Conference Series*, pp. 361.

Böhm-Vitense, E. (1958, January). Über die Wasserstoffkonvektionszone in Sternen verschiedener Effektivtemperaturen und Leuchtkräfte. Mit 5 Textabbildungen. *ZAp* 46, 108.

Böhm-Vitense, E. (1990). *Introduction to Stellar Astrophysics*.

Bolton, C. T. (1972, Feb). Identification of Cygnus X-1 with HDE 226868. *Nature* 235(5336), 271–273.

Bombaci, I. (1996, January). The maximum mass of a neutron star. *A&A* 305, 871.

Bondi, H. and F. Hoyle (1944). On the mechanism of accretion by stars. *MNRAS* 104, 273.

Bowyer, S., E. T. Byram, T. A. Chubb, and H. Friedman (1965, January). Cosmic X-ray Sources. *Science* 147(3656), 394–398.

Bozzo, E., M. Falanga, and L. Stella (2008, August). Are There Magnetars in High-Mass X-Ray Binaries? The Case of Supergiant Fast X-Ray Transients. *ApJ* 683, 1031–1044.

Bozzo, E., L. Oskinova, A. Feldmeier, and M. Falanga (2016, May). Clumpy wind accretion in supergiant neutron star high mass X-ray binaries. *A&A* 589, A102.

Braes, L. L. E. and G. K. Miley (1971, July). Detection of Radio Emission from Cygnus X-1. *Nature* 232, 246.

Braun, H. and N. Langer (1993, March). On the evolution of secondary components in massive close binary systems. *Space Sci. Rev.* 66, 401–404.

Breivik, K., S. Chatterjee, and S. L. Larson (2017, November). Revealing Black Holes with Gaia. *ApJ* 850(1), L13.

Brocksopp, C., A. E. Tarasov, V. M. Lyuty, and P. Roche (1999, Mar). An improved orbital ephemeris for Cygnus X-1. *A&A* 343, 861–864.

Brott, I. (2011). *Modeling populations of rotationally mixed massive stars*. Ph. D. thesis, Sterrenkundig Instituut Utrecht, The Netherlands.

Brott, I., S. E. de Mink, M. Cantiello, N. Langer, A. de Koter, C. J. Evans, I. Hunter, C. Trundle, and J. S. Vink (2011, June). Rotating massive main-sequence stars. I. Grids of evolutionary models and isochrones. *A&A* 530, A115.

Brown, G. E., A. Heger, N. Langer, C.-H. Lee, S. Wellstein, and H. A. Bethe (2001, October). Formation of high mass X-ray black hole binaries. *New A* 6, 457–470.

Bu, D.-F. and X.-H. Yang (2019, April). What is the real accretion rate on to a black hole for low-angular-momentum accretion? *MNRAS* 484(2), 1724–1734.

Burnard, D. J., J. Arons, and S. M. Lea (1983, March). Accretion onto magnetized neutron stars - X-ray pulsars with intermediate rotation rates. *ApJ* 266, 175–187.

Camenzind, M. (2007). *Compact objects in astrophysics : white dwarfs, neutron stars, and black holes*.

Castor, J. I., D. C. Abbott, and R. I. Klein (1975, Jan). Radiation-driven winds in Of stars. *ApJ* 195, 157–174.

Cenci, E., L. Sala, A. Lupi, P. R. Capelo, and M. Dotti (2021, January). Black hole spin evolution in warped accretion discs. *MNRAS* 500(3), 3719–3727.

Chandrasekhar, S. (1931, July). The Maximum Mass of Ideal White Dwarfs. *ApJ* 74, 81.

Chassande-Mottin, E., M. Hendry, P. J. Sutton, and S. Márka (2011, February). Multimessenger astronomy with the Einstein Telescope. *General Relativity and Gravitation* 43(2), 437–464.

Chaty, S. (2013, December). Optical/infrared observations unveiling the formation, nature and evolution of High-Mass X-ray Binaries. *Advances in Space Research* 52, 2132–2142.

Chaty, S., F. Fortin, F. García, and F. Fogantini (2019, December). The dark side of supergiant High-Mass X-ray Binaries. In L. M. Oskinova, E. Bozzo, T. Bulik, and D. R. Gies (Eds.), *High-mass X-ray Binaries: Illuminating the Passage from Massive Binaries to Merging Compact Objects*, Volume 346, pp. 161–169.

Chaty, S., F. Rahoui, C. Foellmi, J. A. Tomsick, J. Rodriguez, and R. Walter (2008, June). Multi-wavelength observations of Galactic hard X-ray sources discovered by INTEGRAL. I. The nature of the companion star. *A&A* 484, 783–800.

Chawla, C., S. Chatterjee, K. Breivik, C. K. Moorthy, J. J. Andrews, and R. E. Sanderson (2022, June). Gaia May Detect Hundreds of Well-characterized Stellar Black Holes. *ApJ* 931(2), 107.

Chené, A. N., C. Foellmi, S. V. Marchenko, N. St-Louis, A. F. J. Moffat, D. Ballereau, J. Chauville, J. Zorec, and C. A. Poteet (2011, June). A 10-h period revealed in optical spectra of the highly variable WN8 Wolf-Rayet star WR 123. *A&A* 530, A151.

Chiosi, C. and A. Maeder (1986, January). The evolution of massive stars with mass loss. *ARA&A* 24, 329–375.

Chu, Y. H. and R. R. Treffers (1981, October). Galactic ring nebulae associated with Wolf-Rayet stars. II. M 1-67 : a nebula braked by the interstellar medium. *ApJ* 249, 586–591.

Clark, J. S., S. P. Goodwin, P. A. Crowther, L. Kaper, M. Fairbairn, N. Langer, and C. Brocksopp (2002, September). Physical parameters of the high-mass X-ray binary $\text{J}[\text{ASTROBJ}]\text{4U1700-37}\text{J}/\text{ASTROBJ}$. *A&A* 392, 909–920.

Clayton, D. D. (1968). *Principles of stellar evolution and nucleosynthesis*.

Cochetti, Y. R., C. Arcos, S. Kanaan, A. Meilland, L. S. Cidale, and M. Curé (2019, January). Spectro-interferometric observations of a sample of Be stars. Setting limits to the geometry and kinematics of stable Be disks. *A&A* 621, A123.

Colbert, E. J. M. and R. F. Mushotzky (1999, July). The Nature of Accreting Black Holes in Nearby Galaxy Nuclei. *ApJ* 519(1), 89–107.

Coleiro, A., S. Chaty, J. A. Zurita Heras, F. Rahoui, and J. A. Tomsick (2013, December). Infrared identification of high-mass X-ray binaries discovered by INTEGRAL. *A&A* 560, A108.

Conti, P. S. (1978, February). Stellar parameters of five early type companions of X-ray sources. *A&A* 63, 225–235.

Conti, P. S., M. E. Leep, and D. N. Perry (1983, May). The spectra of Wolf-Rayet stars. I. Optical line strengths and the hydrogen-to-helium ratios in WN type stars. *ApJ* 268, 228–245.

Corbet, R. H. D. (1984, December). Be/neutron star binaries - A relationship between orbital period and neutron star spin period. *A&A* 141, 91–93.

Corbet, R. H. D. (1986, June). The three types of high-mass X-ray pulsator. *MNRAS* 220, 1047–1056.

Couch, S. M., E. Chatzopoulos, W. D. Arnett, and F. X. Timmes (2015, July). The Three-dimensional Evolution to Core Collapse of a Massive Star. *ApJ* 808(1), L21.

Courvoisier, T. J. L. (2013). *High Energy Astrophysics*.

Cox, J. P. and R. T. Giuli (1968). *Principles of stellar structure*.

Cromartie, H. T., E. Fonseca, S. M. Ransom, P. B. Demorest, Z. Arzoumanian, H. Blumer, P. R. Brook, M. E. DeCesar, T. Dolch, J. A. Ellis, R. D. Ferdman, E. C. Ferrara, N. Garver-Daniels, P. A. Gentile, M. L. Jones, M. T. Lam, D. R. Lorimer, R. S. Lynch, M. A. McLaughlin, C. Ng, D. J. Nice, T. T. Pennucci, R. Spiewak, I. H. Stairs, K. Stovall, J. K. Swiggum, and W. W. Zhu (2020, January). Relativistic Shapiro delay measurements of an extremely massive millisecond pulsar. *Nature Astronomy* 4, 72–76.

Crowther, P. A. (2007, September). Physical Properties of Wolf-Rayet Stars. *ARA&A* 45, 177–219.

Crowther, P. A., P. S. Broos, L. K. Townsley, A. M. T. Pollock, K. A. Tehrani, and M. Gagne (2022, July). X-ray properties of early-type stars in the Tarantula Nebula from T-ReX. *arXiv e-prints*, arXiv:2207.08836.

Curé, M., R. Meneses, I. Araya, C. Arcos, G. Peña, N. Machuca, and A. Rodriguez (2022, August). Revisiting viscous transonic decretion disks of Be stars. *A&A* 664, A185.

Dalton, W. W. and C. L. Sarazin (1995, February). High-mass X-ray binary populations. I: Galactic modeling. *ApJ* 440, 280–296.

Davies, R. E., A. C. Fabian, and J. E. Pringle (1979, March). Spindown of neutron stars in close binary systems. *MNRAS* 186, 779–782.

Davies, R. E. and J. E. Pringle (1981, July). Spindown of neutron stars in close binary systems. II. *MNRAS* 196, 209–224.

Davis, R. and L. Hartmann (1983, July). Constraints on the inclination and masses of the HDE 226868/Cygnus X-1 system from the observations. *ApJ* 270, 671–677.

De Donder, E., D. Vanbeveren, and J. van Bever (1997, February). The number of O-type runaways, the number of O and Wolf-Rayet stars with a compact companion and the formation rate of double pulsars predicted by massive close binary evolution. *A&A* 318, 812–818.

de Kool, M. (1990, July). Common Envelope Evolution and Double Cores of Planetary Nebulae. *ApJ* 358, 189.

De Loore, C. and J. P. De Greve (1975, July). Evolution of Massive Close Binaries. I: The X-Ray Binary Stage. *Ap&SS* 35(2), 241–247.

De Loore, C., J. P. De Greve, and H. J. G. L. M. Lamers (1977, October). Evolution of massive stars with mass loss by stellar wind. *A&A* 61, 251–259.

de Mink, S. E., I. Brott, M. Cantiello, R. G. Izzard, N. Langer, and H. Sana (2012, December). Challenges for Understanding the Evolution of Massive Stars: Rotation, Binarity, and Mergers. In L. Drissen, C. Robert, N. St-Louis, and A. F. J. Moffat (Eds.), *Proceedings of a Scientific Meeting in Honor of Anthony F. J. Moffat*, Volume 465 of *Astronomical Society of the Pacific Conference Series*, pp. 65.

de Mink, S. E., O. R. Pols, and R. W. Hilditch (2007, June). Efficiency of mass transfer in massive close binaries. Tests from double-lined eclipsing binaries in the SMC. *A&A* 467(3), 1181–1196.

Dermine, T., A. Jorissen, L. Siess, and A. Frankowski (2009, November). Radiation pressure and pulsation effects on the Roche lobe. *A&A* 507, 891–899.

Dessart, L., S.-C. Yoon, D. R. Aguilera-Dena, and N. Langer (2020, October). Supernovae Ib and Ic from the explosion of helium stars. *A&A* 642, A106.

Done, C. and P. T. Zycki (1999, April). Relativistic distortions in the X-ray spectrum of CYG X-1. *MNRAS* 305(2), 457–468.

Drissen, L., C. Robert, R. Lamontagne, A. F. J. Moffat, N. St-Louis, N. van Weeren, and A. M. van Genderen (1989, August). Photometry and Polarimetry of the Unusual WN5 Star EZ Canis Majoris. *ApJ* 343, 426.

Dsilva, K., T. Shenar, H. Sana, and P. Marchant (2022, August). A spectroscopic multiplicity survey of Galactic Wolf-Rayet stars. II. The northern WNE sequence. *A&A* 664, A93.

Duflot, M., P. Figon, and N. Meyssonier (1995, December). Vitesses radiales. Catalogue WEB: Wilson Evans Batten. Subtitle: Radial velocities: The Wilson-Evans-Batten catalogue. *A&AS* 114, 269.

Dunstall, P. R., P. L. Dufton, H. Sana, C. J. Evans, I. D. Howarth, S. Simón-Díaz, S. E. de Mink, N. Langer, J. Maíz Apellániz, and W. D. Taylor (2015, August). The VLT-FLAMES Tarantula Survey. XXII. Multiplicity properties of the B-type stars. *A&A* 580, A93.

Ebisawa, K., K. Mitsuda, and T. Hanawa (1991, January). Application of a general relativistic accretion disk model to LMC X-1, LMC X-3, X1608 - 522, and X1636 - 536. *ApJ* 367, 213–220.

Eggleton, P. P. (1983, May). Approximations to the radii of Roche lobes. *ApJ* 268, 368.

Einstein, A. (1915, January). Die Feldgleichungen der Gravitation. *Sitzungsberichte der Königlich Preussischen Akademie der Wissenschaften*, 844–847.

Ekşi, K. Y., İ. C. Andaç, S. Çıkıntıoğlu, A. A. Gençali, C. Güngör, and F. Öztekin (2015, March). The ultraluminous X-ray source NuSTAR J095551+6940.8: a magnetar in a high-mass X-ray binary. *MNRAS* 448, L40–L42.

El Mellah, I., J. O. Sundqvist, and R. Keppens (2018, April). Accretion from a clumpy massive-star wind in supergiant X-ray binaries. *MNRAS* 475, 3240–3252.

Eldridge, J. J. and E. R. Stanway (2022, August). New Insights into the Evolution of Massive Stars and Their Effects on Our Understanding of Early Galaxies. *ARA&A* 60, 455–494.

Elsner, R. F. and F. K. Lamb (1977, August). Accretion by magnetic neutron stars. I - Magnetospheric structure and stability. *ApJ* 215, 897–913.

Erkut, M. H. and K. Y. Ekşi (2019, December). Ultra-luminous X-ray sources as neutron stars propelling and accreting at super-critical rates in high-mass X-ray binaries. In L. M. Oskinova, E. Bozzo, T. Bulik, and D. R. Gies (Eds.), *High-mass X-ray Binaries: Illuminating the Passage from Massive Binaries to Merging Compact Objects*, Volume 346, pp. 259–263.

Ertl, T., M. Ugliano, H.-T. Janka, A. Marek, and A. Arcones (2016, April). Erratum: “Progenitor-explosion Connection and Remnant Birth Masses for Neutrino-driven Supernovae of Iron-core Progenitors” [\[A href="/abs/2012ApJ...757...69U"\]](https://abs/2012ApJ...757...69U) (2012, *ApJ*, 757, 69) [\[A\]](https://abs/2012ApJ...757...69U). *ApJ* 821(1), 69.

Esin, A. A., J. E. McClintock, and R. Narayan (1997, November). Advection-Dominated Accretion and the Spectral States of Black Hole X-Ray Binaries: Application to Nova Muscae 1991. *ApJ* 489(2), 865–889.

Evans, C., W. Taylor, H. Sana, V. Hénault-Brunet, T. Bagnoli, N. Bastian, J. Bestenlehner, A. Bonanos, E. Bressert, I. Brott, M. Campbell, M. Cantiello, G. Carraro, S. Clark, E. Costa, P. Crowther, A. de Koter, S. E. de Mink, E. Doran, P. Dufton, P. Dunstall, M. Garcia, M. Gieles, G. Gräfener, A. Herrero, I. Howarth, R. Izzard, K. Köhler, N. Langer, D. Lennon, J. Maíz Apellániz, N. Markova, P. Najarro, J. Puls, O. Ramirez, C. Sabín-Sanjulián, S. Simón-Díaz, S. Smartt, V. Stroud, J. van Loon, J. S. Vink, and N. Walborn (2011, September). The VLT FLAMES Tarantula Survey. *The Messenger* 145, 33–38.

Fabrika, S. (2004). The jets and supercritical accretion disk in SS433. *Astrophysics and Space Physics Reviews* 12, 1–152.

Fabrika, S. N., K. E. Atapin, A. S. Vinokurov, and O. N. Sholukhova (2021, January). Ultraluminous X-Ray Sources. *Astrophysical Bulletin* 76(1), 6–38.

Falanga, M., E. Bozzo, A. Lutovinov, J. M. Bonnet-Bidaud, Y. Fetisova, and J. Puls (2015, May). Ephemeris, orbital decay, and masses of ten eclipsing high-mass X-ray binaries. *A&A* 577, A130.

Farrell, S. A., M. Servillat, K. Wiersema, D. Barret, O. Godet, I. Heywood, T. J. Maccarone, S. R. Oates, B. Plazolles, and N. A. Webb (2011, May). Exploring the nature of the brightest hyper-luminous X-ray source. *Astronomische Nachrichten* 332(4), 392.

Feldmeier, A., J. Puls, and A. W. A. Pauldrach (1997, June). A possible origin for X-rays from O stars. *A&A* 322, 878–895.

Firmani, C., G. Koenigsberger, G. F. Bisiacchi, A. F. J. Moffat, and J. Isserstedt (1980, July). The binary nature of the single-line Wolf-Rayet star EZ CMa=HD 50896. *ApJ* 239, 607–621.

Flannery, B. P. (1977, January). Mass Transfer Effects in Binary Star Evolution. In M. D. Papagiannis (Ed.), *Eighth Texas Symposium on Relativistic Astrophysics*, Volume 302, pp. 36.

Flores, A., G. Koenigsberger, O. Cardona, and L. de la Cruz (2007, June). The Wolf-Rayet Stars HD 4004 and HD 50896: Two of a Kind. *AJ* 133(6), 2859–2865.

Flower, P. J. (1996, September). Transformations from Theoretical Hertzsprung-Russell Diagrams to Color-Magnitude Diagrams: Effective Temperatures, B-V Colors, and Bolometric Corrections. *ApJ* 469, 355.

Foellmi, C. and A. F. J. Moffat (2002, January). Are Peculiar Wolf-Rayet Stars of Type WN8 Thorne-Zytkow Objects? In M. M. Shara (Ed.), *Stellar Collisions, Mergers and their Consequences*, Volume 263 of *Astronomical Society of the Pacific Conference Series*, pp. 123.

Foellmi, C., A. F. J. Moffat, and M. A. Guerrero (2003, Jan). Wolf-Rayet binaries in the Magellanic Clouds and implications for massive-star evolution - I. Small Magellanic Cloud. *Monthly Notices of the Royal Astronomical Society* 338(2), 360–388.

Fossati, L., N. Castro, M. Schöller, S. Hubrig, N. Langer, T. Morel, M. Briquet, A. Herrero, N. Przybilla, H. Sana, F. R. N. Schneider, A. de Koter, and BOB Collaboration (2015, October). B fields in OB stars (BOB): Low-resolution FORS2 spectropolarimetry of the first sample of 50 massive stars. *A&A* 582, A45.

Frank, J., A. King, and D. J. Raine (2002, January). *Accretion Power in Astrophysics: Third Edition*.

Frank, J., A. R. King, and D. J. Raine (1985). *Accretion power in astrophysics*.

Fryer, C. L. and A. Heger (2005, April). Binary Merger Progenitors for Gamma-Ray Bursts and Hypernovae. *ApJ* 623(1), 302–313.

Gagné, M., G. Fehon, M. R. Savoy, C. A. Cartagena, D. H. Cohen, and S. P. Owocki (2012, December). An X-Ray Survey of Colliding Wind Binaries. In L. Drissen, C. Robert, N. St-Louis, and A. F. J. Moffat (Eds.), *Proceedings of a Scientific Meeting in Honor of Anthony F. J. Moffat*, Volume 465 of *Astronomical Society of the Pacific Conference Series*, pp. 301.

Gaia Collaboration, P. Panuzzo, T. Mazeh, F. Arenou, B. Holl, E. Caffau, A. Jorissen, C. Babusiaux, P. Gavras, J. Sahlmann, U. Bastian, Ł. Wyrzykowski, L. Eyer, N. Leclerc, N. Bauchet, A. Bombrun, N. Mowlavi, G. M. Seabroke, D. Teyssier, E. Balbinot, A. Helmi, A. G. A. Brown, A. Vallenari, T. Prusti, J. H. J. de Bruijne, A. Barbier, M. Biermann, O. L. Creevey, C. Ducourant, D. W. Evans, R. Guerra, A. Hutton, C. Jordi, S. A. Klioner, U. Lammers, L. Lindegren, X. Luri, F. Mignard, C. Nicolas, S. Randich, P. Sartoretti, R. Smiljanic, P. Tanga, N. A. Walton, C. Aerts, C. A. L. Bailer-Jones, M. Cropper, R. Drimmel, F. Jansen, D. Katz, M. G. Lattanzi, C. Soubiran, F. Thévenin, F. van Leeuwen, R. Andrae, M. Audard, J. Bakker, R. Blomme, J. Castañeda, F. De Angeli, C. Fabricius, M. Fouesneau, Y. Frémat, L. Galluccio, A. Guerrier, U. Heiter, E. Masana, R. Messineo, K. Nienartowicz, F. Pailler, F. Riclet, W. Roux, R. Sordo, G. Gracia-Abril, J. Portell, M. Altmann, K. Benson, J. Berthier, P. W. Burgess, D. Busonero, G. Busso, C. Cacciari, H. Cánovas, J. M. Carrasco, B. Carry, A. Cellino, N. Cheek, G. Clementini, Y. Damerdji, M. Davidson, P. de Teodoro, L. Delchambre, A. Dell’Oro, E. Fraile Garcia, D. Garabato, P. García-Lario, R. Haigron, N. C. Hambly, D. L. Harrison, D. Hatzidimitriou, J. Hernández, D. Hestroffer, S. T. Hodgkin, S. Jamal, G. Jevardat de Fombelle, S. Jordan, A. Krone-Martins, A. C. Lanzafame, W. Löffler, A. Lorca, O. Marchal, P. M. Marrese, A. Moitinho, K. Muinonen, M. Nuñez Campos, I. Oreshina-Slezak, P. Osborne, E. Pancino, T. Pauwels, A. Recio-Blanco, M. Riello, L. Rimoldini, A. C. Robin, T. Roegiers, L. M. Sarro, M. Schultheis, M. Smith, A. Sozzetti, E. Utrilla, M. van Leeuwen, K. Weingrill, U. Abbas, P. Ábrahám, A. Abreu Aramburu, S. Ahmed, G. Altavilla, M. A. Álvarez, F. Anders, R. I. Anderson, E. Anglada Varela, T. Antoja, S. Baig, D. Baines, S. G. Baker, L. Balaguer-Núñez, Z. Balog, C. Barache, M. Barros, M. A.

Barstow, S. Bartolomé, D. Bashi, J. L. Bassilana, N. Baudeau, U. Becciani, L. R. Bedin, I. Bellas-Velidis, M. Bellazzini, W. Beordo, M. Bernet, C. Bertolotto, S. Bertone, L. Bianchi, A. Binnenfeld, S. Blanco-Cuaresma, J. Bland-Hawthorn, A. Blazere, T. Boch, D. Bossini, S. Bouquillon, A. Bragaglia, J. Braine, E. Bratsolis, E. Breedt, A. Bressan, N. Brouillet, E. Brugaletta, B. Bucciarelli, A. G. Butkevich, R. Buzzi, A. Camut, R. Cancelliere, T. Cantat-Gaudin, D. Capilla Guilarte, R. Carballo, T. Carlucci, M. I. Carnerero, J. Carretero, S. Carton, L. Casamiquela, A. Casey, M. Castellani, A. Castro-Ginard, L. Ceraj, V. Cesare, P. Charlot, C. Chaudet, L. Chemin, A. Chiavassa, N. Chornay, D. Chosson, W. J. Cooper, T. Cornez, S. Cowell, M. Crosta, C. Crowley, M. Cruz Reyes, C. Dafonte, M. Dal Ponte, M. David, P. de Laverny, F. De Luise, R. De March, A. de Torres, E. F. del Peloso, M. Delbo, A. Delgado, J. B. Delisle, C. Demouchy, E. Denis, T. E. Dharmawardena, F. Di Giacomo, C. Diener, E. Distefano, C. Dolding, K. Dsilva, H. Enke, C. Fabre, M. Fabrizio, S. Faigler, M. Fatović, G. Fedorets, J. Fernández-Hernández, P. Fernique, F. Figueras, C. Fouron, F. Frakoudi, M. Gai, M. Galinier, A. Garcia-Serrano, M. García-Torres, A. Garofalo, E. Gerlach, R. Geyer, P. Giacobbe, G. Gilmore, S. Girona, G. Giuffrida, A. Gomboc, A. Gomez, I. González-Santamaría, E. Gosset, M. Granvik, V. Gregori Barrera, R. Gutiérrez-Sánchez, M. Haywood, A. Helmer, S. L. Hidalgo, T. Hilger, D. Hobbs, C. Hottier, H. E. Huckle, Ó. Jiménez-Arranz, J. Juaristi Campillo, Z. Kaczmarek, P. Kervella, S. Khanna, M. Kontizas, G. Kordopatis, A. J. Korn, Á. Kóspál, Z. Kostrzewska-Rutkowska, K. Kruszyńska, M. Kun, S. Lambert, A. F. Lanza, Y. Lebreton, T. Lebzelter, S. Leccia, G. Lecoutre, S. Liao, L. Liberato, E. Licata, E. Livanou, A. Lobel, J. López-Miralles, C. Loup, M. Madarász, L. Mahy, R. G. Mann, M. Manteiga, C. P. Marcellino, J. M. Marchant, M. Marconi, D. Marín Pina, S. Marinoni, D. J. Marshall, J. Martín Lozano, L. Martin Polo, J. M. Martín-Fleitas, G. Marton, D. Mascarenhas, A. Masip, A. Mastrobuono-Battisti, P. J. McMillan, J. Meichsner, J. Merc, S. Messina, N. R. Millar, A. Mints, D. Mohamed, D. Molina, R. Molinaro, L. Molnár, M. Monguió, P. Montegriffo, L. Monti, A. Mora, R. Morbidelli, D. Morris, R. Mudimadugula, T. Muraveva, I. Musella, Z. Nagy, N. Nardetto, C. Navarrete, S. Oh, C. Ordenovic, O. Orenstein, C. Pagani, I. Pagano, L. Palaversa, P. A. Palicio, L. Pallas-Quintela, M. Pawlak, A. Penttilä, P. Pesciullesi, M. Pinamonti, E. Plachy, L. Planquart, G. Plum, E. Poggio, D. Pourbaix, A. M. Price-Whelan, L. Pulone, V. Rabin, M. Rainer, C. M. Raiteri, P. Ramos, M. Ramos-Lerate, M. Ratajczak, P. Re Fiorentin, S. Regibo, C. Reylé, V. Ripepi, A. Riva, H. W. Rix, G. Rixon, G. Robert, N. Robichon, C. Robin, M. Romero-Gómez, N. Rowell, D. Ruz Mieres, K. A. Rybicki, G. Sadowski, A. Sagristà Sellés, N. Sanna, R. Santoveña, M. Sarasso, M. H. Sarmiento, C. Sarrate Riera, E. Sciacca, D. Ségransan, M. Semczuk, S. Shahaf, A. Siebert, E. Slezak, R. L. Smart, O. N. Snaith, E. Solano, F. Solitro, D. Souami, J. Souchay, E. Spitoni, F. Spoto, L. A. Squillante, I. A. Steele, H. Steidelmüller, J. Surdej, L. Szabados, F. Taris, M. B. Taylor, R. Teixeira, T. Tepper-Garcia, W. Thuillot, L. Tolomei, N. Tonello, F. Torra, G. Torralba Elipe, M. Trabucchi, E. Trentin, M. Tsantaki, C. Turon, A. Ulla, N. Unger, I. Valtchanov, O. Vanel, A. Vecchiato, D. Vicente, E. Villar, M. Weiler, H. Zhao, J. Zorec, S. Zucker, A. Župić, and T. Zwitter (2024, June). Discovery of a dormant 33 solar-mass black hole in pre-release Gaia astrometry. *A&A* 686, L2.

Gaskin, J. A., D. A. Swartz, A. Vikhlinin, F. Özel, K. E. Gelmis, J. W. Arenberg, S. R. Bandler, M. W. Bautz, M. M. Civitani, A. Dominguez, M. E. Eckart, A. D. Falcone, E. Figueroa-Feliciano, M. D. Freeman, H. M. Günther, K. A. Havey, R. K. Heilmann, K. Kilaru, R. P. Kraft, K. S. McCarley, R. L. McEntaffer, G. Pareschi, W. Purcell, P. B. Reid, M. L. Schattenburg, D. A. Schwartz, E. D. Schwartz, H. D. Tananbaum, G. R. Tremblay, W. W. Zhang, and J. A. Zuhone (2019, April). Lynx X-Ray Observatory: an overview. *Journal of Astronomical Telescopes, Instruments, and Systems* 5, 021001.

Ge, H., M. S. Hjellming, R. F. Webbink, X. Chen, and Z. Han (2010, July). Adiabatic Mass Loss in Binary Stars. I. Computational Method. *ApJ* 717(2), 724–738.

Giacconi, R., P. Gorenstein, H. Gursky, and J. R. Waters (1967, June). An X-Ray Survey of the Cygnus Region. *ApJ* 148, L119.

Giacconi, R., E. Kellogg, P. Gorenstein, H. Gursky, and H. Tananbaum (1971, April). An X-Ray Scan of the Galactic Plane from UHURU. *ApJ* 165, L27.

Giacobbo, N., M. Mapelli, and M. Spera (2018, March). Merging black hole binaries: the effects of progenitor's metallicity, mass-loss rate and Eddington factor. *MNRAS* 474(3), 2959–2974.

Gies, D. R. and C. T. Bolton (1986, May). The Optical Spectrum of HDE 226868 = Cygnus X-1. III. A Focused Stellar Wind Model for He II lambda 4686 Emission. *ApJ* 304, 389.

Gies, D. R., C. T. Bolton, R. Fender, A. Herrero, T. C. Hillwig, L. Kaper, M. V. McSwain, J. Thomson, D. J. Wallace, and P. J. Wiita (2003, December). Wind Accretion and State Transitions in the Black Hole Binary Cyg X-1. In *American Astronomical Society Meeting Abstracts*, Volume 203 of *American Astronomical Society Meeting Abstracts*, pp. 81.06.

Giménez-García, A., T. Shenar, J. M. Torrejón, L. Osokinova, S. Martínez-Núñez, W. R. Hamann, J. J. Rodes-Roca, A. González-Galán, J. Alonso-Santiago, C. González-Fernández, G. Bernabeu, and A. Sander (2016, June). Measuring the stellar wind parameters in IGR J17544-2619 and Vela X-1 constrains the accretion physics in supergiant fast X-ray transient and classical supergiant X-ray binaries. *A&A* 591, A26.

Gold, T. (1969, January). Rotating Neutron Stars and the Nature of Pulsars. *Nature* 221, 25–27.

Gosnell, N. M., E. M. Leiner, R. D. Mathieu, A. M. Geller, C. Knigge, A. Sills, and N. W. C. Leigh (2019, November). Constraining Mass-transfer Histories of Blue Straggler Stars with COS Spectroscopy of White Dwarf Companions. *ApJ* 885(1), 45.

Gosset, E., Y. Nazé, J. F. Claeskens, G. Rauw, J. M. Vreux, and H. Sana (2005, January). An XMM-Newton look at the Wolf-Rayet star WR 40. The star itself, its nebula and its neighbours. *A&A* 429, 685–704.

Gourgouliatos, K. N., T. S. Wood, and R. Hollerbach (2016, April). Magnetic field evolution in magnetar crusts through three-dimensional simulations. *Proceedings of the National Academy of Science* 113(15), 3944–3949.

Graczyk, D., G. Pietrzyński, B. Pilecki, I. B. Thompson, W. Gieren, P. Konorski, A. Udalski, and I. Soszyński (2013, February). The distance to the Small Magellanic Cloud from eclipsing binaries. In R. de Grijs (Ed.), *Advancing the Physics of Cosmic Distances*, Volume 289 of *IAU Symposium*, pp. 222–225.

Gräfener, G. (2021, March). Physics and evolution of the most massive stars in 30 Doradus. Mass loss, envelope inflation, and a variable upper stellar mass limit. *A&A* 647, A13.

Gräfener, G. and W. R. Hamann (2008, May). Mass loss from late-type WN stars and its Z-dependence. Very massive stars approaching the Eddington limit. *A&A* 482(3), 945–960.

Gräfener, G., S. P. Owocki, and J. S. Vink (2012, February). Stellar envelope inflation near the Eddington limit. Implications for the radii of Wolf-Rayet stars and luminous blue variables. *A&A* 538, A40.

Grassitelli, L., A. N. Chené, D. Sanyal, N. Langer, N. St-Louis, J. M. Bestenlehner, and L. Fossati (2016, May). Diagnostics of the unstable envelopes of Wolf-Rayet stars. *A&A* 590, A12.

Gray, D. F. (2005). *The Observation and Analysis of Stellar Photospheres*.

Grunhut, J. H., G. A. Wade, C. Neiner, M. E. Oksala, V. Petit, E. Alecian, D. A. Bohlen-der, J. C. Bouret, H. F. Henrichs, G. A. J. Hussain, O. Kochukhov, and MiMeS Collaboration (2017, February). The MiMeS survey of Magnetism in Massive Stars: magnetic analysis of the O-type stars. *MNRAS* 465(2), 2432–2470.

Guerrero, M. A. and Y.-H. Chu (2008, July). An X-Ray Survey of Wolf-Rayet Stars in the Magellanic Clouds. I. The Chandra ACIS Data Set. *ApJS* 177(1), 216–237.

Guzik, J. A. and C. C. Lovekin (2012, July). Pulsations and Hydrodynamics of Luminous Blue Variable Stars. *The Astronomical Review* 7(3), 13–47.

Haberl, F. and N. E. White (1990, September). The X-Ray Absorption Spectrum of VELA X-1. *ApJ* 361, 225.

Haiman, Z. and A. Loeb (1997, July). Signatures of Stellar Reionization of the Universe. *ApJ* 483(1), 21–37.

Hainich, R., D. Pasemann, H. Todt, T. Shenar, A. Sander, and W.-R. Hamann (2015, September). Wolf-Rayet stars in the Small Magellanic Cloud. I. Analysis of the single WN stars. *A&A* 581, A21.

Hamann, W. R., G. Gräfener, and A. Liermann (2006, Oct). The Galactic WN stars. Spectral analyses with line-blanketed model atmospheres versus stellar evolution models with and without rotation. *A&A* 457(3), 1015–1031.

Hamann, W.-R., G. Gräfener, A. Liermann, R. Hainich, A. A. C. Sander, T. Shenar, V. Ramachandran, H. Todt, and L. M. Oskinova (2019, April). The Galactic WN stars revisited. Impact of Gaia distances on fundamental stellar parameters. *arXiv e-prints*.

Hanawa, T. (1989, June). X-ray emission from accretion disks in low-mass X-ray binaries. *ApJ* 341, 948–954.

Hanuschik, R. W. (1996, April). On the structure of Be star disks. *A&A* 308, 170–179.

Harding, A. K. and M. Leventhal (1992, June). Can accretion onto isolated neutron stars produce γ -ray bursts? *Nature* 357(6377), 388–389.

Hastings, B., N. Langer, C. Wang, A. Schootemeijer, and A. P. Milone (2021, September). Stringent upper limit on Be star fractions produced by binary interaction. *A&A* 653, A144.

Hastings, B., C. Wang, and N. Langer (2020, January). The single star path to Be stars. *A&A* 633, A165.

Heger, A., C. L. Fryer, S. E. Woosley, N. Langer, and D. H. Hartmann (2003, July). How Massive Single Stars End Their Life. *ApJ* 591(1), 288–300.

Heger, A. and N. Langer (1996, Nov). Stationary hydrodynamic models of Wolf-Rayet stars with optically thick winds. *A&A* 315, 421–431.

Heinzeller, D. and W. J. Duschl (2007, January). On the Eddington limit in accretion discs. *MNRAS* 374(3), 1146–1154.

Heise, J. and J. in't Zand (2006, April). *Fast X-ray transients and X-ray flashes*, pp. 267–278.

Henneco, J., F. R. N. Schneider, and E. Laplace (2024, February). Contact tracing of binary stars: Pathways to stellar mergers. *A&A* 682, A169.

Herdeiro, C. A. R. and E. Radu (2015, June). Asymptotically flat black holes with scalar hair: A review. *International Journal of Modern Physics D* 24(9), 1542014–219.

Herold, H. (1979, May). Compton and Thomson scattering in strong magnetic fields. *Phys. Rev. D* 19, 2868–2875.

Hewish, A., S. J. Bell, J. D. H. Pilkington, P. F. Scott, and R. A. Collins (1968, February). Observation of a Rapidly Pulsating Radio Source. *Nature* 217, 709–713.

Higgins, E. R., A. A. C. Sander, J. S. Vink, and R. Hirschi (2021, August). Evolution of Wolf-Rayet stars as black hole progenitors. *MNRAS* 505(4), 4874–4889.

Hillier, D. J., R. P. Kudritzki, A. W. Pauldrach, D. Baade, J. P. Cassinelli, J. Puls, and J. H. M. M. Schmitt (1993, September). The 0.1-2.5-KEV X-Ray Spectrum of the O4F-STAR Zeta-Puppis. *A&A* 276, 117.

Hirai, R. and I. Mandel (2021, November). Conditions for accretion disc formation and observability of wind-accreting X-ray binaries. *PASA* 38, e056.

Hjellming, M. S. and R. F. Webbink (1987, July). Thresholds for rapid mass transfer in binary systems. I - Polytropic models. *ApJ* 318, 794–808.

Hjellming, R. M. and C. M. Wade (1971, November). Radio Spectrum of Cygnus X-1. *Nature* 234(5325), 138.

Humphreys, R. M. and K. Davidson (1979, September). Studies of luminous stars in nearby galaxies. III - Comments on the evolution of the most massive stars in the Milky Way and the Large Magellanic Cloud. *ApJ* 232, 409–420.

Iben, Icko, J. and M. Livio (1993, December). Common Envelopes in Binary Star Evolution. *PASP* 105, 1373.

Ignace, R., L. M. Osokinova, and C. Foulon (2000, Oct). Exospheric models for the X-ray emission from single Wolf-Rayet stars. *MNRAS* 318(1), 214–226.

Ikhsanov, N. R. (2001, March). On the duration of the subsonic propeller state of neutron stars in wind-fed mass-exchange close binary systems. *A&A* 368, L5–L7.

Ikhsanov, N. R., V. M. Larionov, and N. G. Beskrovnaya (2001, Jun). On the accretion flow geometry in A0535+26. *A&A* 372, 227–232.

Israel, G. L., A. Belfiore, L. Stella, P. Esposito, P. Casella, A. De Luca, M. Marelli, A. Papitto, M. Perri, S. Puccetti, G. A. R. Castillo, D. Salvetti, A. Tiengo, L. Zampieri, D. D'Agostino, J. Greiner, F. Haberl, G. Novara, R. Salvaterra, R. Turolla, M. Watson, J. Wilms, and A. Wolter (2017, February). An accreting pulsar with extreme properties drives an ultraluminous x-ray source in NGC 5907. *Science* 355, 817–819.

Israel, G. L., A. Papitto, P. Esposito, L. Stella, L. Zampieri, A. Belfiore, G. A. Rodríguez Castillo, A. De Luca, A. Tiengo, F. Haberl, J. Greiner, R. Salvaterra, S. Sandrelli, and G. Lisini (2017, March). Discovery of a 0.42-s pulsar in the ultraluminous X-ray source NGC 7793 P13. *MNRAS* 466, L48–L52.

Ivanova, N. (2011, April). Common Envelope: On the Mass and the Fate of the Remnant. *ApJ* 730(2), 76.

Ivanova, N. (2015). *Binary Evolution: Roche Lobe Overflow and Blue Stragglers*, pp. 179.

Ivanova, N. and S. Chaichenets (2011, April). Common Envelope: Enthalpy Consideration. *ApJ* 731(2), L36.

Izzard, R. G., P. D. Hall, T. M. Tauris, and C. A. Tout (2012, August). Common envelope evolution. In *Planetary Nebulae: An Eye to the Future*, Volume 283, pp. 95–102.

Janka, H.-T. (2012, November). Explosion Mechanisms of Core-Collapse Supernovae. *Annual Review of Nuclear and Particle Science* 62(1), 407–451.

Jansky, K. G. (1933, July). Radio Waves from Outside the Solar System. *Nature* 132, 66.

Jenke, P. A., M. H. Finger, C. A. Wilson-Hodge, and A. Camero-Arranz (2012, November). Orbital Decay and Evidence of Disk Formation in the X-Ray Binary Pulsar OAO 1657-415. *ApJ* 759, 124.

Jiang, L., S.-B. Qian, J. Zhang, and N. Liu (2015, December). 1SWASP J075102.16+342405.3: A deep overcontact binary system with a period under the short period cut-off. *PASJ* 67, 118.

Kaaret, P., H. Feng, and T. P. Roberts (2017, August). Ultraluminous X-Ray Sources. *ARA&A* 55, 303–341.

Kalogera, V. and R. F. Webbink (1996, February). Formation of Low-Mass X-Ray Binaries. I. Constraints on Hydrogen-rich Donors at the Onset of the X-Ray Phase. *ApJ* 458, 301.

Kaper, L., A. van der Meer, and F. Najarro (2006, October). VLT/UVES spectroscopy of Wray 977, the hypergiant companion to the X-ray pulsar `ASTROBJ;GX301-2`. *A&A* 457, 595–610.

Karino, S. (2016, December). The nature of the X-ray pulsar in M 31: An intermediate-mass X-ray binary? *PASJ* 68, 93.

Kelley, R. L., S. Rappaport, G. W. Clark, and L. D. Petro (1983, May). Orbital period changes in Centaurus X-3. *ApJ* 268, 790–799.

Kharchenko, N. V., R. D. Scholz, A. E. Piskunov, S. Röser, and E. Schilbach (2007, November). Astrophysical supplements to the ASCC-2.5: Ia. Radial velocities of ~ 55000 stars and mean radial velocities of 516 Galactic open clusters and associations. *Astronomische Nachrichten* 328(9), 889.

King, A. (1995). Accretion in close binaries. *X-ray Binaries*, 419–456.

King, A. (2001, September). Ultraluminous X-ray Sources in External Galaxies. In *Two Years of Science with Chandra*, pp. 1012.

King, A. and J.-P. Lasota (2019, March). No magnetars in ULXs. *arXiv e-prints*.

Kippenhahn, R. and A. Weigert (1967, January). Entwicklung in engen Doppelsternsystemen I. Massenaustausch vor und nach Beendigung des zentralen Wasserstoff-Brennens. *ZAp* 65, 251.

Kippenhahn, R. and A. Weigert (1990). *Stellar Structure and Evolution*.

Kippenhahn, R. and A. Weigert (1994). *Stellar Structure and Evolution*.

Kippenhahn, R., A. Weigert, and A. Weiss (2013). *Stellar Structure and Evolution*.

Klencki, J., A. Istrate, G. Nelemans, and O. Pols (2022, June). Partial-envelope stripping and nuclear-timescale mass transfer from evolved supergiants at low metallicity. *A&A* 662, A56.

Kobulnicky, H. A. and C. L. Fryer (2007, November). A New Look at the Binary Characteristics of Massive Stars. *ApJ* 670(1), 747–765.

Kobulnicky, H. A., D. C. Kiminki, M. J. Lundquist, J. Burke, J. Chapman, E. Keller, K. Lester, E. K. Rolen, E. Topel, A. Bhattacharjee, R. A. Smullen, C. A. Vargas Álvarez, J. C. Runnoe, D. A. Dale, and M. M. Brotherton (2014, August). Toward Complete Statistics of Massive Binary Stars: Penultimate Results from the Cygnus OB2 Radial Velocity Survey. *ApJS* 213(2), 34.

Köhler, K., N. Langer, A. de Koter, S. E. de Mink, P. A. Crowther, C. J. Evans, G. Gräfener, H. Sana, D. Sanyal, F. R. N. Schneider, and J. S. Vink (2015, January). The evolution of rotating very massive stars with LMC composition. *A&A* 573, A71.

Kolb, U. and H. Ritter (1990, September). A comparative study of the evolution of a close binary using a standard and an improved technique for computing mass transfer. *A&A* 236, 385–392.

Körding, E., H. Falcke, and S. Markoff (2002, January). Population X: Are the super-Eddington X-ray sources beamed jets in microblazars or intermediate mass black holes? *A&A* 382, L13–L16.

Kotake, K., K. Sato, and K. Takahashi (2006, April). Explosion mechanism, neutrino burst and gravitational wave in core-collapse supernovae. *Reports on Progress in Physics* 69(4), 971–1143.

Krawczynski, H. (2012, August). Tests of General Relativity in the Strong-gravity Regime Based on X-Ray Spectropolarimetric Observations of Black Holes in X-Ray Binaries. *ApJ* 754(2), 133.

Kreykenbohm, I., W. Coburn, J. Wilms, P. Kretschmar, R. Staubert, W. A. Heindl, and R. E. Rothschild (2002, November). Confirmation of two cyclotron lines in Vela X-1. *A&A* 395, 129–140.

Kreykenbohm, I., J. Wilms, P. Kretschmar, J. M. Torrejón, K. Pottschmidt, M. Hanké, A. Santangelo, C. Ferrigno, and R. Staubert (2008, December). High variability in Vela X-1: giant flares and off states. *A&A* 492(2), 511–525.

Kruckow, M. U. (2018, June). *Binary star population synthesis - Progenitors of gravitational wave driven mergers*. Ph. D. thesis, Rheinische Friedrich Wilhelms University of Bonn, Germany.

Kruckow, M. U., T. M. Tauris, N. Langer, M. Kramer, and R. G. Izzard (2018, December). Progenitors of gravitational wave mergers: binary evolution with the stellar grid-based code COMBINE. *MNRAS* 481(2), 1908–1949.

Kudritzki, R.-P. and J. Puls (2000, January). Winds from Hot Stars. *ARA&A* 38, 613–666.

Kurfürst, P., A. Feldmeier, and J. Krtička (2018, June). Two-dimensional modeling of density and thermal structure of dense circumstellar outflowing disks. *A&A* 613, A75.

Lai, D., F. A. Rasio, and S. L. Shapiro (1994, January). Hydrodynamic instability and coalescence of binary neutron stars. *ApJ* 420, 811–829.

Lamers, H. J. G. L. M. (1991). The Winds of O-Stars - Part Five - Tests of the Accuracy of the Radiation Driven Wind Models. In L. Crivellari, I. Hubeny, and D. G. Hummer (Eds.), *NATO Advanced Science Institutes (ASI) Series C*, Volume 341 of *NATO Advanced Science Institutes (ASI) Series C*, pp. 311.

Lamers, H. J. G. L. M. and J. P. Cassinelli (1999). *Introduction to Stellar Winds*.

Lamers, H. J. G. L. M. and E. L. Fitzpatrick (1988, January). The relationship between the Eddington limit, the observed upper luminosity limit for massive stars, and the luminous blue variables. *ApJ* 324, 279–287.

Lamers, H. J. G. L. M. and L. B. F. M. Waters (1987, August). Constraints for models of Be stars derived from UV and IRAS observations. *A&A* 182, 80–90.

Landau, L. D. and E. M. Lifschitz (1976). *Band 2 Klassische Feldtheorie*. Berlin, Boston: De Gruyter.

Langer, N. (2012, September). Presupernova Evolution of Massive Single and Binary Stars. *ARA&A* 50, 107–164.

Langer, N. and R. P. Kudritzki (2014, April). The spectroscopic Hertzsprung-Russell diagram. *A&A* 564, A52.

Langer, N., C. Schürmann, K. Stoll, P. Marchant, D. J. Lennon, L. Mahy, S. E. de Mink, M. Quast, W. Riedel, H. Sana, P. Schneider, A. Schootemeijer, C. Wang, L. A. Almeida, J. M. Bestenlehner, J. Bodensteiner, N. Castro, S. Clark, P. A. Crowther, P. Dufton, C. J. Evans, L. Fossati, G. Gräfener, L. Grassitelli, N. Grin, B. Hastings, A. Herrero, A. de Koter, A. Menon, L. Patrick, J. Puls, M. Renzo, A. A. C. Sander, F. R. N. Schneider, K. Sen, T. Shenar, S. Simón-Días, T. M. Tauris, F. Tramper, J. S. Vink, and X. T. Xu (2020, June). Properties of OB star-black hole systems derived from detailed binary evolution models. *A&A* 638, A39.

Lee, U., Y. Osaki, and H. Saio (1991, May). Viscous excretion discs around Be stars. *MNRAS* 250, 432–437.

Leonard, P. J. T. (1996, October). The Implications of the Binary Properties of the M67 Blue Stragglers. *ApJ* 470, 521.

Leutenegger, M. A., D. H. Cohen, J. Zsargó, E. M. Martell, J. P. MacArthur, S. P. Owocki, M. Gagné, and D. J. Hillier (2010, August). Modeling Broadband X-ray Absorption of Massive Star Winds. *ApJ* 719, 1767–1774.

Levine, A., S. Rappaport, J. E. Deeter, P. E. Boynton, and F. Nagase (1993, June). Discovery of orbital decay in SMC X-1. *ApJ* 410, 328–341.

Levine, A. M., S. A. Rappaport, and G. Zojcheski (2000, September). Orbital Decay in LMC X-4. *ApJ* 541, 194–202.

Lewin, W. H. G., J. van Paradijs, and E. P. J. van den Heuvel (1995). X-ray binaries. *X-ray Binaries*.

Li, X. and Z. Wang (1995, December). X-Ray Pulsars: Their Masses, Radii and Equations of State. *Ap&SS* 234(1), 39–48.

Lipunov, V. M. (1992). *Astrophysics of Neutron Stars*.

Liu, H., A. B. Abdikamalov, D. Ayzenberg, C. Bambi, T. Dauser, J. A. García, and S. Nampalliwar (2019, Jun). Testing the kerr hypothesis using x-ray reflection spectroscopy with nustar data of cygnus x-1 in the soft state. *Phys. Rev. D* 99, 123007.

Livio, M., N. Soker, M. de Kool, and G. J. Savonije (1986, February). On accretion of angular momentum from an inhomogeneous medium. *MNRAS* 218, 593–604.

Long, K. S., S. Dodorico, P. A. Charles, and M. A. Dopita (1981, June). Observations of the X-ray sources in the nearby SC galaxy M33. *ApJ* 246, L61–L64.

Long, M., M. M. Romanova, and R. V. E. Lovelace (2005, December). Locking of the Rotation of Disk-Accreting Magnetized Stars. *ApJ* 634(2), 1214–1222.

Lucy, L. B. and P. M. Solomon (1970, March). Mass Loss by Hot Stars. *ApJ* 159, 879.

Luri, X., A. G. A. Brown, L. M. Sarro, F. Arenou, C. A. L. Bailer-Jones, A. Castro-Ginard, J. de Bruijne, T. Prusti, C. Babusiaux, and H. E. Delgado (2018, August). Gaia Data Release 2. Using Gaia parallaxes. *A&A* 616, A9.

Lynden-Bell, D. (1969, August). Galactic Nuclei as Collapsed Old Quasars. *Nature* 223(5207), 690–694.

Mac Low, M.-M., D. S. Balsara, J. Kim, and M. A. de Avillez (2005, June). The Distribution of Pressures in a Supernova-driven Interstellar Medium. I. Magnetized Medium. *ApJ* 626(2), 864–876.

Madhusudhan, N., S. Rappaport, P. Podsiadlowski, and L. Nelson (2008, December). Models for the Observable System Parameters of Ultraluminous X-Ray Sources. *ApJ* 688, 1235–1249.

Maitra, C., S. Carpano, F. Haberl, and G. Vasilopoulos (2018, November). NGC 300 ULX1: A new ULX pulsar in NGC 300. *arXiv e-prints*.

Manousakis, A. and R. Walter (2011, May). The nature of the absorber in the INTEGRAL highly obscured sgHMXB IGR J17252-3616. *ArXiv e-prints*.

Manousakis, A., R. Walter, and J. M. Blondin (2012, November). Neutron star masses from hydrodynamical effects in obscured supergiant high mass X-ray binaries. *A&A* 547, A20.

Marchant, P., N. Langer, P. Podsiadlowski, T. M. Tauris, S. de Mink, I. Mandel, and T. J. Moriya (2017, August). Ultra-luminous X-ray sources and neutron-star-black-hole mergers from very massive close binaries at low metallicity. *A&A* 604, A55.

Marchant, P., N. Langer, P. Podsiadlowski, T. M. Tauris, and T. J. Moriya (2016, April). A new route towards merging massive black holes. *A&A* 588, A50.

Marchant, P., K. M. W. Pappas, M. Gallegos-Garcia, C. P. L. Berry, R. E. Taam, V. Kalogera, and P. Podsiadlowski (2021, June). The role of mass transfer and common envelope evolution in the formation of merging binary black holes. *A&A* 650, A107.

Marchenko, S. V., A. F. J. Moffat, and P. A. Crowther (2010, November). Population I Wolf-Rayet Runaway Stars: The Case of WR124 and its Expanding Nebula M1-67. *ApJ* 724(1), L90–L94.

Marchenko, S. V., A. F. J. Moffat, P. A. Crowther, A.-N. Chené, M. De Serres, P. R. J. Eenens, G. M. Hill, J. Moran, and T. Morel (2004, September). Hydrogen in the atmosphere of the evolved WN3 Wolf-Rayet star WR 3: defying an evolutionary paradigm? *MNRAS* 353, 153–161.

Marchenko, S. V., A. F. J. Moffat, K. A. van der Hucht, W. Seggewiss, H. Schrijver, B. Stenholm, I. Lundstrom, D. Y. A. Setia Gunawan, W. Sutantyo, E. P. J. van den Heuvel, J. P. de Cuyper, and A. E. Gomez (1998, March). Wolf-Rayet stars and O-star runaways with HIPPARCOS. II. Photometry. *A&A* 331, 1022–1036.

Marett-Crosby, M. (2013). *Twenty-Five Astronomical Observations That Changed the World*.

Martins, F., D. Schaerer, and D. J. Hillier (2005, June). A new calibration of stellar parameters of Galactic O stars. *A&A* 436(3), 1049–1065.

Massey, P. and P. S. Conti (1981, February). Spectroscopic studies of Wolf-rayet stars with absorption lines. V. HD 9974, a single WN3 ? *ApJ* 244, 173–178.

Matsuda, T., M. Inoue, and K. Sawada (1987, June). Spin-up and spin-down of an accreting compact object. *MNRAS* 226, 785–811.

McGill, M. A., T. A. A. Sigut, and C. E. Jones (2013, January). The Effect of Density on the Thermal Structure of Gravitationally Darkened Be Star Disks. *ApJS* 204(1), 2.

McKee, C. F. and E. C. Ostriker (2007, September). Theory of Star Formation. *ARA&A* 45(1), 565–687.

McLean, I. S. (1980, March). Periodic variations in the linear polarization of HD 50896 : a new Wolf-Rayet binary ? *ApJ* 236, L149–L153.

Medvedev, M. V. and N. Murray (2002, December). Hot Settling Accretion Flow onto a Spinning Black Hole. *ApJ* 581(1), 431–437.

Menon, A., N. Langer, S. E. de Mink, S. Justham, K. Sen, D. Szécsi, A. de Koter, M. Abdul-Masih, H. Sana, L. Mahy, and P. Marchant (2021, November). Detailed evolutionary models of massive contact binaries - I. Model grids and synthetic populations for the Magellanic Clouds. *MNRAS* 507(4), 5013–5033.

Mestel, L. (1968, January). Magnetic braking by a stellar wind-I. *MNRAS* 138, 359.

Meurs, E. J. A. and E. P. J. van den Heuvel (1989, December). The number of evolved early-type close binaries in the Galaxy. *A&A* 226, 88–107.

Miller-Jones, J. C. A., A. Bahramian, J. A. Orosz, I. Mandel, L. Gou, T. J. Maccarone, C. J. Neijssel, X. Zhao, J. Ziolkowski, M. J. Reid, P. Uttley, X. Zheng, D.-Y. Byun, R. Dodson, V. Grinberg, T. Jung, J.-S. Kim, B. Marcote, S. Markoff, M. J. Rioja, A. P. Rushton, D. M. Russell, G. R. Sivakoff, A. J. Tetarenko, V. Tudose, and J. Wilms (2021, March). Cygnus X-1 contains a 21–solar mass black hole—Implications for massive star winds. *Science* 371(6533), 1046–1049.

Misner, C. W., K. S. Thorne, and J. A. Wheeler (2017). *Gravitation*.

Misra, D., T. Fragos, T. M. Tauris, E. Zapartas, and D. R. Aguilera-Dena (2020, October). The origin of pulsating ultra-luminous X-ray sources: Low- and intermediate-mass X-ray binaries containing neutron star accretors. *A&A* 642, A174.

Misra, D., K. Kovlakas, T. Fragos, J. J. Andrews, S. S. Bavera, E. Zapartas, Z. Xing, A. Dotter, K. A. Rocha, P. M. Srivastava, and M. Sun (2024, February). Exploring the nature of ultra-luminous X-ray sources across stellar population ages using detailed binary evolution calculations. *A&A* 682, A69.

Moffat, A. F. J., R. Lamontagne, M. M. Shara, and H. A. McAlister (1986, Jun). On Wolf-Rayet stars with unshifted absorption lines. *AJ* 91, 1392–1399.

Morel, T., N. St-Louis, and S. V. Marchenko (1997, June). Optical Spectroscopy of EZ Canis Majoris: Indication for Large-Scale Structures in a Wolf-Rayet Wind. *ApJ* 482(1), 470–489.

Motch, C., M. W. Pakull, R. Soria, F. Grisé, and G. Pietrzyński (2014, October). A mass of less than 15 solar masses for the black hole in an ultraluminous X-ray source. *Nature* 514, 198–201.

Muijres, L. E., J. S. Vink, A. de Koter, P. E. Müller, and N. Langer (2012, January). Predictions for mass-loss rates and terminal wind velocities of massive O-type stars. *A&A* 537, A37.

Munoz, M., A. F. J. Moffat, G. M. Hill, T. Shenar, N. D. Richardson, H. Pablo, N. St-Louis, and T. Ramiaramanantsoa (2017, May). WR 148: identifying the companion of an extreme runaway massive binary*. *MNRAS* 467(3), 3105–3121.

Nagase, F., S. Hayakawa, N. Sato, K. Masai, and H. Inoue (1986, January). Circumstellar matter in the VELA X-1/HD 77581 system. *PASJ* 38, 547–569.

Nazé, Y., E. Gosset, and Q. Marechal (2021, March). New X-ray detections of known Wolf-Rayet stars. *MNRAS* 501(3), 4214–4225.

Nazé, Y., G. Rauw, H. Sana, and M. F. Corcoran (2013, July). X-ray properties of the young open clusters HM1 and IC 2944/2948. *A&A* 555, A83.

Negueruela, I. (2010, May). Stellar Wind Accretion in High-Mass X-Ray Binaries. In J. Martí, P. L. Luque-Escamilla, and J. A. Combi (Eds.), *High Energy Phenomena in Massive Stars*, Volume 422 of *Astronomical Society of the Pacific Conference Series*, pp. 57.

Novikov, I. D. and K. S. Thorne (1973, January). Astrophysics of black holes. In *Black Holes (Les Astres Occlus)*, pp. 343–450.

O'Connor, E. and C. D. Ott (2011, April). Black Hole Formation in Failing Core-Collapse Supernovae. *ApJ* 730(2), 70.

Oda, M., P. Gorenstein, H. Gursky, E. Kellogg, E. Schreier, H. Tananbaum, and R. Giacconi (1971, May). X-Ray Pulsations from Cygnus X-1 Observed from UHURU. *ApJ* 166, L1.

Odaka, H., D. Khangulyan, Y. T. Tanaka, S. Watanabe, T. Takahashi, and K. Makishima (2013, April). Short-term Variability of X-Rays from Accreting Neutron Star Vela X-1. I. Suzaku Observations. *ApJ* 767(1), 70.

Orosz, J. A., J. E. McClintock, J. P. Aufdenberg, R. A. Remillard, M. J. Reid, R. Narayan, and L. Gou (2011, Dec). The Mass of the Black Hole in Cygnus X-1. *ApJ* 742(2), 84.

Osokinova, L. M. (2015, January). X-ray emission from single WR stars. In W.-R. Hamann, A. Sander, and H. Todt (Eds.), *Wolf-Rayet Stars*, pp. 295–300.

Osokinova, L. M., A. Feldmeier, and P. Kretschmar (2012, April). Clumped stellar winds in supergiant high-mass X-ray binaries: X-ray variability and photoionization. *MNRAS* 421(4), 2820–2831.

Osokinova, L. M., K. G. Gayley, W. R. Hamann, D. P. Huenemoerder, R. Ignace, and A. M. T. Pollock (2012, March). High-resolution X-Ray Spectroscopy Reveals the Special Nature of Wolf-Rayet Star Winds. *ApJ* 747(2), L25.

Packet, W. (1981, September). On the spin-up of the mass accreting component in a close binary system. *A&A* 102(1), 17–19.

Paczynski, B. (1976, January). Common Envelope Binaries. In P. Eggleton, S. Mitton, and J. Whelan (Eds.), *Structure and Evolution of Close Binary Systems*, Volume 73, pp. 75.

Padovani, P. and M. Cirasuolo (2023, January). The Extremely Large Telescope. *Contemporary Physics* 64(1), 47–64.

Pagel, B. E. J. (2009). *Nucleosynthesis and Chemical Evolution of Galaxies*.

Pauldrach, A. (1987, September). Radiation driven winds of hot luminous stars. III - Detailed statistical equilibrium calculations for hydrogen to zinc. *A&A* 183, 295–313.

Pauli, D., N. Langer, D. R. Aguilera-Dena, C. Wang, and P. Marchant (2022, November). A synthetic population of Wolf-Rayet stars in the LMC based on detailed single and binary star evolution models. *A&A* 667, A58.

Pavlovskii, K. and N. Ivanova (2015, June). Mass transfer from giant donors. *MNRAS* 449, 4415–4427.

Pavlovskii, K., N. Ivanova, K. Belczynski, and K. X. Van (2017, February). Stability of mass transfer from massive giants: double black hole binary formation and ultraluminous X-ray sources. *MNRAS* 465, 2092–2100.

Pejcha, O. (2020). The Explosion Mechanism of Core-Collapse Supernovae and Its Observational Signatures. In *Reviews in Frontiers of Modern Astrophysics; From Space Debris to Cosmology*, pp. 189–211.

Perna, R., E. Bozzo, and L. Stella (2006, March). On the Spin-up/Spin-down Transitions in Accreting X-Ray Binaries. *ApJ* 639(1), 363–376.

Peters, P. C. (1964, November). Gravitational Radiation and the Motion of Two Point Masses. *Physical Review* 136(4B), 1224–1232.

Pietrzyński, G., D. Graczyk, W. Gieren, I. B. Thompson, B. Pilecki, A. Udalski, I. Soszyński, S. Kozłowski, P. Konorski, K. Suchomska, G. Bono, P. G. P. Moroni, S. Villanova, N. Nardetto, F. Bresolin, R. P. Kudritzki, J. Storm, A. Gallenne, R. Smolec, D. Minniti, M. Kubiak, M. K. Szymański, R. Poleski, Ł. Wyrzykowski, K. Ulaczyk, P. Pietrukowicz, M. Górska, and P. Karczmarek (2013, March). An eclipsing-binary distance to the Large Magellanic Cloud accurate to two per cent. *Nature* 495, 76–79.

Pittard, J. M. and B. Dawson (2018, July). Colliding stellar winds structure and X-ray emission. *MNRAS* 477, 5640–5645.

Podsiadlowski, P. (2001, January). Common-Envelope Evolution and Stellar Mergers. In P. Podsiadlowski, S. Rappaport, A. R. King, F. D'Antona, and L. Burderi (Eds.), *Evolution of Binary and Multiple Star Systems*, Volume 229 of *Astronomical Society of the Pacific Conference Series*, pp. 239.

Pollock, A. M. T. (1989, December). Comments on the Einstein X-Ray Variability of HD 50896 and Other Wolf-Rayet Stars. *ApJ* 347, 409.

Pols, O. R., J. Cote, L. B. F. M. Waters, and J. Heise (1991, January). The formation of Be stars through close binary evolution. *A&A* 241, 419.

Portegies Zwart, S. F., D. Pooley, and W. H. G. Lewin (2002, August). A Dozen Colliding-Wind X-Ray Binaries in the Star Cluster R136 in the 30 Doradus Region. *ApJ* 574, 762–770.

Porter, J. M. and T. Rivinius (2003, October). Classical Be Stars. *PASP* 115(812), 1153–1170.

Potter, A. T. and C. A. Tout (2010, February). Magnetic field evolution of white dwarfs in strongly interacting binary star systems. *MNRAS* 402, 1072–1080.

Poutanen, J., G. Lipunova, S. Fabrika, A. G. Butkevich, and P. Abolmasov (2007, May). Supercritically accreting stellar mass black holes as ultraluminous X-ray sources. *MNRAS* 377(3), 1187–1194.

Poveda, A., J. Ruiz, and C. Allen (1967, April). Run-away Stars as the Result of the Gravitational Collapse of Proto-stellar Clusters. *Boletin de los Observatorios Tonantzintla y Tacubaya* 4, 86–90.

Prandtl, L. (1925, January). 7. Bericht über Untersuchungen zur ausgebildeten Turbulenz. *Zeitschrift Angewandte Mathematik und Mechanik* 5(2), 136–139.

Pratt, J. P. and P. A. Strittmatter (1976, February). Slow mass transfer in semidetached binaries. *ApJ* 204, L29–L33.

Predehl, P., R. Andritschke, V. Arefiev, V. Babyshkin, O. Batanov, W. Becker, H. Böhringer, A. Bogomolov, T. Boller, K. Borm, W. Bornemann, H. Bräuninger, M. Brüggen, H. Brunner, M. Brusa, E. Bulbul, M. Buntov, V. Burwitz, W. Burkert, N. Clerc, E. Churazov, D. Coutinho, T. Dauser, K. Dennerl, V. Doroshenko, J. Eder, V. Emberger, T. Eraerts, A. Finoguenov, M. Freyberg, P. Friedrich, S. Friedrich, M. Fürmetz, A. Georgakakis, M. Gilfanov, S. Granato, C. Grossberger, A. Gueguen, P. Gureev, F. Haberl, O. Hälker, G. Hartner, G. Hasinger, H. Huber, L. Ji, A. v. Kienlin, W. Kink, F. Korotkov, I. Kreykenbohm, G. Lamer, I. Lomakin, I. Lapshov, T. Liu, C. Maitra, N. Meidinger, B. Menz, A. Merloni, T. Mernik, B. Mican, J. Mohr, S. Müller, K. Nandra, V. Nazarov, F. Pacaud, M. Pavlinsky, E. Perinati, E. Pfeffermann, D. Pietschner, M. E. Ramos-Ceja, A. Rau, J. Reiffers, T. H. Reiprich, J. Robrade, M. Salvato, J. Sanders, A. Santangelo, M. Sasaki, H. Scheuerle, C. Schmid, J. Schmitt, A. Schwone, A. Shirshakov, M. Steinmetz, I. Stewart, L. Strüder, R. Sunyaev, C. Tenzner, L. Tiedemann, J. Trümper, V. Voron, P. Weber, J. Wilms, and V. Yaroshenko (2021, March). The eROSITA X-ray telescope on SRG. *A&A* 647, A1.

Prialnik, D. (2009). *An Introduction to the Theory of Stellar Structure and Evolution*.

Prilutskii, O. F. and V. V. Usov (1976, February). X rays from Wolf-Rayet binaries. *Soviet Ast.* 20, 2.

Prinja, R. K., M. J. Barlow, and I. D. Howarth (1990, October). Terminal Velocities for a Large Sample of O Stars, B Supergiants, and Wolf-Rayet Stars. *ApJ* 361, 607.

Puls, J., R. P. Kudritzki, A. Herrero, A. W. A. Pauldrach, S. M. Haser, D. J. Lennon, R. Gabler, S. A. Voels, J. M. Vilchez, S. Wachter, and A. Feldmeier (1996, Jan). O-star mass-loss and wind momentum rates in the Galaxy and the Magellanic Clouds Observations and theoretical predictions. *A&A* 305, 171.

Qian, S.-B., L.-Y. Zhu, L. Liu, X.-D. Zhang, X.-D. Shi, J.-J. He, and J. Zhang (2020, October). Contact binaries at different evolutionary stages. *Research in Astronomy and Astrophysics* 20(10), 163.

Quast, M., N. Langer, and T. M. Tauris (2019, August). Mass transfer on a nuclear timescale in models of supergiant and ultra-luminous X-ray binaries. *A&A* 628, A19.

Ramírez-Agudelo, O. H., H. Sana, A. de Koter, F. Tramper, N. J. Grin, F. R. N. Schneider, N. Langer, J. Puls, N. Markova, J. M. Bestenlehner, N. Castro, P. A. Crowther, C. J. Evans, M. García, G. Gräfener, A. Herrero, B. van Kempen, D. J. Lennon, J. Maíz Apellániz, F. Najarro, C. Sabín-Sanjulián, S. Simón-Díaz, W. D. Taylor, and J. S. Vink (2017, April). The VLT-FLAMES Tarantula Survey . XXIV. Stellar properties of the O-type giants and supergiants in 30 Doradus. *A&A* 600, A81.

Rappaport, S., R. Doxsey, and W. Zaumen (1971, September). A Search for X-Ray Pulsations from Cygnus X-1. *ApJ* 168, L43.

Rauw, G. and Y. Nazé (2016, September). X-ray emission from interacting wind massive binaries: A review of 15 years of progress. *Advances in Space Research* 58(5), 761–781.

Rawls, M. L., J. A. Orosz, J. E. McClintock, M. A. P. Torres, C. D. Bailyn, and M. M. Buxton (2011, March). Refined Neutron Star Mass Determinations for Six Eclipsing X-Ray Pulsar Binaries. *ApJ* 730(1), 25.

Regev, O., O. M. Umurhan, and P. A. Yecko (2016). *Modern Fluid Dynamics for Physics and Astrophysics* - (1st ed. 2016 ed.). Berlin, Heidelberg: Springer.

Reig, P. (2011, March). Be/X-ray binaries. *Ap&SS* 332, 1–29.

Reig, P. and P. Roche (1999, June). Discovery of two new persistent Be/X-ray pulsar systems. *MNRAS* 306(1), 100–106.

Repetto, S., A. P. Igoshev, and G. Nelemans (2017, May). The Galactic distribution of X-ray binaries and its implications for compact object formation and natal kicks. *MNRAS* 467(1), 298–310.

Rezzolla, L., E. R. Most, and L. R. Weih (2018, January). Using Gravitational-wave Observations and Quasi-universal Relations to Constrain the Maximum Mass of Neutron Stars. *ApJ* 852(2), L25.

Ridgway, S. T., R. R. Joyce, N. M. White, and R. F. Wing (1980, Jan). Effective temperatures of late-type stars : the field giants from K0 to M6. *ApJ* 235, 126–137.

Rivinius, T., A. C. Carciofi, and C. Martayan (2013, October). Classical Be stars. Rapidly rotating B stars with viscous Keplerian decretion disks. *A&A Rev.* 21, 69.

Robert, C., A. F. J. Moffat, L. Drissen, R. Lamontagne, W. Seggewiss, V. S. Niemela, M. A. Cerruti, P. Barrett, J. Bailey, J. Garcia, and S. Tapia (1992, September). Photometry, Polarimetry, Spectroscopy, and Spectropolarimetry of the Enigmatic Wolf-Rayet Star EZ Canis Majoris. *ApJ* 397, 277.

Roberts, W. W. (1969, October). Large-Scale Shock Formation in Spiral Galaxies and its Implications on Star Formation. *ApJ* 158, 123.

Rubin, B. C., M. H. Finger, B. A. Harmon, W. S. Paciesas, G. J. Fishman, R. B. Wilson, C. A. Wilson, M. N. Brock, M. S. Briggs, G. N. Pendleton, L. R. Cominsky, and M. S. Roberts (1996, March). Observations of 4U 1700-37 with BATSE. *ApJ* 459, 259.

Ruiz, M., S. L. Shapiro, and A. Tsokaros (2018, January). GW170817, general relativistic magnetohydrodynamic simulations, and the neutron star maximum mass. *Phys. Rev. D* 97(2), 021501.

Russell, H. N. (1914, May). Relations Between the Spectra and Other Characteristics of the Stars. *Popular Astronomy* 22, 275–294.

Ruszkowski, M. and M. C. Begelman (2003, March). Eddington Limit and Radiative Transfer in Highly Inhomogeneous Atmospheres. *ApJ* 586, 384–388.

Sadowski, A., M. Bursa, M. Abramowicz, W. Kluźniak, J. P. Lasota, R. Moderski, and M. Safarzadeh (2011, August). Spinning up black holes with super-critical accretion flows. *A&A* 532, A41.

Safi Harb, S., H. Ogelman, and K. Dennerl (1996, January). Orbital Decay in the X-Ray Binary LMC X-4. *ApJ* 456, L37.

Sahu, K. C., J. Anderson, S. Casertano, H. E. Bond, A. Udalski, M. Dominik, A. Calamida, A. Bellini, T. M. Brown, M. Rejkuba, V. Bajaj, N. Kains, H. C. Ferguson, C. L. Fryer, P. Yock, P. Mróz, S. Kozłowski, P. Pietrukowicz, R. Poleski, J. Skowron, I. Soszyński, M. K. Szymański, K. Ulaczyk, Ł. Wyrzykowski, R. K. Barry, D. P. Bennett, I. A. Bond, Y. Hirao, S. I. Silva, I. Kondo, N. Koshimoto, C. Ranc, N. J. Rattenbury, T. Sumi, D. Suzuki, P. J. Tristram, A. Vandorou, J.-P. Beaulieu, J.-B. Marquette, A. Cole, P. Fouqué, K. Hill, S. Dieters, C. Coutures, D. Dominis-Prester, C. Bennett, E. Bachelet, J. Menzies, M. Albrow, K. Pollard, A. Gould, J. C. Yee, W. Allen, L. A. Almeida, G. Christie, J. Drummond, A. Gal-Yam, E. Gorbikov, F. Jablonski, C.-U. Lee, D. Maoz, I. Manulis, J. McCormick, T. Natusch, R. W. Pogge, Y. Shvartzvald, U. G. Jørgensen, K. A. Alsubai, M. I. Andersen, V. Bozza, S. C. Novati, M. Burgdorf, T. C. Hinse, M. Hundertmark, T.-O. Husser, E. Kerins, P. Longa-Peña, L. Mancini, M. Penny, S. Rahvar, D. Ricci, S. Sajadian, J. Skottfelt, C. Snodgrass, J. Southworth, J. Tregloan-Reed, J. Wambsganss, O. Wertz, Y. Tsapras, R. A. Street, D. M. Bramich, K. Horne, I. A. Steele, and RoboNet Collaboration (2022, July). An Isolated Stellar-mass Black Hole Detected through Astrometric Microlensing. *ApJ* 933(1), 83.

Sako, M., D. A. Liedahl, S. M. Kahn, and F. Paerels (1999, November). The X-Ray Spectrum and Global Structure of the Stellar Wind in VELA X-1. *ApJ* 525(2), 921–934.

Salgado, J., J. González-Núñez, R. Gutiérrez-Sánchez, J. C. Segovia, J. Durán, J. L. Hernández, and C. Arviset (2017, October). The ESA Gaia Archive: Data Release 1. *Astronomy and Computing* 21, 22–26.

Sana, H., A. de Koter, S. E. de Mink, P. R. Dunstall, C. J. Evans, V. Hénault-Brunet, J. Maíz Apellániz, O. H. Ramírez-Agudelo, W. D. Taylor, N. R. Walborn, J. S. Clark, P. A. Crowther, A. Herrero, M. Gieles, N. Langer, D. J. Lennon, and J. S. Vink (2013, February). The VLT-FLAMES Tarantula Survey. VIII. Multiplicity properties of the O-type star population. *A&A* 550, A107.

Sana, H., S. E. de Mink, A. de Koter, N. Langer, C. J. Evans, M. Gieles, E. Gosset, R. G. Izzard, J. B. Le Bouquin, and F. R. N. Schneider (2012, July). Binary Interaction Dominates the Evolution of Massive Stars. *Science* 337(6093), 444.

Sana, H., E. Gosset, and C. J. Evans (2009, December). The massive star binary fraction in young open clusters - II. NGC6611 (Eagle Nebula). *MNRAS* 400(3), 1479–1492.

Sana, H., E. Gosset, Y. Nazé, G. Rauw, and N. Linder (2008, May). The massive star binary fraction in young open clusters - I. NGC 6231 revisited. *MNRAS* 386(1), 447–460.

Sana, H., G. James, and E. Gosset (2011, September). The massive star binary fraction in young open clusters - III. IC 2944 and the Cen OB2 association. *MNRAS* 416(2), 817–831.

Sana, H., J. B. Le Bouquin, S. Lacour, J. P. Berger, G. Duvert, L. Gauchet, B. Norris, J. Olofsson, D. Pickel, G. Zins, O. Absil, A. de Koter, K. Kratter, O. Schnurr, and H. Zinnecker (2014, November). Southern Massive Stars at High Angular Resolution: Observational Campaign and Companion Detection. *ApJS* 215(1), 15.

Sander, A., H. Todt, R. Hainich, and W. R. Hamann (2014, March). The Wolf-Rayet stars in M 31. I. Analysis of the late-type WN stars. *A&A* 563, A89.

Sander, A. A. C., F. Fürst, P. Kretschmar, L. M. Oskinova, H. Todt, R. Hainich, T. Shenar, and W.-R. Hamann (2018, February). Coupling hydrodynamics with comoving frame radiative transfer. II. Stellar wind stratification in the high-mass X-ray binary Vela X-1. *A&A* 610, A60.

Sanyal, D., L. Grassitelli, N. Langer, and J. M. Bestenlehner (2015, August). Massive main-sequence stars evolving at the Eddington limit. *A&A* 580, A20.

Savonije, G. J. (1978, January). Roche-lobe overflow in X-ray binaries. *A&A* 62, 317–338.

Savonije, G. J. (1979, January). Roche-lobe overflow and massive X-ray binary systems. *A&A* 71, 352–358.

Schafer, R. A. (1991). *XSPEC, an x-ray spectral fitting package : version 2 of the user's guide.*

Schmutz, W. and G. Koenigsberger (2019, April). Long uninterrupted photometric observations of the Wolf-Rayet star EZ CMa by the Toronto BRITE satellite reveal a very fast apsidal motion. *A&A* 624, L3.

Schneider, F. R. N., N. Langer, A. de Koter, I. Brott, R. G. Izzard, and H. H. B. Lau (2014, Oct). Bonnsai: a Bayesian tool for comparing stars with stellar evolution models. *A&A* 570, A66.

Schootemeijer, A. and N. Langer (2018, March). Wolf-Rayet stars in the Small Magellanic Cloud as testbed for massive star evolution. *A&A* 611, A75.

Schootemeijer, A., T. Shenar, N. Langer, N. Grin, H. Sana, G. G. C. Schürmann, C. Wang, and X. T. Xu (2024, June). An absence of binary companions to Wolf-Rayet stars in the Small Magellanic Cloud: implications for mass loss and black hole masses at low metallicity. *arXiv e-prints*, arXiv:2406.01420.

Schulz, N. S., W. Cui, C. R. Canizares, H. L. Marshall, J. C. Lee, J. M. Miller, and W. H. G. Lewin (2002, February). The First High-Resolution X-Ray Spectrum of Cygnus X-1: Soft X-Ray Ionization and Absorption. *ApJ* 565(2), 1141–1149.

Schwarzschild, K. (1906, January). On the equilibrium of the Sun’s atmosphere. *Nachrichten von der Königlichen Gesellschaft der Wissenschaften zu Göttingen. Math.-phys. Klasse* 195, 41–53.

Schwarzschild, K. (1916, January). Über das Gravitationsfeld eines Massenpunktes nach der Einsteinschen Theorie. *Sitzungsberichte der Königlich Preussischen Akademie der Wissenschaften*, 189–196.

Sen, K., I. El Mellah, N. Langer, X.-T. Xu, M. Quast, and D. Pauli (2024, June). Whispering in the dark: faint X-ray emission from black holes with OB star companions. *arXiv e-prints*, arXiv:2406.08596.

Sen, K., X. T. Xu, N. Langer, I. El Mellah, C. Schürmann, and M. Quast (2021, August). X-ray emission from BH+O star binaries expected to descend from the observed galactic WR+O binaries. *A&A* 652, A138.

Seward, F. D., W. R. Forman, R. Giacconi, R. E. Griffiths, J. Harnden, F. R., C. Jones, and J. P. Pye (1979, November). X-rays from Eta Carinae and the surrounding nebula. *ApJ* 234, L55–L58.

Shakura, N. I. (1973, April). Disk Model of Gas Accretion on a Relativistic Star in a Close Binary System. *Soviet Ast.* 16, 756.

Shakura, N. I., K. A. Postnov, A. Y. Kochetkova, and L. Hjalmarsdotter (2014, January). Theory of wind accretion. In *European Physical Journal Web of Conferences*, Volume 64 of *European Physical Journal Web of Conferences*, pp. 02001.

Shakura, N. I. and R. A. Sunyaev (1973, January). Black holes in binary systems. Observational appearance. *A&A* 24, 337–355.

Shao, Y. and X.-D. Li (2019, November). Population Synthesis of Black Hole Binaries with Normal-star Companions. I. Detached Systems. *ApJ* 885(2), 151.

Shao, Y. and X.-D. Li (2020, August). Population Synthesis of Black Hole X-Ray Binaries. *ApJ* 898(2), 143.

Shapiro, S. L. and A. P. Lightman (1976, March). Black holes in X-ray binaries - Marginal existence and rotation reversals of accretion disks. *ApJ* 204, 555–560.

Shapiro, S. L. and S. A. Teukolsky (1986). *Black Holes, White Dwarfs and Neutron Stars: The Physics of Compact Objects*.

Shenar, T., H. Sana, L. Mahy, K. El-Badry, P. Marchant, N. Langer, C. Hawcroft, M. Fabry, K. Sen, L. A. Almeida, M. Abdul-Masih, J. Bodensteiner, P. A. Crowther, M. Gieles, M. Gromadzki, V. Hénault-Brunet, A. Herrero, A. d. Kotter, P. Iwanek, S. Kozłowski, D. J. Lennon, J. M. Apellániz, P. Mróz, A. F. J. Moffat, A. Picco, P. Pietrukowicz, R. Poleski, K. Rybicki, F. R. N. Schneider, D. M. Skowron, J. Skowron, I. Soszyński, M. K. Szymański, S. Toonen, A. Udalski, K. Ulaczyk, J. S. Vink, and M. Wrona (2022, July). An X-ray-quiet black hole born with a negligible kick in a massive binary within the Large Magellanic Cloud. *Nature Astronomy*.

Shenar, T., H. Sana, L. Mahy, J. Maiz Apellániz, P. A. Crowther, M. Gromadzki, A. Herrero, N. Langer, P. Marchant, F. R. N. Schneider, K. Sen, I. Soszynski, and S. Toonen (2022, July). The Tarantula Massive Binary Monitoring VI: Characterisation of hidden companions in 51 single-lined O-type binaries, a flat mass-ratio distribution, and black-hole binary candidates. *arXiv e-prints*, arXiv:2207.07674.

Shimura, T. and F. Takahara (1995, June). On the spectral hardening factor of the X-ray emission from accretion disks in black hole candidates. *ApJ* 445, 780–788.

Shklovsky, I. S. (1967, April). On the Nature of the Source of X-Ray Emission of Sco XR-1. *ApJ* 148, L1.

Shore, S. N. (1994, January). Observations and physical processes in binary stars. In *Saas-Fee Advanced Course 22: Interacting Binaries*, pp. 1–133.

Siedentopf, H. (1935, June). Konvektion in Sternatmosphären. III. *Astronomische Nachrichten* 255(9), 157.

Skinner, S., M. Güdel, W. Schmutz, and S. Zhekov (2006, August). X-ray Observations of Binary and Single Wolf-Rayet Stars with XMM-Newton and Chandra. *Ap&SS* 304(1-4), 97–99.

Skinner, S. L., W. Schmutz, M. Güdel, and S. Zhekov (2019, January). High energy processes in Wolf-Rayet stars. *Astronomische Nachrichten* 340(50), 50–53.

Skinner, S. L., W. Schmutz, M. Güdel, and S. A. Zhekov (2021, May). XMM-Newton X-Ray Observations of the Unusual Wolf-Rayet Star WR 66. *Research Notes of the American Astronomical Society* 5(5), 125.

Skinner, S. L., S. A. Zhekov, M. Güdel, and W. Schmutz (2002, November). XMM-Newton and Very Large Array Observations of the Variable Wolf-Rayet Star EZ Canis Majoris: Evidence for a Close Companion? *ApJ* 579(2), 764–773.

Skinner, S. L., S. A. Zhekov, M. Güdel, W. Schmutz, and K. R. Sokal (2012, May). New X-Ray Detections of WNL Stars. *AJ* 143(5), 116.

Skumanich, A. (1972, February). Time Scales for Ca II Emission Decay, Rotational Braking, and Lithium Depletion. *ApJ* 171, 565.

Smartt, S. J., J. J. Eldridge, R. M. Crockett, and J. R. Maund (2009, May). The death of massive stars - I. Observational constraints on the progenitors of Type II-P supernovae. *MNRAS* 395(3), 1409–1437.

Smith, A. R. H. and R. B. Mann (2014, April). Looking inside a black hole. *Classical and Quantum Gravity* 31(8), 082001.

Smith, N. (2014, August). Mass Loss: Its Effect on the Evolution and Fate of High-Mass Stars. *ARA&A* 52, 487–528.

Smith, N. and S. P. Owocki (2006, July). On the Role of Continuum-driven Eruptions in the Evolution of Very Massive Stars and Population III Stars. *ApJ* 645(1), L45–L48.

Soberman, G. E., E. S. Phinney, and E. P. J. van den Heuvel (1997, November). Stability criteria for mass transfer in binary stellar evolution. *A&A* 327, 620–635.

Socrates, A. and S. W. Davis (2006, November). Ultraluminous X-Ray Sources Powered by Radiatively Efficient Two-Phase Super-Eddington Accretion onto Stellar-Mass Black Holes. *ApJ* 651, 1049–1058.

Sonoi, T., H.-G. Ludwig, M.-A. Dupret, J. Montalbán, R. Samadi, K. Belkacem, E. Cafau, and M.-J. Goupil (2019, January). Calibration of mixing-length parameter α for MLT and FST models by matching with CO⁵BOLD models. *A&A* 621, A84.

Sridhar, N., L. Sironi, and A. M. Beloborodov (2021, November). Comptonization by reconnection plasmoids in black hole coronae I: Magnetically dominated pair plasma. *MNRAS* 507(4), 5625–5640.

Stella, L., N. E. White, and R. Rosner (1986, September). Intermittent stellar wind accretion and the long-term activity of Population I binary systems containing an X-ray pulsar. *ApJ* 308, 669–679.

Stevens, I. R., J. M. Blondin, and A. M. T. Pollock (1992, February). Colliding winds from early-type stars in binary systems. *ApJ* 386, 265–287.

Stevens, I. R. and A. J. Willis (1988, October). The expected X-ray luminosity of HD 50896. *MNRAS* 234, 783–797.

Struve, O. (1931, March). On the Origin of Bright Lines in Spectra of Stars of Class B. *ApJ* 73, 94.

Sugizaki, M., K. Mitsuda, H. Kaneda, K. Matsuzaki, S. Yamauchi, and K. Koyama (2001, June). VizieR Online Data Catalog: ASCA Galactic Plane Survey faint X-ray sources (Sugizak+, 2001). *VizieR Online Data Catalog*, J/ApJS/134/77.

Sukhbold, T., T. Ertl, S. E. Woosley, J. M. Brown, and H.-T. Janka (2016, April). Core-collapse Supernovae from 9 to 120 Solar Masses Based on Neutrino-powered Explosions. *ApJ* 821, 38.

Swartz, D. A., K. K. Ghosh, A. F. Tennant, and K. Wu (2004, October). The Ultraluminous X-Ray Source Population from the Chandra Archive of Galaxies. *ApJS* 154(2), 519–539.

Szécsi, D., N. Langer, S.-C. Yoon, D. Sanyal, S. de Mink, C. J. Evans, and T. Dermine (2015, September). Low-metallicity massive single stars with rotation. Evolutionary models applicable to I Zwicky 18. *A&A* 581, A15.

Taam, R. E. and P. M. Ricker (2010, March). Common envelope evolution. *New A Rev.* 54(3-6), 65–71.

Taam, R. E. and E. L. Sandquist (2000, January). Common Envelope Evolution of Massive Binary Stars. *ARA&A* 38, 113–141.

Taani, A., S. Karino, L. Song, C. Zhang, and S. Chaty (2018, August). A New Set of Parameters of High-Mass X-ray Binaries Found with their Cyclotron Lines. *arXiv e-prints*.

Tauris, T. M. (2001, January). On the Pre-RLO Spin-Orbit Couplings in LMXBs. In P. Podsiadlowski, S. Rappaport, A. R. King, F. D’Antona, and L. Burderi (Eds.), *Evolution of Binary and Multiple Star Systems*, Volume 229 of *Astronomical Society of the Pacific Conference Series*, pp. 145.

Tauris, T. M. (2012, Feb). Spin-Down of Radio Millisecond Pulsars at Genesis. *Science* 335(6068), 561.

Tauris, T. M., M. Kramer, P. C. C. Freire, N. Wex, H.-T. Janka, N. Langer, P. Podsiadlowski, E. Bozzo, S. Chaty, M. U. Kruckow, E. P. J. van den Heuvel, J. Antoniadis, R. P. Breton, and D. J. Champion (2017, September). Formation of Double Neutron Star Systems. *ApJ* 846, 170.

Tauris, T. M. and G. J. Savonije (1999, October). Formation of millisecond pulsars. I. Evolution of low-mass X-ray binaries with $P_{\text{orb}} \gtrsim 2$ days. *A&A* 350, 928–944.

Tauris, T. M. and G. J. Savonije (2001, January). Spin-Orbit Coupling in X-ray Binaries. In C. Kouveliotou, J. Ventura, and E. van den Heuvel (Eds.), *The Neutron Star - Black Hole Connection*, Volume 567, pp. 337.

Tauris, T. M. and R. J. Tacke (1998, February). Runaway velocities of stellar components originating from disrupted binaries via asymmetric supernova explosions. *A&A* 330, 1047–1059.

Tauris, T. M. and E. P. J. van den Heuvel (2006, April). *Formation and evolution of compact stellar X-ray sources*, pp. 623–665.

Tauris, T. M. and E. P. J. van den Heuvel (2023). *Physics of Binary Star Evolution. From Stars to X-ray Binaries and Gravitational Wave Sources*.

Tauris, T. M., E. P. J. van den Heuvel, and G. J. Savonije (2000, February). Formation of Millisecond Pulsars with Heavy White Dwarf Companions: Extreme Mass Transfer on Subthermal Timescales. *ApJ* 530(2), L93–L96.

Thompson, T. A., A. Burrows, and P. A. Pinto (2003, July). Shock Breakout in Core-Collapse Supernovae and Its Neutrino Signature. *ApJ* 592(1), 434–456.

Timmes, F. X., S. E. Woosley, and T. A. Weaver (1996, February). The Neutron Star and Black Hole Initial Mass Function. *ApJ* 457, 834.

Toalá, J. A., D. M. Bowman, T. Van Reeth, H. Todt, K. Dsilva, T. Shenar, G. Koenigsberger, S. Estrada-Dorado, L. M. Oskinova, and W. R. Hamann (2022, August). Multiple variability time-scales of the early nitrogen-rich Wolf-Rayet star WR 7. *MNRAS* 514(2), 2269–2277.

Toalá, J. A., M. A. Guerrero, Y. H. Chu, and R. A. Gruendl (2015, January). On the diffuse X-ray emission from the Wolf-Rayet bubble NGC 2359. *MNRAS* 446(1), 1083–1089.

Toalá, J. A., L. M. Oskinova, W. R. Hamann, R. Ignace, A. A. C. Sander, T. Shenar, H. Todt, Y. H. Chu, M. A. Guerrero, R. Hainich, and J. M. Torrejón (2018, December). On the Apparent Absence of Wolf-Rayet+Neutron Star Systems: The Curious Case of WR124. *ApJ* 869(1), L11.

Toropina, O. D., M. M. Romanova, and R. V. E. Lovelace (2006, September). Spinning-down of moving magnetars in the propeller regime. *MNRAS* 371(2), 569–576.

Torres, A. V., P. S. Conti, and P. Massey (1986, January). Spectroscopic Studies of Wolf-Rayet Stars. III. The WC Subclass. *ApJ* 300, 379.

Torres, G. (2010, Nov). On the Use of Empirical Bolometric Corrections for Stars. *AJ* 140(5), 1158–1162.

Tripathi, A., M. Zhou, A. B. Abdikamalov, D. Ayzenberg, C. Bambi, L. Gou, V. Grinberg, H. Liu, and J. F. Steiner (2020, July). Testing General Relativity with the Stellar-mass Black Hole in LMC X-1 Using the Continuum-fitting Method. *ApJ* 897(1), 84.

Tutukov, A. and L. Yungelson (1973). Evolution of massive close binaries. *Nauchnye Informatsii* 27, 70.

Ugliano, M., H.-T. Janka, A. Marek, and A. Arcones (2012, September). Progenitor-explosion Connection and Remnant Birth Masses for Neutrino-driven Supernovae of Iron-core Progenitors. *ApJ* 757, 69.

Ulmer, A. and E. L. Fitzpatrick (1998, September). Revisiting the Modified Eddington Limit for Massive Stars. *ApJ* 504, 200–206.

Underhill, A. B. (1968, January). The Wolf-Rayet Stars. *ARA&A* 6, 39.

Usov, V. V. (1992, April). Stellar wind collision and X-ray generation in massive binaries. *ApJ* 389, 635–648.

van den Heuvel, E. P. J. (1994, January). Interacting binaries: topics in close binary evolution. In *Saas-Fee Advanced Course 22: Interacting Binaries*, pp. 263–474.

van den Heuvel, E. P. J. (2019, December). High-Mass X-ray Binaries: progenitors of double compact objects. In L. M. Oskinova, E. Bozzo, T. Bulik, and D. R. Gies (Eds.), *High-mass X-ray Binaries: Illuminating the Passage from Massive Binaries to Merging Compact Objects*, Volume 346, pp. 1–13.

van den Heuvel, E. P. J. and C. De Loore (1973, June). The nature of X-ray binaries III. Evolution of massive close binaries with one collapsed component - with a possible application to Cygnus X-3. *A&A* 25, 387–395.

Van den Heuvel, E. P. J., S. F. Portegies Zwart, and S. E. de Mink (2017, January). Forming short-period Wolf-Rayet/X-ray binaries and double black holes through stable mass transfer. *ArXiv e-prints*.

van der Hucht, K. A. (2001, Feb). The VIIth catalogue of galactic Wolf-Rayet stars. *New A Rev.* 45(3), 135–232.

van der Klis, M. and J. M. Bonnet-Bidaud (1984, June). The orbital parameters and the X-ray pulsation of VELA X-1 (4U 0900 - 40). *A&A* 135, 155–170.

Vanbeveren, D., N. Mennekens, E. P. J. van den Heuvel, and J. Van Bever (2020, April). Evidence from high-mass X-ray binaries that Galactic WR components of WR+O binaries end their life with a supernova explosion. *A&A* 636, A99.

Venn, K. A. (1999, June). A-Type Supergiant Abundances in the Small Magellanic Cloud: Probes of Evolution. *ApJ* 518(1), 405–421.

Ventura, J. (2003, January). The Theory of Cyclotron Lines in Accreting X-ray Pulsars. In E. P. van den Heuvel, L. Kaper, E. Rol, and R. A. M. J. Wijers (Eds.), *From X-ray Binaries to Gamma-Ray Bursts: Jan van Paradijs Memorial Symposium*, Volume 308 of *Astronomical Society of the Pacific Conference Series*, pp. 271.

Verbunt, F. (1992). Origin and Evolution of X-Ray Binaries. In Y. Tanaka and K. Koyama (Eds.), *Frontiers Science Series*, pp. 57.

Verner, D. A. and D. G. Yakovlev (1995, January). Analytic FITS for partial photoionization cross sections. *A&AS* 109, 125–133.

Vigna-Gómez, A., M. Wassink, J. Klencki, A. Istrate, G. Nelemans, and I. Mandel (2022, April). Stellar response after stripping as a model for common-envelope outcomes. *MNRAS* 511(2), 2326–2338.

Villaseñor, J. I., W. D. Taylor, C. J. Evans, O. H. Ramírez-Agudelo, H. Sana, L. A. Almeida, S. E. de Mink, P. L. Dufton, and N. Langer (2021, November). The B-type binaries characterization programme I. Orbital solutions for the 30 Doradus population. *MNRAS* 507(4), 5348–5375.

Vink, J. S. (2017, November). Winds from stripped low-mass helium stars and Wolf-Rayet stars. *A&A* 607, L8.

Vink, J. S. (2022, August). Theory and Diagnostics of Hot Star Mass Loss. *ARA&A* 60, 203–246.

Vink, J. S., A. de Koter, and H. J. G. L. M. Lamers (2001, April). Mass-loss predictions for O and B stars as a function of metallicity. *A&A* 369, 574–588.

Voges, W., W. Pietsch, C. Reppin, J. Truemper, E. Kendziorra, and R. Staubert (1982, December). Cyclotron lines in the hard X-ray spectrum of HER X-1. *ApJ* 263, 803–813.

Vrtilek, S. D., B. S. Boroson, A. Hunacek, D. Gies, and C. T. Bolton (2008, May). Ultraviolet Observations of the X-Ray Photoionized Wind of Cygnus X-1 during X-Ray Soft/High State. *ApJ* 678(2), 1248–1262.

Walter, R., A. A. Lutovinov, E. Bozzo, and S. S. Tsygankov (2015, August). High-mass X-ray binaries in the Milky Way. A closer look with INTEGRAL. *A&A Rev.* 23, 2.

Walter, R. and J. Zurita Heras (2007, December). Probing clumpy stellar winds with a neutron star. *A&A* 476(1), 335–340.

Wang, Y.-M. (1981, September). Spin-reversed accretion as the cause of intermittent spindown in slow X-ray pulsars. *A&A* 102, 36–44.

Watanabe, S., M. Sako, M. Ishida, Y. Ishisaki, S. M. Kahn, T. Kohmura, F. Nagase, F. Paerels, and T. Takahashi (2006, November). X-Ray Spectral Study of the Photoionized Stellar Wind in Vela X-1. *ApJ* 651(1), 421–437.

Waters, L. B. F. M., E. P. J. van den Heuvel, A. R. Taylor, G. M. H. J. Habets, and P. Persi (1988, June). Evidence for low-velocity winds in Be/X-ray binaries. *A&A* 198, 200–210.

Webbink, R. F. (1984, February). Double white dwarfs as progenitors of R Coronae Borealis stars and type I supernovae. *ApJ* 277, 355–360.

Webster, B. L. and P. Murdin (1972, January). Cygnus X-1-a Spectroscopic Binary with a Heavy Companion ? *Nature* 235(5332), 37–38.

Wickramasinghe, D. T. and L. Ferrario (2000, July). Magnetism in Isolated and Binary White Dwarfs. *PASP* 112, 873–924.

Wilson, C. A., M. H. Finger, and A. Camero-Arranz (2008, May). Outbursts Large and Small from EXO 2030+375. *ApJ* 678(2), 1263–1272.

Woosley, S. E. (2019, June). The Evolution of Massive Helium Stars, Including Mass Loss. *ApJ* 878(1), 49.

Woosley, S. E., A. Heger, and T. A. Weaver (2002, November). The evolution and explosion of massive stars. *Reviews of Modern Physics* 74(4), 1015–1071.

Yoon, S.-C., S. E. Woosley, and N. Langer (2010, December). Type Ib/c Supernovae in Binary Systems. I. Evolution and Properties of the Progenitor Stars. *ApJ* 725, 940–954.

Yuan, F. and R. Narayan (2014, August). Hot Accretion Flows Around Black Holes. *ARA&A* 52, 529–588.

Yusof, N., R. Hirschi, G. Meynet, P. A. Crowther, S. Ekström, U. Frischknecht, C. Georgy, H. Abu Kassim, and O. Schnurr (2013, August). Evolution and fate of very massive stars. *MNRAS* 433(2), 1114–1132.

Zdziarski, A. A., J. Mikolajewska, and K. Belczynski (2013, February). Cyg X-3: a low-mass black hole or a neutron star. *MNRAS* 429, L104–L108.

Zhekov, S. A. (2012, May). X-rays from colliding stellar winds: the case of close Wolf-Rayet+O binary systems. *MNRAS* 422(2), 1332–1342.

Zhou, C., H. Feng, and F. Bian (2023, April). Identification of a Helium Donor Star in NGC 247 ULX-1. *ApJ* 947(2), 52.

Ziolkowski, J. (2014, May). Determination of the masses of the components of the HDE 226868/Cyg X-1 binary system. *MNRAS* 440, L61–L65.

Appendix A

Appendix to Chapter 2

Mass transfer on a nuclear timescale in models of supergiant and ultra-luminous X-ray binaries

M. Quast¹, N. Langer^{1,2}, and T. M. Tauris^{3,4}

¹ Argelander-Institut für Astronomie, Universität Bonn, Auf dem Hügel 71, 53121 Bonn, Germany
e-mail: mquast@astro.uni-bonn.de

² Max-Planck-Institut für Radioastronomie, Auf dem Hügel 69, 53121 Bonn, Germany

³ Aarhus Institute of Advanced Studies (AIAS), Aarhus University, Høegh-Guldbergs Gade 6B, 8000 Aarhus C, Denmark

⁴ Department of Physics and Astronomy, Aarhus University, Ny Munkegade 120, 8000 Aarhus C, Denmark

Received 12 March 2019 / Accepted 12 May 2019

ABSTRACT

Context. The origin and number of the Galactic supergiant X-ray binaries is currently not well understood. They consist of an evolved massive star and a neutron star or black-hole companion. X-rays are thought to be generated from the accretion of wind material donated by the supergiant, while mass transfer due to Roche-lobe overflow is mostly disregarded because the high mass ratios of these systems are thought to render this process unstable.

Aims. We investigate how the proximity of supergiant donor stars to the Eddington limit, and their advanced evolutionary stage, may influence the evolution of massive and ultra-luminous X-ray binaries with supergiant donor stars (SGXBs and ULXs).

Methods. We constructed models of massive stars with different internal hydrogen and helium gradients (H/He gradients) and different hydrogen-rich envelope masses, and exposed them to slow mass-loss to probe the response of the stellar radius. In addition, we computed the corresponding Roche-lobe overflow mass-transfer evolution with our detailed binary stellar evolution code, approximating the compact objects as point masses.

Results. We find that a H/He gradient in the layers beneath the surface, as it is likely present in the well-studied donor stars of observed SGXBs, can enable mass transfer in SGXBs on a nuclear timescale with a black-hole or a neutron star accretor, even for mass ratios in excess of 20. In our binary evolution models, the donor stars rapidly decrease their thermal equilibrium radius and can therefore cope with the inevitably strong orbital contraction imposed by the high mass ratio. We find that the orbital period derivatives of our models agree well with empirical values. We argue that the SGXB phase may be preceded by a common-envelope evolution. The envelope inflation near the Eddington limit means that this mechanism more likely occurs at high metallicity.

Conclusion. Our results open a new perspective for understanding that SGXBs are numerous in our Galaxy and are almost completely absent in the Small Magellanic Cloud. Our results may also offer a way to find more ULX systems, to detect mass transfer on nuclear timescales in ULX systems even with neutron star accretors, and shed new light on the origin of the strong B-field in these neutron stars.

Key words. binaries: general – stars: massive – X-rays: binaries

1. Introduction

X-ray binaries represent an evolved stage of the evolution of massive binary systems (Verbunt et al. 1992; Tauris & van den Heuvel 2006; Marchant et al. 2017). They contain an ordinary star, the mass donor, and a compact object, namely a neutron star (NS) or a black hole (BH). In these systems, X-ray radiation is released by the accretion of matter that is released by the mass donor onto the compact companion (Frank et al. 2002). Depending on the mass of the donor star, X-ray binaries are divided into low-mass (LMXBs) and high-mass X-ray binaries (HMXBs).

High-mass X-ray binaries may also help us to understand rare ultra-luminous X-ray sources (ULXs; Kaaret et al. 2017), their more luminous cousins in the X-ray sky. Furthermore, HMXBs may be progenitors of merging BHs (Marchant et al. 2016) and NSs (Tauris et al. 2017), and thus have a direct connection to the gravitational-wave signals detected by the Virgo interferometer, which is part of the Laser Interferometer Gravitational-Wave Observatory (LIGO; Abbott et al. 2016, 2017). A study of HMXBs, their formation and evolution thus provides a better understanding of future results from gravitational-wave surveys.

While the mass-transfer and accretion processes in LMXBs are quite well understood (Tauris & van den Heuvel 2006), our knowledge of these processes in HMXBs is more limited. The mass-transfer mode in HMXBs is thought to be either wind accretion (Shakura et al. 2014) or Roche-lobe overflow (RLO; Savonije 1978). Because the first mode requires an extreme stellar wind with mass-loss rates of the order of several $10^{-5} M_{\odot} \text{ yr}^{-1}$ to achieve the observed X-ray luminosities, this is only expected to occur in HMXBs. RLO is often thought to occur in LMXBs because it provides a sufficiently high mass-transfer rate to explain the luminous X-ray emission. In HMXBs, however, RLO is expected to lead to a rapid shrinking of the orbit as the result of the high mass ratio between the donor star and the accretor, leading to a common-envelope (CE) phase. Van den Heuvel et al. (2017) argued that systems with a mass ratio $\gtrsim 3.5$ would always undergo unstable RLO mass-transfer. This would mean that a system containing an O star ($\gtrsim 20 M_{\odot}$) and an NS ($< 3 M_{\odot}$) would quickly enter a CE phase. In this case, the resulting X-ray lifetime cannot exceed the thermal timescale of the donor star. Savonije (1978) indeed found an X-ray lifetime of only 3×10^4 yr for a system with a mass ratio of 16, which is of the order of the thermal timescale of the O star.

High-mass X-ray binaries are subdivided into two main groups (Lewin et al. 1995). The first group harbours an evolved O- or B-type supergiant. These systems typically have a short orbital period (Walter et al. 2015), indicating that the supergiant might be close to filling its Roche lobe. The two mass-transfer modes, wind mass-transfer and RLO, could explain the persistent and luminous X-ray emission. The binaries of the second, more numerous, subgroup consist of an early Be-type donor and a compact object. The appearance of emission lines indicates the existence of a circumstellar disc of material that is thought to be streaming off the nearly critically rotating B star along its equatorial plane. Orbiting its host, the compact object eventually penetrates this disc and accretes matter at this stage (Apparao 1985). This process is seen as a transient X-ray source recurring within a few 10–100 days, corresponding to the period of the wide and eccentric orbit. This inefficient accretion mode does not greatly affect the orbital separation. Thus, the expected X-ray lifetime is the main-sequence time of a B star, about a dozen million years. Building on this, Meurs & van den Heuvel (1989) estimated the total number of X-ray binaries in our galaxy that host supergiants (SGXB) and Be stars (BeXBs). Taking observational biases into account, they expected that about 30 SGXB and 3000 BeXBs host X-ray binaries in the Milky Way. The fraction of SGXBs to BeXBs reflects the ratio between their expected X-ray life times, that is, thermal to nuclear timescale, which is roughly 1/100. This estimate agreed well with observations at the time (Lewin et al. 1995).

Bird et al. (2007; see also Bird et al. 2010) discovered that some SGXBs show peculiar behaviour. While some of them show X-ray transients on a timescale of a few hours (Heise & in't Zand 2006), a second group has a characteristic high absorption corresponding to a column density of $N_{\mathrm{H}} \geq 10^{23} \mathrm{cm}^{-2}$ (Manousakis et al. 2012). The first subgroup of SGXBs is referred to as supergiant fast X-ray transients (SFXTs). The other group is called obscured SGXBs. The mechanisms leading to their formation as well as the role these mechanism play in the evolution of SGXBs are poorly understood. The configuration of the obscured SGXBs has been considered to extend from the existence of a cocoon of dust that enshrouds the whole system (Chaty et al. 2008) to an unusually slow and dense stellar wind ($v_{\infty} \sim 400 \mathrm{km s}^{-1}$) (Manousakis & Walter 2012). While a dust cocoon could indeed form as the result of CE evolution, it is not obvious why a supergiant donor should exhibit a very slow wind velocity because neither observations nor numerical calculations suggest such slow winds for single stars. It is therefore reasonable to assume that the high attenuation might be connected to the existence of a companion and is not an intrinsic attribute of a supergiant.

Recently, Walter et al. (2015) reported 20 new SGXBs and 8 new BeXBs found by ESA's International Gamma-Ray Astrophysics Laboratory (INTEGRAL). This leads to a total number of 36 SGXBs and 60 BeXBs known in the Milky Way. The current observed number of supergiant systems therefore appears to be too high to be explained by thermal timescale RLO of SGXBs. A way to address this problem is to postulate wind accretion in SGXBs (Shakura et al. 2014; Bozzo et al. 2016). However, population synthesis studies by Dalton & Sarazin (1995) predicted a number ratio of SGXBs/BeXBs of $\lesssim 0.15$, even if wind accretion is assumed to be the main mass-transfer mode.

On the other hand, stabilising processes during RLO are a highly debated field of research (Ivanova 2015; Dermine et al. 2009; Blondin & Owen 1997; Savonije 1979). Pratt & Strittmatter (1976) discussed mass-transfer stabilisation due to the rotational slow-down of the donor star, caused by tidal

breaking, and the subsequently diminishing centrifugal force in its outer layers. Stabilisation by widening of the Roche-lobe due to mass loss by a stellar wind was studied by Basko et al. (1977). Hjellming & Webbink (1987) investigated mass transfer on dynamical timescales using semi-analytical models. They found that any initial stability due to the rapid adiabatic expansion of the primary's outer layer will switch to an unstable mode if these layers are super-adiabatic. Tauris et al. (2000) discovered the possibility of long-term stable mass transfer even if the mass ratio exceeds a value of 4. More recently, Pavlovskii et al. (2017) showed that RLO can be stable if the primary is a post-main-sequence star (case B mass transfer) that has already expanded through the Hertzsprung gap but has not yet developed a deep convective envelope (see also Pavlovskii & Ivanova 2015).

A similar timescale problem as in the SGXBs may exist in some ULX sources, many of which radiate highly above the Eddington accretion limit of a $\sim 10 M_{\odot}$ BH (Long et al. 1981; Kaaret et al. 2017). An interesting case is the ULX NGC 7793 P13. In this source, X-ray pulses were discovered by Israel et al. (2017b), indicating that the companion is an NS. With an estimated donor star mass of $\sim 20 M_{\odot}$, the mass ratio of the system is high, such that, again, stable mass transfer is not expected to occur. However, wind accretion alone cannot explain the high X-ray luminosity. How NGC 7793 P13 and three more X-ray pulsating ULXs (Bachetti et al. 2014; Israel et al. 2017a; Maitra et al. 2018) form and transfer mass is therefore not well understood.

In this study, we work out conditions under which stable mass transfer on a nuclear timescale can occur even though the donor star is much more massive than the compact companion. We explain our methods for modelling single-star and binary evolution in Sect. 2, including mass transfer to a compact object, and work out the criteria for long-term RLO and the connection of these evolutions to the internal structure of the donor. In Sect. 3 we investigate the sensitivity of the donor star radius to mass loss, and we present our binary evolution models in Sect. 4, including examples of systems with high mass ratios that undergo mass transfer on a nuclear timescale. In Sect. 5 we discuss the possible properties of NS and BH hosting ULXs in the light of our findings. In Sect. 6 we investigate possible paths for the evolution of SGXB and ULX progenitors, and in Sect. 7 we discuss their likely evolutions. Our conclusions are presented in Sect. 8.

2. Method

2.1. Modelling stellar evolution and mass transfer

We used the binary evolution code (BEC), a one-dimensional hydrodynamic Lagrangian code, to solve the equations of stellar structure (Kippenhahn & Weigert 1990) and model the binary interaction (Braun & Langer 1993). The code includes up-to-date physics (Wellstein & Langer 1999; Wellstein et al. 2001) and uses the OPAL opacity tables (Iglesias & Rogers 1996). For convection zones, the mixing length theory (MLT) by Böhm-Vitense (1958) was applied, where we adopted $\alpha_{\mathrm{ML}} = 1.0$ unless stated otherwise. We note that the value of α_{ML} is uncertain (Pinheiro & Fernandes 2013) and may differ for stars in different evolutionary stages and/or mass ranges. Nevertheless, a mixing length parameter of the order of unity is in agreement with observations (Cox & Giuli 1968; Ferraro et al. 2006). The rotation and magnetic fields were not taken into account. For stellar wind mass loss, we followed the assumptions made by Brott et al. (2011), unless stated otherwise.

We investigated the case of X-ray binaries. We evolved an ordinary star with a point-mass companion that represents the NS or BH. The point mass induces mass transfer when the donor star exceeds its Roche radius, and mass is carried to the compact companion accretor via the first Lagrangian point. Here, the Roche lobe is approximated by a sphere of radius R_L that has the same volume as the Roche lobe, following Eggleton (1983),

$$R_L = \frac{0.49q^{2/3}}{0.6q^{2/3} + \ln(1 + q^{1/3})} a, \quad (1)$$

where $q = M_D/M_A$ is the mass ratio of donor and accretor, and a is the orbital separation. The mass-transfer rate was calculated using the method of Kolb & Ritter (1990). When the donor star did not fill its Roche volume, we computed the accretion of stellar wind material onto the compact star using the description of Bondi & Hoyle (1944).

When matter falls onto the compact object, it heats up and releases a large portion of the gained gravitational energy in X-rays. This leads to a feedback on the remaining material, of which the radiative force may expel a certain fraction. Hence the accretion rate and therefore the X-ray luminosity are self-regulated and are usually not expected to exceed the Eddington-accretion rate and luminosity of this object (but see Sect. 4.6). When we write the Eddington luminosity of an accretor with mass M_A as

$$L_{\text{Edd}} = \frac{4\pi c GM_A}{\kappa}, \quad (2)$$

the Eddington accretion rate can be expressed as

$$\dot{M}_{\text{Edd}} = \frac{4\pi GM_A}{\eta c \kappa}, \quad (3)$$

where η is the fraction of rest-mass energy of the accreted material that is released as radiation, and κ is the opacity. We adopted $\eta = 0.06$, assuming a non-rotating BH, and $\eta = \frac{GM_A}{R_c^2}$ for an NS. Furthermore, we assumed only electron-scattering opacity (Kippenhahn & Weigert 1990). Under these assumptions, we may calculate the Eddington-accretion rate as

$$\dot{M}_{\text{Edd}} = \begin{cases} 4.6 \times 10^{-8} \frac{1}{1+X} (M_A/M_\odot)^{-1/3} M_\odot \text{ yr}^{-1} & \text{for NS} \\ 7.3 \times 10^{-8} \frac{1}{1+X} (M_A/M_\odot) M_\odot \text{ yr}^{-1} & \text{for BH,} \end{cases} \quad (4)$$

where we distinguish between NSs and the more massive BHs. In this equation, X is the hydrogen mass fraction of the accreted material. The different scaling of the Eddington rate with respect to the accretor mass arises from different mass-radius relations of BHs and NSs. While the BHs Schwarzschild radius is proportional to its mass, the NSs radius scales as $M_A^{-1/3}$ for a perfect Fermi gas. The NS mass-radius relation was scaled such that a $2 M_\odot$ NS has a radius of 12 km (Demorest et al. 2010). We computed the actual accretion rate as the minimum of the mass-transfer rate \dot{M}_{RLO} and the Eddington rate given by Eq. (4), that is, $\dot{M}_A = \min [\dot{M}_{\text{RLO}}, \dot{M}_{\text{Edd}}]$.

2.2. Internal H/He gradients

Schootemeijer & Langer (2018) derived the internal hydrogen and Helium gradients (H/He gradients) in the hydrogen-rich Wolf-Rayet stars of the SMC. They found that these gradients are different by more than a factor of ten for different objects. Because we show below that these gradients can play a key role

in stabilising the mass transfer in SGXBs, we consider it as a free parameter in our models.

We evolved three stellar models of solar metallicity (Brott 2011) and initial masses of $50 M_\odot$, $60 M_\odot$, and $80 M_\odot$ to core helium mass fractions of 0.6, 0.7, and 0.8.

Subsequently, we adjusted the helium profile by setting the helium mass fraction above the convective core to

$$Y(m) = \max \left[Y_{\text{core}} + \frac{dY}{dm}(m - m_{\text{core}}), 0.2638 \right], \quad (5)$$

with prescribed fixed values of dY/dm . Here m and Y denote the Lagrangian mass coordinate and the helium abundance, m_{core} is the mass of the convective core, and Y_{core} is its helium abundance. We then relaxed the models thermally, disregarding changes in their chemical profile due to mixing or burning. Then we exposed the models to a constant mass-loss rate of $10^{-5} M_\odot \text{ yr}^{-1}$, which is of the order of magnitude of the mass-transfer rate on a nuclear timescale, $M_D/\tau_{\text{nuc}, D}$, to the response of the stellar radius and derived the mass-radius exponent

$$\zeta_R(M) := \frac{d \ln R}{d \ln M}. \quad (6)$$

The results of this exercise are presented in Sect. 3.1.

While the initial masses of our models are in general higher than the donor masses observed in SGXBs, the masses of the stellar models are in good agreement with observations after the artificial mass loss. The advantage of first producing very massive models and a consequent mass reduction is shown in Sect. 6, where this procedure will provide an interpretation of the over-luminosity found in SGXBs.

2.3. Response of the Roche radius

If mass is transferred from the donor to the accretor, the Roche radius R_L changes due to changing orbital separation. We considered the orbital evolution by changes in stellar masses and hence in mass ratio, by angular momentum loss through the donor's stellar wind, and by angular momentum loss by isotropic re-emission of matter near the compact object. Additional effects, such as spin-up of the compact companion, spin-orbit coupling due to tidal effects, magnetic breaking, and gravitational-wave radiation are neglected.

For a circular orbit, the orbital angular momentum can be written as

$$J = 2\pi a^2 \frac{M_A M_D}{PM}, \quad (7)$$

where a is the orbital separation, M_A and M_D are the accretor mass and the donor mass, $M = M_A + M_D$ and P is the orbital period. Using Kepler's third law to replace P and solving for a , we find

$$a = \frac{MJ^2}{GM_A^2 M_D^2}. \quad (8)$$

The derivative with respect to time provides the change in orbital separation with time as

$$\frac{\dot{a}}{a} = 2\frac{j}{J} - 2\frac{\dot{M}_D}{M_D} - 2\frac{\dot{M}_A}{M_A} + \frac{\dot{M}_D + \dot{M}_A}{M_D + M_A}. \quad (9)$$

Following Tauris & van den Heuvel (2006), we consider the donor mass to decrease by dM_D per time unit. Because only stellar wind and mass transfer can change the orbital separation, we

introduce α as the fraction of dM_D lost in a stellar wind and β as the fraction that is transferred to the accretor and then re-emitted isotropically with the specific orbital angular momentum of the accretor. In our simulations we adopted

$$\alpha = \frac{\dot{M}_{\text{wind}}}{\dot{M}_{\text{wind}} + \dot{M}_{\text{RLO}}} \quad (10)$$

and

$$\beta = \frac{\dot{M}_{\text{MT}} - \dot{M}_A}{\dot{M}_{\text{wind}} + \dot{M}_{\text{RLO}}}. \quad (11)$$

Hence, we have that the accretion efficiency (accreted mass fraction of dM_D) $\epsilon = 1 - \alpha - \beta$. Using this nomenclature, we express the loss of orbital angular momentum as

$$\frac{\dot{J}}{J} = \frac{\alpha + \beta q^2}{1 + q} \frac{\dot{M}_D}{M_D}. \quad (12)$$

Inserting this into Eq. (9), with $M_A = M_D/q$ and $\dot{M}_A = -\epsilon \dot{M}_D$, yields after integration

$$\frac{a}{a_0} = \frac{q_0 + 1}{q + 1} \left(\frac{q}{q_0} \right)^{2(\alpha-1)} \left(\frac{\epsilon q + 1}{\epsilon q_0 + 1} \right)^{3+2(\alpha\epsilon^2+\beta)/(\epsilon(1-\epsilon))}, \quad (13)$$

where the subscript 0 refers to the initial state before the mass loss. Investigation of the limits of Eq. (13) using l'Hospital's rule with respect to α , β , and ϵ helps to understand the orbital behaviour in the extreme cases. For pure wind mass loss ($\alpha = 1$), it is

$$\frac{a}{a_0} = \frac{q_0 + 1}{q + 1}, \quad (14)$$

for dominating mass transfer and re-emission ($\beta = 1$),

$$\frac{a}{a_0} = \frac{q_0 + 1}{q + 1} \left(\frac{q_0}{q} \right)^2 \exp[2(q - q_0)], \quad (15)$$

and for conservative mass transfer ($\epsilon = 1$), we obtain

$$\frac{a}{a_0} = \left(\frac{q + 1}{q_0 + 1} \right)^4 \left(\frac{q_0}{q} \right)^2. \quad (16)$$

In HMXBs, all of the three cases tend to decrease the mass ratio, hence $q < q_0$. Keeping this in mind, we find that the orbit will always widen in the case of wind-dominated mass loss according to Eq. (14). For mass transfer with subsequent re-emission or accretion, we find a decreasing orbital separation because the exponential term in Eq. (15) and the fourth-power term in Eq. (16) dominate the total change in a .

Massive donor stars have a strong stellar wind, which makes wind mass transfer just before RLO unavoidable. In this pre-RLO phase, where the accretion is purely wind fed, orbital changes occur due to mass loss and angular momentum loss of the donor star and mass accretion onto the compact object. It is interesting to study the influence of pure wind accretion on the binary system because the wind mass loss is the main reason of orbital change in the pre-RLO phase. The widening of the orbit increases the Roche radius. However, a main-sequence donor does not increase its radius much for most of its lifetime. This would inhibit RLO until the donor star is relatively evolved.

When we consider pure wind mass loss and subsequent accretion of a mass fraction ϵ , we can rewrite Eqs. (9) and (12) as

$$\frac{\dot{a}}{a} = \left[\frac{2\alpha}{1 + q} + 2\epsilon q - 2 + \frac{\alpha}{1 + q^{-1}} \right] \frac{\dot{M}_D}{M_D}. \quad (17)$$

We note that \dot{M}_D is negative, hence the orbital separation only decreases if

$$\frac{2\alpha}{1 + q} + 2\epsilon q - 2 + \frac{\alpha}{1 + q^{-1}} > 0. \quad (18)$$

This gives us the condition for a decreasing orbital separation in a phase of pure wind accretion as

$$\frac{\alpha}{\epsilon} < \frac{2(q^2 - 1)}{q}. \quad (19)$$

On the other hand, if $v_{\text{wind}}/v_{\text{orb}} \gg 1$ and $q \gg 1$, the Bondi-Hoyle formula

$$\dot{M}_{\text{acc}} = \frac{G^2 M_A^2}{v_{\text{wind}}^4 a^2} \dot{M}_{\text{wind}} \quad (20)$$

can be expressed in terms of orbital and wind velocity

$$\epsilon = \frac{\dot{M}_{\text{acc}}}{\dot{M}_{\text{wind}}} = \left(\frac{v_{\text{orb}}}{v_{\text{wind}}} \right)^4 \left(\frac{1}{q + 1} \right)^2, \quad (21)$$

and hence the condition for a shrinking orbit is

$$\left(\frac{v_{\text{wind}}}{v_{\text{orb}}} \right)^4 (q + 1)^2 - 1 < \frac{2(q^2 - 1)}{q}. \quad (22)$$

Because $(v_{\text{wind}}/v_{\text{orb}})^4 \gg 1$ and $q^2 \gg 1$, we simplify the criterion to

$$\frac{v_{\text{wind}}}{v_{\text{orb}}} < \sqrt[4]{\frac{2}{q}}. \quad (23)$$

For an initially well-detached binary system that hosts a supergiant donor, the orbit is quite likely to widen because the orbital velocity will barely exceed a few 100 km s^{-1} , while the wind velocity can be an order of magnitude higher. It is therefore difficult to start RLO during the early main-sequence phase of the donor star. The stellar wind widens the orbit while the donor radius increases hardly at all. A faster expansion, for instance, in the advanced stage of core hydrogen burning ($Y_{\text{core}} \sim 0.8$), might overcome the orbital increase induced by the wind mass loss and start a RLO phase, however. We conclude that donor stars in RLO systems are therefore likely to be evolved.

We describe the change in Roche radius by defining a mass-radius exponent similar to Eq. (6) as

$$\zeta_L(M) := \frac{d \ln R_L}{d \ln M}. \quad (24)$$

With this description of the orbital evolution, we find an analytical expression for the Roche-lobe responses to mass transfer as a function of mass ratio (Tauris & van den Heuvel 2006) as

$$\zeta_L(q) = [1 + (1 - \beta)q] \Psi + (5 - 3\beta)q, \quad (25)$$

where

$$\Psi = -\frac{4}{3} - \frac{q}{1 + q} - \frac{0.4 + 1/3q^{-1/3} (1 + q^{1/3})^{-1}}{0.6 + q^{-2/3} \ln(1 + q^{1/3})}. \quad (26)$$

Figure 1 shows the mass-radius exponent of the Roche lobe ζ_L plotted as a function of the mass ratio q . Because the typical mass ratio of HMXBs is ≥ 8 , we would need $\zeta_L \geq 12$ in order to find long-term mass transfer through RLO.

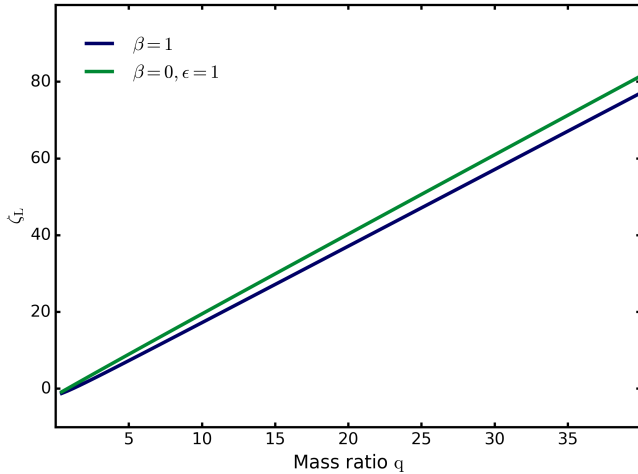


Fig. 1. Mass–radius exponent of the Roche radius (Eq. (25)) as a function of mass ratio q . The different colours denote different mass-loss modes. For the blue line the entire mass is transferred and re-emitted isotropically, while for the green line the entire transferred mass is accreted.

The evolution of an SGXB where the donor star fills its Roche lobe depends on the mass–radius exponents. If $\zeta_R \leq \zeta_L$, the Roche lobe shrinks faster than the star, which will overfill its Roche lobe even more, leading to a higher mass-transfer rate, and so on. This runaway process results in a CE evolution. If $\zeta_R > \zeta_L$, however, the donor radius is more sensitive to mass loss than the Roche radius, and the mass-transfer rate becomes self-regulated and can be estimated using the donor mass and its nuclear timescale as $\dot{M} \approx M_D/\tau_{\text{nuc}}$ (Soberman et al. 1997).

2.4. Binary evolution models

After investigating the mass–radius exponent of our single-star models, we selected those with high values of ζ_R . We added point-mass companions with 2 or $10 M_\odot$ and started the binary evolution. The initial orbital separation was selected such that the Roche radius exceeded the initial photospheric radius of the donor by 3%. We used the method described above to calculate the mass transfer and the accretion rate. We evolved the models with BEC until the hydrogen in the core of the donor star was exhausted or the mass-transfer rates exceeded $\sim 10^{-2} M_\odot \text{ yr}^{-1}$, where we assumed that the mass transfer becomes dynamically unstable and the system enters a CE phase. Subsequently, we calculated the X-ray lifetime, defined as the time interval where the compact companion accretes at a higher rate than $10^{-13} M_\odot \text{ yr}^{-1}$, which corresponds to an X-ray luminosity of $\sim 10^{33} \text{ erg s}^{-1}$.

3. Results from single-star models

3.1. Response of the stellar radius

Here, we explore how the radii of our potential donor stars are affected by mass loss on a nuclear timescale. The resulting values of ζ_R can then be compared to the functions ζ_L plotted in Fig. 1 to obtain an estimate for which mass ratios we can expect stable mass transfer.

Figure 2 shows the mass–radius exponent ζ_R of our $60 M_\odot$ model evolved to a central helium mass fraction of $Y_c = 0.8$. At the start of our mass-loss experiment, the model has a mass of $51 M_\odot$, a convective core of $\sim 32 M_\odot$, and a H/He gradient of about $0.2 M_\odot^{-1}$ in the core-envelope transition zone.

We stripped the mass through a constant mass-loss rate of $10^{-5} M_\odot \text{ yr}^{-1}$. As explained above, this rate is sufficiently low to maintain thermal equilibrium inside the model. Figure 2 shows that with decreasing stellar mass, the mass–radius exponent is low and negative at first because the stellar luminosity-to-mass ratio decreases. However, when He-enriched layers approach the surface, the mass–radius exponent climbs to values of 30, before it drops again to a low value when the stellar core is exposed. A value of $\zeta_D = 30$ implies that a mass decrease by 1% induced the radius of the star to decrease by 30%. According to Fig. 1, such high values of ζ_D could give rise to a phase of stable mass transfer even for mass ratios as high as 15.

The drastic shrinkage of our models is related to the transition from a hydrogen-rich supergiant stage, with a radius of about $68 R_\odot$, to a much more compact and hydrogen-poor Wolf–Rayet-type structure with $6 R_\odot$. This is eminent from the correlation of the mass–radius exponent with the change in surface helium abundance, as shown in Fig. 2. Here, we note that the mass–radius exponent changes sign and evolves to high values somewhat before helium-enriched layers reach the surface of the star because the average envelope properties determine its radius. This is in agreement with previous stellar structure and evolution calculations (e.g. Köhler et al. 2015; Schootemeijer & Langer 2018).

Figure 3 shows that the internal H/He gradient is a suitable way to tune the mass–radius exponent ζ_D in our models. It depicts the result of the same experiment as explained above, but for six models with different steepness of the H/He-gradient. The models with steeper gradients reach higher values of ζ_D , even exceeding $\zeta_D = 40$ in the most extreme case. While this may appear surprising at first because such high values of the mass–radius exponent have not yet been reported in the literature, it is a simple consequence of the mass in the transition layer between the He-rich core and the H-rich envelope, $\Delta M_{\text{H/He}}$, becoming very low for a steep internal H/He gradient, and $\zeta_D \simeq (R_H - R_{\text{He}})M/(R_{\text{He}}\Delta M_{\text{H/He}})$ becoming higher the lower $\Delta M_{\text{H/He}} \rightarrow 0$. Here, R_H is the stellar radius in the H-rich state, and R_{He} is the radius in the He-rich state, while M is the mass of the star.

Infinite H/He gradients, although not strictly excluded, are not expected in massive stars. However, it is important to point out that the range in steepness explored in Fig. 3 remains well within the range that has been derived by Schootemeijer & Langer (2018) from the observed properties of the WN-type Wolf–Rayet stars in the SMC. As we discuss in Sect. 5 below, this group of stars is quite relevant here because SGXBs may evolve into WN-type Wolf–Rayet binaries.

The mass–radius exponents of all our single-star models ($50 M_\odot$, $60 M_\odot$, and $80 M_\odot$) and core helium abundances (0.6, 0.7, 0.8) are shown in the appendix (Figs. A.1–A.3), where we explore six different H/He gradients per models, as in Fig. 3. These figures show that in addition to the clear correlation between the mass–radius exponent and the helium gradient, higher mass–radius exponents are also obtained for a higher initial mass and for a later evolutionary stage (larger core helium mass fraction). Figure 4 summarises these results by showing the maximum value of the mass–radius exponent ζ_R as a function of the adopted internal helium gradient dY/dm for all our single-star models.

3.2. Influence of stellar inflation

In their analysis of the massive single star evolutionary models for LMC composition of Brott et al. (2011), Köhler et al. (2015),

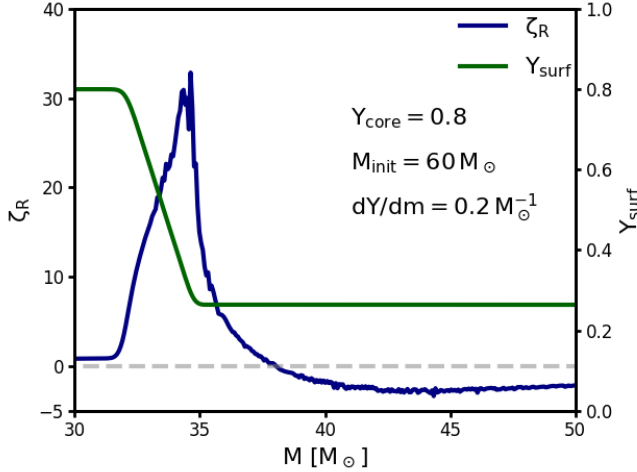


Fig. 2. Mass–radius exponent (blue) of our initial $60 M_{\odot}$ model evolved to a central helium abundance of 0.8, and a H/He gradient of $0.2 M_{\odot}^{-1}$ that is then exposed to a constant mass-loss rate of $10^{-5} M_{\odot} \text{yr}^{-1}$ as a function of the remaining stellar mass. The green line gives the surface helium abundance. Because mixing is inhibited during the mass-loss phase, the surface helium-abundance evolution reflects the internal helium profile of the initial model.

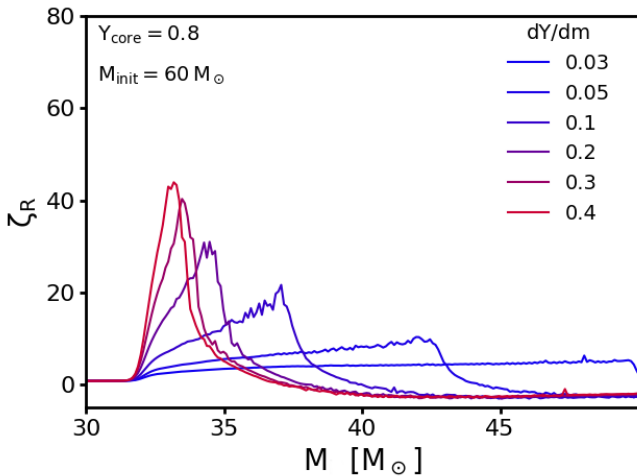


Fig. 3. Mass–radius exponent of our initial $60 M_{\odot}$ model in the same way as for the blue line in Fig. 2, but here for models where the internal helium gradient dY/dm has been artificially adjusted (see Sect. 2) to values indicated in the legend.

and Sanyal et al. (2015) found that the envelopes of models for stars above $\sim 40 M_{\odot}$ are inflated because they exceed the Eddington-limit in their subsurface layers. Whether such inflated envelopes (see Fig. 5, e.g.) exist in reality is still a matter of debate, although they have been confirmed by 3D radiation-hydrodynamic calculations (Jiang et al. 2015).

The mass of the inflated envelope is mostly very low, that is, about $10^{-6} M_{\odot}$ in our models. However, its radius may be of the order of the radius of the un-inflated stellar interior. Obviously, radius inflation may play a great role in binary evolution. It is therefore important to analyse how inflation may affect the mass–radius exponent.

For this purpose, we investigated our $60 M_{\odot}$ single-star model at a core helium mass fraction of $Y_{\text{core}} = 0.8$ and $dY/dm = 0.2 M_{\odot}^{-1}$, from which we constructed three different initial models for our mass-loss experiment. The only difference in these models is the chosen mixing length parameter $\alpha_{\text{ML}} = l/H_{\text{P}}$, were

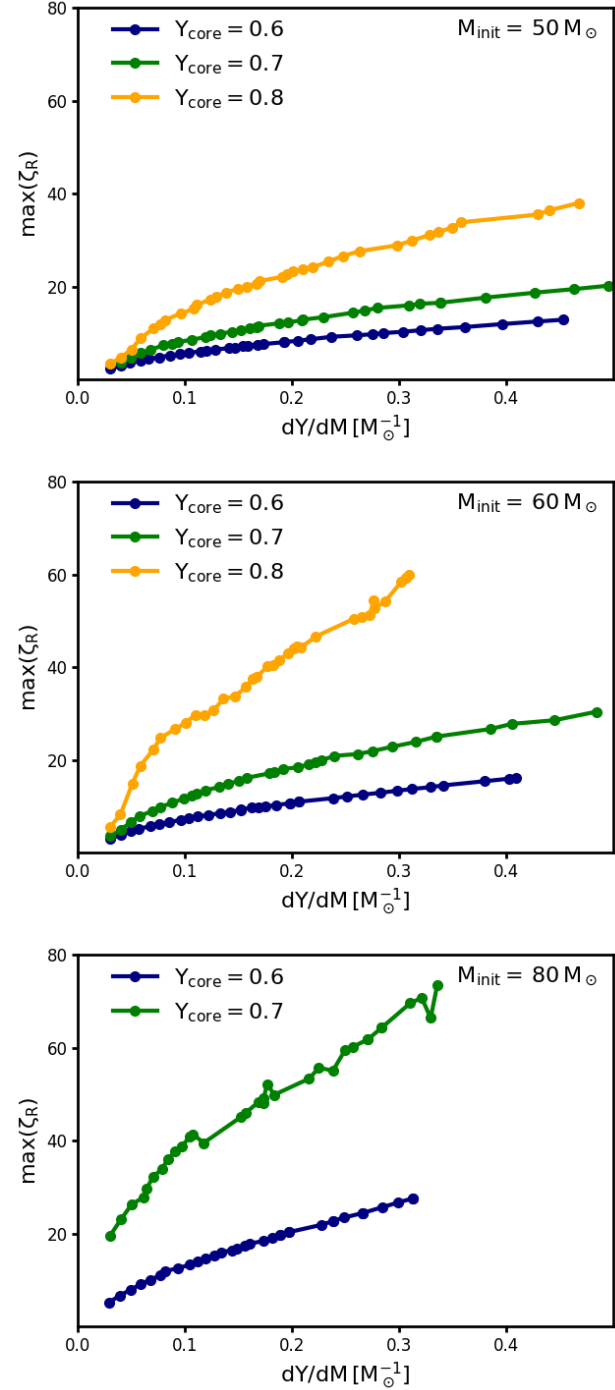


Fig. 4. Maximum value of the mass–radius exponent ζ_R as a function of the chosen internal helium gradient dY/dm for stellar models derived from three different initial masses as indicated in the legends. Different colours indicate different core helium abundances at the start of the mass-loss experiments (see Sect. 2).

l denotes the mixing length and H_{P} the pressure scale height (cf. Sect. 2). We computed models with values for α_{ML} of 1 (our default choice), 1.5, and 50. Whereas the first two values are in the range discussed in comparison to 3D models of convection and real stars (Sonoi et al. 2019), we used $\alpha_{\text{ML}} = 50$ to produce a stellar model in which inflation is suppressed but not absent (cf. Sanyal et al. 2015).

The mass–radius exponents of these three models are plotted in Fig. 6. We find that stellar inflation has a significant effect

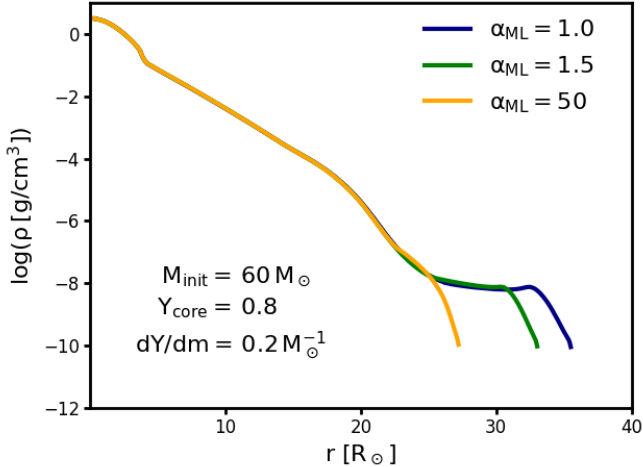


Fig. 5. Mass density as function of radius for our initially $60 M_{\odot}$ models with $Y_{\text{core}} = 0.8$ and $dY/dm = 0.2 M_{\odot}^{-1}$ for three different values of the mixing length parameter α_{ML} , as indicated.

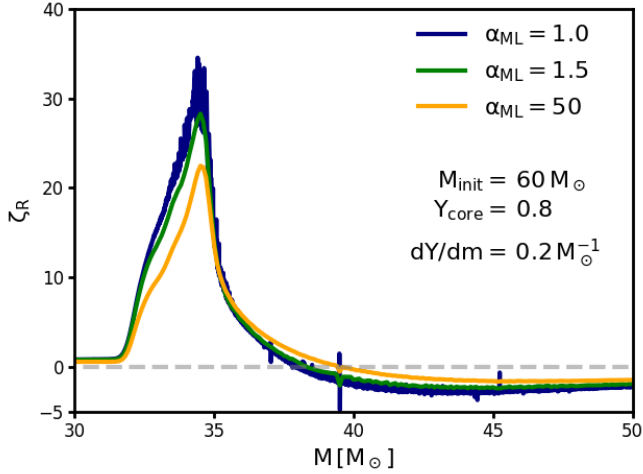


Fig. 6. Mass–radius exponent as function of stellar mass, with the three models displayed in Fig. 5 as initial models before assuming a constant mass-loss rate of $10^{-5} M_{\odot} \text{ yr}^{-1}$. The colours correspond to the density profiles in Fig. 5.

on ζ_R . While for strong inflation ($\alpha_{\text{ML}} = 1$) the maximum value of ζ_R reaches 34, it only reaches 21 when inflation is suppressed ($\alpha_{\text{ML}} = 50$). We also note that the value of the mass–radius exponent is initially more negative for the inflated models. However, the high peak of ζ_R occurs only when a H/He gradient appears beneath the surface.

In Fig. 7 we compare the radius extension of the un-inflated part with that of the inflated envelope layer during the mass-loss experiment for our three models. Here, we followed Sanyal et al. (2015) to define the bottom of the inflated envelope as the point where the gas–pressure contribution $P_{\text{gas}}/(P_{\text{gas}} + P_{\text{rad}})$ drops to 15% for the first time when going from the stellar center outwards. We refer to this position as R_{15} . As the gas–pressure fraction in our model computed with $\alpha_{\text{ML}} = 50$ never drops below 15%, we define the radius R_{30} as the position where the gas–pressure fraction first drops below 30%. The near coincidence of these two radii in the top and middle panel of Fig. 7 suggest that the exact threshold value of the gas–pressure fraction in defining the bottom of the inflated envelop is not important.

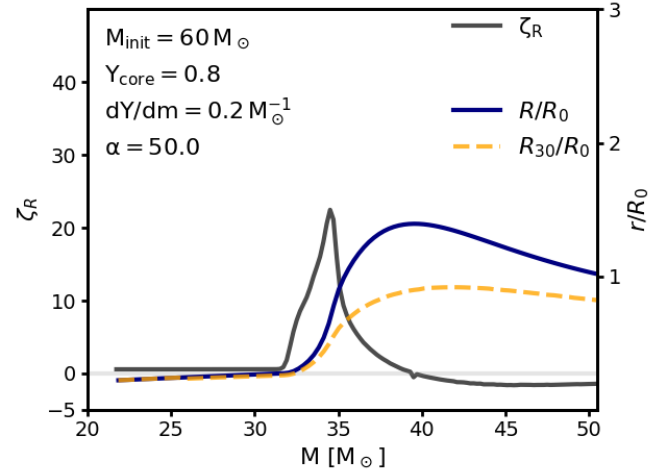
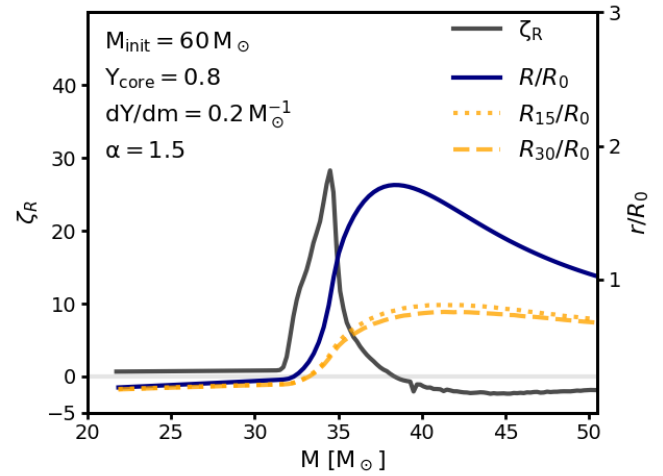
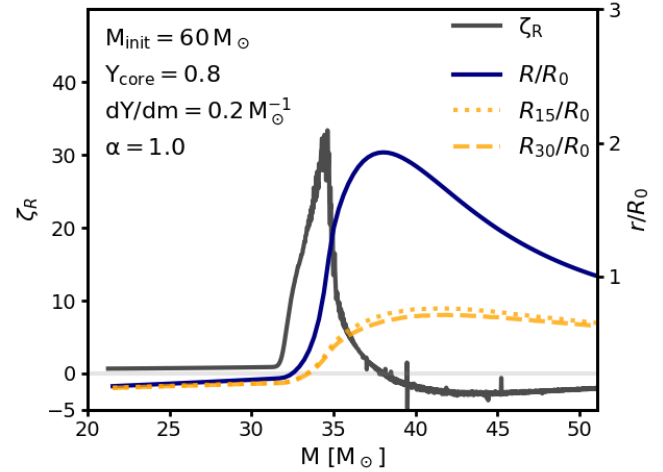


Fig. 7. Mass–radius exponent ζ_R (grey), stellar radius R (blue), and radii where the gas pressure contributes only 15% (R_{15}) and 30% (R_{30}) to the total pressure (see text), as function of the remaining stellar mass for the three models with different values of the mixing length parameter α_{ML} shown in Fig. 6 (the lines for ζ_R are identical). All radii are measured in units of the initial stellar radii R_0 , which can be read off Fig. 5.

Figure 7 shows that before the helium gradient appears beneath the stellar surface (cf. Fig. 2), the stellar radius expands significantly as a result of inflation. This effect is stronger in the model computed with lower α_{ML} because the radius of the un-inflated part of the star (defined through R_{15} and R_{30} in Fig. 7) behaves in the same way in all three cases.

All three models have the same final configuration after they are stripped down to the helium core, therefore Fig. 7 offers a simple explanation of the dependence of the maximum of the mass–radius exponent on the mixing length parameter found in Fig. 6 because inflation is a much smaller effect for hot and compact models (Sanyal et al. 2015). For smaller α_{ML} , the hydrogen-rich models are more extended, and the drop in radius towards the compact stage is thus stronger than when α_{ML} is larger. We conclude that inflation is not a critical factor in producing high mass–radius exponents, but that it can contribute at the quantitative level, that is, it can enhance the mass–radius exponent by factors of the order of 2 for stars that exceed the Eddington limit.

4. Binary evolution models for SGXBs

In the previous section, we found that models of supergiant stars may show very high mass–radius exponents, with values up to ~ 40 . When we compare these to the mass–radius exponents of the Roche radius in Fig. 1, we expect that mass transfer on nuclear timescales may occur even in binaries with mass ratios of 20 or higher. To demonstrate this, we constructed appropriate initial models and combined them with point masses in model binary systems. We then calculated the detailed binary evolution of such systems with our binary evolution code (BEC).

We drew our initial models for these calculations from our $60 M_{\odot}$ models with a central helium mass fraction of $Y_{\text{core}} = 0.8$, from which we took one model with a rather shallow helium gradient ($dY/dm = 0.04 M_{\odot}^{-1}$) and a second one with a helium gradient that was ten times steeper ($dY/dm = 0.4 M_{\odot}^{-1}$). The helium profiles of these two models are shown in Fig. 8. We note that a helium gradient of $dY/dm = 0.04 M_{\odot}^{-1}$ corresponds to the gradient that is left by the retreating convective core during core hydrogen burning, whereas a gradient that is steeper by about ten times can be established above the helium core during hydrogen shell burning, as derived for the SMC Wolf–Rayet stars by Schootemeijer & Langer (2018).

From each of these two models, we constructed five different initial models to calculate the binary evolution by removing the envelope mass down to the mass indicated by labels a to e in the top panel of Fig. 8. The choice of these amounts of removed envelope mass becomes clear from the bottom panel of Fig. 8, which shows the mass–radius exponent of the two models as a function of the remaining mass. It indicates that with the chosen envelope masses, our binary evolution models sample the possible range of the initial mass–radius exponent of the donor star.

For each of the ten initial donor star models described above, we performed several binary evolution calculations. We considered two different compact objects, a $2 M_{\odot}$ NS and a $10 M_{\odot}$ BH. Furthermore, we ran models with different assumptions on the donor star’s stellar wind mass loss, that is, without wind, with a constant stellar wind mass-loss rate, and with the mass-loss rate according to the prescription of Vink et al. (2001). Table B.1 gives an overview of the different binary evolution models, the details of the initial donor star models, and key quantities describing the evolution of the model binaries.

For the following discussion, we label the initial donor star models depending on their initial mass (using letters a to e according to Fig. 8), and numbers 1 or 2 depending on their helium gradient. For instance, model a1 refers to the initial donor star model with a helium slope of $dY/dm = 0.04 M_{\odot}^{-1}$ (orange curve in Fig. 8) and an initial mass of $50 M_{\odot}$, while model e2 has $dY/dm = 0.4 M_{\odot}^{-1}$ (blue curve in Fig. 8) and an initial mass of $32 M_{\odot}$.

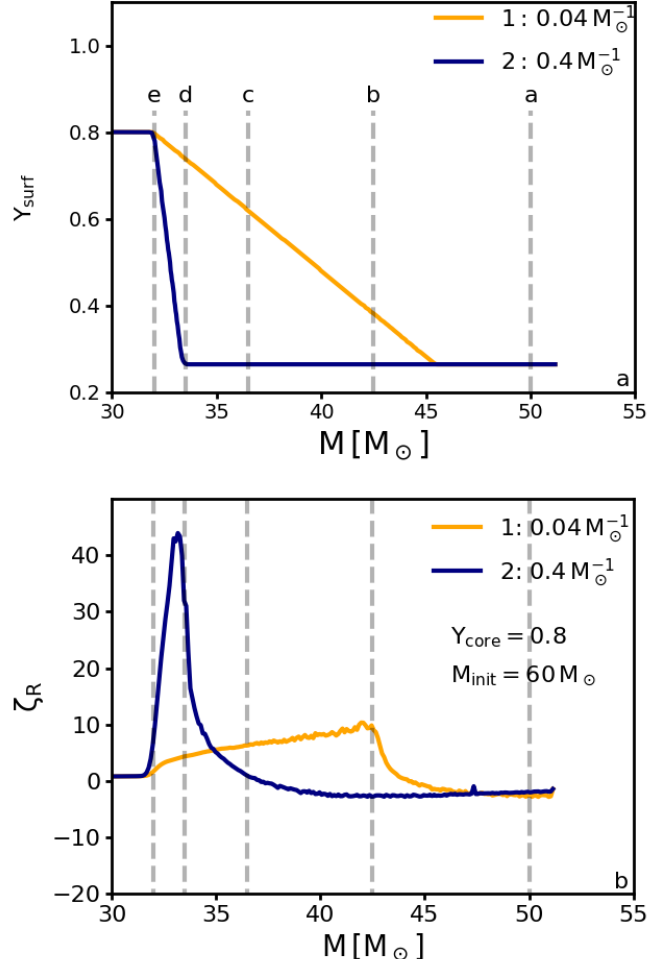


Fig. 8. *Top panel:* helium surface abundance as function of the total mass of the two stellar models from which the initial donor star models for our binary evolution calculations are derived. They are constructed such that mass located above the lines labelled a to e was removed before the binary calculation was started. *Bottom panel:* mass–radius exponent for the models as a function of the remaining stellar mass. Dashed lines correspond to the masses (labels a to e) in the *upper panel*.

We further label the binary evolution models by indicating whether the accretor is a $10 M_{\odot}$ BH or a $2 M_{\odot}$ NS, using two letters (bh or ns). Finally, we indicate whether the donor star undergoes no mass-loss (0), mass loss with a constant rate of $10^{-6} M_{\odot} \text{ yr}^{-1}$ (c), or time-dependent mass loss according to Vink et al. (2001)(v). For instance, the binary model d2ns0 consists of the initial donor model d2 as defined above and an NS accretor. During the binary evolution, the donor loses no mass through stellar wind.

4.1. Detailed example: Donor model d2 with a neutron star companion

Here, we discuss one of our binary evolution models in detail. For this we chose model d2 as donor star, which we placed together with a $2 M_{\odot}$ NS in an orbit of 9.1 d. The initial mass ratio in this binary is 16.8, such that highly unstable mass transfer might be expected. However, the envelope mass of model d2 was chosen such that the steep helium gradient in the initial donor model is located just beneath the surface, such that we expect an initial mass–radius exponent of $\zeta_R \simeq 40$ in this case (Fig. 8).

Figure 9 shows the evolution of the mass-transfer rate as function of time for this model, where stellar wind mass loss is neglected. It shows that after a brief switch-on phase ($\sim 10^4$ yr), the model establishes a rather stationary mass-transfer rate of $3 \times 10^{-6} M_{\odot} \text{ yr}^{-1}$, which is maintained for ~ 250 000 yr. During this time, the orbital period decreased from 9.1 d to 1.4 d. This was possible without leading to a CE situation because the donor star radius shrank from $36 R_{\odot}$ to $10 R_{\odot}$ at the same time. This shrinking of the donor star was enabled by the continuously increasing surface helium abundance during the mass transfer (Fig. 9): the donor star starts the mass-transfer phase as an early B-type supergiant ($T_{\text{eff}} \simeq 25$ kK) and ends it as a late-type WNh star ($T_{\text{eff}} \simeq 50$ kK).

Figure 9 also gives an indication of the X-ray luminosity that might be expected from binaries similar to our system d2ns0. In the evolutionary calculations, we assumed Eddington-limited accretion onto the NS, which would produce an X-ray luminosity of the order of $10^{39} \text{ erg s}^{-1}$ (dashed horizontal line), comparable to what is found in some SGXBs. However, Fig. 9 also shows that if the NS could accrete at super-Eddington rates, X-rays of up to $10^{41} \text{ erg s}^{-1}$ could be achieved. We discuss this possibility further in Sect. 5.1.

The mass transfer lasts for about 0.25 Myr with a mass-transfer rate of $3 \times 10^{-6} M_{\odot} \text{ yr}^{-1}$, which is two orders of magnitude above the Eddington limit of $3.6 \times 10^{-8} M_{\odot} \text{ yr}^{-1}$ of an NS and corresponds to an accretion luminosity $2.5 \times 10^{40} \text{ erg s}^{-1}$ (Fig. 9). The orbital period decreases from nine days to one day. Because the mass-transfer rate is much higher than the Eddington-accretion limit, most of the transferred mass in this calculation is re-emitted. According to Eq. (15), the orbital separation shrinks exponentially with the mass ratio. Because $q \propto M_D$ and M_{RLO} is roughly constant during most of the mass-transfer phase, the orbital separation also shrinks exponentially with respect to time.

During the mass transfer, about $1.5 M_{\odot}$ are removed. Figure 10 shows the evolution of the donor star during the mass-transfer phase in the Hertzsprung–Russel diagram. The evolutionary track starts at $T_{\text{eff}} \simeq 25$ kK). As discussed before, the donor star becomes hotter and slightly more luminous during the mass-transfer phase. Its temperature remains for the longest time between 25 and 40 kK, which coincides with the regime where SGXB donor stars are observed (cf. Sect. 6.1).

The connection of increasing surface helium abundance and increasing effective temperature has been recognized before by Brott (2011) and Köhler et al. (2015) for the evolution of massive single stars. In the cited works, the increasing surface helium abundance was due to rotational mixing and strong wind mass loss. Therefore only massive stellar models ($> 60 M_{\odot}$) with high rotational velocities evolved to the hot part of the Hertzsprung–Russel diagram during core hydrogen burning.

4.2. Models without stellar winds

We first discuss the binary models with a shallow helium gradient of $0.04 M_{\odot}^{-1}$, neglecting stellar wind mass loss. Figure B.2 shows the evolution of mass-transfer rate, orbital period, and donor mass with time for binary models a1bh0, b1bh0, c1bh0, d1bh0, and e1bh0. Of these, models b1bh0 and c1bh0 undergo an extended phase of mass transfer of 0.5 Myr and 0.15 Myr, respectively. Despite the rather high mass ratio of $q \simeq 4$, this is much longer than the thermal timescale of the donor star ($\sim 10^4$ yr).

Figure B.2 also shows the X-ray luminosity corresponding to the mass-transfer rate, assuming an accretion efficiency of a non-rotating BH ($\eta = 0.06$). Because the accretion rate might be

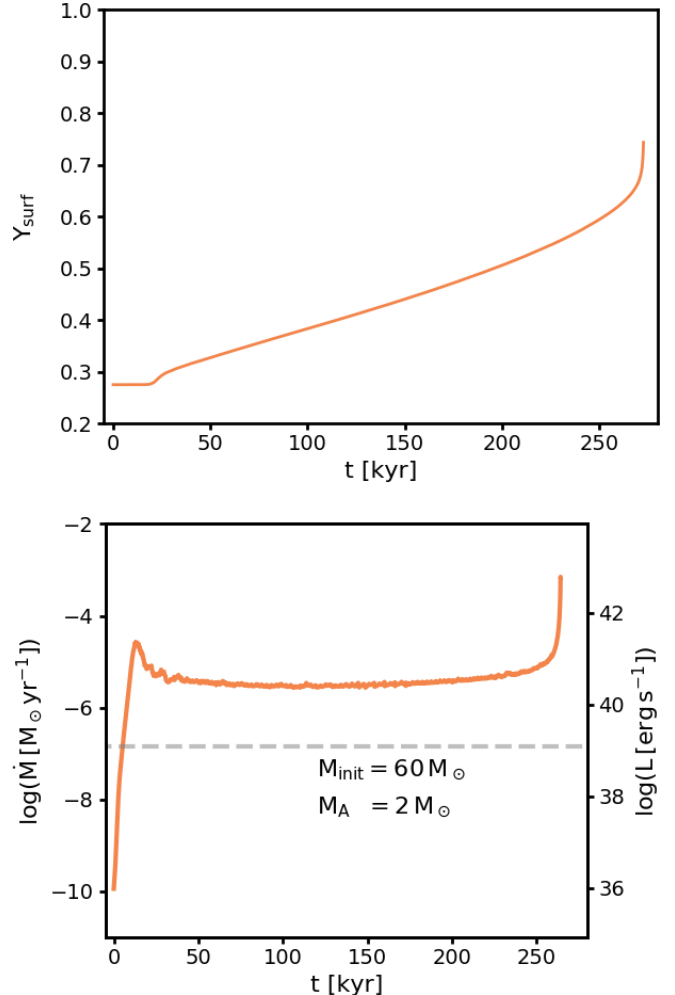


Fig. 9. Evolutionary properties of our model d2ns0, neglecting a $2 M_{\odot}$ NS companion and stellar winds. *Top panel:* surface helium mass fraction of the donor star as function of time during the mass-transfer phase. *Bottom panel:* evolution of the mass-transfer rate for the same model (left Y-axis). The right axis indicates the X-ray luminosity corresponding to the mass-transfer rate (not Eddington limited) assuming an accretion efficiency of $\eta = 0.15$. The dashed line gives the Eddington accretion limit for the NS that is applied in this calculation. Despite the high initial mass ratio of 16.8, the model settles into a stable mass transfer for about 0.25 Myr, with a mass-transfer rate of about the rate of the mass transfer on a nuclear timescale.

Eddington limited, this shows the highest achievable X-ray luminosity, where realistic values are expected between this and the value corresponding to the Eddington-accretion rate for a non-rotating BH. For super-Eddington accretion in these systems, a luminosity up to $\sim 10^{40} \text{ erg s}^{-1}$ could be achieved. This matches the order of magnitude of X-ray luminosities that are observed in ultra-luminous X-ray sources. We note that our models do not only show a high mass-transfer rate, but also a long X-ray lifetime.

It is a remarkable feature of the two binary models b1bh0 and c1bh0 that the mass-transfer rate increases steeply after some hundred thousand years. This occurs at the time where the flat inner part of the helium profile ($Y(m) = 0.8$; cf. Fig. 8) reaches the surface, supporting the idea that a steep H/He gradient is needed to stabilise the mass transfer. As soon as the helium profile close to the surface is flat again, the mass transfer becomes unstable, as expected for a high mass ratio.

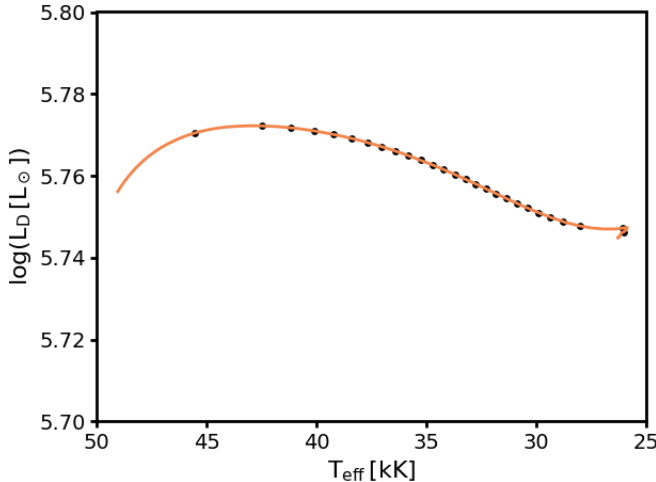


Fig. 10. Hertzsprung–Russel diagram for the donor star of binary model d2ns0. Black dots correspond to time differences of 10^4 yr.

Why do only models b1bh0 and c1bh0 show a long-term mass transfer? As shown by Fig. 8, the donor star of model a1bh0 contains a massive hydrogen-rich envelope. The companion has to remove about $5 M_\odot$ to dig out the H/He transition layer. By doing so, the orbit shrinks dramatically (cf. Table B.1). When we assume that most of the transferred mass is re-emitted, we indeed find according to Eq. (15) that $a/a_0 = 0.42$. This means that the orbital separation and hence the donor radius halve even before the helium gradient scratches the surface.

The mass transfer in models d1bh0 and e1bh0, on the other hand, is not long-term stable because the donor star has already lost so much mass that the helium-rich plateau is close to or even at the surface at the beginning of mass transfer, as is shown in Fig. 8. The donor star in model d1bh0 needs to lose only $1 M_\odot$ to find the flat helium profile in its outer envelope. For a mass-transfer rate on a nuclear timescale of $2 \times 10^{-5} M_\odot$ (Fig. B.2), it would take only $\sim 50 000$ yr to remove this layer. This is of the order of the thermal timescale. This means that mass-transfer on a nuclear timescale can hardly be distinguished from a from a runaway mass-transfer on a thermal timescale.

The evolution of donor models a1 and e1 are also shown, including an NS companion in Fig. B.1. None of these binary models undergoes mass transfer on a nuclear timescale. This is expected because Fig. 8 suggests a maximum mass–radius exponent of $\zeta_R \sim 10$. Because the initial mass ratio is ~ 20 , we find according to Fig. 1 $\zeta_L \sim 30$ and thereby $\zeta_R < \zeta_L$. The Roche radius is more sensitive to mass transfers than the donor radius, therefore a runaway on a thermal timescale is unavoidable. Thus, the mass transfer for donor models a1ns0 and e1ns0 is not sufficiently stabilised by the helium gradient to allow an evolution on a nuclear timescale.

However, our models with a steeper H/He gradient can lead to mass transfer on a nuclear timescale in the case of an NS accretor as well, as we showed in Sect. 4.1. Figure B.1 displays the evolution of the mass-transfer rate for our models a2ns0 to e2ns0, which differ from models a1ns0 to e1ns0 only in the slope of the helium gradient. We see that model d2ns0 alone undergoes mass transfer on a nuclear timescale because the mass ratio is more extreme than in the case of BH accretors. Still, for NS accretors, mass transfer on a nuclear timescale is also clearly possible if the outer envelope of the donor star has a steep H/He gradient.

Finally, Fig. B.2 shows the mass-transfer rates and corresponding luminosities of our binary models that are composed of a donor with a steep H/He gradient ($dY/dm = 0.4 M_\odot^{-1}$) and a $10 M_\odot$ BH companion (models a2bh0 to e2bh0). Similar to the case of donors with the shallower H/He gradient, only models c2bh0 and d2bh0 develop mass transfer on a nuclear timescale. However, because of the higher mass–radius exponents of models c2bh0 and d2bh0, the mass-transfer rates remain somewhat lower. Because of this, and because the initial donor radii of models c2bh0 and d2bh0 are somewhat larger than those of models c1bh0 and d1bh0, the mass transfer lasts for about 650 000 yr in both cases.

Both donor stars start to contract towards core helium ignition, such that the mass-transfer rate drops, and we end our calculations. We consider the further evolution of our systems qualitatively in Sect. 7.

4.3. Models including stellar winds

We showed that our binary models may undergo long-term mass transfer if the H/He transition layer of the donor star is close to the surface. Furthermore, in order to obtain mass transfer on a nuclear timescale, the H/He gradient needs to be steeper for NS accretors than for BH accretors because of the more extreme mass ratio in the former. Here, we debate the question whether an additional mass loss due to a stellar wind mass from the donor star could have an additional, perhaps stabilising, effect. To investigate this, we performed the same binary calculations as in the previous subsection, but with an additional constant donor wind mass-loss rate of $10^{-6} M_\odot \text{ yr}^{-1}$, or, alternatively, with the mass-loss rate as given by Vink et al. (2001). We restrict these calculations to the donor star models that include the steep H/He gradient (donor models a2 to d2).

We start our discussion with the binaries that host a BH accretor (Fig. B.2). Comparing the calculations that include the two wind recipes to those without any wind, we find that they differ only slightly in the case of a constant mass-loss rate. The most important difference here is that the mass-transfer rate does not exceed the Eddington-accretion limit in the late phase of mass transfer when a wind is included. The X-ray lifetime as well as the orbital separation do not change very much compared to Fig. B.2. This is to be expected because the wind mass-loss rate of $10^{-6} M_\odot \text{ yr}^{-1}$ is comparable to the mass-transfer rate in this case.

The situation is different when we include Vink’s mass-loss scheme. The predicted mass-loss rates are higher by an order of magnitude than the constant mass-loss rate discussed before ($\dot{M}_w \sim 10^{-5} M_\odot \text{ yr}^{-1}$), as shown with the dotted line in Fig. B.2. Vink’s wind mass-loss rate in our models is of the same order or even higher than the mass-transfer rate on a nuclear timescale for the corresponding binary models that are inferred without any stellar wind. This means that the donor star can shrink only due to its own wind mass loss. Mass transfer does not occur on a nuclear timescale because the Roche-lobe overflow is no longer self-regulated. In one case (model d2bhv), Roche-lobe overflow is not even initiated because the donor avoids any expansion. As discussed above, any stellar wind will expand the orbital separation. The fast-shrinking donor radius and the expanding orbital separation drive the systems far away from Roche-lobe filling. On the other hand, when the hydrogen-rich envelope is not yet removed or when the former convective core with a flat helium gradient is already at the surface, the radius is no longer sensitive enough to mass loss. In these cases, even a strong stellar wind does not help to maintain a stable system.

In the case of NS accretors, we find that a donor wind could have a substantially stabilising effect. This is shown in the example of model d2bhc in Fig. B.1, for which a constant mass-loss rate of $10^{-6} M_{\odot} \text{ yr}^{-1}$ extends the mass-transfer phase from 250 kyr in case of no wind to more than 600 kyr. However, a higher stellar wind mass-loss rate can have the opposite effect here as well. Model d2bvh does not undergo Roche-lobe overflow. The reason is that model d2 is the donor model with the highest ζ_R (cf. Fig. 8). In the definition of the mass–radius exponent (Eq. (6)), the timescale of radius change reads $\tau = R/\dot{R}$ as $\tau = \zeta_R^{-1} M/\dot{M}$. When the Vink mass-loss recipe is applied, the mass-loss timescale is of the order of the nuclear timescale. Because $\zeta_R \sim 30$ for donor model d2, the timescale for radial changes is much shorter than the nuclear timescale. This means that changes in donor radius are due to the intrinsic mass loss, which decreases the radius in our models, and not to nuclear processes, which would expand the star. This results in a rapid radial shrinking of the donor star even before mass transfer is initiated. When ζ_R is smaller (models a2, b2, c2, and e2) or the mass-loss timescale is longer than the nuclear timescale, which is the case when the constant mass-loss rate is applied, the nuclear evolution of the donor star can increase the radius initially and thus initiate the mass transfer.

We conclude that the donor star winds may play an important role in determining the duration of the mass-transfer phase and thus the X-ray lifetime of SGXBs, which they may extend or decrease. We emphasise that the mass-loss rates of helium-enriched OB supergiants are uncertain by more than a factor of two (Ramírez-Agudelo et al. 2017). In addition, wind clumping (El Mellah et al. 2018) and X-ray emission in SGXBs may affect the donor star wind (e.g. Sander et al. 2018). A more detailed study of the influence of the donor wind on the SGXB evolution is therefore clearly warranted, but is beyond the scope of our present paper.

4.4. Orbital period derivatives

As discussed in Sect. 2.3, mass transfer induces changes in orbital separation. These changes may be observed as changes in orbital period. To show the effect of mass transfer due to Roche-lobe overflow on the orbital period, we derive expressions for the orbital period derivative for the case of pure isotropic re-emission ($\beta = 1$), and for conservative mass transfer ($\epsilon = 1$). Equations (15) and 16 describe the change in orbital separation for these cases.

The derivative of Kepler's third law with respect to time leads to

$$\frac{\dot{P}}{P} = \frac{3 \dot{a}}{2a} - \frac{1}{2} \frac{\dot{M}}{M}. \quad (27)$$

When the change of orbital separation is expressed as $a/a_0 = f(q)$, as in Eqs. (15) and 16, then

$$\frac{\dot{a}}{a} = \frac{d \ln f}{dq} \dot{q}. \quad (28)$$

With $\dot{M} = \dot{M}_1$ for the case of isotropic re-emission, we find

$$\frac{\dot{P}}{P} = \left(3q - 2 \frac{q}{q+1} - 3 \right) \frac{\dot{M}_1}{M_1}, \quad (29)$$

and with $\dot{M} = 0$ for conservative mass transfer,

$$\frac{\dot{P}}{P} = 3(q-1) \frac{\dot{M}_1}{M_1}. \quad (30)$$

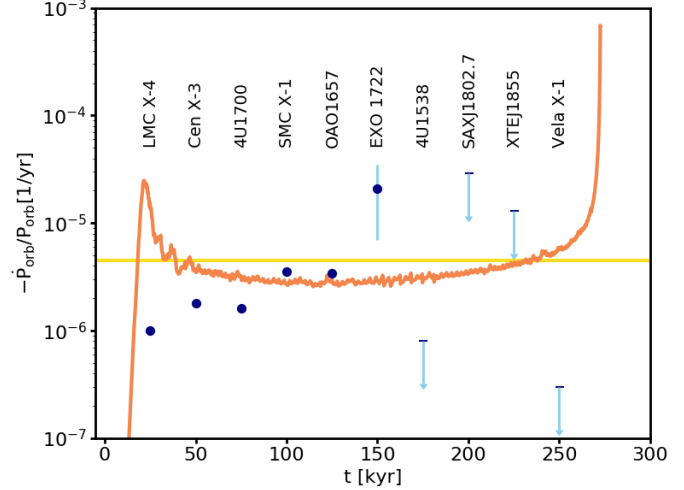


Fig. 11. Evolution of the orbital period derivative \dot{P}/P of our model d2ns0 shown in Fig. 9 as given by the numerical simulation (orange line), together with our analytic estimate for the same model (see text; yellow line). Overplotted are the empirical decay rates of ten SGXBs as inferred by Falanga et al. (2015), who give six measured values with 1σ error bars (blue dots; for most of these, the error bar is smaller than the size of the dot) and four upper limits (blue arrows). We note that the time axis has no meaning for the period derivatives of the observed sources.

For both cases, that is, from Eqs. (29) and (30), a high mass ratio ($q \gg 1$) implies

$$\frac{\dot{P}}{P} \simeq 3q \frac{\dot{M}_1}{M_1}. \quad (31)$$

Thus, we expect the orbital period derivative for mass transfer driven by Roche-lobe overflow to be essentially independent of the accretion rate of the compact object, as long as the mass ratio is high. Furthermore, $\dot{M}_1 < 0$ implies a decrease in orbital period during mass transfer, regardless of how conservative the mass transfer is. Hence, isotropic re-emission and conservative mass transfer lead to an orbital decay at a very similar rate.

The orbital period of model d2ns0, with a donor mass of $\sim 30 M_{\odot}$ (Table B.1) and a mass-transfer rate of $\sim 3 \times 10^{-6} M_{\odot} \text{ yr}^{-1}$ (Fig. 9), decreases with $\dot{P}/P \approx -4.5 \times 10^{-6} \text{ yr}^{-1}$ for either a BH or NS companion. For donor models c2bh0 and d2bh0 with BH companions (Fig. B.2), the orbital decay rate is about one order of magnitude lower, with $\dot{P}/P \approx -6 \times 10^{-7} \text{ yr}^{-1}$. If the H/He gradient is shallower, as in model b1bh0 (Fig. 13), the orbital decay is faster by more than one order of magnitude ($\dot{P}/P \approx -10^{-5} \text{ yr}^{-1}$).

Falanga et al. (2015) compiled and evaluated the orbital period changes of ten eclipsing SGXBs from a multi-decade monitoring campaign. Five sources in their sample showed a significant change in orbital period. All of these five sources showed decaying orbits ($\dot{P}/P < 0$), with rates $|\dot{P}/P| \sim 1 \dots 3 \times 10^{-6} \text{ yr}^{-1}$. The source EXO 1722-363 shows an orbital decay rate of $\dot{P}/P = (-21 \pm 14) \times 10^{-6} \text{ yr}^{-1}$. Although the uncertainty is smaller than the measured value, Falanga et al. (2015) did not label this source as significant. We note that the orbital decay rate is consistent with zero within the 2σ error. For four more sources, no orbital decay within the 1σ environment was observed. We used the 1σ uncertainty provided by Falanga et al. (2015) as an upper limit for the orbital decay rate.

In Fig. 11 we compare the empirical values with the \dot{P}/P -evolution of our model d2ns0 with an NS accretor together with

our analytic estimate for its period derivative. All five sources for which an orbital decay rate was measured with high significance are in good agreement with the decay rate of our model. This means that deviations between the theoretical model and the observed orbital decay rate are not much larger than a factor of two (the time coordinate for the empirical values in Fig. 11 has no meaning). This is remarkable because our models were not tailored to reproduce the observed sources.

The only source that does not fit our model well is Vela X-1. The upper limit of the decay rate lies one order of magnitude below our prediction. Equation (29) suggests that the mass-transfer rate must not exceed a few times 10^{-7} yr^{-1} in order to obtain a decay rate below the upper observation limit. We did not find such low mass-transfer rates in our models with NS accretors. We therefore conclude that the orbital change of Vela X-1 is at least not modelled with our simple prescription. This does not completely rule out Roche-lobe overflow as a possible accretion mode for this source. The low orbital decay rate may be explained if Vela X-1 were just in a transition state between wind-dominated accretion and atmospheric Roche-lobe overflow.

We note that orbital decay may be more complex than discussed in this section. In our simplified description, effects such as tidal interaction (Lecar et al. 1976; van der Klis & Bonnet-Bidaud 1984; Safi Harb et al. 1996; Levine et al. 2000) or the Darwin instability (Lai et al. 1994) are neglected. These mechanisms may also be able to drive orbital decay that is in agreement with the observed decay rates (Kelley et al. 1983; van der Klis & Bonnet-Bidaud 1984; Levine et al. 1993; Rubin et al. 1996; Safi Harb et al. 1996; Jenke et al. 2012). In any case, our calculations show that the observed orbital decay rates of SGXBs may be explained by the simple isotropic re-emission model as long as the mass transfer occurs on the nuclear timescale. The fact that highly non-conservative and conservative mass transfer show the same orbital decay rates for high mass ratios implies that SGXBs and ULXs should show similar values of \dot{P}/P within this prescription.

5. Binary evolution models for ULXs

The Eddington luminosity of a $10 M_{\odot}$ BH is about $3 \times 10^{39} \text{ erg s}^{-1}$. Brighter X-ray sources are considered ultraluminous X-ray sources (ULXs). As the mass-transfer rates on nuclear timescales in our models are in the range $10^{-5} \dots 10^{-6} M_{\odot} \text{ yr}^{-1}$, some of them might be considered as models for ULXs with up to $\sim 10^{41} \text{ erg s}^{-1}$ (cf. Table B.1) if the entire transferred matter were accreted.

5.1. ULXs with neutron star

It has recently been discovered that several ULXs show X-ray pulsations, which is only expected if the compact accretor is an NS (Kaaret et al. 2017). While the Eddington limit of NSs is well below $10^{39} \text{ erg s}^{-1}$, some of the X-ray pulsating ULXs show X-ray luminosities that are clearly in the ULX regime (Bachetti et al. 2014). While beaming effects might help to explain the very high X-ray luminosities (King 2001), some NSs in ULXs have been shown to experience an extreme spin-up on a short timescale, which may require actual accretion onto the NS at rates much above the classical Eddington limit (Israel et al. 2017a, but see King & Lasota 2019). One way to understand such high luminosities from accreting NSs is to invoke magnetic fields with a field strength above $\sim 10^{13} \text{ G}$, which could reduce the radiative opacity of the accreted matter and thus raise the Eddington limit (Herold 1979; Ekşioğlu et al. 2015; Israel et al. 2017a).

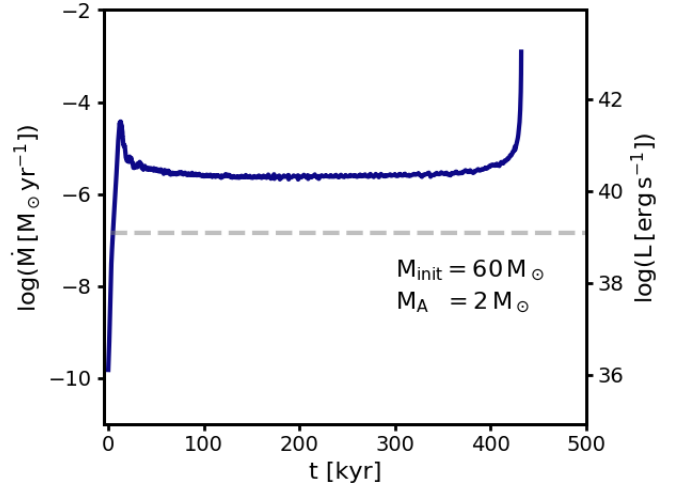


Fig. 12. Evolution of the mass-transfer rate for the same model as shown in Fig. 9 (left Y-axis) (Model d2ns0), but here calculated assuming conservative mass transfer.

It has also been suggested that ULXs that host NSs might host intermediate-mass donor stars (Karino 2016). However, Tauris et al. (2017) argued that corresponding models only work for donor star masses below $7 M_{\odot}$. The donor star in the ULX pulsar in NGC 5907 is constrained to be higher than $\sim 10 M_{\odot}$, and its orbital period is found to be $P_{\text{orb}} = 5.3_{-0.9}^{+2.0} \text{ d}$ (Israel et al. 2017a). Motch et al. (2014) determined the orbital period of the ULX pulsator NGC 7793 P13 to $\sim 64 \text{ d}$, where the mass donor is a B9Ia supergiant of about $20 M_{\odot}$ (Israel et al. 2017b). Except for being ultra-luminous, their parameters are reminiscent of those of the SGXBs.

Our model d2ns0 in Sect. 4.1 obtains a mass-transfer phase on nuclear timescales, with accretion rates that would lead to X-ray luminosities above $10^{40} \text{ erg s}^{-1}$ if the NS could accrete all the matter. In order to probe this situation, we repeated the calculation displayed in Fig. 9, but allowed the NS to accrete the entire transferred matter. While this may not be realistic because a fraction of the transferred matter may always be expelled, it provides the limiting case, with more realistic models bounded by this and the Eddington-limited calculations shown in Sect. 4.1.

Figure 12 shows that the long duration of the X-ray bright mass-transfer phase is not only maintained by the conservative accretion model, but the time span of X-ray emission is almost doubled compared to the Eddington limited model. This is understandable because the mass of the NS grows significantly here, it would likely eventually collapse into a BH, as a total of about $1.4 M_{\odot}$ is transferred, and the thus-reduced mass ratio leads to slightly lower mass transfer rates. However, its X-ray luminosity could still be well over $10^{40} \text{ erg s}^{-1}$ for more than 400 000 yr.

Our models do not attempt to reproduce any of the observed ULXs. However, they show that ULXs with NS accretors may accrete from Roche-lobe overflow for much longer than a thermal timescale of the donor star if their donor star is a helium-enriched supergiant.

5.2. Black-hole companions

Clearly, ULXs can form in binaries when one component is a sufficiently massive BH and the companion transfers mass at a high enough rate. In this situation, it has been recognised that beaming (King 2001; Körding et al. 2002), photon-bubbles (Begelman 2002; Ruszkowski & Begelman 2003), or magnetic

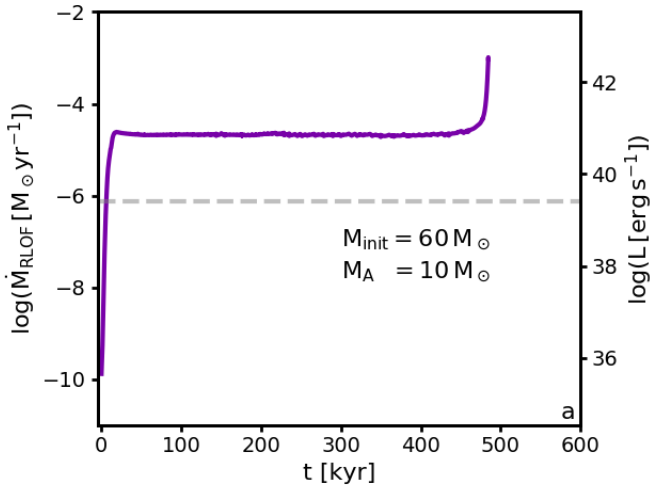


Fig. 13. Evolution of the mass-transfer rate as function of time for our model b1bh0, which starts with a $42.5 M_{\odot}$ supergiant and a $10 M_{\odot}$ BH in an 18 d orbit.

accretion disc coronae (Socrates & Davis 2006) could help to raise the apparent or true Eddington limit, such that ULXs of up to $10^{41} \text{ erg s}^{-1}$ can be explained with stellar mass BHs (Madhusudhan et al. 2008; Marchant et al. 2017).

In order to obtain non-negligible ULX lifetimes, the donor star in these models is usually of comparable or smaller mass than the BH, which severely limits the expected number of ULXs. In our models with helium-enriched donor stars, this restriction can be dropped. Assuming a $10 M_{\odot}$ BH, the initial mass ratio expected in such systems is significantly lower than in the case of an NS companion. Consequently, we find mass transfer on a nuclear timescale in more system when a BH is assumed to be present. In Fig. 13 we highlight our models b1bh0 with a donor star of initially $42.5 M_{\odot}$, which provides a high mass-transfer rate to an initially $10 M_{\odot}$ BH for almost 0.5 Myr, and which could provide an X-ray luminosity of $\sim 10^{41} \text{ erg s}^{-1}$ when super-Eddington accretion is assumed.

In our models with NS accretors, only donor stars with steep H/He gradients led to Roche-lobe overflow phases on nuclear timescales. The mass ratio in systems with $10 M_{\odot}$ BH accretors is lower by five times, which leads to a slower shrinking of the orbit. Therefore even the ten times shallower H/He gradient is sufficient to achieve Roche-lobe overflow on nuclear timescales in these systems. This significantly may widen the parameter space for BH-ULX systems.

6. Implications for the origin of SGXBs

The way in which the donor stars of our supergiant and ULX binary models have been set up may raise doubts whether they are applicable for interpreting the observed systems. In particular, we have shown that mass transfer on a nuclear timescale was only achieved when the chemically homogeneous part of the hydrogen-rich envelop was removed before the mass transfer to the compact companion starts. This raises the question whether this may occur in reality.

6.1. Clues from observations

The first idea, that is, that the H/He transition layer is close to the surface of the donor star, appears to be supported by several observations. Using the data of Conti (1978) and Falanga et al.

(2015), who determined the effective temperatures and surface gravities of several SGXB donors, we can compare the observed donor stars with stellar models in a spectroscopic Hertzsprung–Russel diagram (Langer & Kudritzki 2014). In this diagram, the ordinate values are proportional to the luminosity-to-mass ratio of the stars. Figure 14 shows that the SGXBs do not match single-star tracks of the corresponding mass. This has already been noticed by Conti (1978). For instance, the donor star in Vela X-1 appears close to the $100 M_{\odot}$ track, while its mass, inferred from radial velocity measurements, is only $\sim 25 M_{\odot}$.

Because removing the stellar envelope decreases the mass but does not affect the luminosity significantly, it is not surprising that some of our SGXB models fit the spectroscopic Hertzsprung–Russel diagram position of Vela X-1 and other SGXB donors better than the single-star models. Figure 14 shows that model c2bh0 approaches the position of Vela X-1 near the end of its mass-transfer phase, where the mass of the donor star is about $33 M_{\odot}$ (cf. Table B.1), suggesting an initial donor mass closer to $60 M_{\odot}$. While Vela X-1 has no BH but an NS companion, this comparison shows that the luminosity-to-mass ratio (L/M) of our model may be close to that of the donor star in Vela X-1, implying that it did lose its hydrogen-rich envelope at an earlier stage of its evolution. Figure 14 shows that in all cases for which effective temperature and surface gravity could be determined, the corresponding L/M is well above that of the single-star models. This indicates that all the donor stars have already lost a significant portion, and perhaps all, of their non-enriched massive envelope.

Even more direct evidence for this comes from model atmosphere calculations and fits to observed donor star optical spectra of the SGXBs. An enhanced surface helium abundance was found in 4U 1700-377 (Clark et al. 2002), GX301-2 (Kaper et al. 2006), and Vela X-1 (Sander et al. 2018). A surface helium enrichment is expected to occur only after the chemically homogeneous non-enriched part of the stellar envelope is removed. The implication of the observed helium enrichments is that as a result of mass loss, whether by stellar winds or by Roche-lobe overflow, the donor star radii are currently decreasing. The remarkable circumstance that the donor stars in these systems are nevertheless very near Roche-lobe filling may imply that the orbit shrinks at the same time. This is only expected if the systems were currently undergoing Roche-lobe overflow. We conclude that SGXB observations provide ample evidence in support of the assumption that their donor stars have lost the non-enriched massive hydrogen envelope in a previous evolutionary phase.

We note that it is a consequence of the properties of the SGXBs we discussed that the initial mass of the NS progenitor in these systems must have been quite high, that is, higher than 30 to $40 M_{\odot}$. While BHs are generally expected to form from such massive stars, the presence of NSs in SGXBs could relate to the “island of explosability” at high mass that was found by Ugliano et al. (2012) and Sukhbold et al. (2016) in parametrised core-collapse explosion models. Brown et al. (2001) also suggested that stripped-envelope massive stars, that is, mass donors in close binary systems, tend to form NSs even for initial masses as high as $40 M_{\odot}$.

6.2. Clues from stellar models

The question to ask at this stage is through which mechanism the donor stars in SGXBs lost their H-rich envelopes before they entered the X-ray binary stage. As their initial masses appear all very high, it might be wondered whether the ordinary radiation-driven winds of massive stars are sufficient to reach this goal. Based on the massive star models in the literature (Smith 2014;

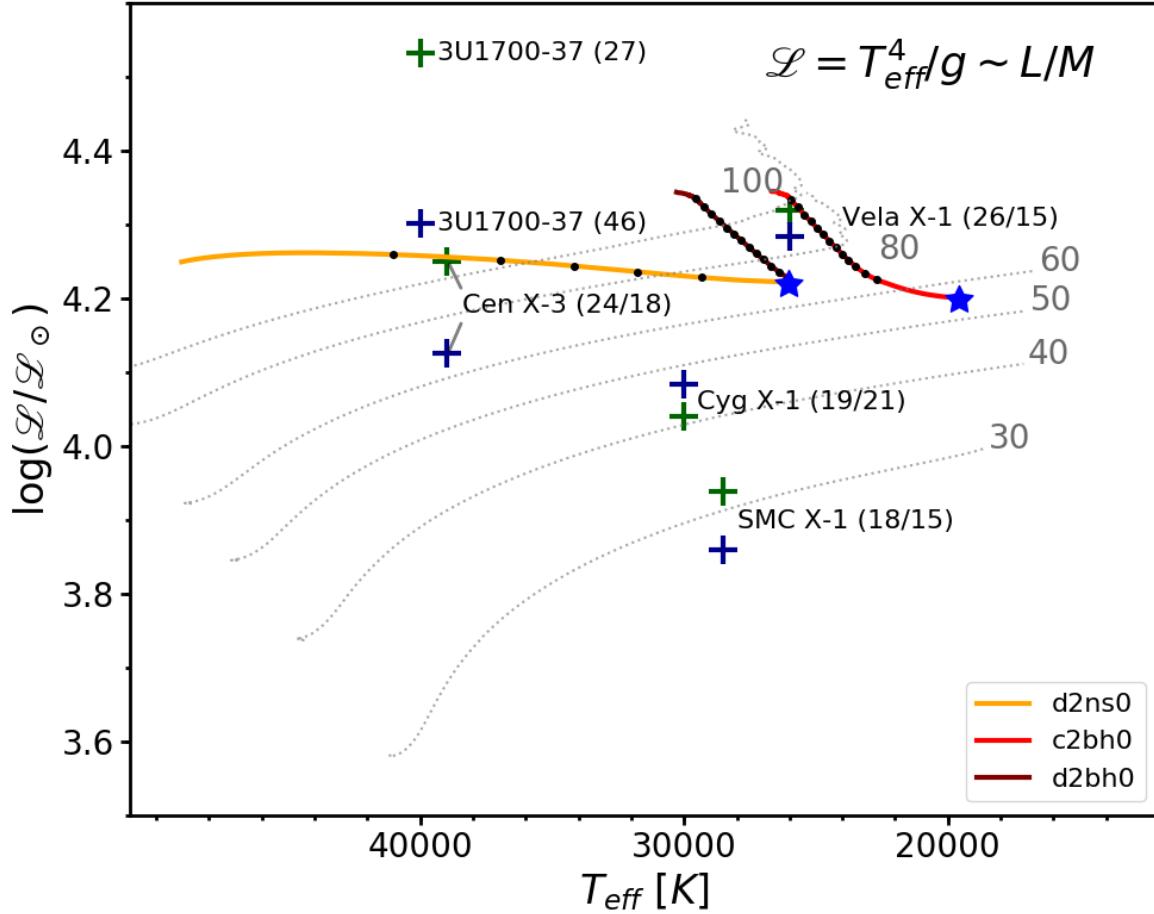


Fig. 14. Spectroscopic Hertzsprung–Russel diagram including data for SGXBs from Conti (1978; green crosses) and Falanga et al. (2015; blue crosses). The name of the source is added to the symbols. The parentheses include the donor masses as measured by Conti (1978) and Falanga et al. (2015). The grey dashed lines are tracks from single-star evolutionary models (Brott et al. 2011). The grey numbers indicate the initial mass of the corresponding stellar model. Red and orange lines indicate the evolution of our binary models. The starting point of each model is labelled with a blue star. The black dots correspond to time steps of 50 000 years.

Brott et al. 2011; Vink et al. 2001) and considering that the wind mass-loss rates for these very massive stars cannot be predicted to better than within a factor of ~ 2 (with some of this coming from the metallicity spread in the Galaxy, e.g.), it may not be a problem to remove the required amounts of mass by stellar winds.

However, this mechanism would require a significant amount of fine-tuning. Because stellar wind mass loss always widens the orbits of binary stars (cf. Eq. (14) in Sect. 2.3), the expansion of the OB star needs to catch up with the increasing Roche radius at exactly the time when the H/He gradient appears near the stellar surface. Figure 1 shows that this is not impossible because the massive star models tend to increase in size as mass is being removed until shortly before helium-enriched layers appear at the stellar surface (see also Fig. 15 below). Only systems within a narrow initial period range would be able to fulfil the timing constraint, however.

The more common situation may be that the donor star fills its Roche radius at a time when the H/He-interface layer is still buried beneath a massive hydrogen-rich envelope. As we showed in Sect. 5, this leads to very high mass-transfer rates and likely to a CE evolution (see also Hjellming & Webbink (1987)). Here, the Roche-lobe overflow could start in the advanced phase of core hydrogen burning, or after core hydrogen exhaustion. While it is beyond the scope of this paper to comprehensively investigate the outcome of such an evolution, we provide a simple estimate as follows.

We show the radius evolution of our $60 M_{\odot}$ model (blue line), assuming mass loss on a nuclear timescale, in Fig. 15, together with the evolution of the Roche radius for our sequences a2bh0 to e2bh0 during the mass-transfer evolution (red lines). At the end of the mass-transfer evolution, a CE phase is expected. The yellow lines in Fig. 15 show the value of the donor Roche radius at a given donor star mass if the CE were removed at the corresponding time, where the Roche radius is obtained from equating the energy release ΔE from the decaying BH orbit with the envelope binding energy E_{bin} of the envelope above this orbit, where

$$\Delta E = -\frac{GM_{D,i}M_A}{2a_i} + \frac{GM_DM_A}{2a} \quad (32)$$

and

$$E_{\text{bin}} = \int_{M_D}^{M_{D,i}} -\frac{Gm}{r} + u dm \quad (33)$$

is the effective binding energy, which includes gravitational binding energy reduced by the thermal energy. Here, $M_{D,i}$ is the donor star mass at the beginning of the CE evolution, M_D is its mass at a putative end stage of the CE evolution, and a_i and a are the corresponding orbital separations. The Roche radius during RLO was directly inferred from the binary calculation. At the point where the binary calculation stops, we used the last calculated donor model, orbital separation, and accretor mass to compute the Roche radius as function of the donor mass as described

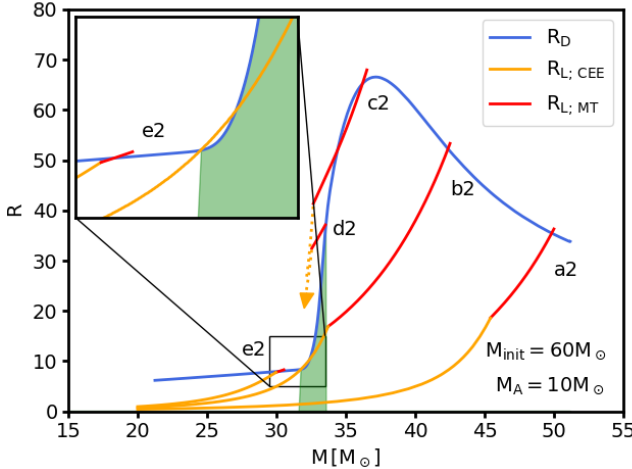


Fig. 15. Donor radius as a function of mass in thermal equilibrium (blue). The red lines show the Roche radius as a function of donor mass during the binary calculation that includes a $10 M_{\odot}$ accretor and no stellar wind of the donor. The yellow lines show the Roche radius after the binary calculation has stopped and CE is initiated. The orbital separation and hence the Roche radius was inferred using the energy budget description of CE. The green area marks the position of the H/He transition layer.

above. The stellar model of the donor at the beginning of the CE evolution defines the envelope binding energy E_{bin} as function of the remaining mass M_{D} . The condition of Roche-lobe filling at the beginning of the CE evolution sets the orbital separation at that time for a given accretor mass. Assuming the accretor mass remains constant allows us to compute the Roche radius after the CE evolution as a function of donor mass M_{D} at that time.

The evolution of our sequence a2bh0 in Fig. 15 provides a case where a merger appears to be the most likely outcome of the CE evolution. At its onset, the donor star mass is about $45 M_{\odot}$ and its H/He transition layer is buried beneath more than $10 M_{\odot}$ of hydrogen-rich envelope. At the same time, it is rather compact ($R_{\text{D}} \approx 20 R_{\odot}$) because of its high mass-transfer rate. The yellow line for sequence a2bh0 in Fig. 15 shows that there is no possible final mass after the CE evolution for which the donor Roche radius would exceed its thermal equilibrium radius. While the donor radius may be smaller than its thermal equilibrium radius during mass transfer or immediately after a CE ejection, the implication is that if at all, it would be able to fit into its Roche radius only for a thermal timescale or less. Afterwards, it would expand and merge with the companion.

However, the picture is different for sequence b2, which is also expected to quickly undergo a CE evolution (cf. Fig. B.2). Figure 15 shows that in this case, the yellow line indicating the donor Roche radius crosses the blue line for the thermal equilibrium radius of the donor. Consequently, this model opens the possibility of a successful CE ejection at a time when the H/He-transition layer of the donor star is at the stellar surface. After this, the expectation is that the nuclear-timescale expansion of the donor would cause it to fill its Roche-lobe again soon, allowing mass transfer on a nuclear timescale onto the compact companion.

While our estimate in Fig. 15 includes many simplifications and is not to be understood as a quantitative model, it shows the interesting possibility that SGXBs can be interpreted as post-CE systems. In this frame, the emerging of the H/He transition layer at the donor surface at the end of the CE evolution is not a matter of fine-tuning, but is naturally produced by the sharp drop of its thermal equilibrium radius at this time. Potentially, all the models with initial masses in between those of sequences b2 and c2

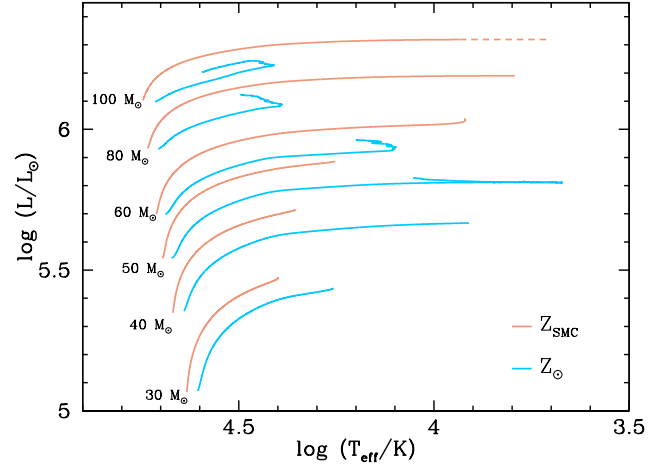


Fig. 16. Evolutionary tracks for solar and SMC metallicity during core hydrogen burning (Brott et al. 2011).

could follow this path. The evolution of sequence b2 shows that in this scenario, a significant portion, or even the main portion, of the hydrogen-rich envelope may be transferred to the compact companion in a mass-transfer event on a thermal timescale before the onset of the CE evolution. The higher this fraction, the higher the chances to avoid a merger during the CE evolution.

We may point out that there are tentative observational counterparts for this type of evolution: the enigmatic X-ray binary SS 433 appears to have a supergiant mass donor that provides mass at the thermal mass-transfer rate (Fabrika 2004). Within our picture, SS 433 may qualitatively correspond to our models b2bh0 or c2bh0 at the time of the first mass-transfer peak (cf. Fig. B.2). It would then evolve into an ordinary SGXB after going through a CE phase (model b2bh0), or after avoiding a CE phase (model c2bh0).

Finally, our CE scenario for the pre-SGXB evolution may relate to the so-called obscured SGXBs that have recently been discovered (Chaty 2013). The ejected envelope may provide enough circumstellar material to produce the obscuration.

6.3. Metallicity dependence

We point out that the scenario for producing the SGXBs, either by well-timed stellar wind mass loss, such that it starts Roche-lobe overflow when the H/He transition layers appear at the surface, or through a pre-mass-transfer CE phase, may be favoured in a high-metallicity environment such as our Galaxy. This becomes clear when we compare the evolutionary tracks of massive single stars for solar metallicity with those computed with an initial composition as that in the SMC (Fig. 16). It shows that the first scenario does not appear to be available at low metallicity: While at solar metallicity, the models lose enough mass to expose their H/He transition layers without the help of a companion star, the low-metallicity models never do this.

In the Milky Way, Humphreys & Davidson (1979) found that the most massive stars avoid the upper right part of the Hertzsprung–Russel diagram. This has been related to the Eddington limit and the instabilities in the so-called luminous blue variables (Lamers & Fitzpatrick 1988; Ulmer & Fitzpatrick 1998; Gräfener et al. 2012; Sanyal et al. 2015). The proximity of the Galactic supergiants to the Eddington limit will therefore likely also facilitate the loss of the hydrogen-rich envelope when a compact companion is present. As a result of the iron opacity, the phenomenon is shifted to much higher luminosities

and masses for low metallicities (Ulmer & Fitzpatrick 1998; Sanyal et al. 2017). Therefore, the mass of the hydrogen-rich envelop in SMC supergiants with compact companions, at the time they would likely fill their Roche-lobe, is likely much higher than in a comparable case in the Galaxy, and an immediate merger may be expected. While in the Milky Way, we have about as many SGXBs as BeXBs (Walter et al. 2015), only one SGXB is known in the SMC, but 81 confirmed BeXBs (Haberl & Sturm 2016). Our model may offer a natural explanation of this strong metallicity dependence.

A metallicity dependence would also be expected for the ULX application of our scenario. Our remarks about the donor stars in SGXBs also hold for ULX supergiant donors. This is particular relevant for ULXs with NS accretors because the mass ratio problem is the strongest in these sources. Consequently, we would preferentially expect ULXs with NSs at high metallicity. Our CE scenario may also have implications for understanding the generation of large-scale magnetic fields in stars. Based on the observation that magnetic white dwarfs are common in cataclysmic variables (CVs) but are absent in wide binaries (Wickramasinghe & Ferrario 2000) and Potter & Tout (2010) argued that the strong magnetic field in CVs with a magnetic white dwarf could be generated during their previous CE evolution. While their model appears only marginally successful, the idea may still apply. If it were transposable to massive X-ray binaries, it could imply that a CE phase in a pre-SGXB evolution may help to induce a strong field in the NS, with the effect of producing a ULX rather than an ordinary SGXB.

7. Evolution of SGXBs and SG-ULXs

We have ended our binary evolution calculations when either the mass-transfer rate exceeded $\sim 10^{-2} M_{\odot} \text{ yr}^{-1}$, or when the models became thermally unstable as a result of core hydrogen exhaustion. Therefore, we can only conjecture about the further evolution of our model binaries and about the evolution of the observed SGXBs and SG-ULXs.

From the time dependence of the mass-transfer rates of our models, it can be concluded that after the H/He transition layer is lost during the nuclear-timescale evolution, the mass-transfer rate increases steeply. This is the case for our models b1bh0 and c1bh0 with BH accretors (Fig. B.2), and for model d2ns0 with an NS accretor (Fig. B.1), also for conservative mass transfer (Fig. 12). According to Hjellming & Webbink (1987), who inferred a maximum mass ratio of 2.14 for a binary to be stable against dynamical runaway, the onset of a CE evolution in these models appears likely. Because at this stage, our models are rather compact and still possess a significant envelope with a hydrogen mass fraction of 20%, we assume that a merger would be the likely outcome.

In another suite of our models, the mass transfer on a nuclear timescale lasts until hydrogen is exhausted in the core of the donor. The ensuing contraction of the donor model leads to a sharp drop of the mass-transfer rate, and the Roche-lobe overflow phase stops (model d2nsc, Fig. B.1, and models d2bh0 and d2bh0, Fig. B.2). We would expect that a hydrogen shell source will ignite in these models, which will expand their envelopes and initiate a mass transfer on a thermal timescale. Again, using the criterion of Hjellming & Webbink (1987), we would expect this to evolve into a CE phase, with a merger of both components as the result. Only two of our models with a time-dependant stellar winds (models b2bhv and c2bhv with BH accretors) are expected to emerge as a Wolf–Rayet–BH binary.

However, our models are artificially constructed and are not self-consistently evolved from the zero-age main-sequence stage.

For models a1 to e1, whose transition layer contains the shallower H/He gradient, the slope is naturally expected from the receding convective core during hydrogen burning. However, the steeper H/He gradient in models a2 to e2 is perhaps only formed after core hydrogen exhaustion (Schootemeijer & Langer 2018). In core helium burning supergiants, the mass transfer on a nuclear timescale might then stop at the time of core helium exhaustion. It may not be excluded that in this case, a merger during the short remaining time to the collapse of the donor star can be avoided, and a short-period double compact binary emerges.

A further investigation of the post-mass-transfer evolution of more self-consistent SGXBs and SG-ULXs clearly appears warranted.

8. Conclusions

We have refuted the long-standing paradigm that mass transfer in binary systems with a high mass ratio must be unstable and can last for at most a thermal timescale of the donor star. We first produced single-star models with mass radius exponents (e.g. Fig. 2) that far exceed those required for stable mass transfer in binaries with high mass ratios (Fig. 1). We then calculated detailed binary evolution models for SGXBs with NS and BH components, and found mass transfer on a nuclear timescale in many of them, with initial donor-to-accretor mass ratios of up to ~ 20 .

The key for the stability of the mass transfer in our models despite the inevitably strong orbital contraction is that their surface helium abundance is increasing. Thereby, the donor stars deflate their radius by a factor of a few during the mass transfer, and evolve from supergiants into Wolf–Rayet stars.

While our models are artificially constructed and not derived from earlier phases of binary evolution, their key feature appears to be supported by observations because the SGXB donors generally appear to be helium rich and overluminous for their mass (Fig. 14).

Furthermore, our models facilitate understanding several observations. The first is the large number of observed SGXBs in the Milky Way, which is proportional to the duration of their X-ray phase. The latter is drastically extended by our models. The second is the discovery of ULXs with supergiant donor stars and NS accretors. Again, in the standard picture, their lifetime is expected to be extremely short. We showed an example with an initial mass ratio of 17 and a ULX phase that due to stable Roche-lobe overflow lasted for more than 400 000 yr.

We argue that the SGXBs in the Milky Way, and perhaps also the ULXs with NS accretors, may have formed in a CE evolution, during which the loss of the H-rich envelope of the donor star was facilitated as it reached its Eddington limit. Such a CE phase might be related to the dense circumstellar medium found in the Galactic obscured SGXBs. While this could remove the fine-tuning problem of producing the SGXBs in their current state, it could also explain the nearly complete lack of SGXBs in the SMC, where stars reach their Eddington limit only at much higher mass.

If ULXs with NS accretors were to correspond to our CE scenario, they would preferentially be expected at high metallicity, and be rare at low metallicity, analogous to the SGXBs. ULXs with massive BH accretors, on the other hand, might have a preference for low metallicities, where the final BH masses are expected to be higher.

This scenario may also shed light on the question of how magnetar fields are created. It would make the ULXs with NS accretors, in which accretion rates of more than two orders of magnitude above the Eddington limit are thought to be enabled by extreme NS magnetic fields, the more massive cousins of polars, that is, CVs in which a main-sequence star sheds mass

onto a magnetic white dwarf. These CVs are also thought to have undergone a previous CE evolution.

It is necessary to produce detailed progenitor models for SGXBs in order to validate the CE scenario. This may be useful as an understanding of the CE evolution of very massive stars as function of metallicity is also required to reliably predict the population of double BH binaries, into which some of the Galactic SGXBs might evolve. At the same time, there may be several avenues to provide stronger observational constraints to the CE evolution of very massive stars, including the search for binaries consisting of OB star and a BH or NS, many of which may have escaped detection so far.

Acknowledgements. We are grateful to Ed van den Heuvel and Philipp Podsiadlowski for useful comments and discussions. TMT acknowledges an AIAS-COFUND Senior Fellowship funded by the European Union's Horizon 2020 Research and Innovation Programme (grant agreement no 754513) and the Aarhus University Research Foundation.

References

Abbott, B. P., Abbott, R., Abbott, T. D., et al. 2016, *Phys. Rev. Lett.*, **116**, 061102

Abbott, B. P., Abbott, R., Abbott, T. D., et al. 2017, *ApJ*, **848**, L12

Apparao, K. M. V. 1985, *ApJ*, **292**, 257

Bachetti, M., Harrison, F. A., Walton, D. J., et al. 2014, *Nature*, **514**, 202

Basko, M. M., Sunyaev, R. A., Hatchett, S., & McCray, R. 1977, *ApJ*, **215**, 276

Begelman, M. C. 2002, *ApJ*, **568**, L97

Bird, A. J., Malizia, A., Bazzano, A., et al. 2007, *VizieR Online Data Catalog*: II/170

Bird, A. J., Bazzano, A., Bassani, L., et al. 2010, *ApJS*, **186**, 1

Blondin, J. M., & Owen, M. P. 1997, *ASP Conf. Ser.*, **121**, 361

Böhm-Vitense, E. 1958, *Z. Astrophys.*, **46**, 108

Bondi, H., & Hoyle, F. 1944, *MNRAS*, **104**, 273

Bozzo, E., Oskinova, L., Feldmeier, A., & Falanga, M. 2016, *A&A*, **589**, A102

Braun, H., & Langer, N. 1993, *Space Sci. Rev.*, **66**, 401

Brott, I. 2011, PhD Thesis, Sterrenkundig Instituut Utrecht, The Netherlands

Brott, I., de Mink, S. E., Cantillo, M., et al. 2011, *A&A*, **530**, A115

Brown, G. E., Heger, A., Langer, N., et al. 2001, *New Astron.*, **6**, 457

Chaty, S. 2013, *AdSpR*, **52**, 2132

Chaty, S., Rahoui, F., Foellmi, C., et al. 2008, *A&A*, **484**, 783

Clark, J. S., Goodwin, S. P., Crowther, P. A., et al. 2002, *A&A*, **392**, 909

Conti, P. S. 1978, *A&A*, **63**, 225

Cox, J. P., & Giuli, R. T. 1968, *Principles of Stellar Structure* (New York: Gordon and Breach)

Dalton, W. W., & Sarazin, C. L. 1995, *ApJ*, **440**, 280

Demorest, P. B., Pennucci, T., Ransom, S. M., Roberts, M. S. E., & Hessels, J. W. T. 2010, *Nature*, **467**, 1081

Dermine, T., Jorissen, A., Siess, L., & Frankowski, A. 2009, *A&A*, **507**, 891

Eggleton, P. P. 1983, *ApJ*, **268**, 368

Ekşioğlu, K. Y., Andaç, İ. C., Çökintoglu, S., et al. 2015, *MNRAS*, **448**, L40

El Mellah, I., Sundqvist, J. O., & Keppens, R. 2018, *MNRAS*, **475**, 3240

Fabrika, S. 2004, *Phys. Rev.*, **12**, 1

Falanga, M., Bozzo, E., Lutovinov, A., et al. 2015, *A&A*, **577**, A130

Ferraro, F. R., Valenti, E., Straniero, O., & Origlia, L. 2006, *ApJ*, **642**, 225

Frank, J., King, A., & Raine, D. J. 2002, *Accretion Power in Astrophysics*, 3rd edn., 398

Gräfener, G., Owocki, S. P., & Vink, J. S. 2012, *A&A*, **538**, A40

Haberl, F., & Sturm, R. 2016, *A&A*, **586**, A81

Heise, J., & in't Zand, J. 2006, in *Fast X-ray Transients and X-ray Flashes*, eds. W. H. G. Lewin, & M. van der Klis, 267

Herold, H. 1979, *Phys. Rev. D*, **19**, 2868

Hjellming, M. S., & Webbink, R. F. 1987, *ApJ*, **318**, 794

Humphreys, R. M., & Davidson, K. 1979, *ApJ*, **232**, 409

Iglesias, C. A., & Rogers, F. J. 1996, *ApJ*, **464**, 943

Israel, G. L., Belfiore, A., Stella, L., et al. 2017a, *Science*, **355**, 817

Israel, G. L., Papitto, A., Esposito, P., et al. 2017b, *MNRAS*, **466**, L48

Ivanova, N. 2015, in *Binary Evolution: Roche Lobe Overflow and Blue Stragglers*, eds. H. M. J. Boffin, G. Carraro, & G. Beccari, 179

Jenke, P. A., Finger, M. H., Wilson-Hodge, C. A., & Camero-Arranz, A. 2012, *ApJ*, **759**, 124

Jiang, L., Qian, S.-B., Zhang, J., & Liu, N. 2015, *PASJ*, **67**, 118

Kaaret, P., Feng, H., & Roberts, T. P. 2017, *ARA&A*, **55**, 303

Kaper, L., van der Meer, A., & Najarro, F. 2006, *A&A*, **457**, 595

Karino, S. 2016, *PASJ*, **68**, 93

Kelley, R. L., Rappaport, S., Clark, G. W., & Petro, L. D. 1983, *ApJ*, **268**, 790

King, A. 2001, *Two Years of Science with Chandra*, 1012

King, A., & Lasota, J.-P. 2019, *MNRAS*, **485**, 3588

Kippenhahn, R., & Weigert, A. 1990, *Stellar Structure and Evolution* (Berlin, Heidelberg: Springer-Verlag), 192

Köhler, K., Langer, N., de Koter, A., et al. 2015, *A&A*, **573**, A71

Kolb, U., & Ritter, H. 1990, *A&A*, **236**, 385

Körding, E., Falcke, H., & Markoff, S. 2002, *A&A*, **382**, L13

Lai, D., Rasio, F. A., & Shapiro, S. L. 1994, *ApJ*, **420**, 811

Lamers, H. J. G. L. M., & Fitzpatrick, E. L. 1988, *ApJ*, **324**, 279

Langer, N., & Kudritzki, R. P. 2014, *A&A*, **564**, A52

Lecar, M., Wheeler, J. C., & McKee, C. F. 1976, *ApJ*, **205**, 556

Levine, A., Rappaport, S., Deeter, J. E., Boynton, P. E., & Nagase, F. 1993, *ApJ*, **410**, 328

Levine, A. M., Rappaport, S. A., & Zojcheski, G. 2000, *ApJ*, **541**, 194

Lewin, W. H. G., van Paradijs, J., & van den Heuvel, E. P. J. 1995, *X-ray Binaries* (Cambridge, MA: Cambridge University Press)

Long, K. S., Dodorico, S., Charles, P. A., & Dopita, M. A. 1981, *ApJ*, **246**, L61

Madhusudhan, N., Rappaport, S., Podsiadlowski, P., & Nelson, L. 2008, *ApJ*, **688**, 1235

Maitra, C., Carpano, S., Haberl, F., & Vasilopoulos, G. 2018, ArXiv e-prints [arXiv:1811.04807]

Manousakis, A., & Walter, R. 2012, *A&A*, **547**, A20

Manousakis, A., Walter, R., & Blondin, J. M. 2012, *A&A*, **547**, A20

Marchant, P., Langer, N., Podsiadlowski, P., Tauris, T. M., & Moriya, T. J. 2016, *A&A*, **588**, A50

Marchant, P., Langer, N., Podsiadlowski, P., et al. 2017, *A&A*, **604**, A55

Meurs, E. J. A., & van den Heuvel, E. P. J. 1989, *A&A*, **226**, 88

Motch, C., Pakull, M. W., Soria, R., Grisé, F., & Pietrzyński, G. 2014, *Nature*, **514**, 198

Pavlovskii, K., & Ivanova, N. 2015, *MNRAS*, **449**, 4415

Pavlovskii, K., Ivanova, N., Belczynski, K., & Van, K. X. 2017, *MNRAS*, **465**, 2092

Pinheiro, F. J. G., & Fernandes, J. 2013, *MNRAS*, **433**, 2893

Potter, A. T., & Tout, C. A. 2010, *MNRAS*, **402**, 1072

Pratt, J. P., & Strittmatter, P. A. 1976, *ApJ*, **204**, L29

Ramírez-Agudelo, O. H., Sana, H., de Koter, A., et al. 2017, *A&A*, **600**, A81

Rubin, B. C., Finger, M. H., Harmon, B. A., et al. 1996, *ApJ*, **459**, 259

Ruszkowski, M., & Begelman, M. C. 2003, *ApJ*, **586**, 384

Safi Harb, S., Ogelman, H., & Dennerl, K. 1996, *ApJ*, **456**, L37

Sander, A. A. C., Fürst, F., Kretschmar, P., et al. 2018, *A&A*, **610**, A60

Sanyal, D., Grassitelli, L., Langer, N., & Bestenlehner, J. M. 2015, *A&A*, **580**, A20

Sanyal, D., Langer, N., Szécsi, D.-C., Yoon, S., & Grassitelli, L. 2017, *A&A*, **597**, A71

Savonije, G. J. 1978, *A&A*, **62**, 317

Savonije, G. J. 1979, *A&A*, **71**, 352

Schootemeijer, A., & Langer, N. 2018, *A&A*, **611**, A75

Shakura, N. I., Postnov, K. A., Kochetkova, A. Y., & Hjalmarsdotter, L. 2014, *Eur. Phys. J. Web Conf.*, **64**, 02001

Smith, N. 2014, *ARA&A*, **52**, 487

Soberman, G. E., Phinney, E. S., & van den Heuvel, E. P. J. 1997, *A&A*, **327**, 620

Socrates, A., & Davis, S. W. 2006, *ApJ*, **651**, 1049

Sonoi, T., Ludwig, H.-G., Dupret, M.-A., et al. 2019, *A&A*, **621**, A84

Sukhbold, T., Ertl, T., Woosley, S. E., Brown, J. M., & Janka, H.-T. 2016, *ApJ*, **821**, 38

Tauris, T. M., van den Heuvel, E. P. J., & Savonije, G. J. 2000, *ApJ*, **530**, L93

Tauris, T. M., & van den Heuvel, E. P. J. 2006, in *Formation and Evolution of Compact Stellar X-ray Sources*, eds. W. H. G. Lewin, & M. van der Klis, 623

Tauris, T. M., Kramer, M., Freire, P. C. C., et al. 2017, *ApJ*, **846**, 170

Ugliano, M., Janka, H.-T., Marek, A., & Arcones, A. 2012, *ApJ*, **757**, 69

Ulmer, A., & Fitzpatrick, E. L. 1998, *ApJ*, **504**, 200

Van den Heuvel, E. P. J., Portegies Zwart, S. F., & de Mink, S. E. 2017, *MNRAS*, **471**, 4256

van der Klis, M., & Bonnet-Bidaud, J. M. 1984, *A&A*, **135**, 155

Verbunt, F. 1992, in *Frontiers Science Series*, eds. Y. Tanaka, & K. Koyama (Tokyo: Universal Academy Press), 57

Vink, J. S., de Koter, A., & Lamers, H. J. G. L. M. 2001, *A&A*, **369**, 574

Walter, R., Lutovinov, A. A., Bozzo, E., & Tsygankov, S. S. 2015, *A&ARv*, **23**, 2

Wellstein, S., & Langer, N. 1999, *A&A*, **350**, 148

Wellstein, S., Langer, N., & Braun, H. 2001, *A&A*, **369**, 939

Wickramasinghe, D. T., & Ferrario, L. 2000, *PASP*, **112**, 873

Appendix A: Mass–radius exponents for all stellar models

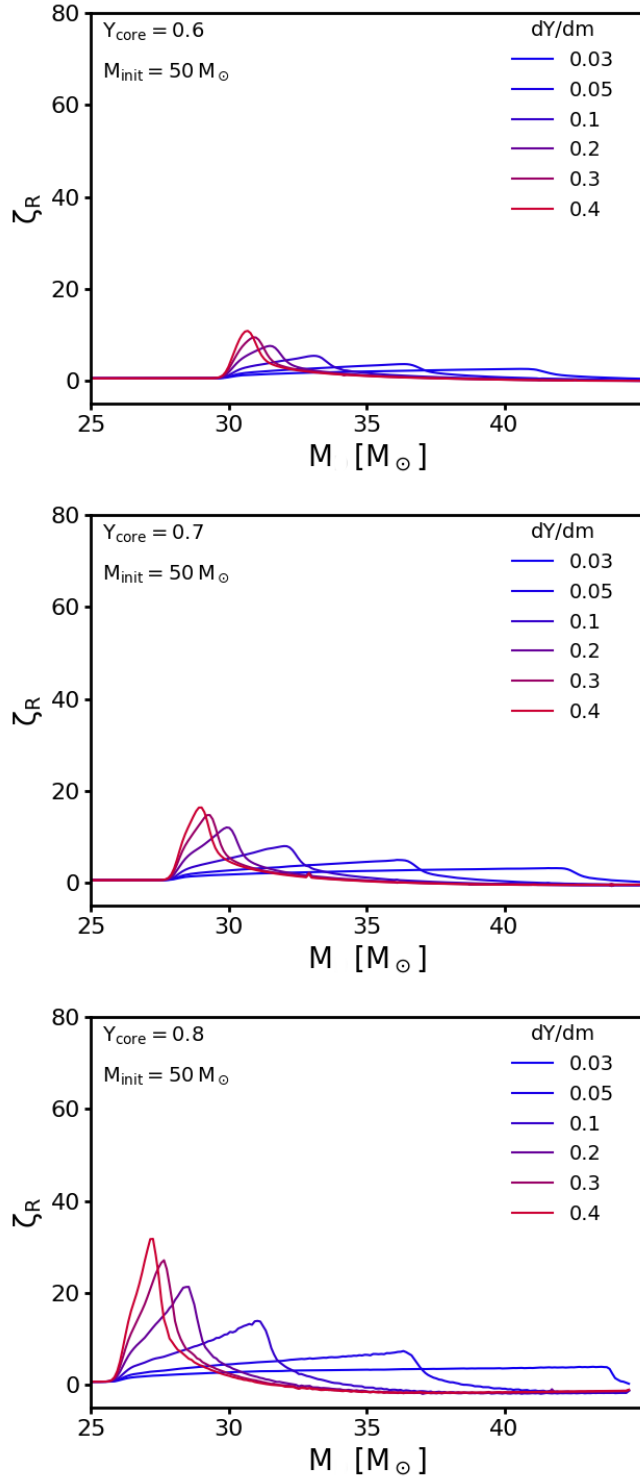


Fig. A.1. Mass–radius exponent as function of mass for our model with an initially $50 M_{\odot}$ star for different core helium abundances.

Because the response of the stellar radius to slow mass loss is the key for obtaining mass transfer on a nuclear timescale in our supergiant X-ray binaries, we show here the corresponding

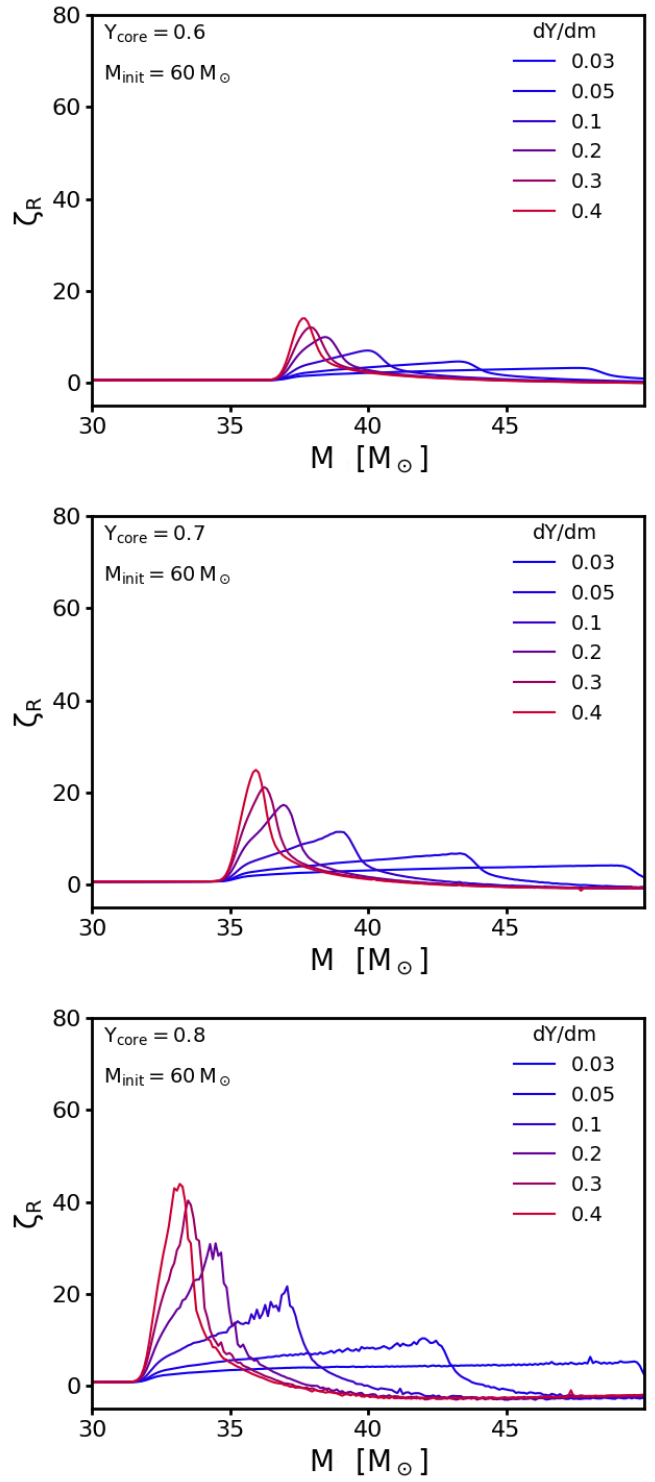


Fig. A.2. As Fig. A.1, but for our $60 M_{\odot}$ star model.

mass–radius exponents ζ_R for all of our stellar models. We encountered convergence problems for the model with an initially $80 M_{\odot}$ star with a core helium mass fraction of $Y_c = 0.8$ and steep helium profiles (Fig. A.3 bottom). For helium gradients steeper than $0.05 M_{\odot}^{-1}$, the numerical problems arose when the outer edge of the helium gradient came to the surface. Thus, ζ_R could not reach its peak value.

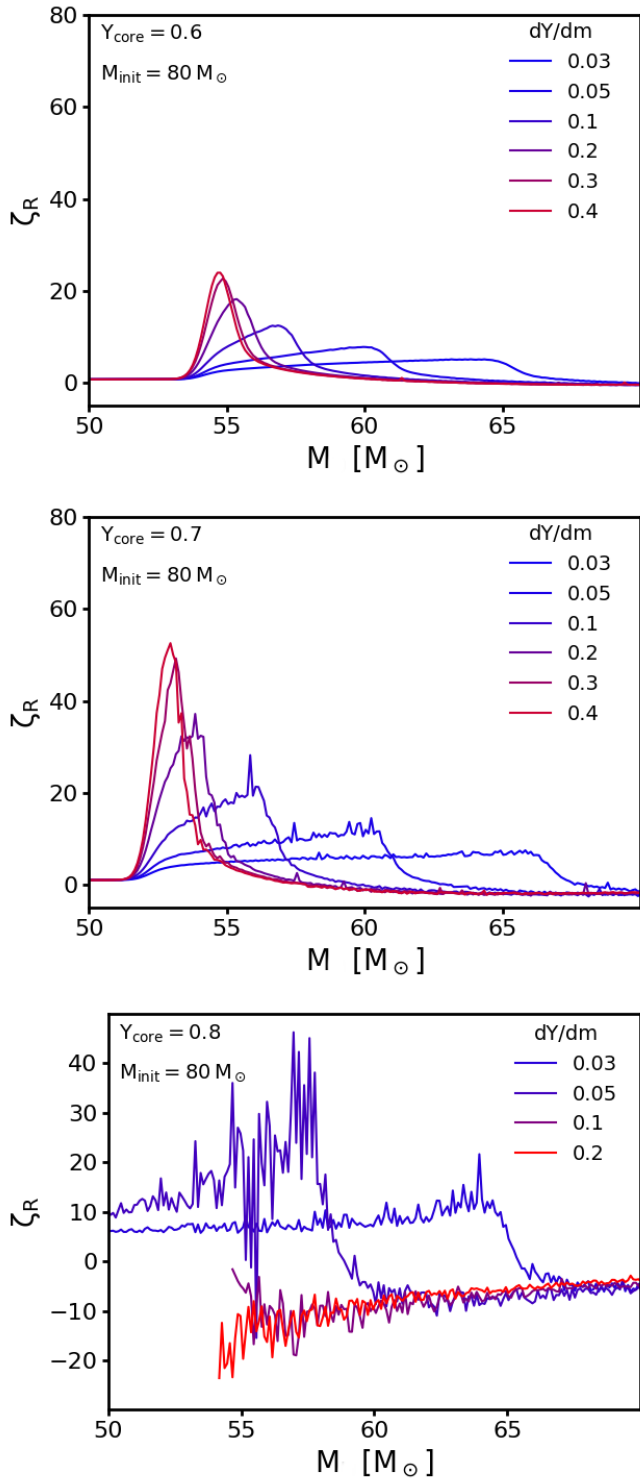


Fig. A.3. As Fig. A.1, but for our $80 M_{\odot}$ star model.

Appendix B: Details for our binary evolution models

In Figs. B.1 and B.2 we show the time evolution of the mass-transfer rate for all our binary evolution models (except for the conservative systems; see Fig. 12). Table B.1 gives the key parameters of all binary models we computed here. It also gives the X-ray lifetime t_X , which we define as the time period during which the accretion luminosity exceeds $10^{33} \text{ erg s}^{-1}$. To estimate this, we introduce the quantities $L_{X,\text{Edd}}$ defined as the Eddington-limited accretion luminosity after half of the X-ray lifetime has passed. We define the quantity $L_{X,\text{max}}$ in the same manner as $L_{X,\text{Edd}}$, but under the condition that the accretion was not Eddington limited, that is, as if the entire transferred mass were accreted by the compact object. We instead use the luminosity values in the middle of the mass-transfer phase because the arithmetic mean over time would be distorted by the initial peaks of the mass-transfer rate that appear in some calculations. In some models these peaks are two orders of magnitude above the long-term mass-transfer rate and last for roughly a tenth of the mass-transfer phase. The arithmetic mean would hence be shifted by one order of magnitude above the long-term X-ray luminosity. Our definition avoids this distortion and gives a better estimate of the typical luminosity during the mass transfer.

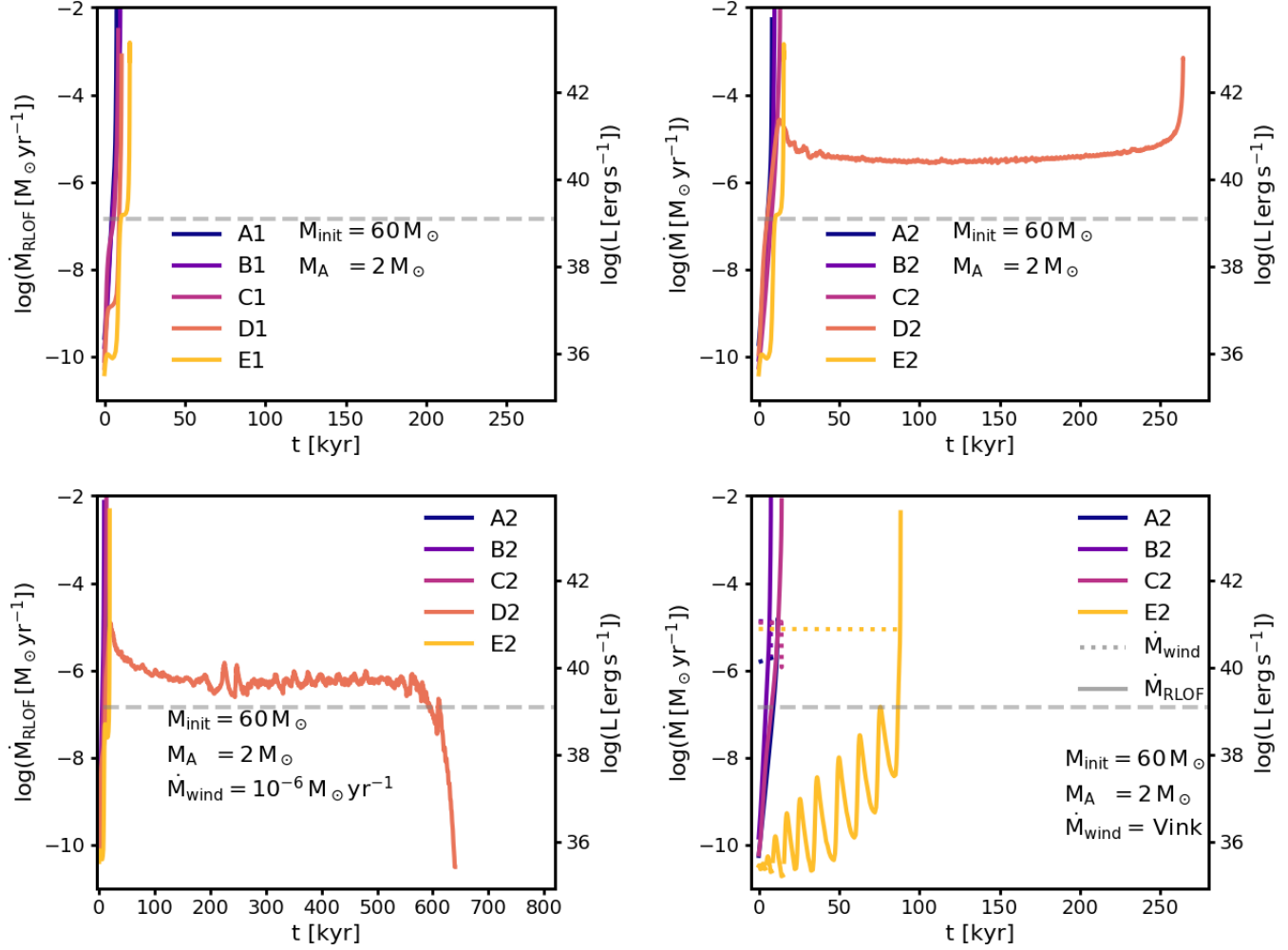


Fig. B.1. Evolution of the mass-transfer rate for three initial models and an NS accretor. The right axis indicates the X-ray luminosity corresponding to the mass-transfer rate (not Eddington limited) assuming an accretion efficiency of $\eta = 0.15$. The dashed line indicates the Eddington-accretion limit of the accretor.

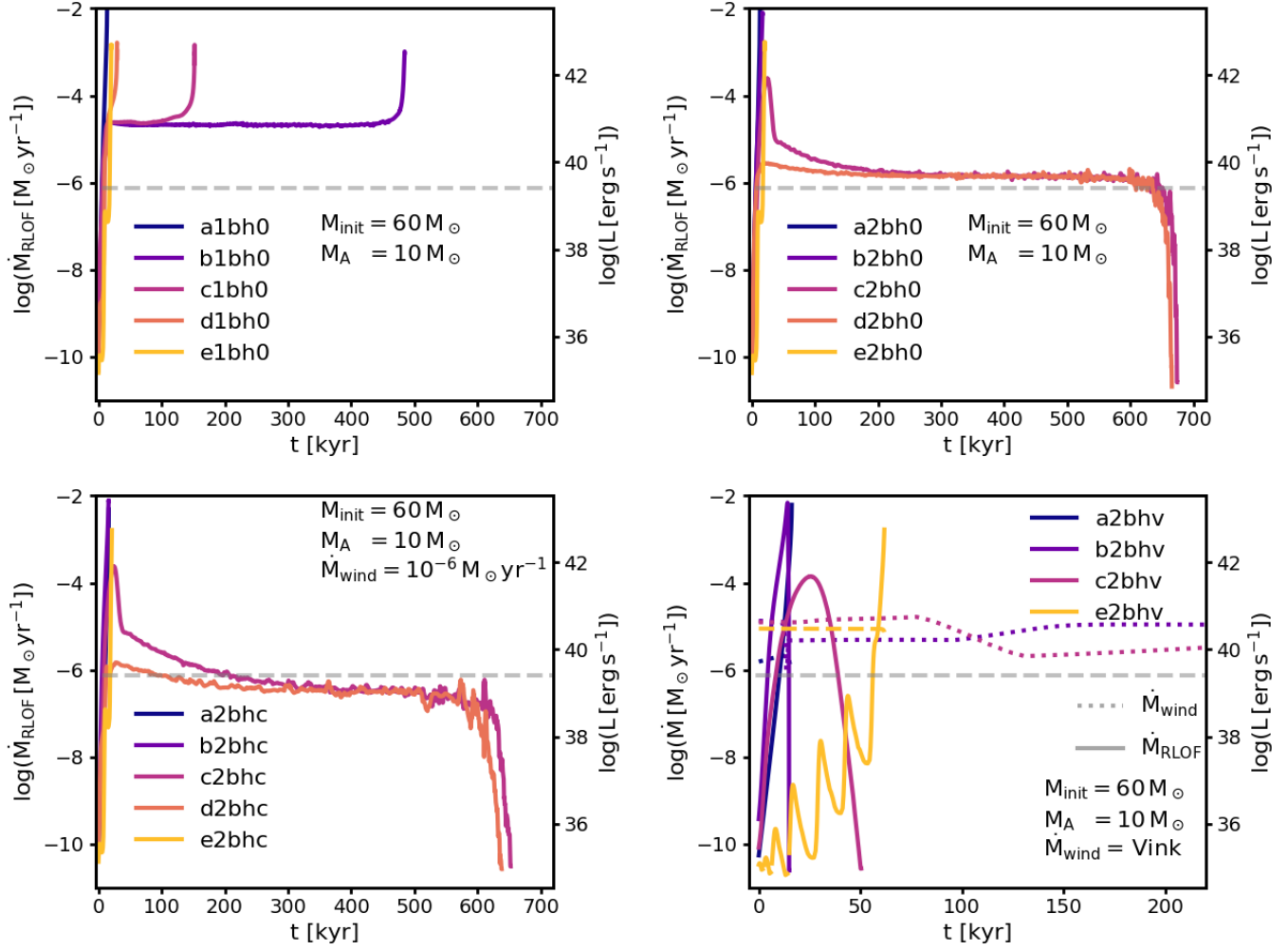


Fig. B.2. Similar to Fig. B.1, but with a BH accretor, $\eta = 0.06$.

Table B.1. Summary table of our computed binary evolution models.

Model	$M_{\text{CC, init}}$ [M_{\odot}]	\dot{M}_{wind} [$M_{\odot} \text{ yr}^{-1}$]	$\frac{dY}{dm}$ [M_{\odot}^{-1}]	M_{init} [M_{\odot}]	$\log(L_{\text{init}})$ [L_{\odot}]	$T_{\text{eff, init}}$ [kK]	$\log(\mathcal{L}_{\text{init}})$ [\mathcal{L}_{\odot}]	R_{init} [R_{\odot}]	$Y_{\text{S, init}}$	P_{init} [d]	t_X [kyr]	$L_{\text{X, Edd}}$ [erg s^{-1}]	$L_{\text{X, max}}$ [erg s^{-1}]	M_{final} [M_{\odot}]	$\log(L_{\text{final}})$ [L_{\odot}]	$T_{\text{eff, final}}$ [kK]	$\log(\mathcal{L}_{\text{final}})$ [\mathcal{L}_{\odot}]	R_{final} [R_{\odot}]	$Y_{\text{S, final}}$	P_{final} [d]
a1bh0	10	–	0.04	50.0	5.88	24	4.18	49	0.26	14.1	13	2.5×10^{39}	1.9×10^{40}	38.4	5.29	38	3.70	10	0.48	1.5
b1bh0	10	–	0.04	42.5	5.85	22	4.22	53	0.28	17.9	484	2.5×10^{39}	7.5×10^{40}	30.9	5.79	45	4.30	13	0.80	2.5
c1bh0	10	–	0.04	36.5	5.80	41	4.24	16	0.58	3.2	152	2.5×10^{39}	7.9×10^{40}	31.7	5.73	52	4.23	9	0.80	1.4
d1bh0	10	–	0.04	33.5	5.75	50	4.23	10	0.72	1.7	29	2.5×10^{39}	8.0×10^{40}	31.8	5.70	53	4.20	8	0.80	1.3
e1bh0	10	–	0.04	30.5	5.69	53	4.20	8	0.80	1.3	20	7.2×10^{38}	7.2×10^{38}	30.0	5.65	53	4.17	8	0.80	1.2
a1ns0	2	–	0.04	50.0	5.88	24	4.18	49	0.26	11.0	7	3.1×10^{38}	4.2×10^{38}	49.3	5.73	30	4.04	26	0.26	4.0
b1ns0	2	–	0.04	42.5	5.85	22	4.22	53	0.28	13.9	9	3.1×10^{38}	1.5×10^{39}	41.5	5.75	33	4.13	23	0.32	3.7
c1ns0	2	–	0.04	36.5	5.80	41	4.24	16	0.58	2.5	8	3.1×10^{38}	5.6×10^{38}	36.3	5.77	43	4.21	14	0.58	1.9
d1ns0	2	–	0.04	33.5	5.75	50	4.23	10	0.72	1.3	10	1.4×10^{37}	1.4×10^{37}	33.5	5.75	50	4.22	10	0.73	1.2
e1ns0	2	–	0.04	30.5	5.69	53	4.20	8	0.80	1.0	15	4.1×10^{36}	4.1×10^{36}	30.5	5.68	53	4.20	8	0.80	1.0
a2bh0	10	–	0.4	50.0	5.83	27	4.13	35	0.26	8.7	13	2.5×10^{39}	3.0×10^{39}	45.4	5.49	31	3.83	19	0.26	3.4
b2bh0	10	–	0.4	42.5	5.79	22	4.16	52	0.26	17.3	17	2.5×10^{39}	2.8×10^{40}	33.7	5.61	35	4.08	17	0.27	3.6
c2bh0	10	–	0.4	36.5	5.76	19	4.20	66	0.26	27.5	674	2.6×10^{39}	4.9×10^{39}	32.7	5.86	26	4.34	40	0.55	14.1
d2bh0	10	–	0.4	33.5	5.74	26	4.22	36	0.27	11.7	665	2.6×10^{39}	4.5×10^{39}	32.5	5.86	30	4.35	31	0.59	9.8
e2bh0	10	–	0.4	30.5	5.69	53	4.20	8	0.80	1.3	20	7.1×10^{38}	7.1×10^{38}	30.0	5.65	53	4.17	8	0.80	1.2
a2ns0	2	–	0.4	50.0	5.83	27	4.13	35	0.26	6.8	8	3.1×10^{38}	3.1×10^{38}	49.8	5.78	29	4.09	30	0.26	4.9
b2ns0	2	–	0.4	42.5	5.79	22	4.16	52	0.26	13.4	9	3.1×10^{38}	3.1×10^{38}	41.2	6.11	47	4.49	17	0.26	2.3
c2ns0	2	–	0.4	36.5	5.76	19	4.20	66	0.26	21.3	13	2.8×10^{38}	2.8×10^{38}	35.2	5.59	32	4.04	20	0.26	3.3
d2ns0	2	–	0.4	33.5	5.74	26	4.22	36	0.27	9.1	264	3.1×10^{38}	2.5×10^{40}	32.1	5.76	49	4.25	10	0.74	1.4
e2ns0	2	–	0.4	30.5	5.69	53	4.20	8	0.80	1.0	15	2.1×10^{36}	2.1×10^{36}	30.5	5.68	53	4.19	8	0.80	1.0
a2bhc	10	10^{-6}	0.4	50.0	5.83	27	4.13	35	0.26	8.7	16	3.5×10^{38}	3.5×10^{38}	48.0	5.74	30	4.06	27	0.26	5.7
b2bhc	10	10^{-6}	0.4	42.5	5.79	22	4.16	52	0.26	17.3	16	2.5×10^{39}	3.9×10^{40}	33.4	5.62	36	4.10	17	0.27	3.4
c2bhc	10	10^{-6}	0.4	36.5	5.76	19	4.20	66	0.26	27.5	652	1.5×10^{39}	1.5×10^{39}	32.7	5.86	25	4.34	42	0.54	16.4
d2bhc	10	10^{-6}	0.4	33.5	5.74	26	4.22	36	0.27	11.7	637	1.3×10^{39}	1.2×10^{39}	32.6	5.86	29	4.34	32	0.59	11.4
e2bhc	10	10^{-6}	0.4	30.5	5.69	53	4.20	8	0.80	1.3	21	4.3×10^{38}	4.3×10^{38}	29.9	5.64	53	4.17	8	0.80	1.2
a2bhw	10	Vink	0.4	50.0	5.83	27	4.13	35	0.26	8.7	16	3.4×10^{38}	3.3×10^{38}	47.7	5.73	30	4.05	26	0.26	5.5
b2bhw	10	Vink	0.4	42.5	5.79	22	4.16	52	0.26	17.3	14	2.5×10^{39}	1.2×10^{41}	25.9	5.80	47	4.39	12	0.80	3.6
c2bhw	10	Vink	0.4	36.5	5.76	19	4.20	66	0.26	27.5	50	2.5×10^{39}	4.8×10^{41}	28.2	5.85	45	4.40	14	0.80	22.6
e2bhw	10	Vink	0.4	30.5	5.69	53	4.20	8	0.80	1.3	59	1.0×10^{38}	4.7×10^{37}	28.5	5.62	52	4.16	8	0.80	1.2
a2nsc	2	10^{-6}	0.4	50.0	5.83	27	4.13	35	0.26	6.8	12	8.7×10^{37}	8.5×10^{37}	49.9	5.82	28	4.12	34	0.26	6.1
b2nsc	2	10^{-6}	0.4	42.5	5.79	22	4.16	52	0.26	13.4	8	4.1×10^{38}	4.1×10^{38}	42.0	5.71	26	4.08	33	0.26	6.4
c2nsc	2	10^{-6}	0.4	36.5	5.76	19	4.20	66	0.26	21.3	13	4.3×10^{38}	3.9×10^{38}	35.3	5.63	30	4.08	23	0.26	4.2
d2nsc	2	10^{-6}	0.4	33.5	5.74	26	4.22	36	0.27	9.1	639	1.3×10^{39}	5.3×10^{39}	32.3	5.87	38	4.36	20	0.67	4.9
e2nsc	2	10^{-6}	0.4	30.5	5.69	53	4.20	8	0.80	1.0	18	2.1×10^{38}	2.1×10^{38}	30.3	5.63	54	4.15	7	0.80	0.9
a2nsv	2	Vink	0.4	50.0	5.83	27	4.13	35	0.26	6.8	11	7.4×10^{37}	7.1×10^{37}	49.9	5.83	27	4.13	36	0.26	6.7
b2nsv	2	Vink	0.4	42.5	5.79	22	4.16	52	0.26	13.4	7	4.2×10^{38}	4.0×10^{38}	41.7	5.69	27	4.07	30	0.26	5.7
c2nsv	2	Vink	0.4	36.5	5.76	19	4.20	66	0.26	21.3	14	1.1×10^{39}	6.2×10^{38}	35.1	5.64	30	4.10	24	0.26	4.4
e2nsv	2	Vink	0.4	30.5	5.69	53	4.20	8	0.80	1.0	85	2.8×10^{37}	8.3×10^{35}	28.8	5.61	53	4.15	8	0.80	0.9
d2bh0 cons.	10	–	0.4	33.5	5.74	26	4.22	36	0.27	11.7	664	4.8×10^{39}	4.8×10^{39}	32.5	5.86	30	4.34	31	0.59	9.7
d2ns0 cons.	2	–	0.4	33.5	5.74	26	4.22	36	0.27	9.1	431	9.1×10^{39}	9.1×10^{39}	31.8	5.77	48	4.27	11	0.80	1.6

Notes. All models assume Eddington limited accretion and isotropic re-emission, except for the last two models, which are computed assuming conservative mass transfer. The first column indicates the name of the binary model (cf., Fig. 8), and $M_{\text{cc, init}}$ is the initial mass of the compact companion. \dot{M}_{wind} indicates the adopted wind mass loss recipe, $\frac{dY}{dm}$ measures the helium gradient within the donor star. M , L , and T_{eff} refer to the donor's mass, luminosity and effective temperature, and $\mathcal{L} = T_{\text{eff}}^4 / g$. R is the donor's radius, Y_{S} is its surface helium abundance, P is the binary's orbital period, t_X is the X-ray lifetime, and $L_{\text{X, Edd}}$ and $L_{\text{X, max}}$ are the X-ray luminosities in the middle of the mass-transfer phase assuming Eddington limited accretion or conservative mass transfer onto the compact object, respectively (see text). Subscripts *init* and *final* refer to the times of the onset of mass transfer, and the end of the calculations, respectively.

Appendix B

Appendix to Chapter 3

B.1 Column density

Suppose the companion revolves the donor star in a circular orbit with orbital separation a . Choose a coordinate system such that the x -direction is parallel to the line of sight and the y -direction is perpendicular to x within the orbital plane. Let φ be the angle between the connection line from the primary to the secondary and the x -axis. Further $x_C = \cos(\varphi)$ and $y_C = \sin(\varphi)$ denote the coordinates of the companion at the moment.

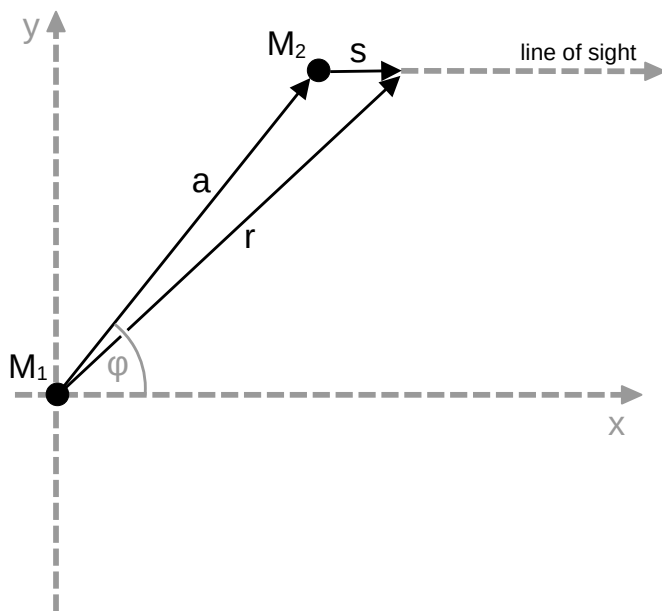


Figure B.1.

The column density is obtained by integrating the wind density profile along the line of sight from the companion to the observer. Let s be the distance of a specific point on the line of sight from the companion, and r the distance of that point from the primary. Then,

the column density of the companion is given by

$$\Sigma = \int_0^\infty \rho \, ds. \quad (\text{B.1})$$

Assuming a β -law for the wind velocity, the mass density of the stellar wind at a certain point is given by

$$\rho = \frac{\dot{M}_1}{4\pi v_\infty} \times \frac{1}{r^2(1 - \frac{R_1}{r})^\beta} \quad (\text{B.2})$$

From the geometry in Fig.B.1 we immediately find

$$s = \sqrt{r^2 - y_C^2} - x_C. \quad (\text{B.3})$$

Note that when integration along the line of sight, only s and r change; thus, x_C is a constant. We consequently find

$$ds = \frac{r}{\sqrt{r^2 - y_C^2}} dr \quad (\text{B.4})$$

and thus, the column density can be written as

$$\Sigma = \frac{\dot{M}_1}{4\pi v_\infty} \times \int_a^\infty \frac{1}{(1 - \frac{R_1}{r})^\beta r \sqrt{r^2 - y_C^2}} dr. \quad (\text{B.5})$$

This equation reduces to Eq. 3.39 for $\varphi = 0$, i.e., $y_C = 0$. Generally, the integral in Eq. B.5 must be solved numerically. However, an analytic solution can be found for $\beta = 0$. We simplify the equation by scaling all lengths to R_1 , thereby introducing dimensionless variables $\tilde{r} = r/R_1$ and $\tilde{a} = a/R_1$. Eq. B.5 then becomes

$$\Sigma = \frac{\dot{M}_1}{4\pi v_\infty R_1} \times \Phi_\varphi(\tilde{a}, \beta), \quad (\text{B.6})$$

where

$$\Phi_\varphi(\tilde{a}, \beta) = \int_{\tilde{a}}^\infty \frac{1}{(1 - \tilde{r}^{-1})^\beta \tilde{r} \sqrt{\tilde{r}^2 - \sin^2(\varphi)\tilde{a}^2}} d\tilde{r}. \quad (\text{B.7})$$

We already found the integrals for $\varphi = 0$ and arbitrary values for β (cf. Eq. 3.39)

$$\Phi_0(\tilde{a}, \beta) = \begin{cases} -\ln(1 - \tilde{a}^{-1}) & : \beta = 1 \\ \frac{1 - (1 - \tilde{a}^{-1})^{1-\beta}}{1-\beta} & : \text{else} \end{cases}. \quad (\text{B.8})$$

Setting $\beta = 0$ corresponds to the situation where the wind material has terminal velocity throughout the whole wind profile. This is a good approximation if the orbital separation is much larger than the wind acceleration zone. Computing the antiderivative of the

integrand yields

$$\Phi_\varphi(\tilde{a}, 0) = \left[\frac{1}{\sin(\varphi)\tilde{a}} \cdot \arctan\left(\frac{\sqrt{\tilde{r}^2 - \sin(\varphi)^2\tilde{a}^2}}{\sin(\varphi)\tilde{a}}\right) \right]_{\tilde{a}}^\infty. \quad (\text{B.9})$$

Plugging in the integration boundaries, this simplifies to

$$\Phi_\varphi(\tilde{a}, 0) = \frac{\varphi}{\sin(\varphi)\tilde{a}}, \quad (\text{B.10})$$

where φ is measured in radians. From Eq. B.8 we find that

$$\Phi_0(\tilde{a}, 0) = \frac{1}{\tilde{a}}. \quad (\text{B.11})$$

This shows that the integral and, consequently, the column density is larger by a factor of $\varphi / \sin(\varphi)$ if $\varphi \neq 0$, i.e.,

$$\Sigma = \frac{\varphi}{\sin(\varphi)} \cdot \Sigma_0 \quad (\text{B.12})$$

where Σ_0 is the column density given in Eq. 3.39. Note that this factor can become arbitrarily large and diverges as φ approaches π . In this case, the companion is on the opposite side of the primary with respect to the observer, and thus, basically, all flux in the direction of the line of sight is absorbed. However, due to its orbital motion, the companion will change its position and, hence, its column density.

The smallest value of column density is reached if the companion is closest to the observer. In this case, it reaches a minimum value φ_{\min} . Assuming circular orbits, we find the constellation of minimum column density as sketched in B.2. We immediately find that the angle of minimum column density is given by

$$\varphi_{\min} = \frac{\pi}{2} - i \quad (\text{B.13})$$

and therefore, the minimum column density the companion has during one orbit is given by

$$\Sigma_{\min} = \frac{\pi - 2i}{2 \cos(i)} \cdot \Sigma_0. \quad (\text{B.14})$$

Using L'Hospital's rule shows that the minimum column density is between Σ_0 , if $i = \frac{\pi}{2}$, and $\frac{\pi}{2}\Sigma_0$, if $i = 0$.

B.2 Neutron star accretion

B.2.1 Case determination

Define the accretion radius

$$R_A = \frac{2GM_2}{v_w^2}, \quad (\text{B.15})$$

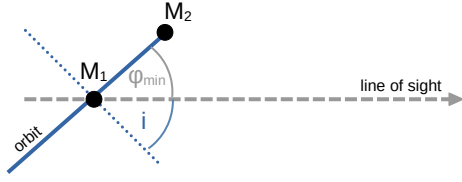


Figure B.2.: Companion in the position of minimum column density. The orbital plane (blue straight line) is viewed edge off. The blue dotted line marks the orbital normal. Orbital inclination i and the angle φ_{\min} add up to $\pi/2$.

and the co-rotation radius

$$R_{\text{co}} = \left(\frac{GM_2 P_s^2}{4\pi^2} \right)^{1/3}. \quad (\text{B.16})$$

The magnetospheric radius is defined by the distance where the ram pressure (ρv) of the wind material equals the pressure of the NS's magnetic field. If this distance is large enough that the gravity of the NS can be neglected (i.e., $\sqrt{\frac{2GM_2}{r}} \ll v_w$), the dominant contribution to the ram pressure stems from the velocity. In this case, the magnetospheric radius can be expressed as (Davies and Pringle 1981; Bozzo et al. 2008)

$$R_{\text{mag}} = \left(\frac{a^2 \mu^2}{2\dot{M}_A v_w} \right)^{1/6}. \quad (\text{B.17})$$

B.2.2 Super-Keplerian Magnetic Inhibition

If $R_{\text{mag}} > R_A$, R_{co} , the wind is captured by the magnetic field rather than by the gravity of the NS. In this case, we follow Toropina et al. (2006) by assuming that the kinetic energy of the wind material is radiated in X-rays at the shock front that forms at R_{mag} . Hence, we compute the luminosity as

$$L_{\text{shock}} = \frac{1}{2} \pi \rho_w v_w^3 R_{\text{mag}}^2. \quad (\text{B.18})$$

In addition to the shock luminosity, matter captured by the magnetic field is forced to rotate with super-Keplerian velocity. The acceleration of the matter results in a dissipation of the NS's rotational energy (Perna et al. 2006) with the rate $\dot{E}_{\text{rot}} \sim \dot{M}_A \left(\frac{2\pi R_{\text{mag}}}{P} \right)^2$. If we assume that this energy is subsequently converted into heat and radiated away, we estimate the dissipation luminosity as (Bozzo et al. 2008)

$$L_{\text{diss}} = 4\pi^3 \rho_w v_w R_{\text{mag}}^4 P_s^{-2} \quad (\text{B.19})$$

We add the shock luminosity and the dissipation luminosity to infer the total X-ray luminosity in this regime.

B.2.3 Sub-Keplerian Magnetic Inhibition

If $R_A < R_{\text{mag}} < R_{\text{co}}$ the matter dragged by the magnetic field, creating Kelvin-Helmholtz instabilities (Harding and Leventhal 1992) and consequent mass inflow. Since the material is shocked at R_{mag} we apply the Rankine-Hugoniot conditions to compute the density and the velocity of the post-shocked material

$$\rho_{\text{ps}} = 4\rho_w \quad \text{and} \quad v_{\text{ps}} = \frac{v_w}{4}. \quad (\text{B.20})$$

The mass inflow rate by Kelvin-Helmholtz instabilities can then be computed by using (Burnard et al. 1983)

$$\dot{M}_{\text{KH}} = 2\pi R_{\text{mag}}^2 \rho_{\text{ps}} v_{\text{ent}}, \quad (\text{B.21})$$

where

$$v_{\text{ent}} = v_{\text{sh}} \eta_{\text{KH}} x^{1/2} (1 + x)^{-1} \quad (\text{B.22})$$

is the velocity at which the inflowing material enters the magnetosphere. In this definition, the shear velocity is estimated as the maximum post-shock velocity and the rotational velocity of the field lines at R_{mag}

$$v_{\text{sh}} = \max \left[v_{\text{ps}}, \frac{2\pi R_{\text{mag}}}{P_s} \right]. \quad (\text{B.23})$$

In accordance to Bozzo et al. (2008) we assume an efficiency factor of $\eta_{\text{KH}} = 0.1$. The quantity $x := \rho_i/\rho_e$ is the ratio of the mass density inside and outside the magnetospheric boundary. If we assume that the Kelvin-Helmholtz unstable layer has the size hR_{mag} Eq. 8 from Bozzo et al. (2008) together with Eq. B.22 of this paper implies that

$$x^{1/2}(1 + x) = \frac{v_{\text{sh}} \sqrt{R_{\text{mag}}}}{\sqrt{2GM_2}} \frac{\eta_{\text{KH}}}{h}. \quad (\text{B.24})$$

We assume $h = 1$. Consequently, the right-hand side of this equation is given, and we solve it for x . Then Eqn. B.21 and B.22 provide the accretion rate. The corresponding luminosity is given by

$$L_{\text{KH}} = \frac{G\dot{M}_{\text{KH}} M_2}{R_{\text{NS}}}. \quad (\text{B.25})$$

B.2.4 Supersonic propeller

If $R_{\text{co}} < R_{\text{mag}} < R_A$ matter is captured by the gravity of the NS rather than by its magnetic field. The material flows inward, reaching the magnetopause, where the magnetic stress becomes important, and the magnetic field drags the plasma. Since the magnetopause lies outside the co-rotation radius, the centrifugal force is stronger than gravity, inhibiting efficient accretion. The fact that the matter is halted at R_{mag} gives rise to an atmosphere that is quasi-stationary on a dynamical timescale (Davies et al. 1979; Davies and Pringle 1981).

Consequently, the atmosphere can be modeled using a polytropic law $P \propto \rho^{1+1/n}$. Density and pressure may be written as functions of the distance r from the NS (Bozzo et al. 2008)

$$\rho(r) = \rho_{\text{ps}} \left[1 + \frac{1}{1+n} \frac{8R_A}{r} \right]^n \quad (\text{B.26})$$

$$P(r) = \rho_{\text{ps}} v_{\text{ps}}^2 \left[1 + \frac{1}{1+n} \frac{8R_A}{r} \right]^{1+n} \quad (\text{B.27})$$

Note that the pressure in Eq. B.27 is different from the dynamical wind pressure that we used to compute the magnetospheric radius. In order to compute R_{mag} we must therefore equate the pressure at the bottom of the atmosphere $P(R_{\text{mag}})$ with the magnetic stress. This yields the equation

$$R_{\text{mag}}^{-6} \left[1 + \frac{16R_A}{3R_{\text{mag}}} \right]^{-3/2} = \frac{2\dot{M}_A v_w}{\mu^2 R_A} \quad (\text{B.28})$$

which can be solved numerically for R_{mag} . Here we assumed an effective polytropic index of $n = 1/2$ as discussed by Davies and Pringle (1981).

The interaction of the plasma with the magnetic field results in a dissipation of the NS's rotational energy with a rate of (Bozzo et al. 2008)

$$L_{\text{diss}} = 2\pi R_{\text{mag}}^2 \rho(R_{\text{mag}}) v_{\text{ff}}^3(R_{\text{mag}}). \quad (\text{B.29})$$

We neglect the additional luminosity that originates at the shock formed at R_A .

B.2.5 Subsonic propeller

If $R_{\text{mag}} < R_A$, R_{co} the NS is surrounded by a convective envelope if the mass-accretion rate \dot{M}_A is smaller than a critical value \dot{M}_{crit} (Ikhsanov 2001). Similar to the supersonic propeller regime, the magnetospheric radius is given by Eq. B.27, where the polytropic index $n = 3/2$, since the atmosphere is supposed to be adiabatic due to convection. Correspondingly

$$R_{\text{mag}}^{-6} \left[1 + \frac{16R_A}{5R_{\text{mag}}} \right]^{-5/2} = \frac{2\dot{M}_A v_w}{\mu^2 R_A} \quad (\text{B.30})$$

has to be solved to infer the magnetospheric radius. In this case, the dissipation of the NS's rotational energy due to the coupling of the magnetic field heats the plasma. Davies and Pringle (1981) discussed the process of energy transport processes, arguing that the cooling of the plasma is either due to radiative cooling via thermal bremsstrahlung or due to convection. The latter prohibits efficient accretion. This means direct accretion can only occur if the convective efficiency parameter (Cox and Giuli 1968)

$$\Gamma = \frac{\text{Excess heat content of convective blob}}{\text{Energy radiated in the lifetime of a blob}} \quad (\text{B.31})$$

is smaller than unity. Davies and Pringle (1981) and Ikhsanov (2001) showed that Γ at R_{mag} can be approximated by

$$\Gamma = \frac{v_{\text{rot}}^3(R_{\text{mag}})t_{\text{br}}}{v_{\text{ff}}^2(R_{\text{mag}})R_{\text{mag}}} \quad (\text{B.32})$$

where the cooling timescale of the bremsstrahlung is

$$t_{\text{br}} = 6.3 \times 10^4 \left(\frac{T}{10^9 \text{ K}} \right)^{1/2} \left(\frac{n_{\text{dens}}}{10^{11} \text{ cm}^{-3}} \right)^{-1} \text{ s.} \quad (\text{B.33})$$

The temperature is computed from the released gravitational energy

$$T = \frac{GM_2 m_p}{R_{\text{mag}} k_B}. \quad (\text{B.34})$$

The number density n_{dens} is obtained from the mass density ρ at the bottom of the atmosphere by applying Eq. B.26 at $r = R_{\text{mag}}$ and $n = 3/2$ for a convective, i.e., adiabatic envelope. Using $v_{\text{rot}}(r) = \frac{2\pi r}{P}$, Eq. B.32 together with the condition $\Gamma > 1$ can be as

$$P_s < P_{\text{br}} \quad (\text{B.35})$$

where

$$P_{\text{br}} = \frac{2\pi}{(2GM_2)^{1/3}} R_{\text{mag}} t_{\text{br}}^{1/3}. \quad (\text{B.36})$$

If this condition applies, accretion is still inefficient and dominated by Kelvin-Helmholtz instabilities. We then apply the same scheme as discussed in the sub-Keplerian magnetic inhibition regime to infer L_{KH} which is supposed to be the X-ray luminosity in this case.

B.2.6 Direct accretion regime

If in addition to the conditions of the previous section $P_s > P_{\text{br}}$ we suppose direct accretion onto the NSs surface. The X-ray luminosity is computed from the gravitational energy that is radiated away

$$L_X = \frac{GM_2 \dot{M}_A}{R_{\text{NS}}} \quad (\text{B.37})$$

B.3 Stellar parameters of the grid models

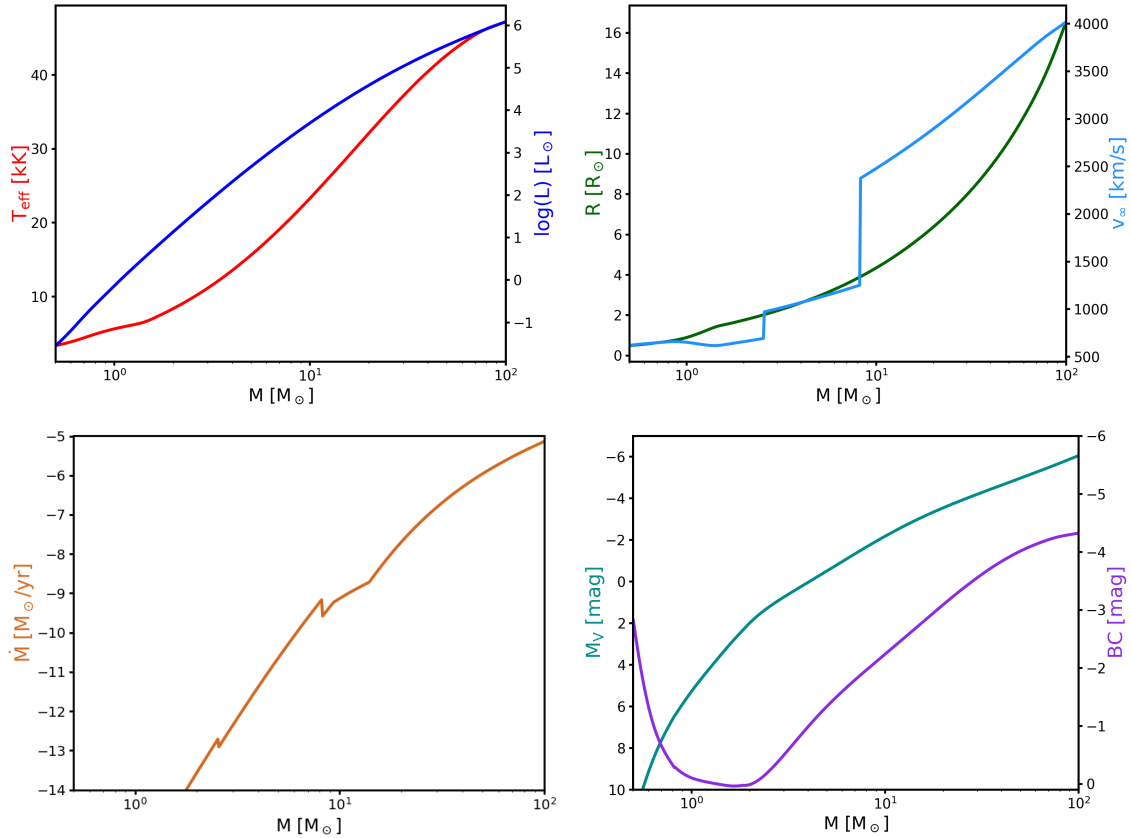
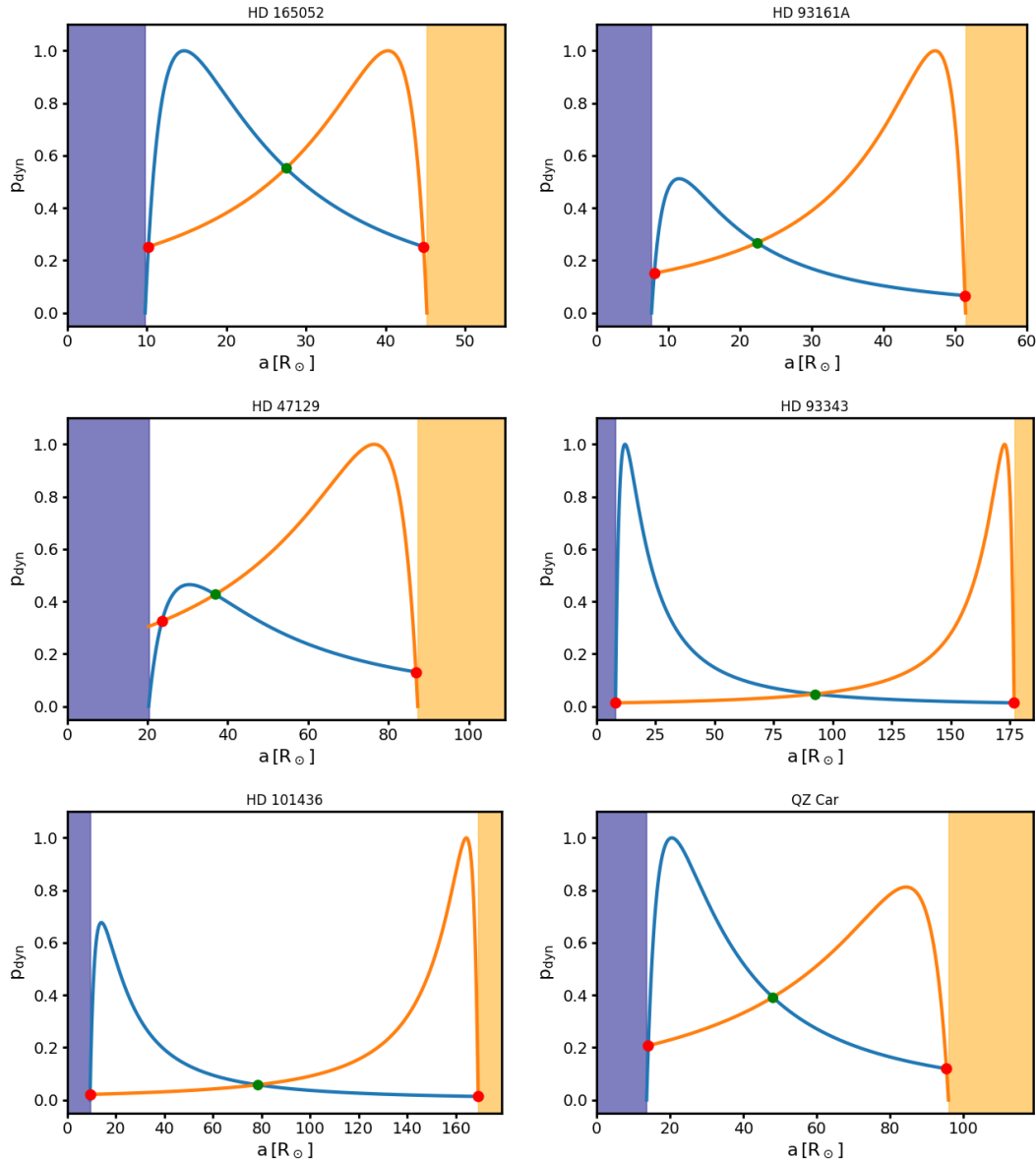
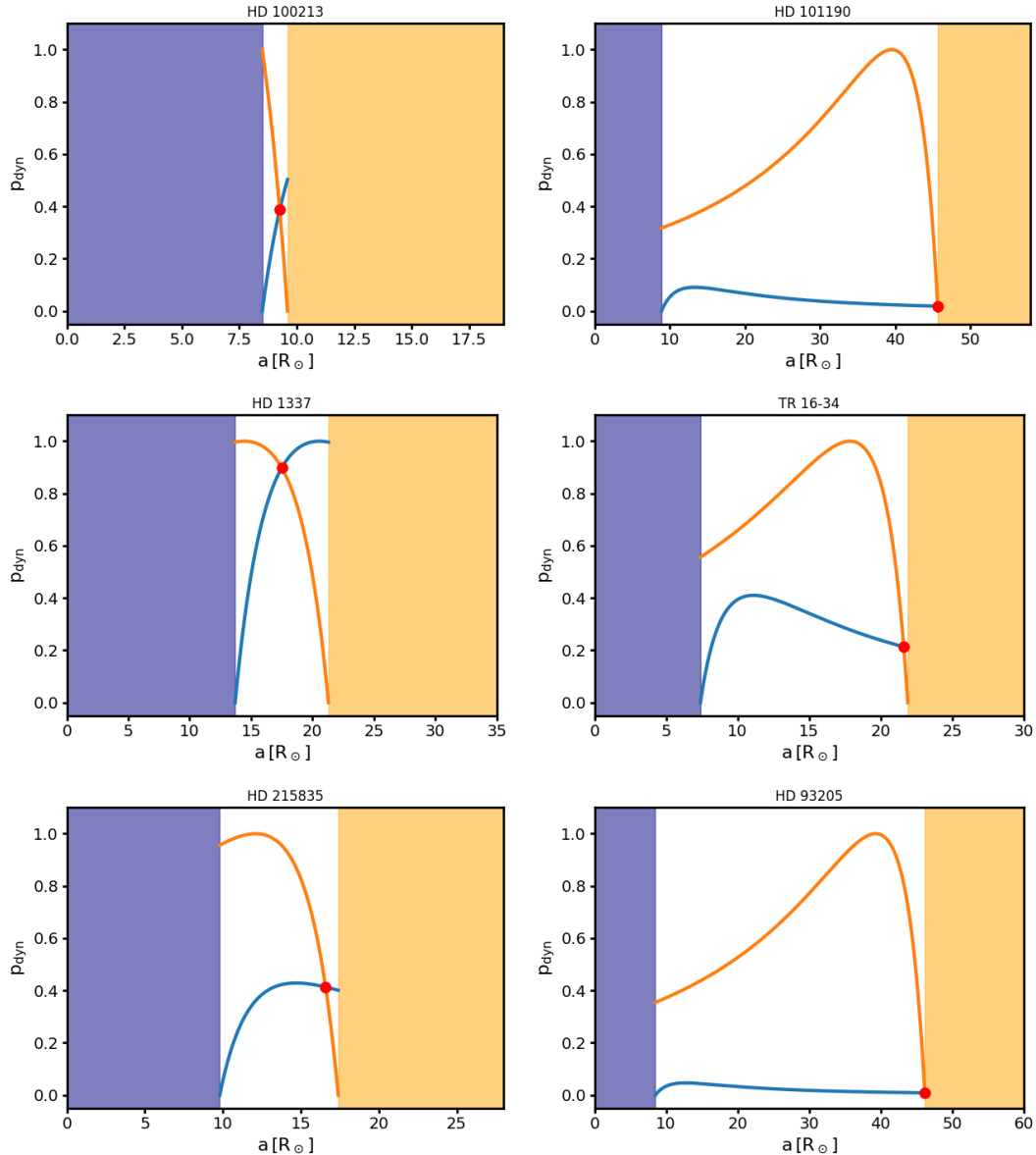
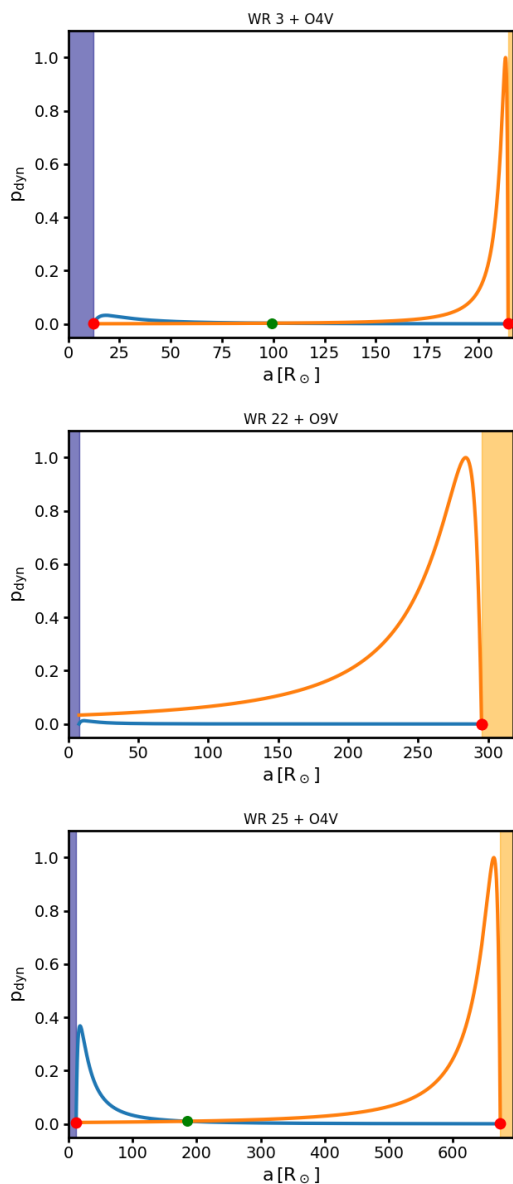


Figure B.3.: Stellar parameters and wind parameters as a function of the stellar mass. The radii and luminosities are inferred from the models of Brott et al. (2011) for solar metallicity. The other parameters are computed as described in the text.

B.4 Dynamical pressure in colliding wind binaries







Appendix C

Appendix to Chapter 4

C.1 Diagnostic diagrams of WR stars in the SMC

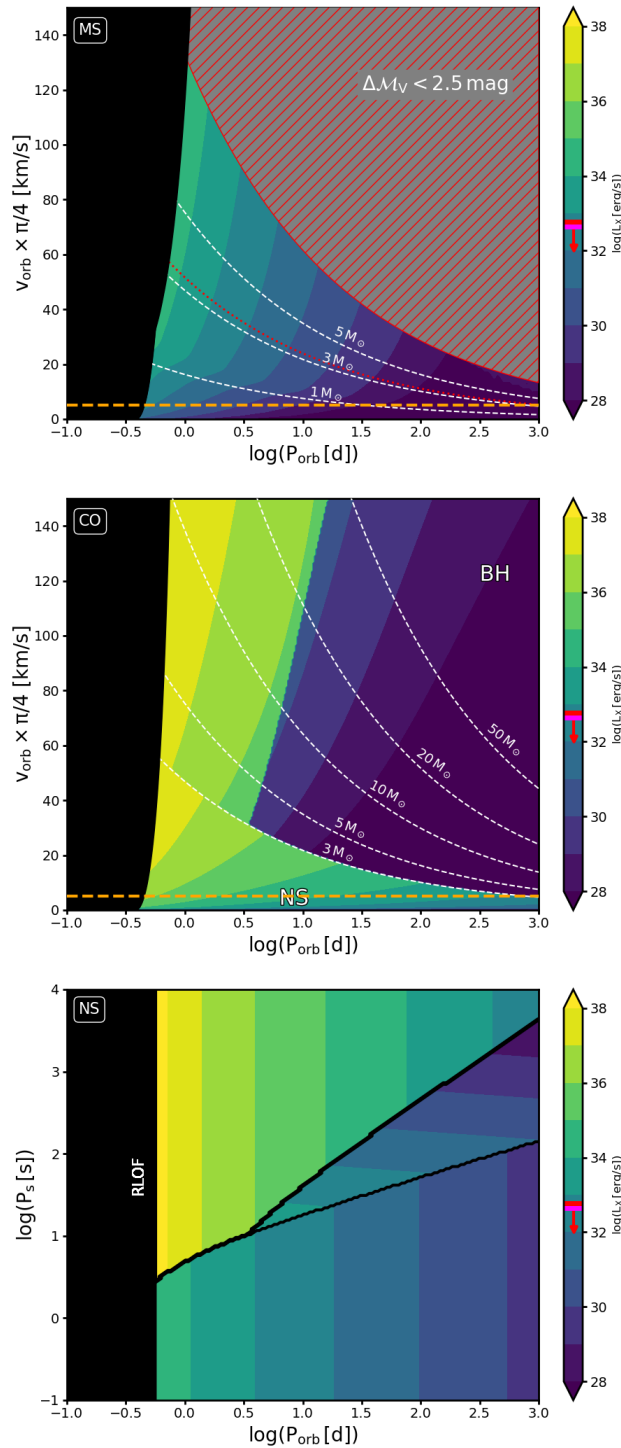


Figure C.1.: Diagnostic diagrams for SMC AB 1. Assumed parameters of the WR star can be found in Tab. 4.1. The upper limit of the X-ray luminosity is estimated in Sec. 4.2.

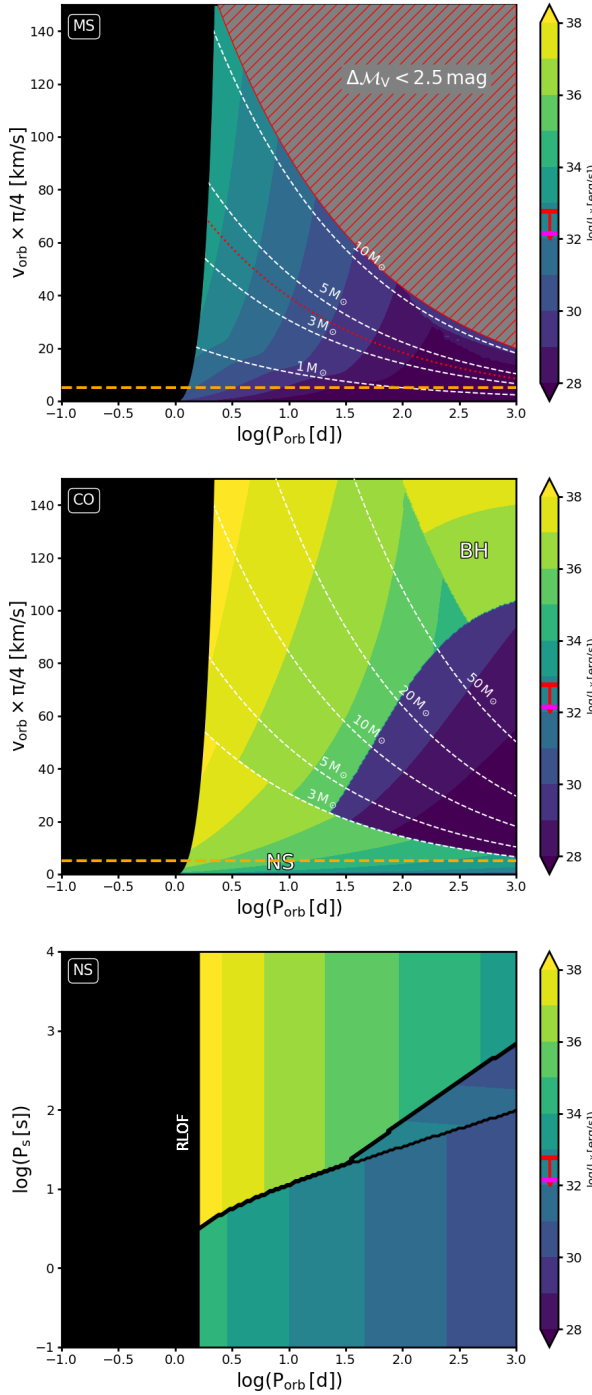


Figure C.2.: Diagnostic diagrams for SMC AB 2. Assumed parameters of the WR star can be found in Tab. 4.1. The upper limit of the X-ray luminosity is estimated in Sec. 4.2.

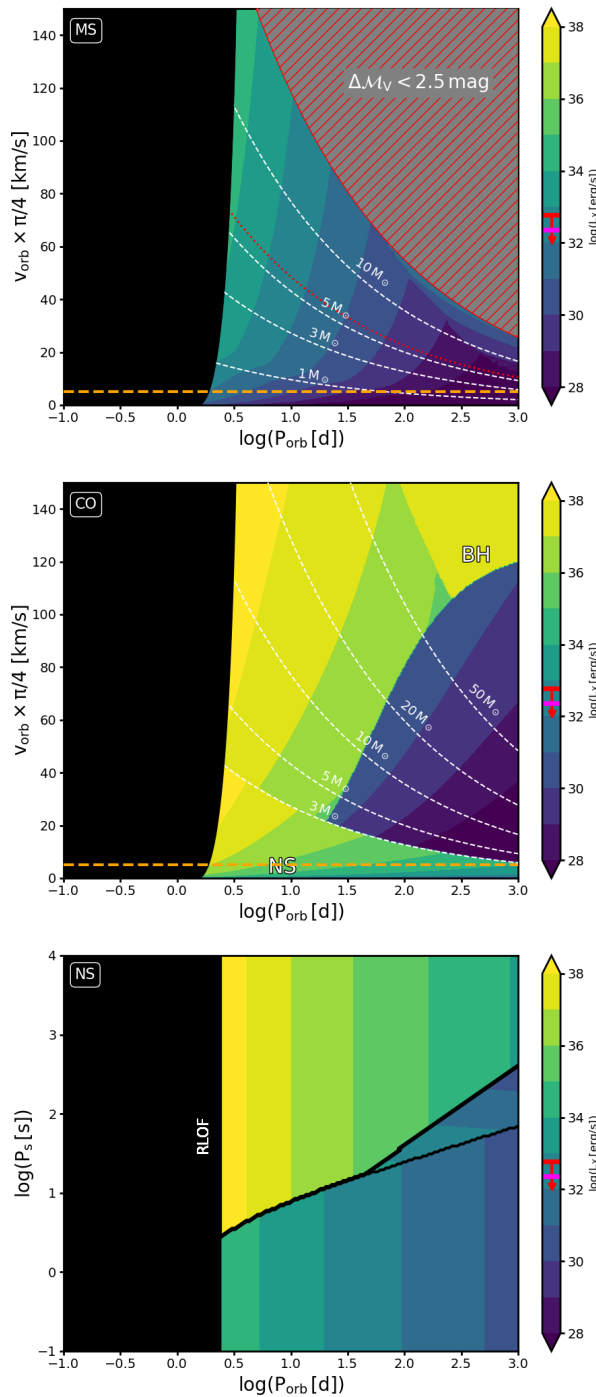


Figure C.3.: Diagnostic diagrams for SMC AB 4. Assumed parameters of the WR star can be found in Tab. 4.1. The upper limit of the X-ray luminosity is estimated in Sec. 4.2.

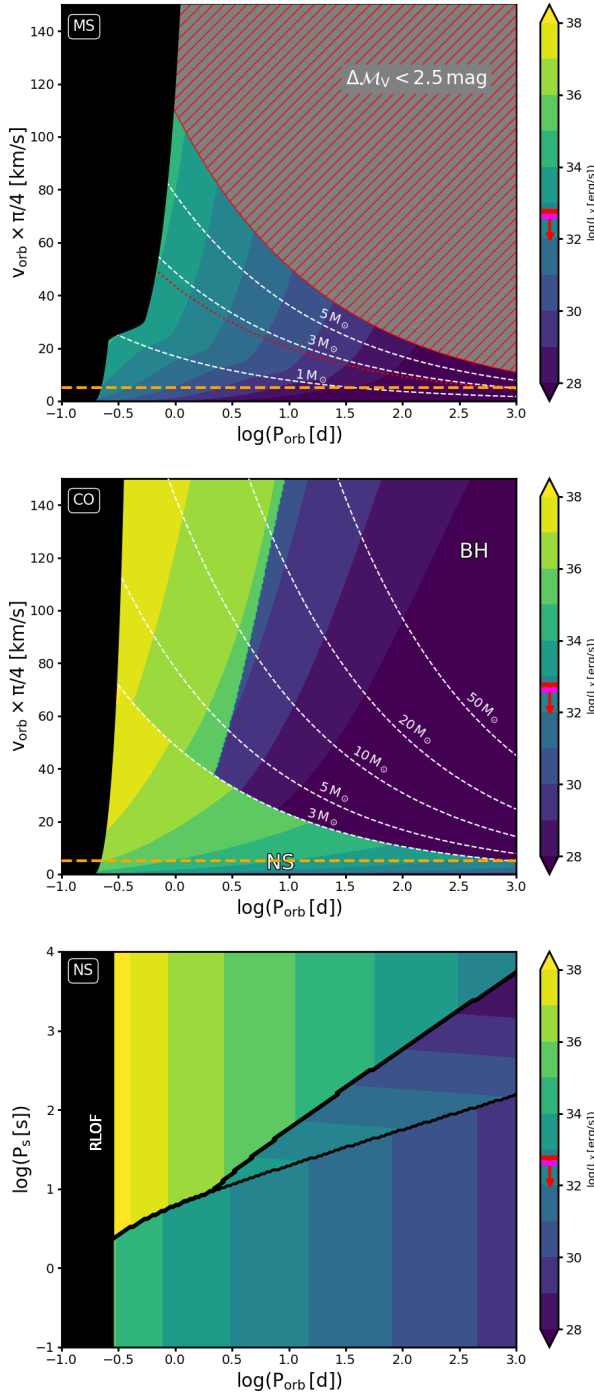


Figure C.4.: Diagnostic diagrams for SMC AB 9. Assumed parameters of the WR star can be found in Tab. 4.1. The upper limit of the X-ray luminosity is estimated in Sec. 4.2.

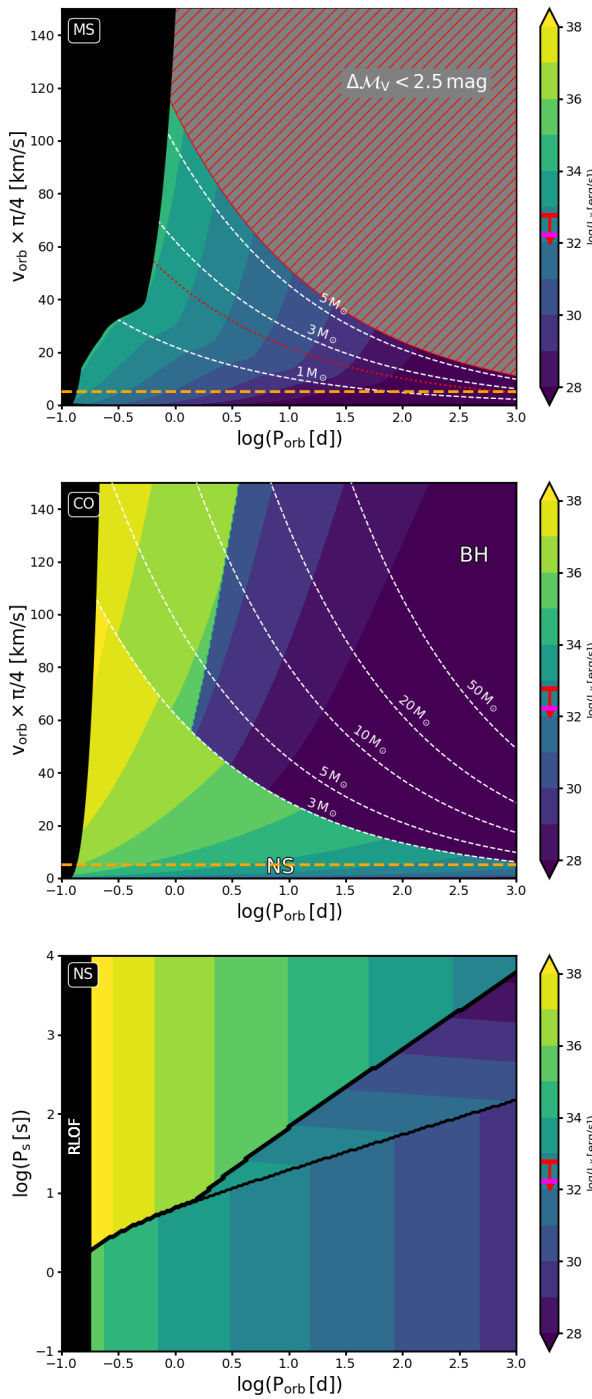


Figure C.5.: Diagnostic diagrams for SMC AB 10. Assumed parameters of the WR star can be found in Tab. 4.1. The upper limit of the X-ray luminosity is estimated in Sec. 4.2.

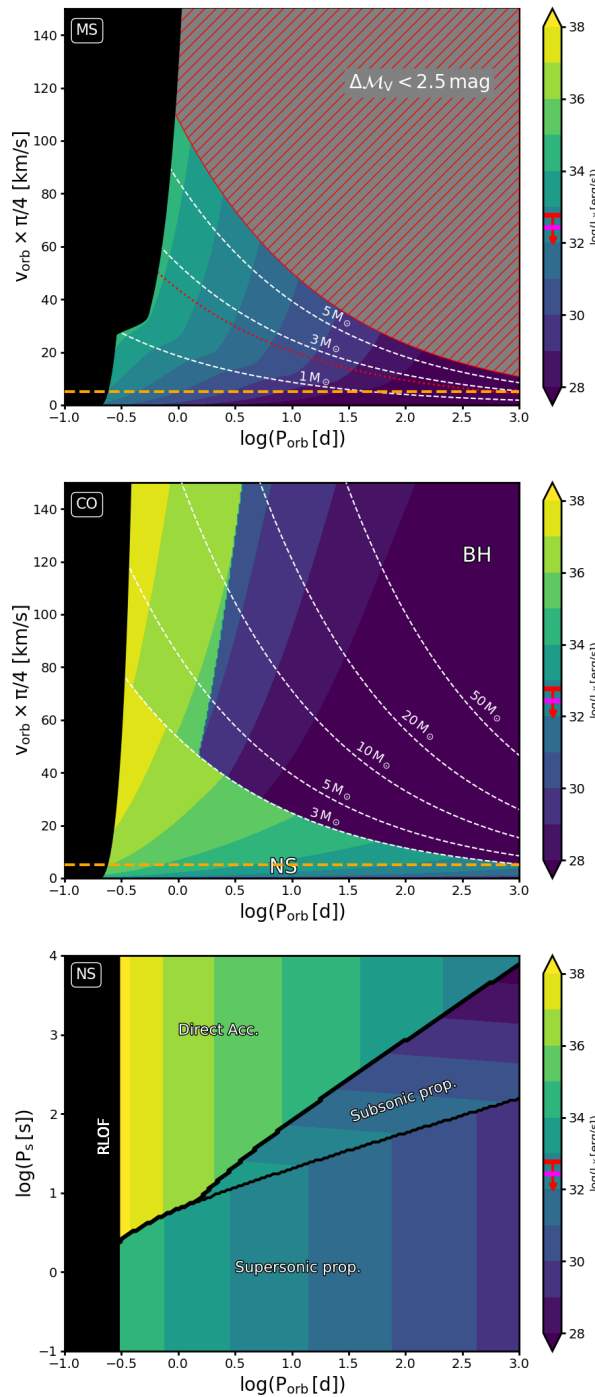


Figure C.6.: Diagnostic diagrams for SMC AB 11. Assumed parameters of the WR star can be found in Tab. 4.1. The upper limit of the X-ray luminosity is estimated in Sec. 4.2.

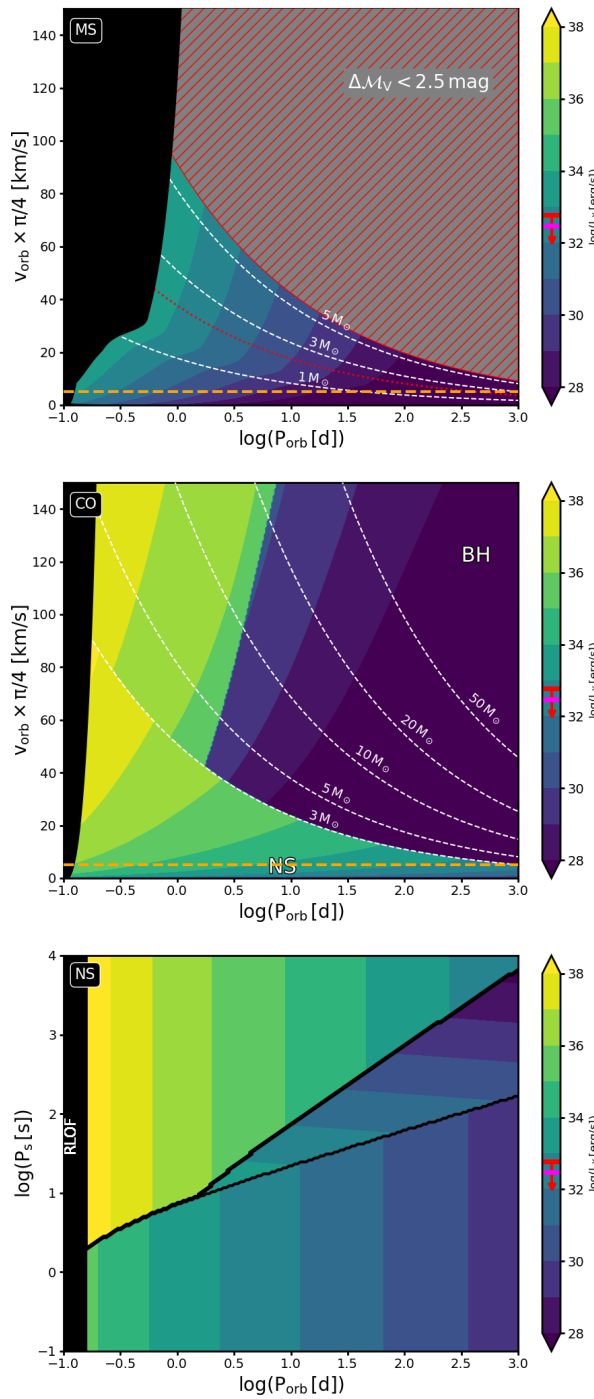


Figure C.7.: Diagnostic diagrams for SMC AB 12. Assumed stellar parameters of the WR star can be found in Tab. 4.1. The upper limit of the X-ray luminosity is estimated in Sec. 4.2.

C.2 Diagnostic diagrams of Galactic WN 8 stars

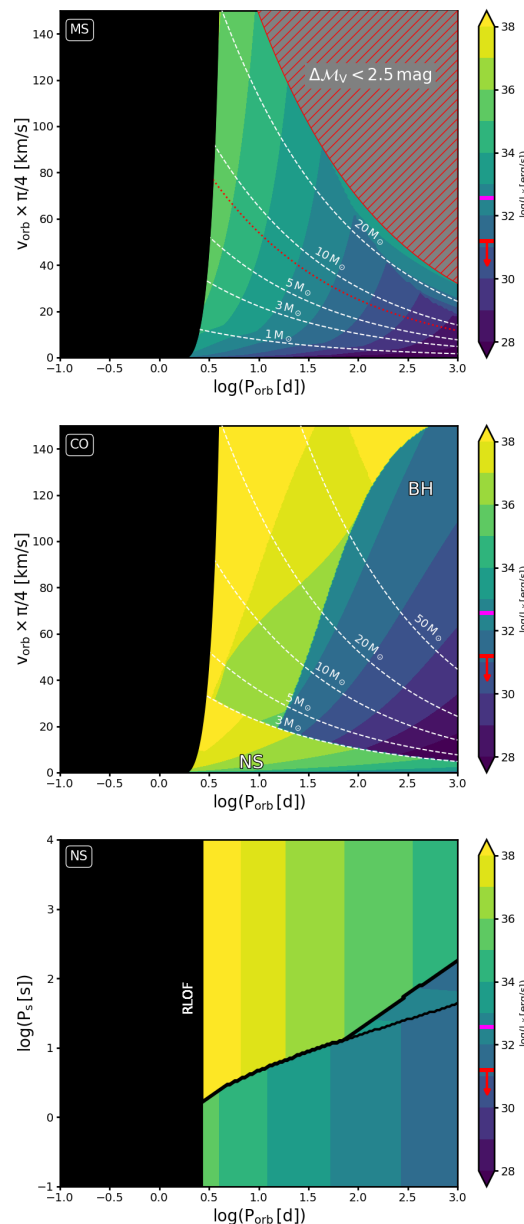


Figure C.8.: Diagnostic diagrams for WR 12. Assumed stellar parameters of the WR star can be found in Table 4.5. Upper limit of the observed X-ray luminosity according to Nazé et al. (2021).

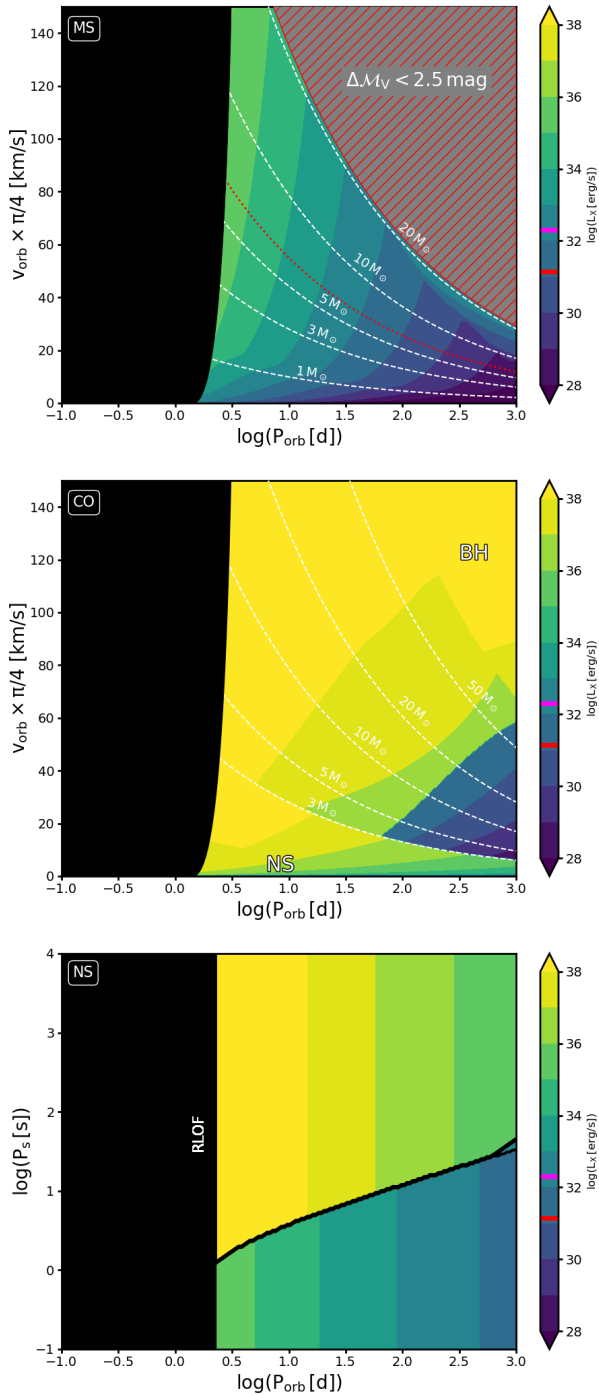


Figure C.9.: Diagnostic diagrams for WR 16. Assumed stellar parameters of the WR star can be found in Table 4.5. Observed X-ray luminosity according to Skinner et al. (2012).

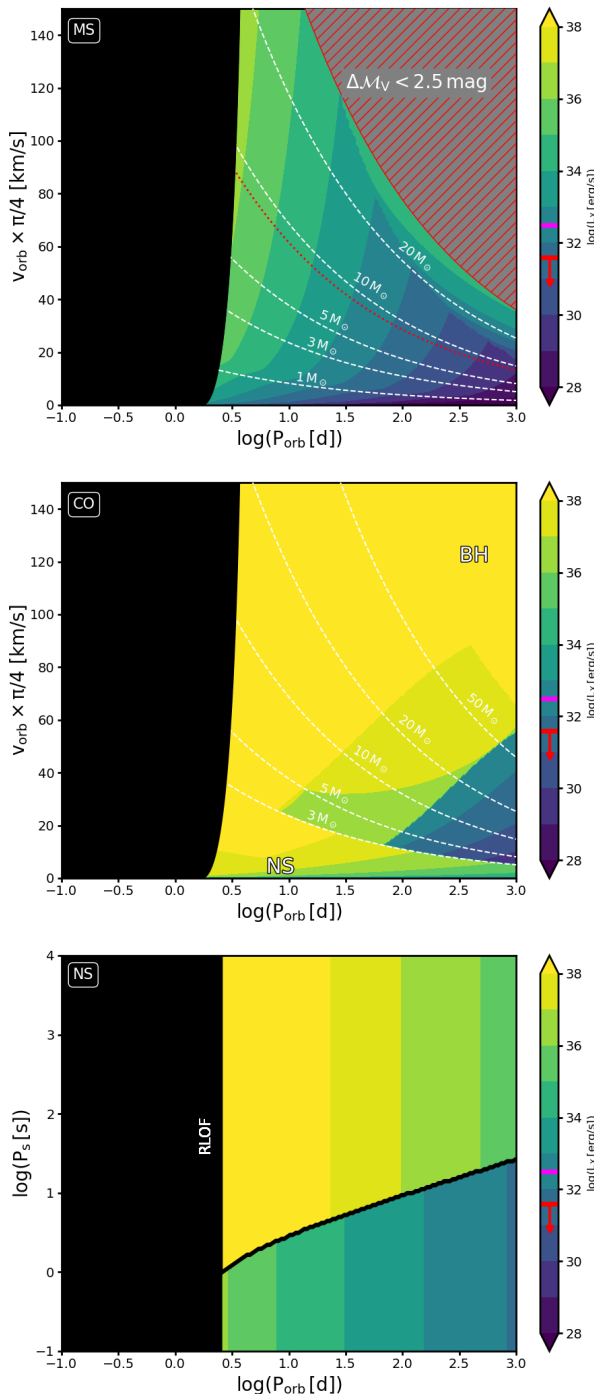


Figure C.10.: Diagnostic diagrams for WR 40. Assumed stellar parameters of the WR star can be found in Table 4.5. Upper limit of the observed X-ray luminosity according to Gosset et al. (2005).

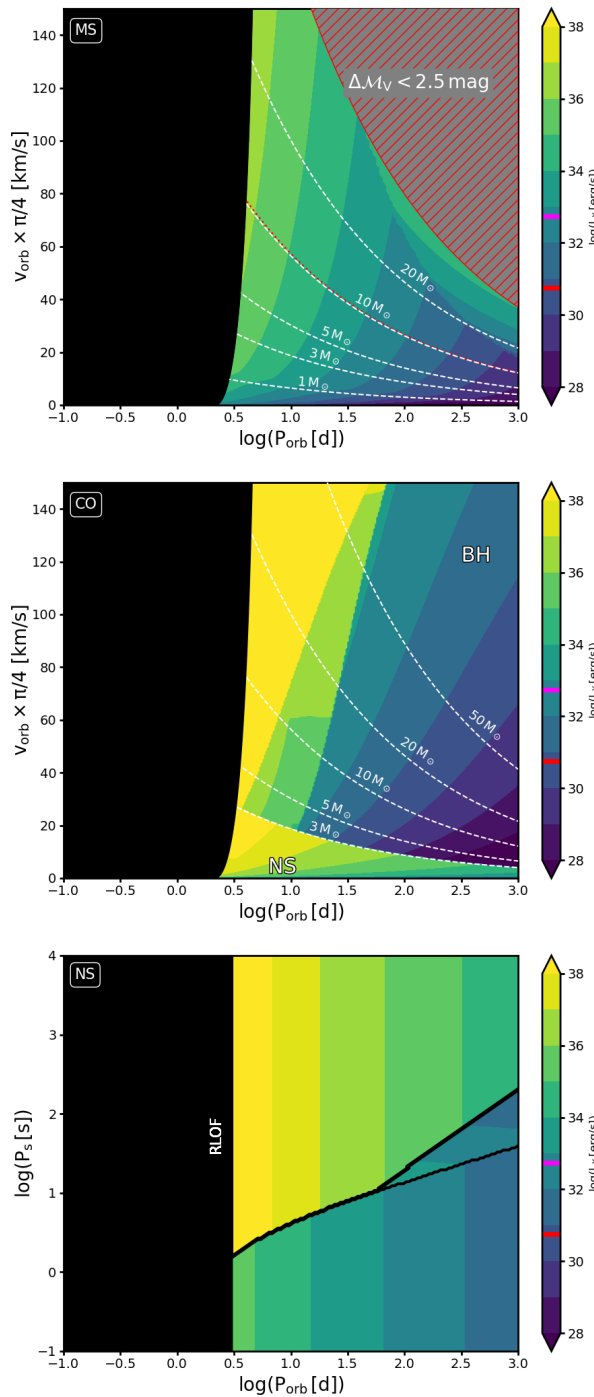


Figure C.11.: Diagnostic diagrams for WR 66. Assumed stellar parameters of the WR star can be found in Table 4.5. Observed X-ray luminosity according to Skinner et al. (2021).

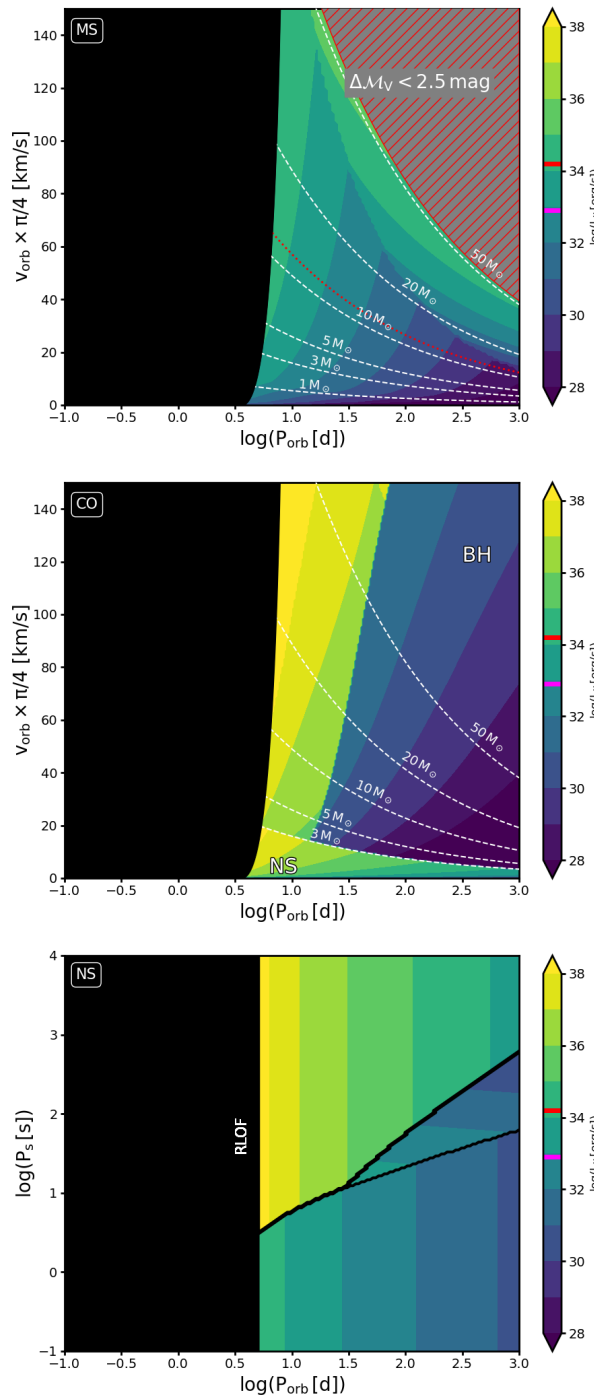


Figure C.12.: Diagnostic diagrams for WR 89. Assumed stellar parameters of the WR star can be found in Table 4.5. Observed X-ray luminosity according to Nazé et al. (2013).

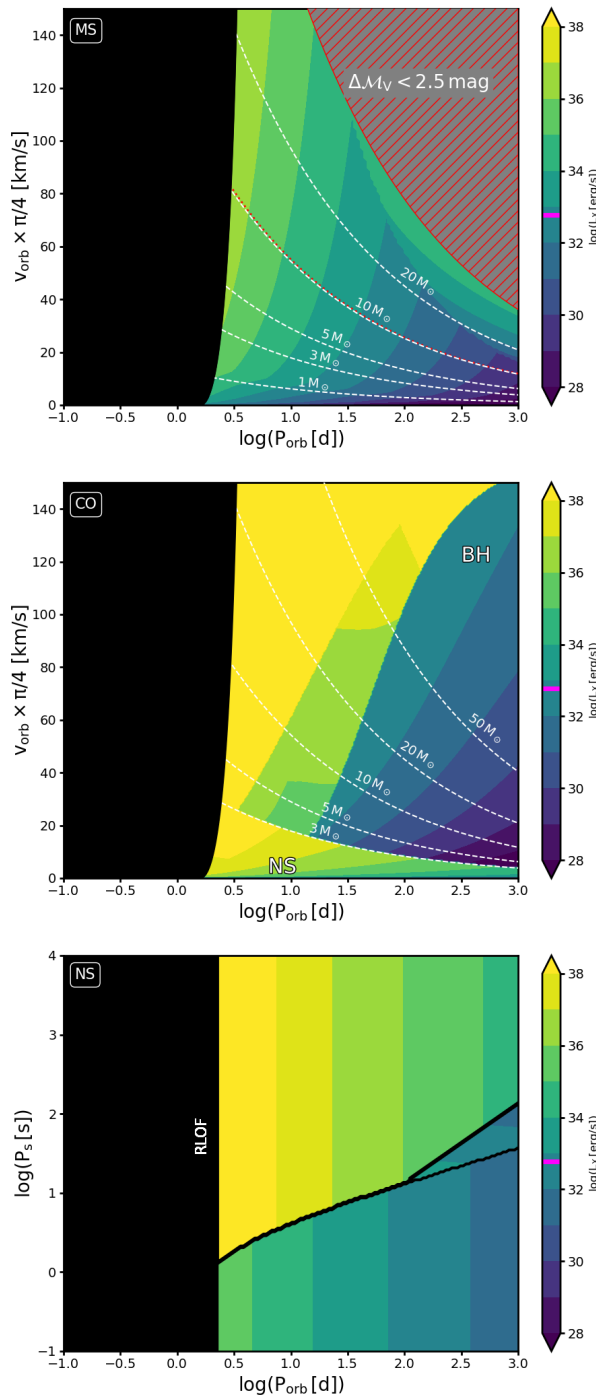


Figure C.13.: Diagnostic diagrams for WR 107. Assumed stellar parameters of the WR star can be found in Table 4.5.

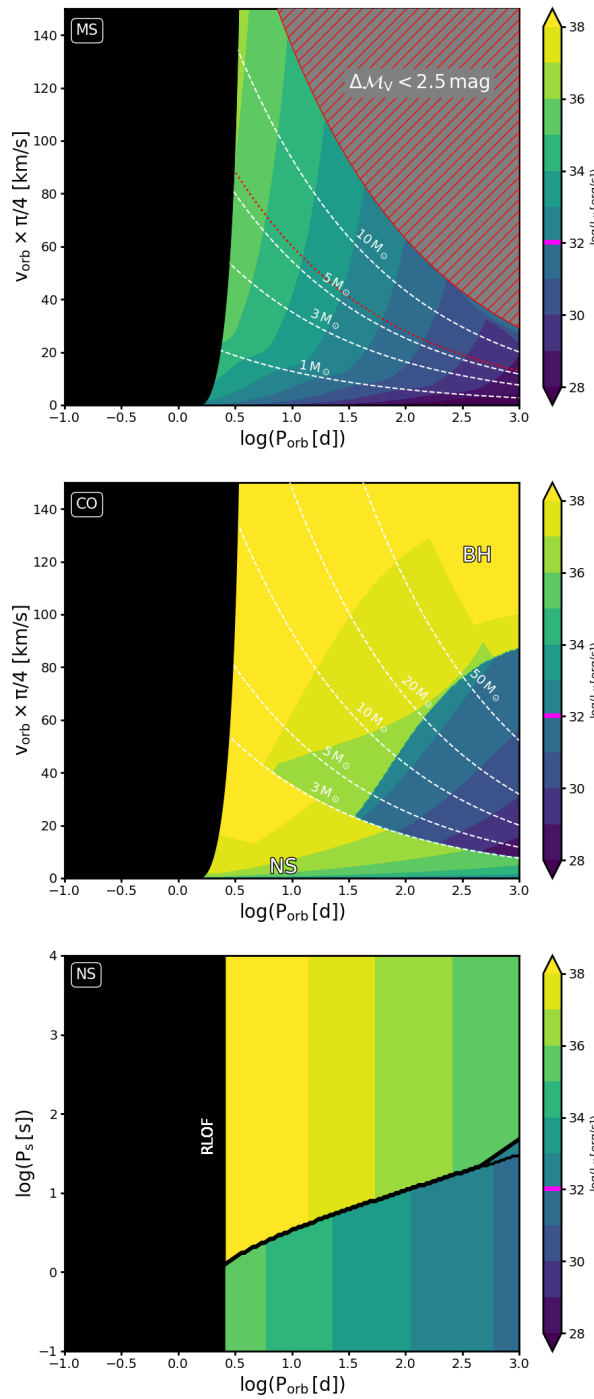


Figure C.14.: Diagnostic diagrams for WR 116. Assumed stellar parameters of the WR star can be found in Table 4.5.

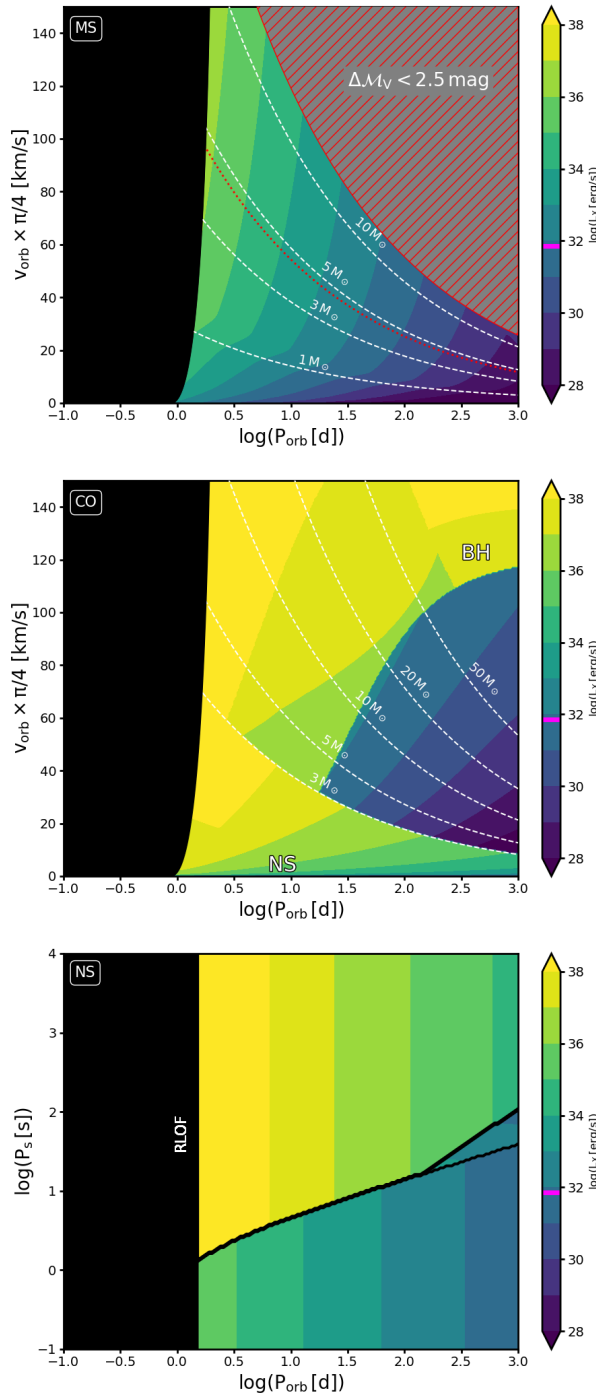


Figure C.15.: Diagnostic diagrams for WR 123. Assumed stellar parameters of the WR star can be found in Table 4.5.

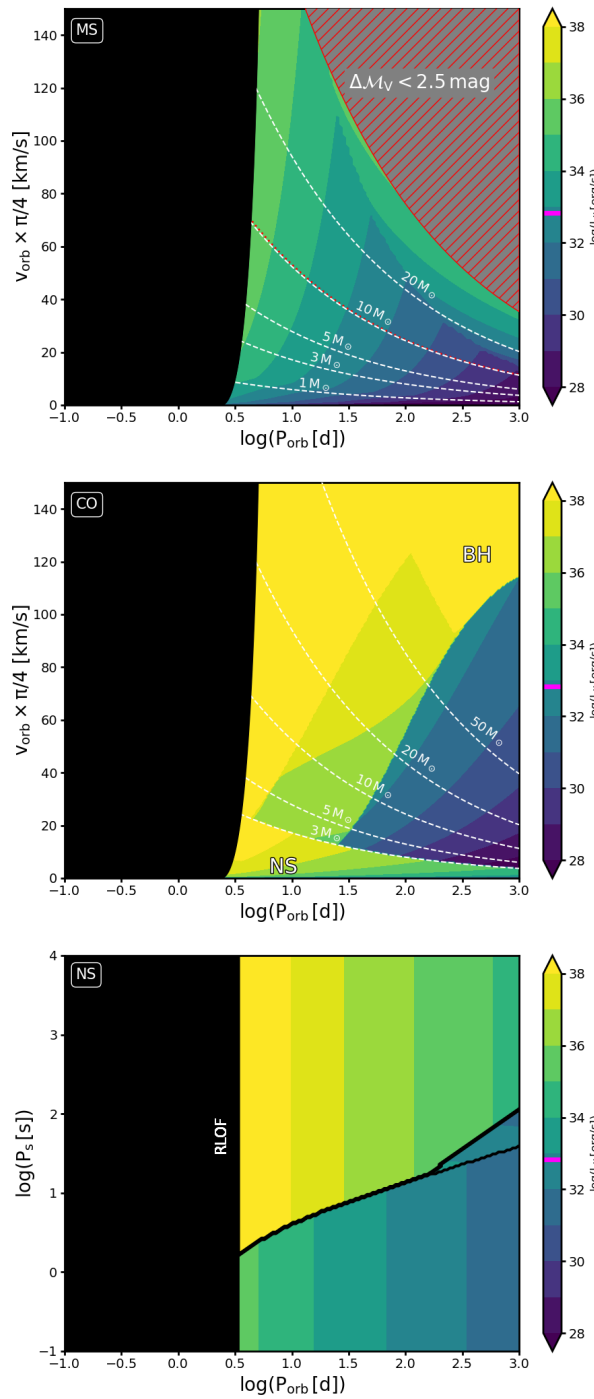


Figure C.16.: Diagnostic diagrams for WR 130. Assumed stellar parameters of the WR star can be found in Table 4.5.

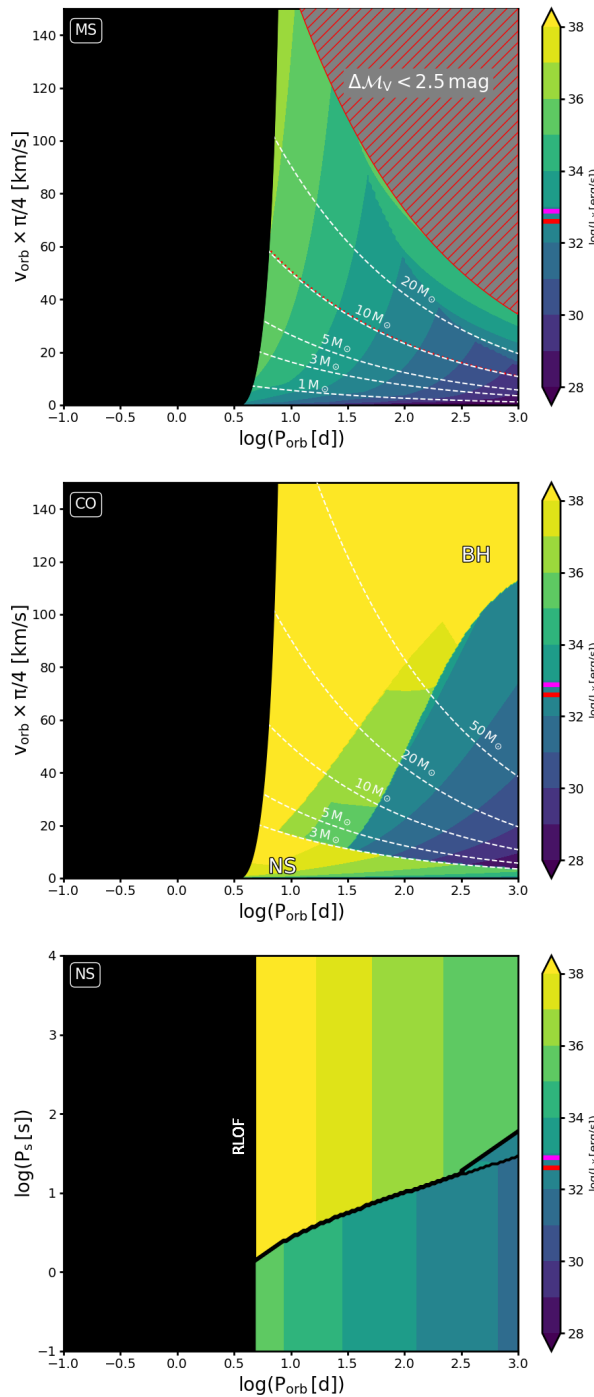


Figure C.17.: Diagnostic diagrams for WR 147. Assumed stellar parameters of the WR star can be found in Table 4.5. Observed X-ray luminosity according to Skinner et al. (2006).

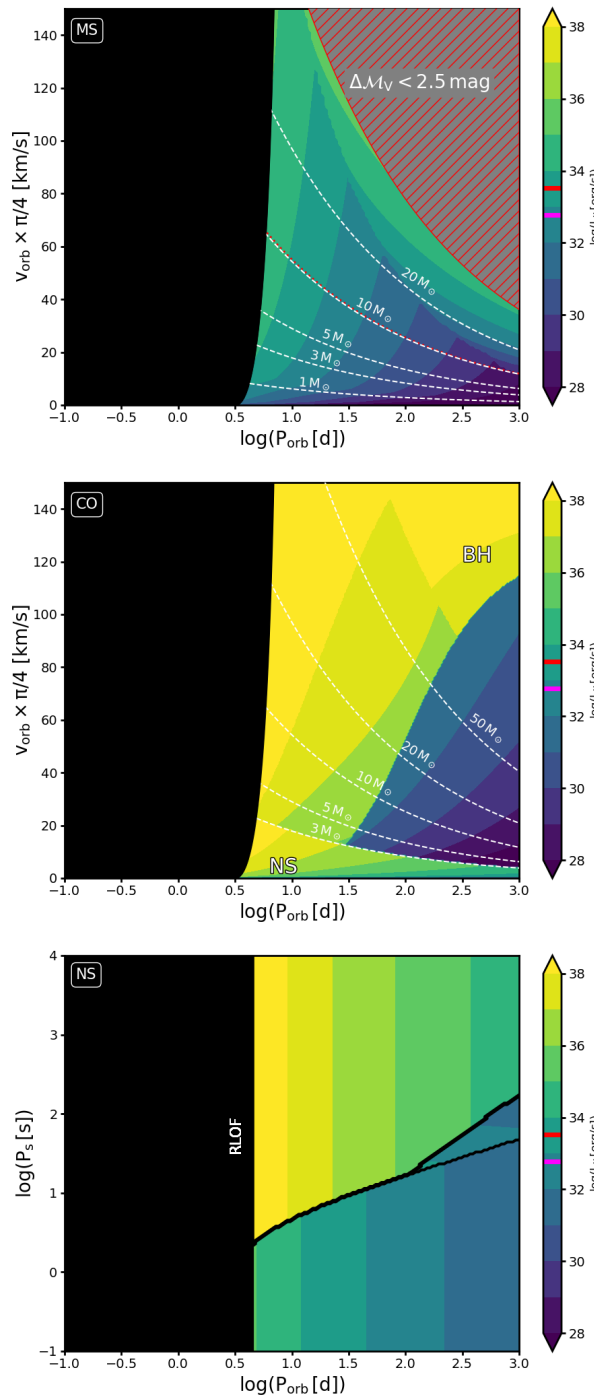


Figure C.18.: Diagnostic diagrams for WR 148. Assumed stellar parameters of the WR star can be found in Table 4.5. Observed X-ray luminosity according to Zhekov (2012).

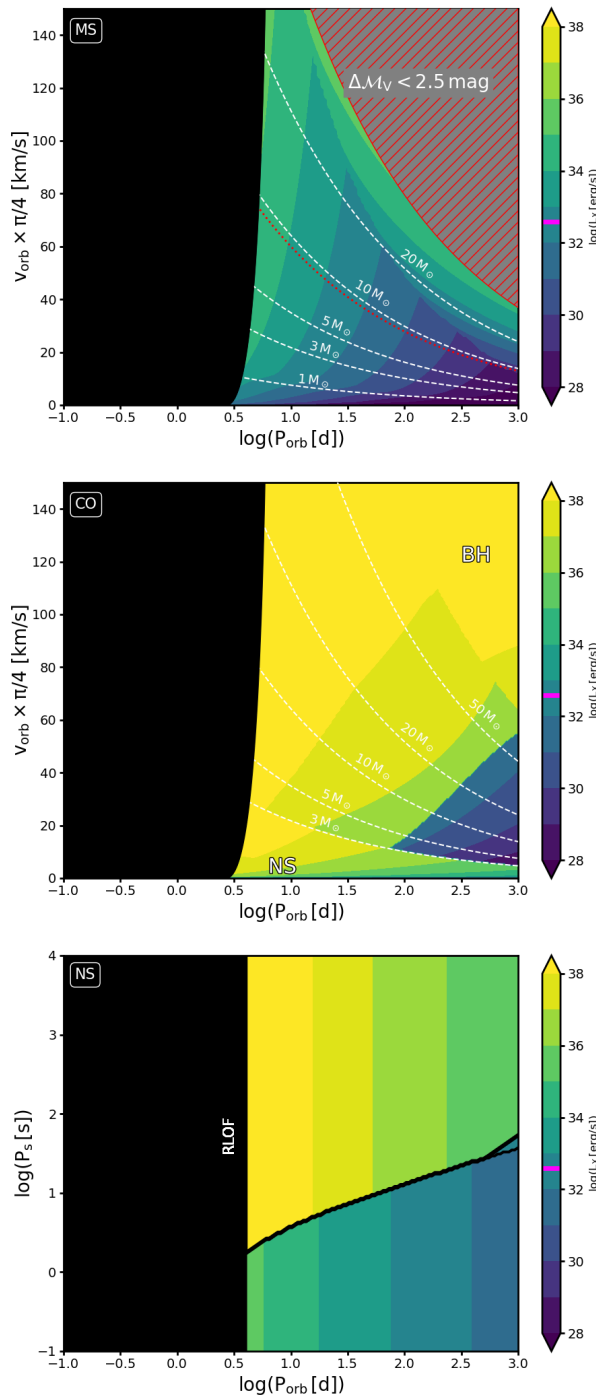


Figure C.19.: Diagnostic diagrams for WR 156. Assumed stellar parameters of the WR star can be found in Table 4.5.

C.3 Diagnostic diagrams of TMBM SB1 and uncertain SB2

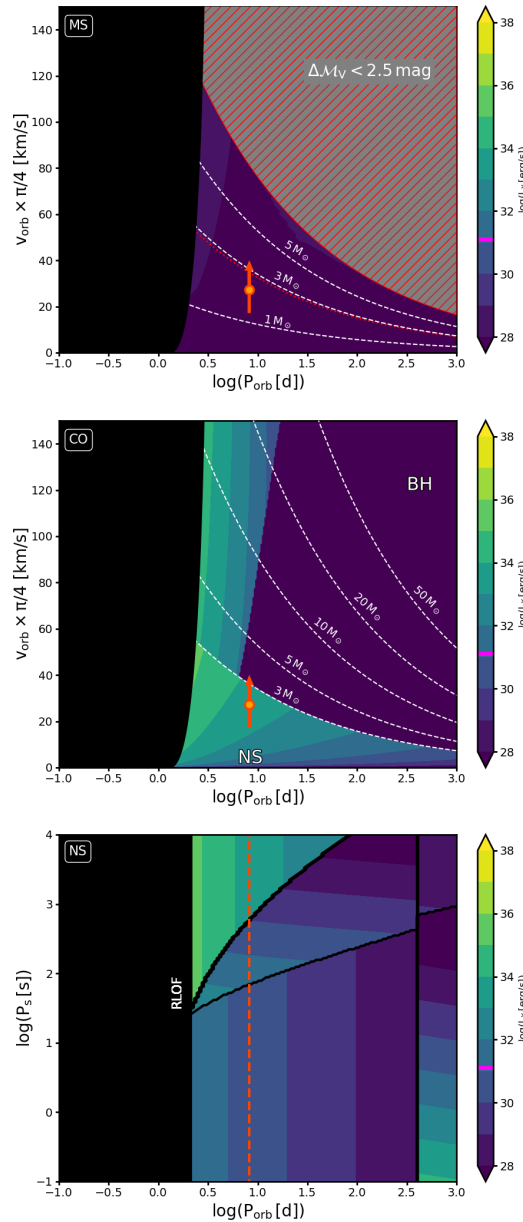


Figure C.20.: Diagnostic diagrams for VFTS 225. Assumed stellar parameters can be found in Tab. 4.7. A MS companion cannot be excluded regarding X-rays or brightness. BH would be close to the transition regime of an accretion disc and may be detectable. A directly accreting NS would produce a detectable amount of X-rays. However, even a spin period of 100 s would lead to faint X-ray radiation due to the propeller effect.

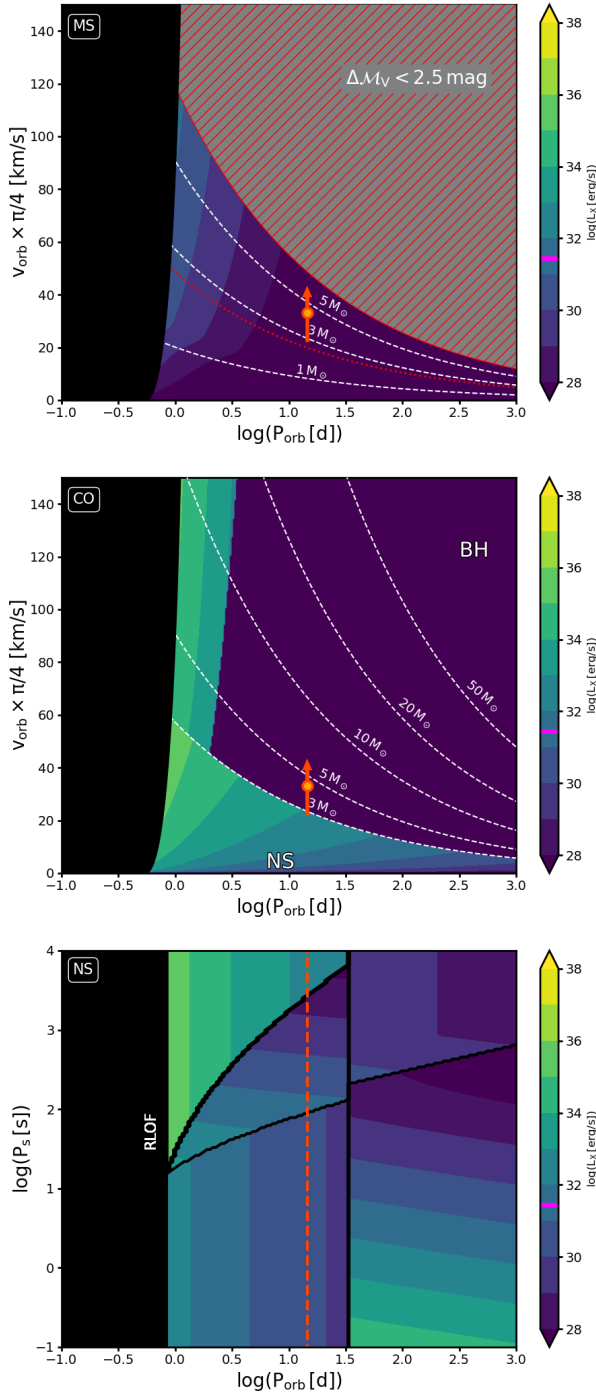


Figure C.21.: Diagnostic diagrams for VFTS 619. Assumed stellar parameters can be found in Tab. 4.7. A MS companion may be detectable in the optical spectrum. A BH would be X-ray quiet. The lower limit of the companion mass makes a NS companion unlikely.

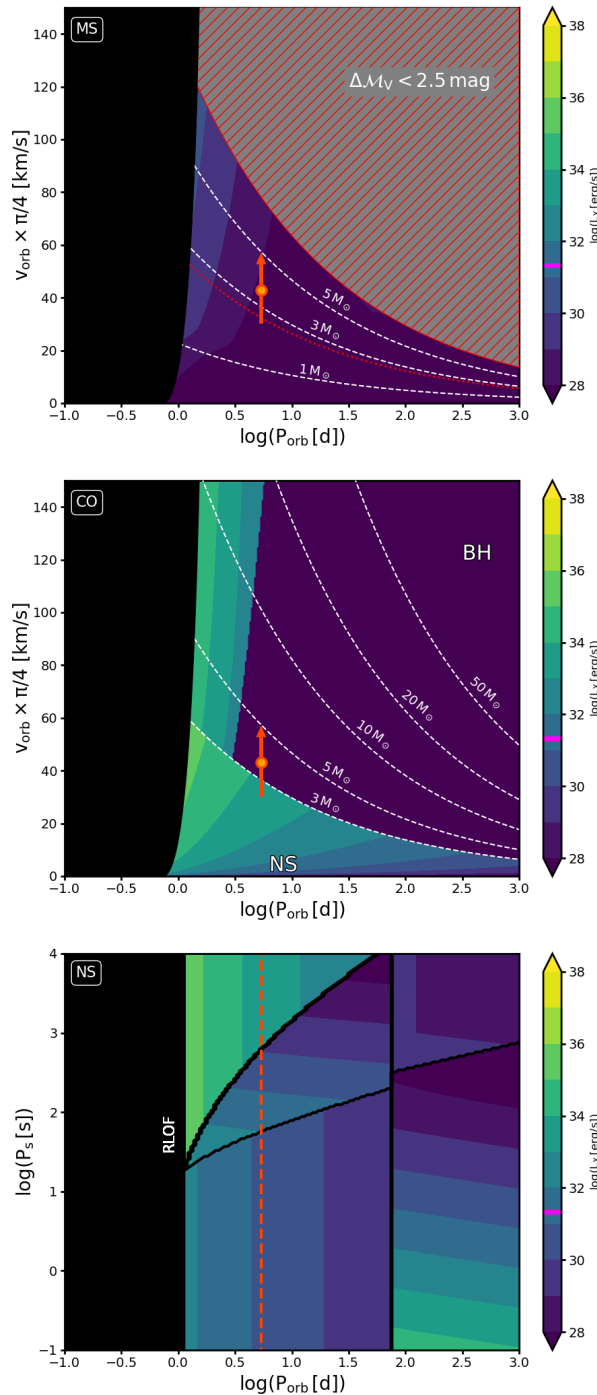


Figure C.22.: Diagnostic diagrams for VFTS 631. Assumed stellar parameters can be found in Tab. 4.7.

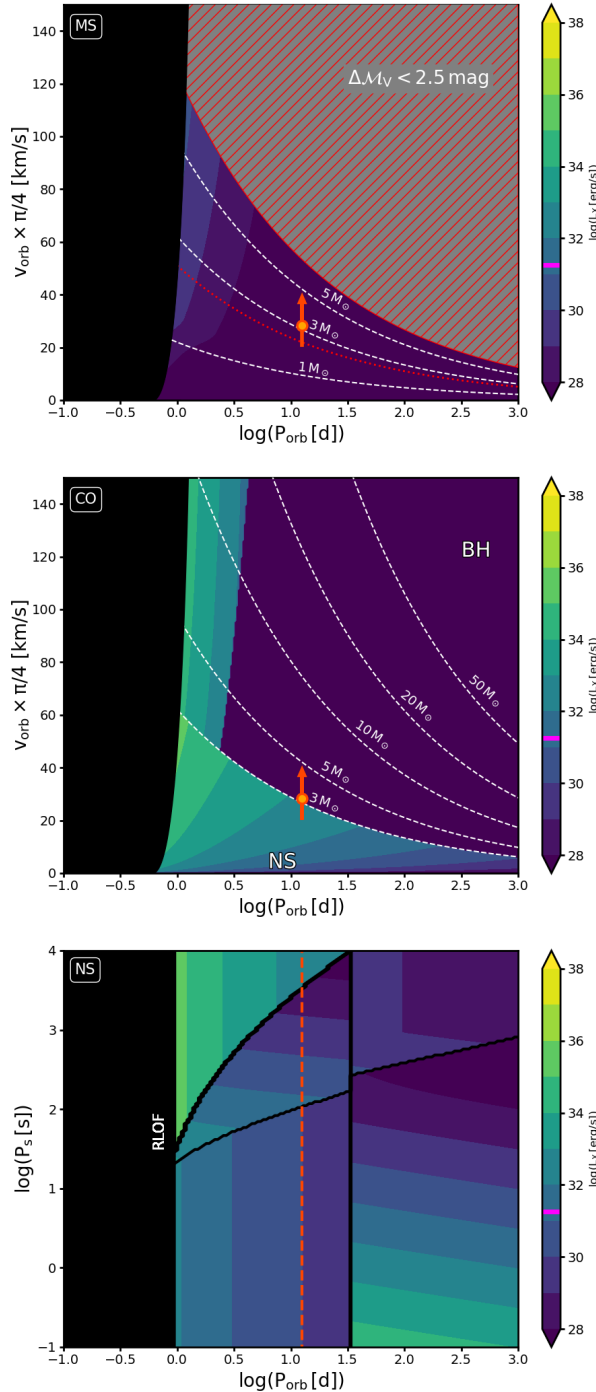


Figure C.23.: Diagnostic diagrams for VFTS 645. Assumed stellar parameters can be found in Tab. 4.7.

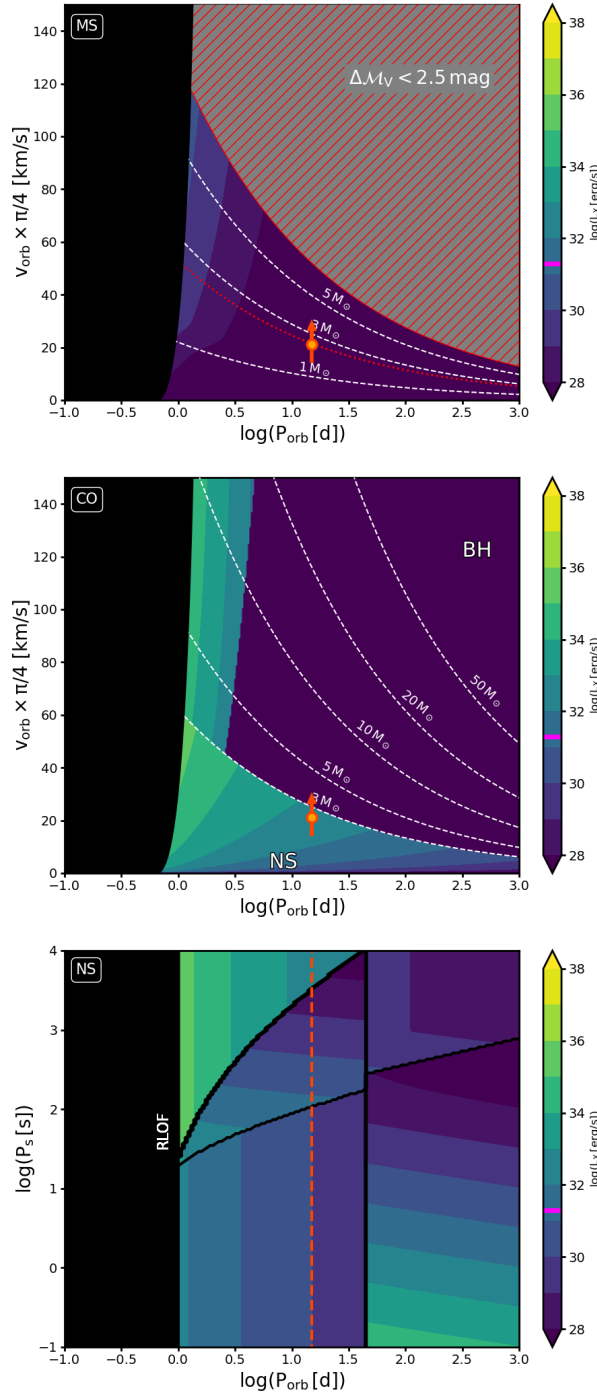


Figure C.24.: Diagnostic diagrams for VFTS 743. Assumed stellar parameters can be found in Tab. 4.7.

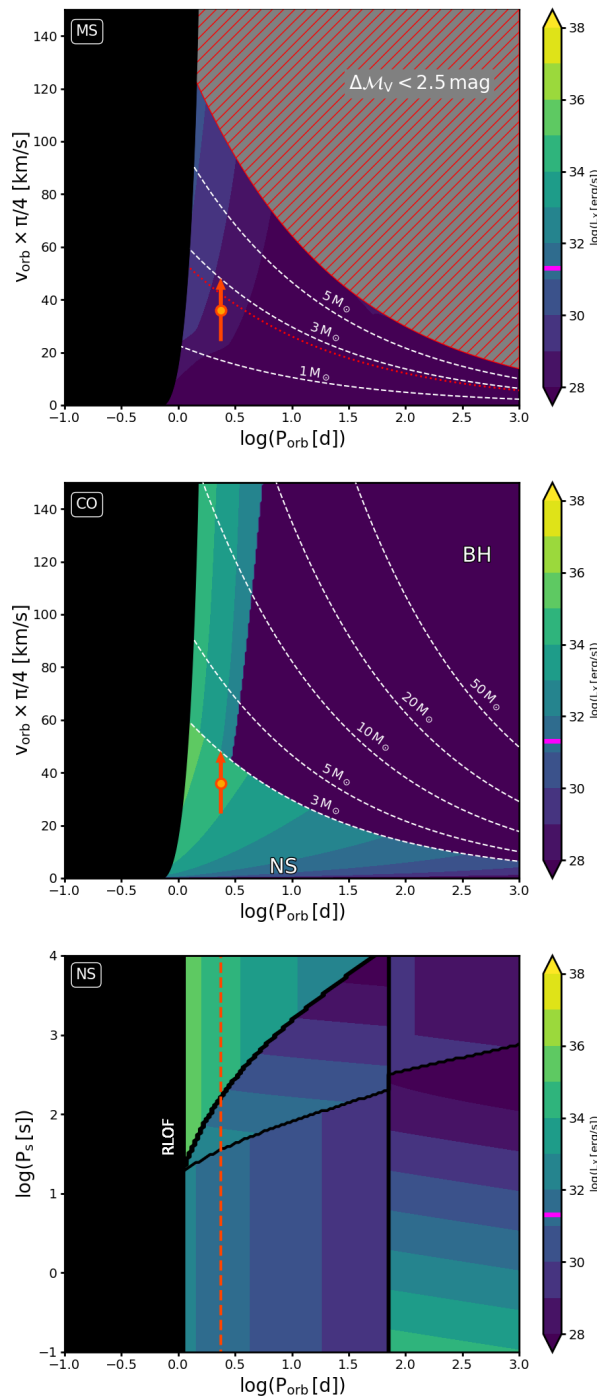


Figure C.25.: Diagnostic diagrams for VFTS 769. Assumed stellar parameters can be found in Tab. 4.7.

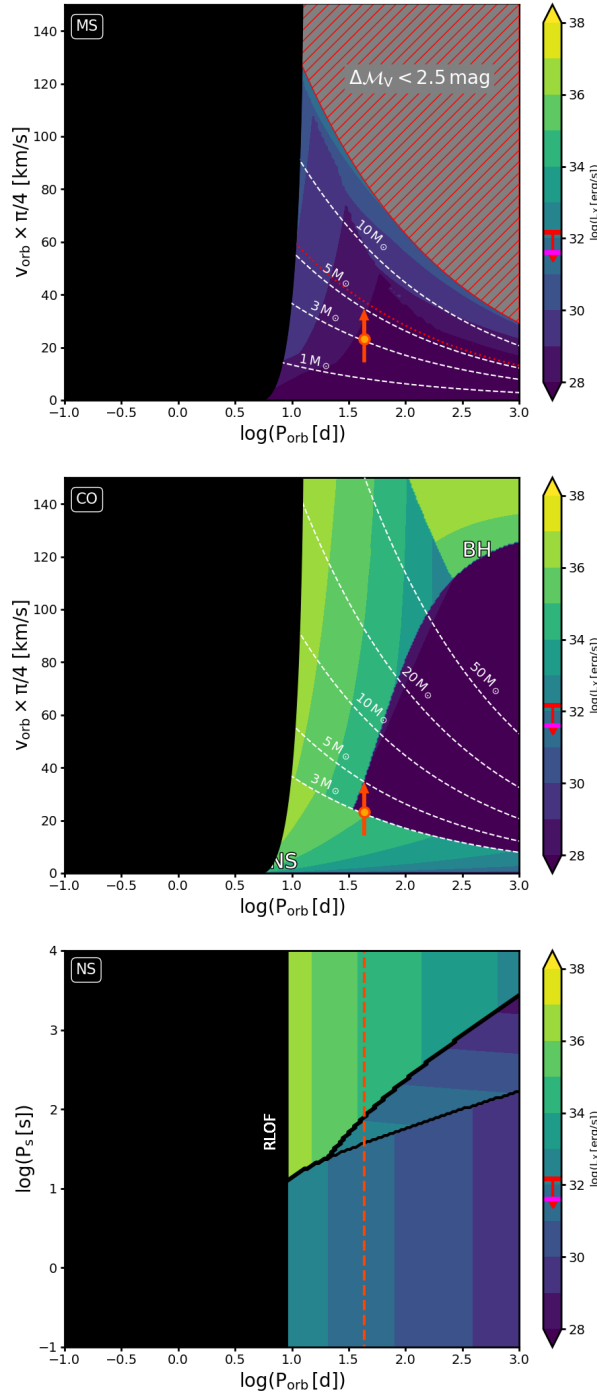


Figure C.26.: Diagnostic diagrams for VFTS 827. Assumed stellar parameters can be found in Tab. 4.7.

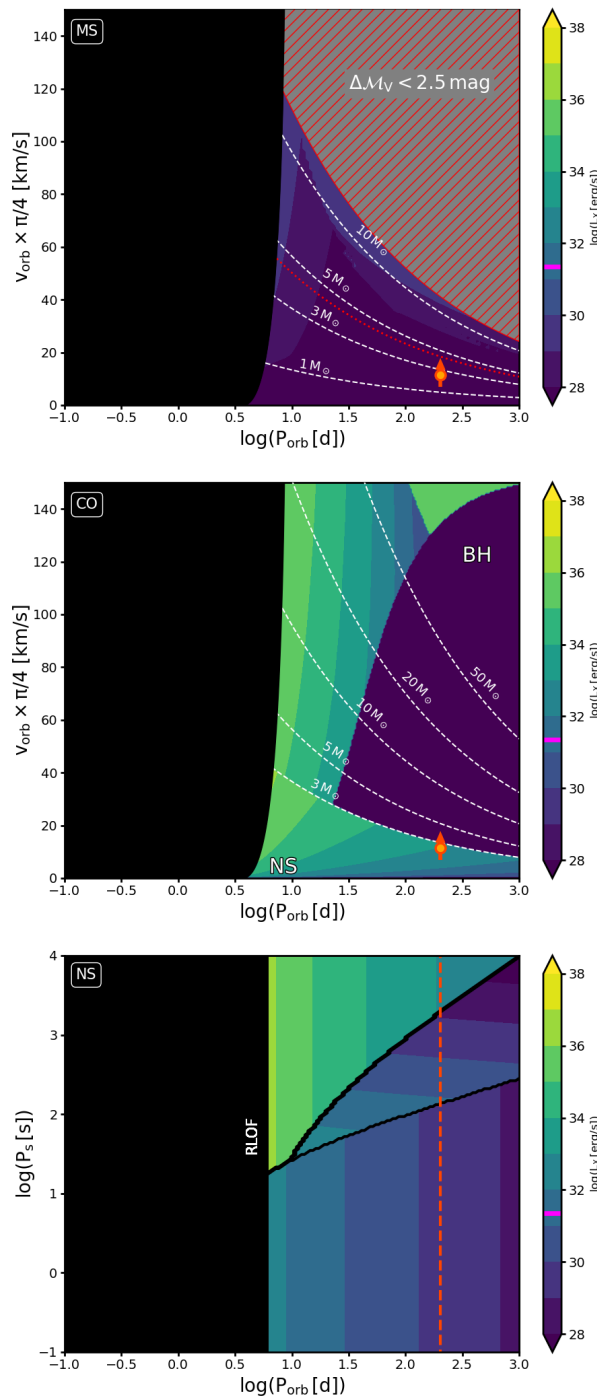


Figure C.27.: Diagnostic diagrams for VFTS 829. Assumed stellar parameters can be found in Tab. 4.7.

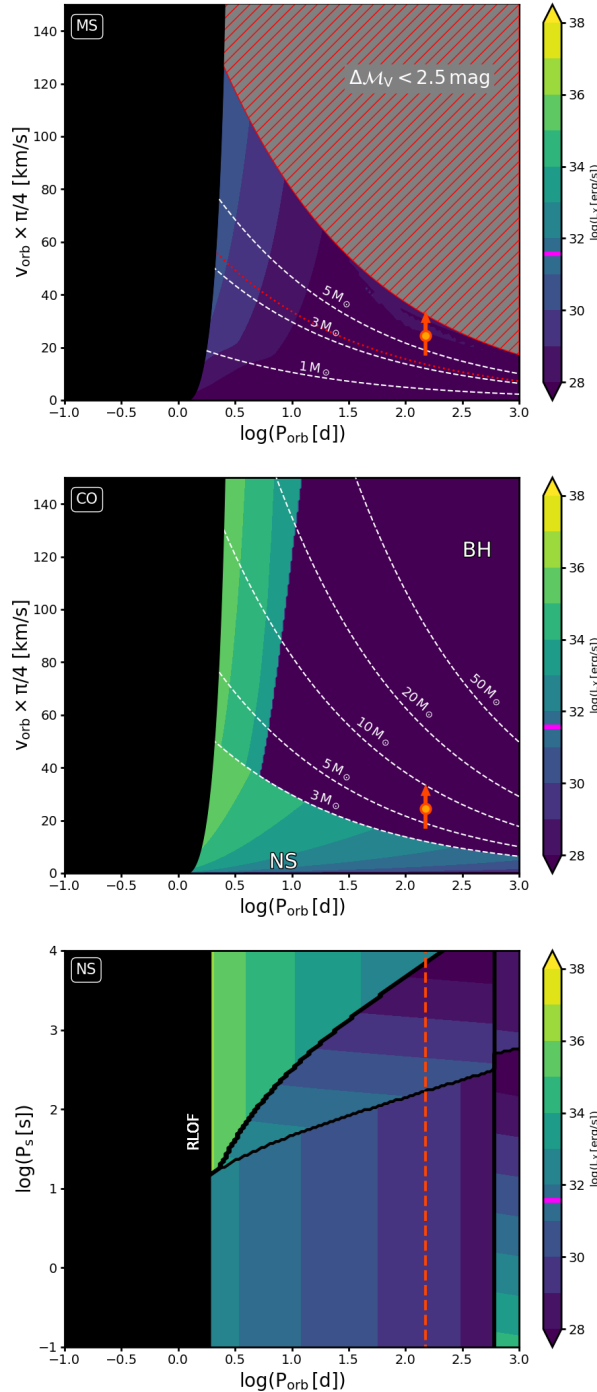


Figure C.28.: Diagnostic diagrams for VFTS 73. Assumed stellar parameters can be found in Tab. 4.8.

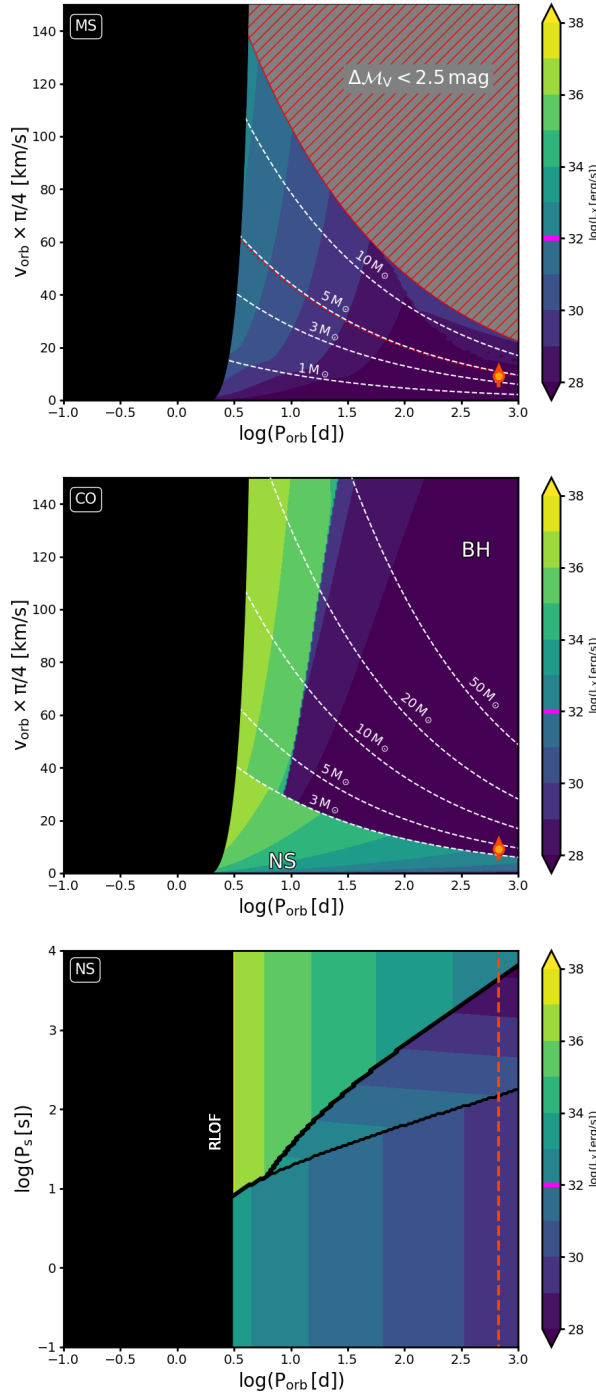


Figure C.29.: Diagnostic diagrams for VFTS 171. Assumed stellar parameters can be found in Tab. 4.8.

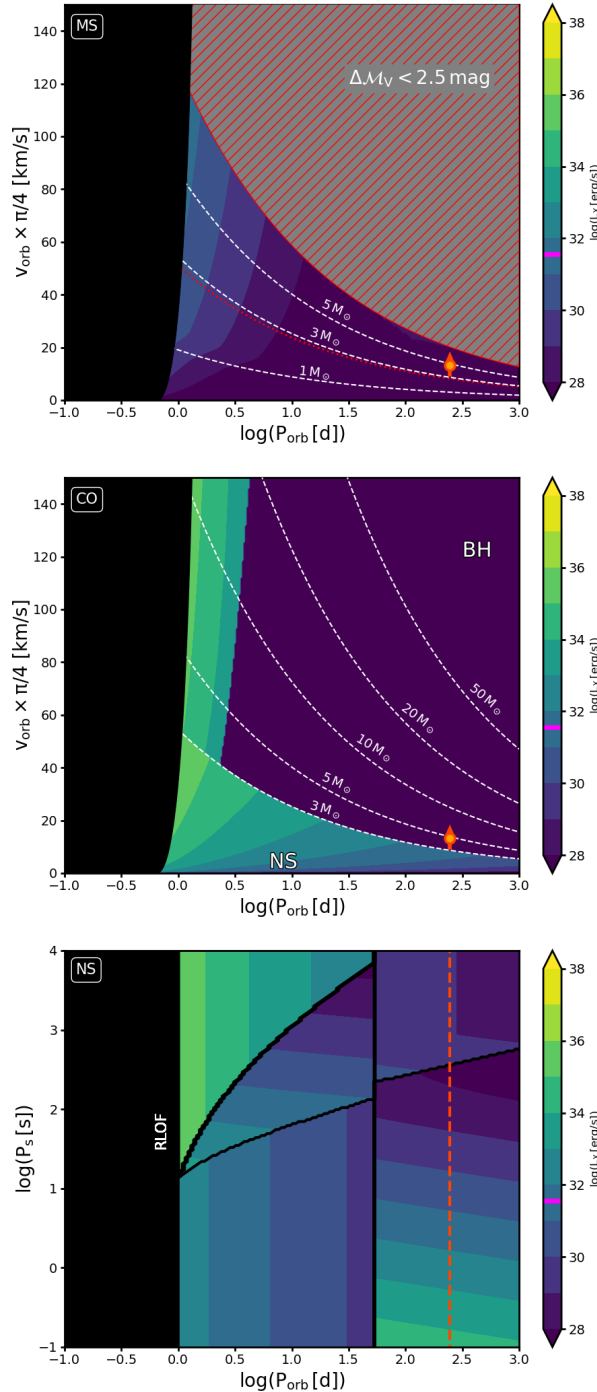


Figure C.30.: Diagnostic diagrams for VFTS 256. Assumed stellar parameters can be found in Tab. 4.8.

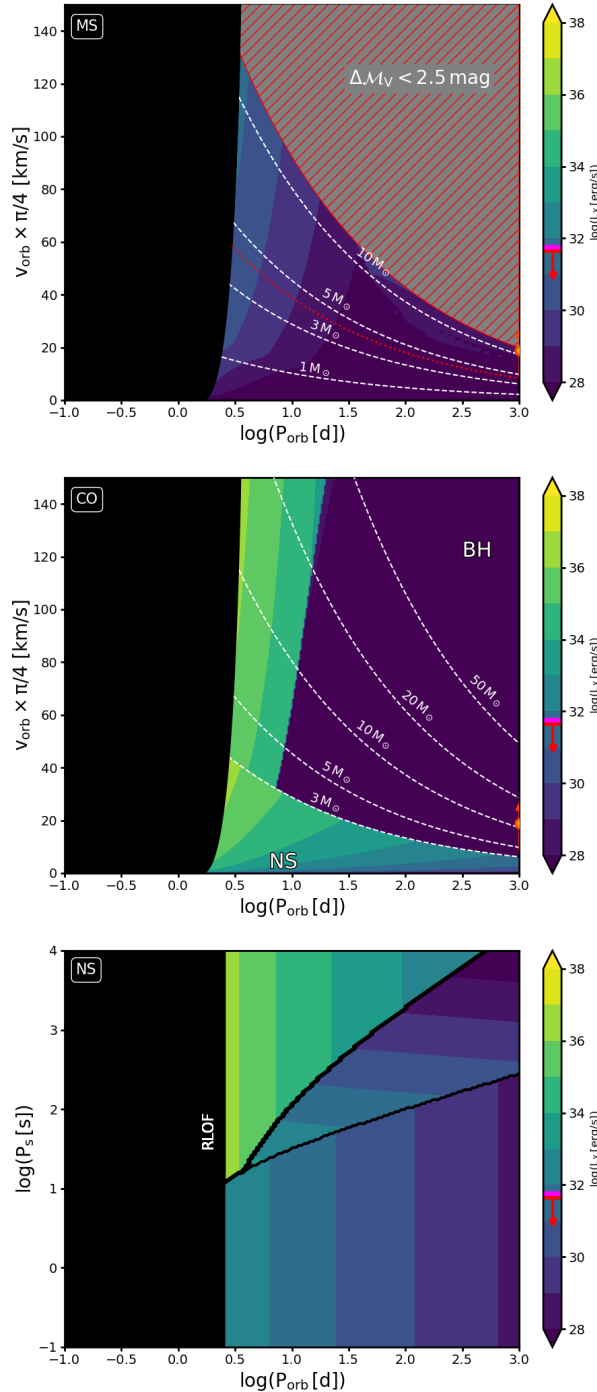


Figure C.31.: Diagnostic diagrams for VFTS 332. Assumed stellar parameters can be found in Tab. 4.8.

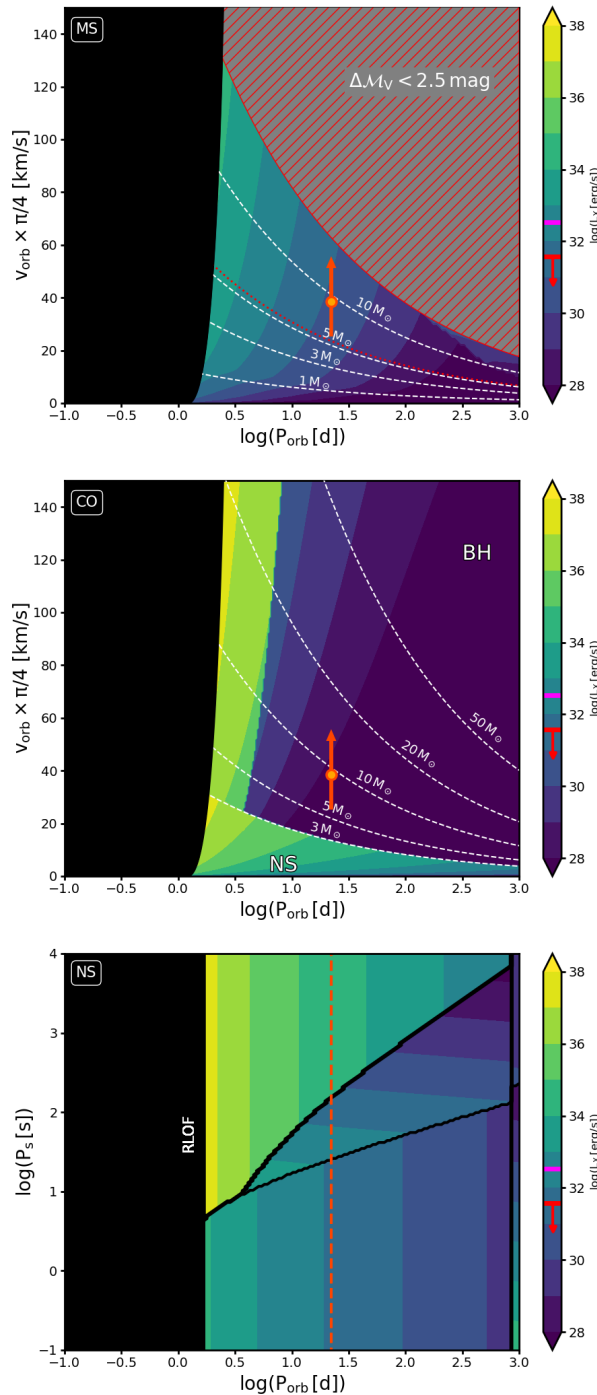


Figure C.32.: Diagnostic diagrams for VFTS 409. Assumed stellar parameters can be found in Tab. 4.8.

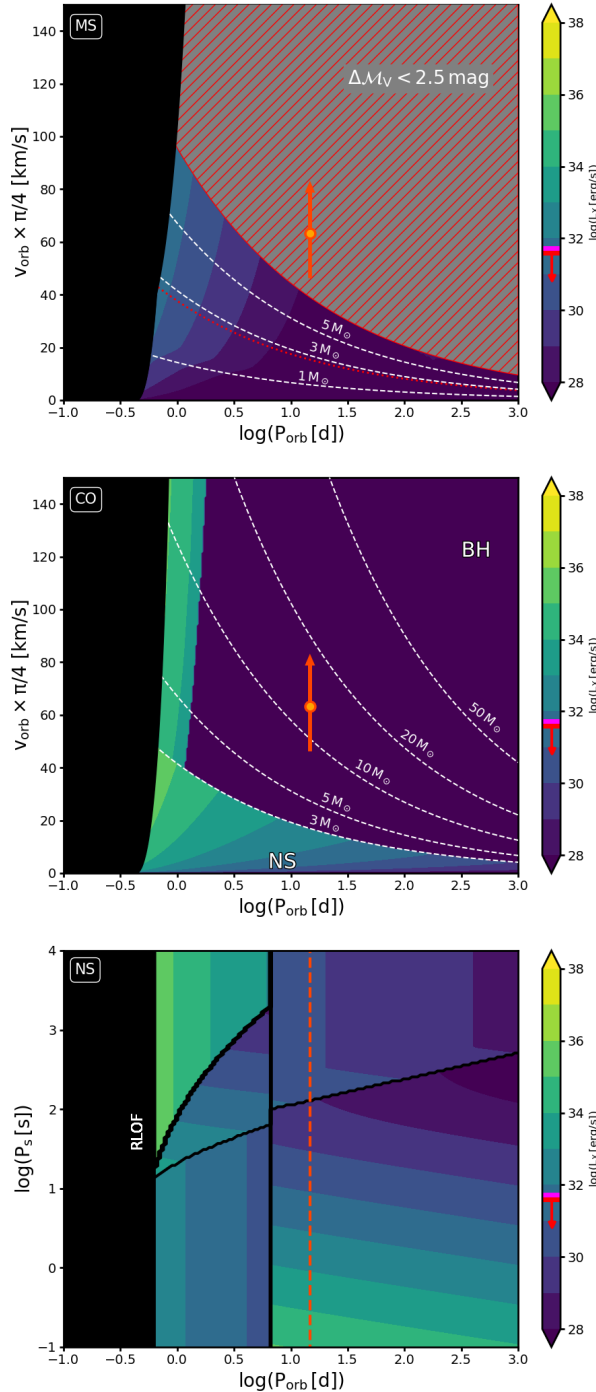


Figure C.33.: Diagnostic diagrams for VFTS 479. Assumed stellar parameters can be found in Tab. 4.8.

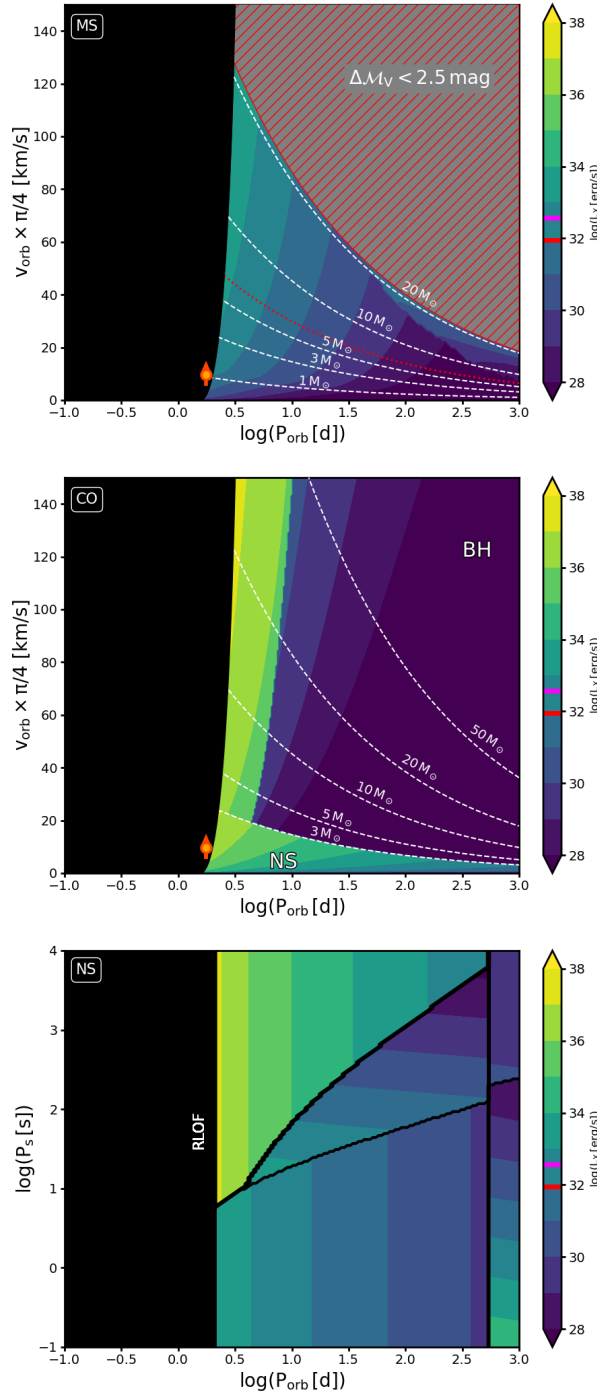


Figure C.34.: Diagnostic diagrams for VFTS 603. Assumed stellar parameters can be found in Tab. 4.8.

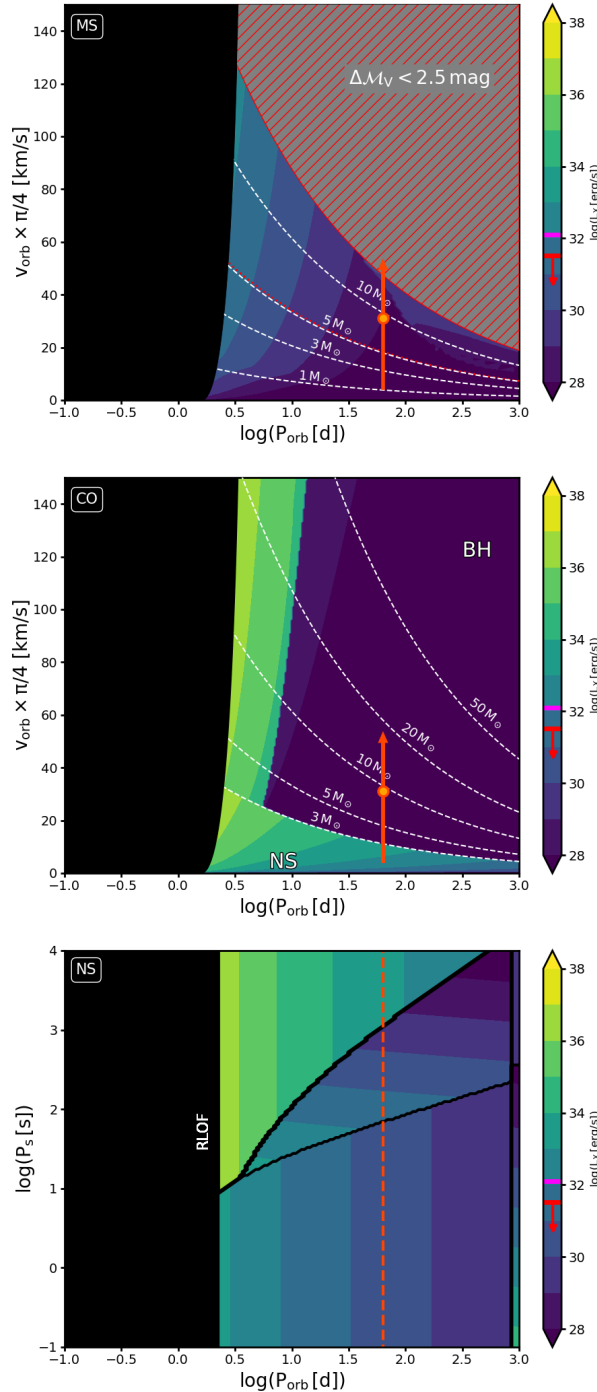


Figure C.35.: Diagnostic diagrams for VFTS 657. Assumed stellar parameters can be found in Tab. 4.8.

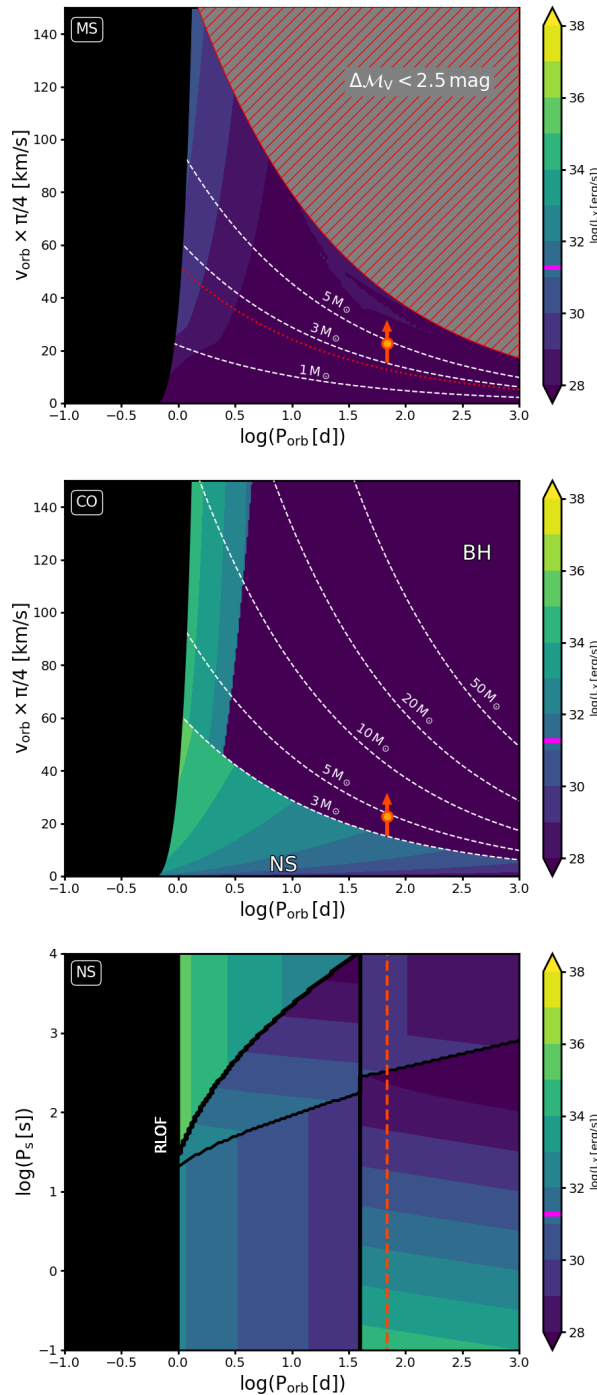


Figure C.36.: Diagnostic diagrams for VFTS 736. Assumed stellar parameters can be found in Tab. 4.8.

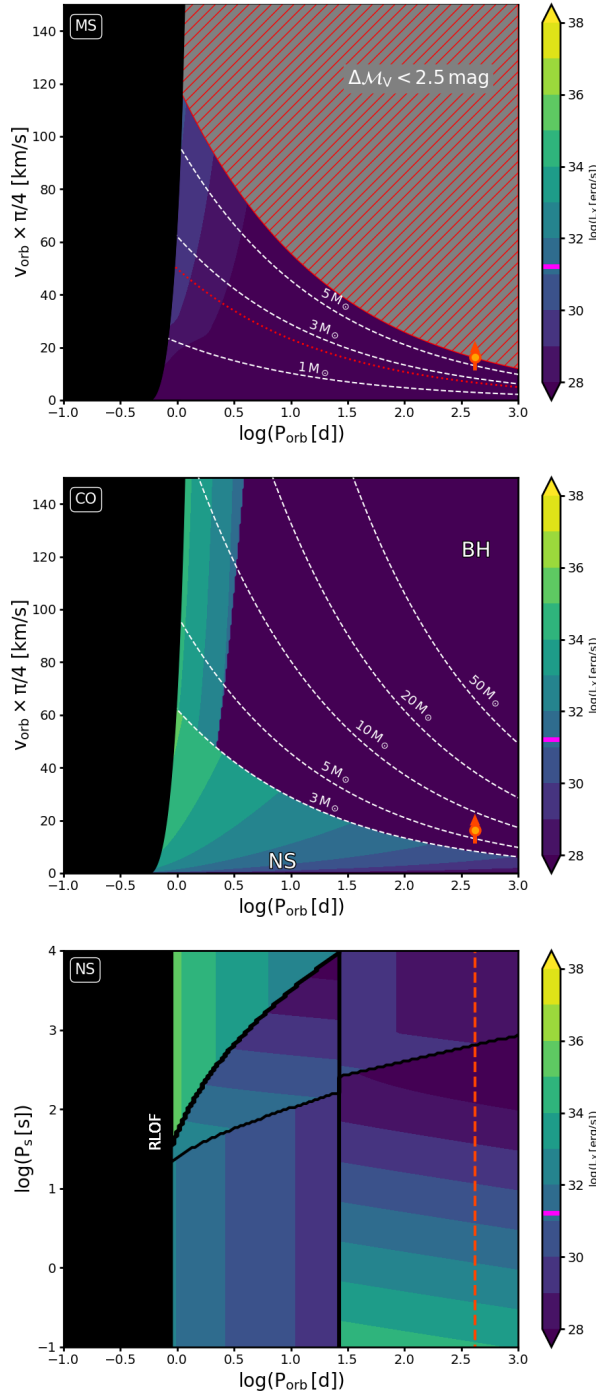


Figure C.37.: Diagnostic diagrams for VFTS 750. Assumed stellar parameters can be found in Tab. 4.8.

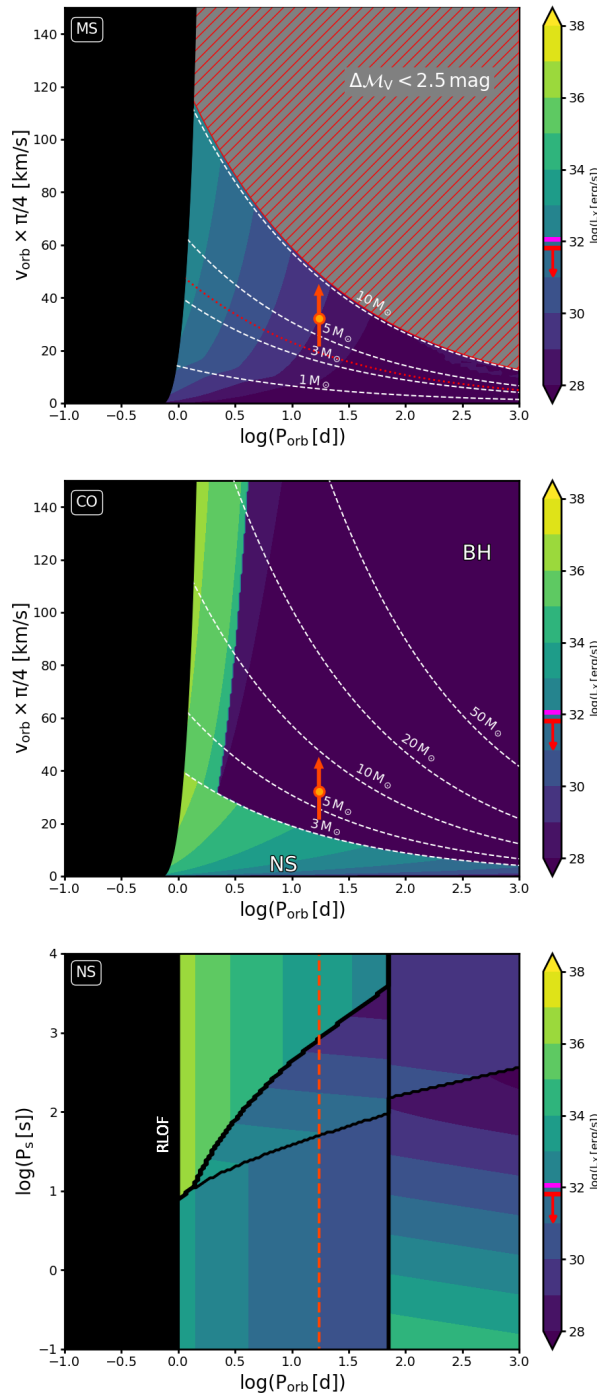


Figure C.38.: Diagnostic diagrams for VFTS 812. Assumed stellar parameters can be found in Tab. 4.8.

C.4 Catalog of diagnostic diagrams

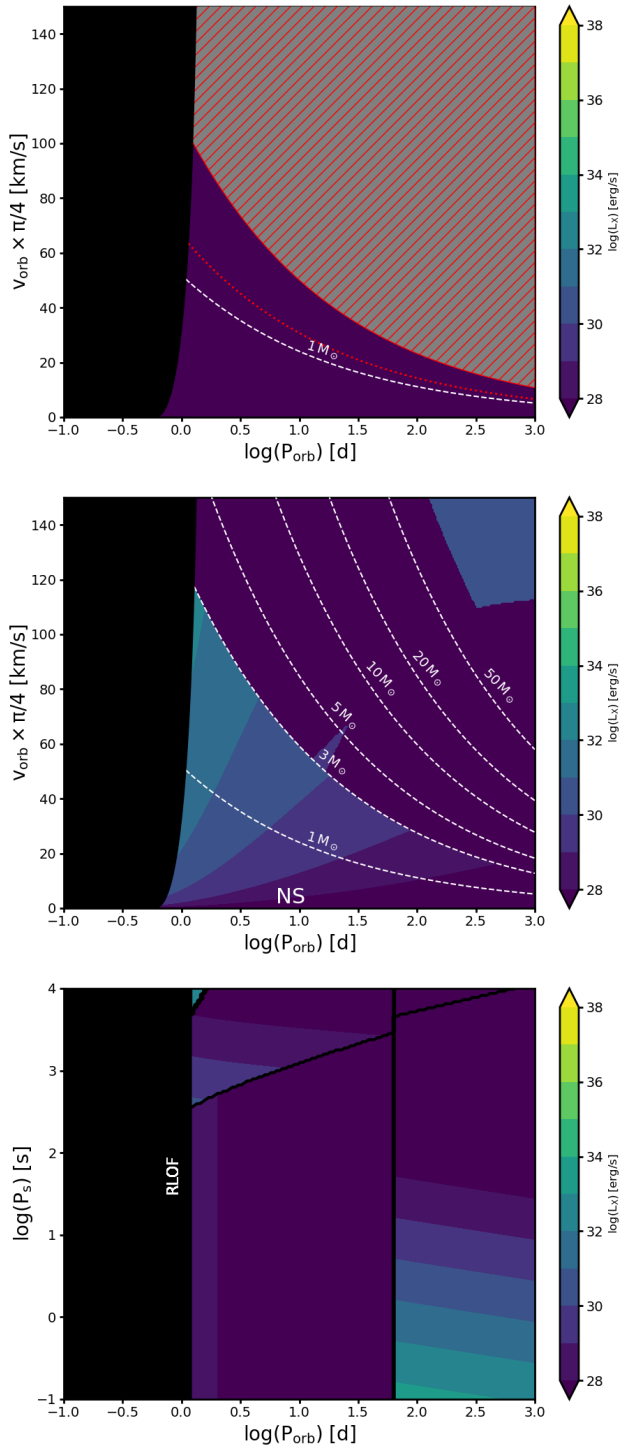


Figure C.39.: Diagnostic diagrams for a star with $T_{\text{eff}} = 15 \text{ kK}$ and $\log(g/\text{cm s}^{-2}) = 3.8$. Assumed stellar parameters can be found in Tab. 4.9.

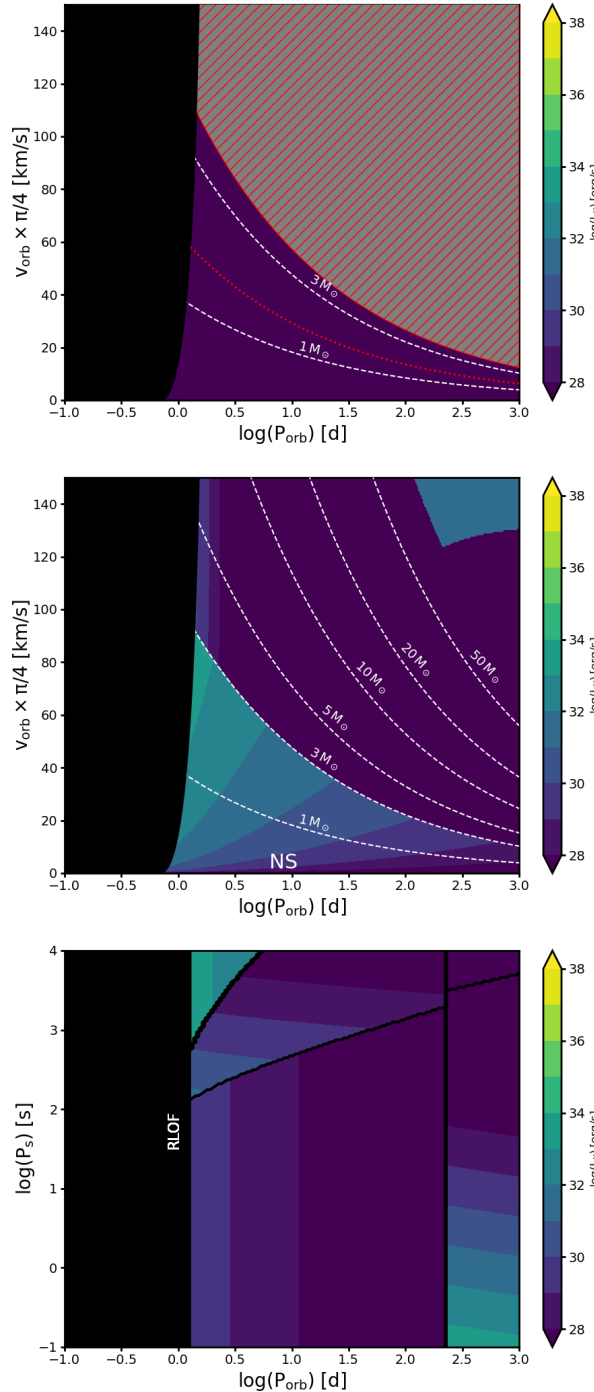


Figure C.40.: Diagnostic diagrams for a star with $T_{\text{eff}} = 20 \text{ kK}$ and $\log(g/\text{cm s}^{-2}) = 3.8$. Assumed stellar parameters can be found in Tab. 4.9.

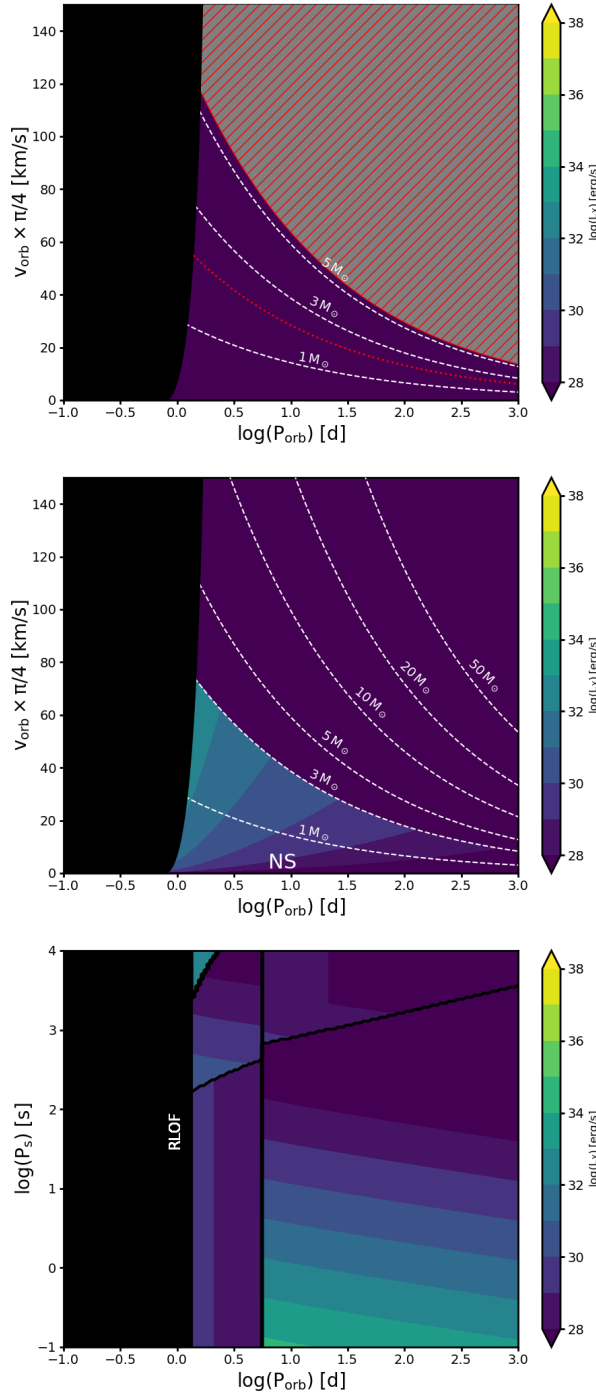


Figure C.41.: Diagnostic diagrams for a star with $T_{\text{eff}} = 25 \text{ kK}$ and $\log(g/\text{cm s}^{-2}) = 3.8$. Assumed stellar parameters can be found in Tab. 4.9.

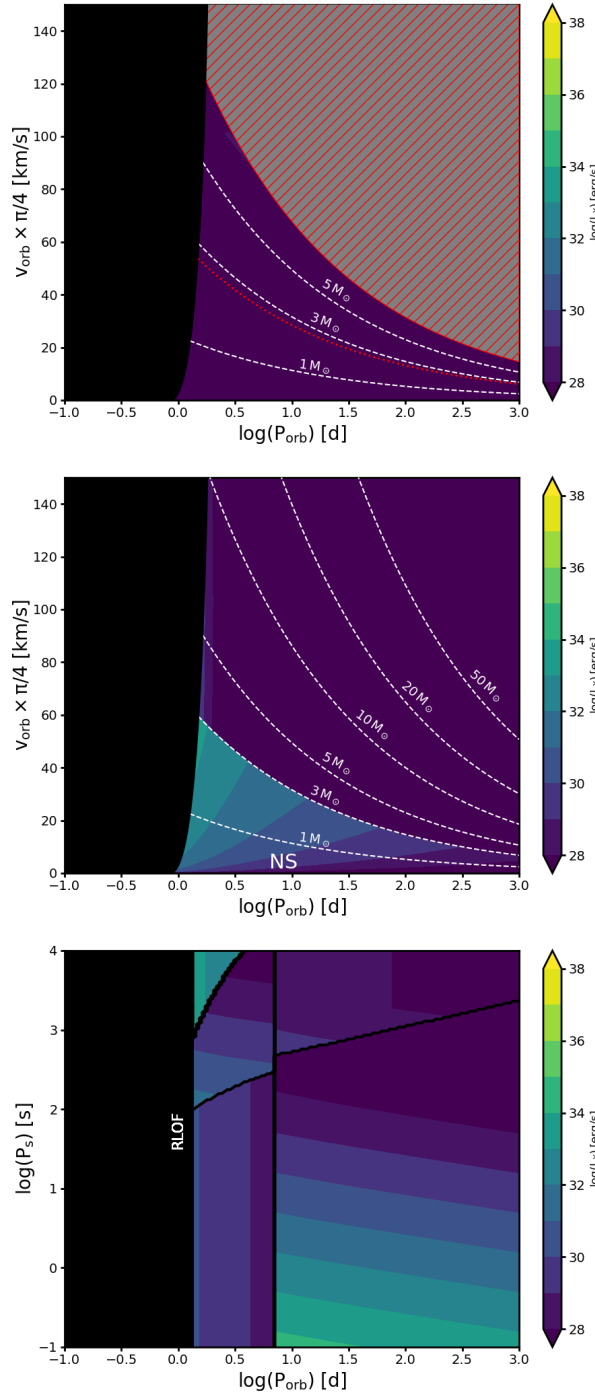


Figure C.42.: Diagnostic diagrams for a star with $T_{\text{eff}} = 30 \text{ kK}$ and $\log(g/\text{cm s}^{-2}) = 3.8$. Assumed stellar parameters can be found in Tab. 4.9.

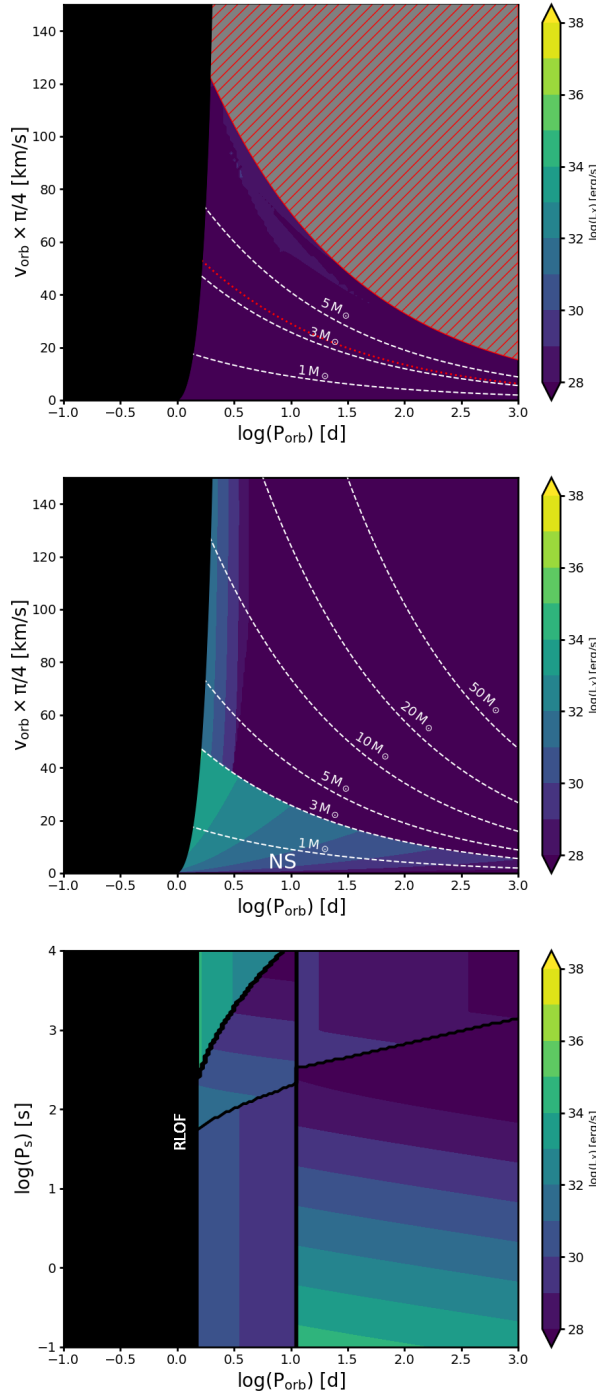


Figure C.43.: Diagnostic diagrams for a star with $T_{\text{eff}} = 35 \text{ kK}$ and $\log(g/\text{cm s}^{-2}) = 3.8$. Assumed stellar parameters can be found in Tab. 4.9.

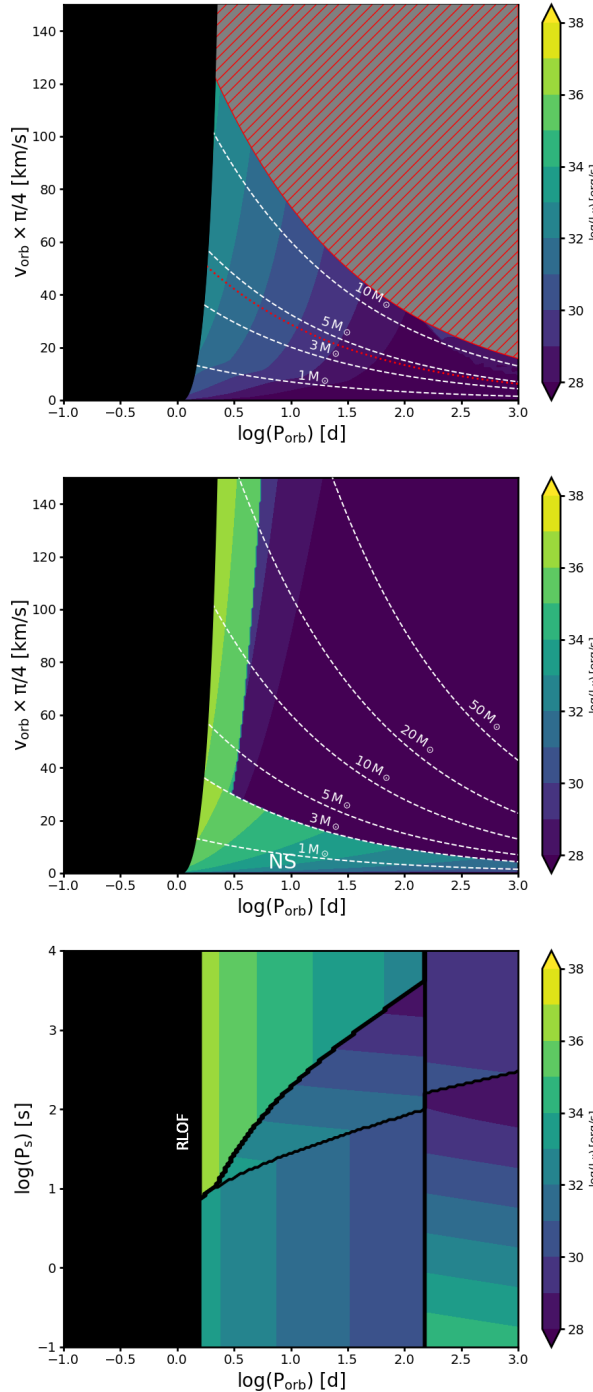


Figure C.44.: Diagnostic diagrams for a star with $T_{\text{eff}} = 40 \text{ kK}$ and $\log(g/\text{cm s}^{-2}) = 3.8$. Assumed stellar parameters can be found in Tab. 4.9.

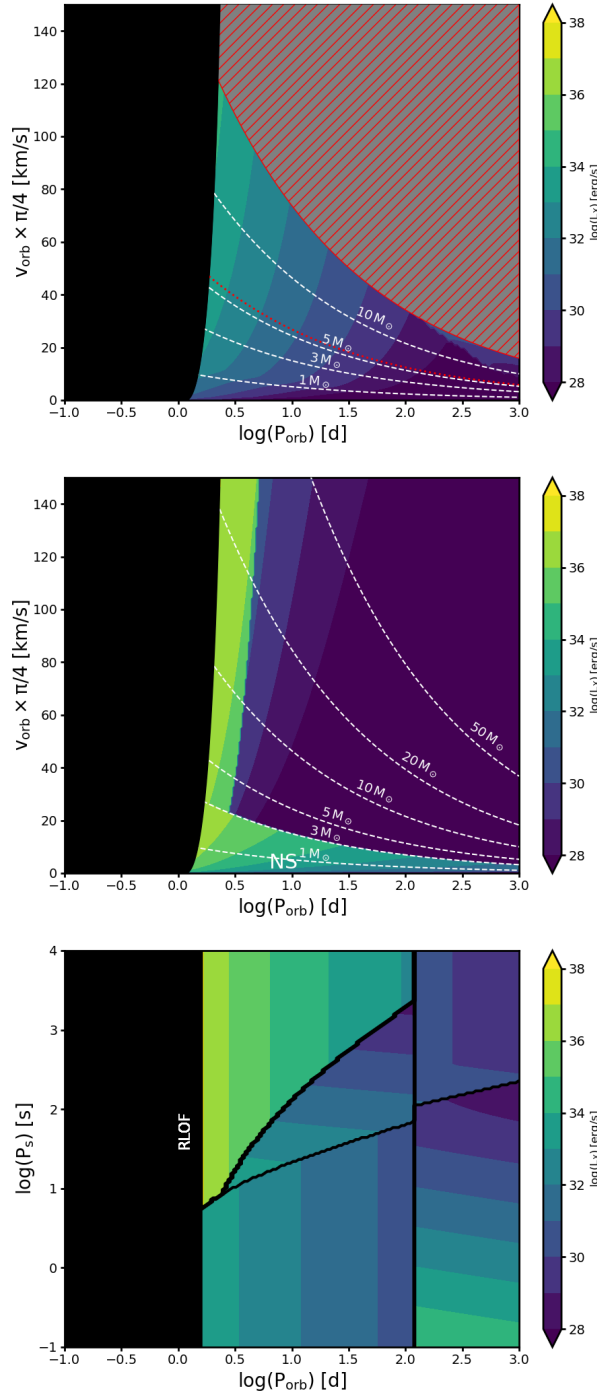


Figure C.45.: Diagnostic diagrams for a star with $T_{\text{eff}} = 45 \text{ kK}$ and $\log(g/\text{cm s}^{-2}) = 3.8$. Assumed stellar parameters can be found in Tab. 4.9.

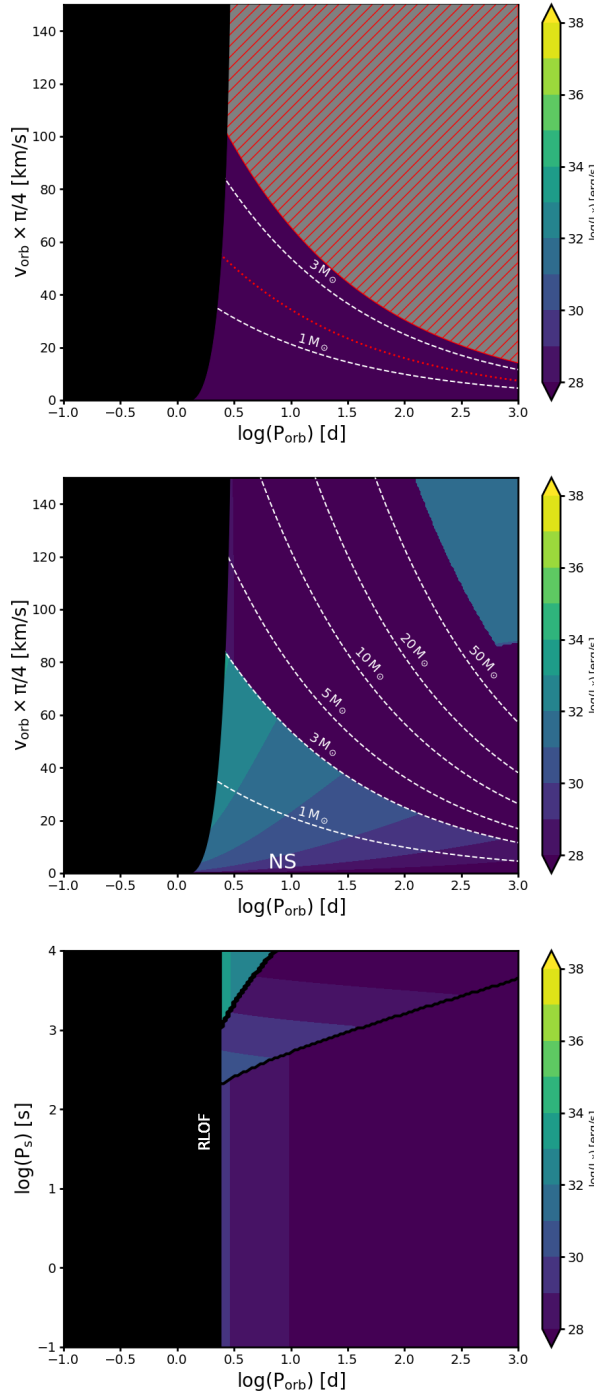


Figure C.46.: Diagnostic diagrams for a star with $T_{\text{eff}} = 15 \text{ kK}$ and $\log(g/\text{cm s}^{-2}) = 3.4$. Assumed stellar parameters can be found in Tab. 4.9.

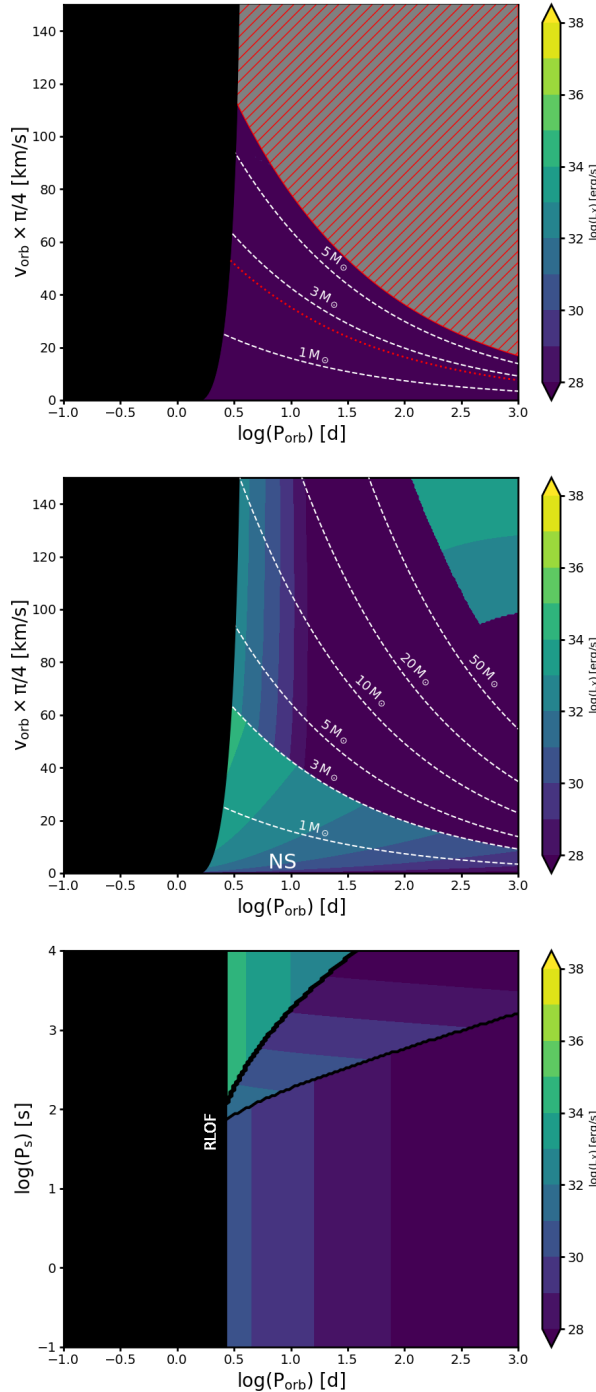


Figure C.47.: Diagnostic diagrams for a star with $T_{\text{eff}} = 20 \text{ kK}$ and $\log(g/(\text{cm s}^{-2})) = 3.4$. Assumed stellar parameters can be found in Tab. 4.9.

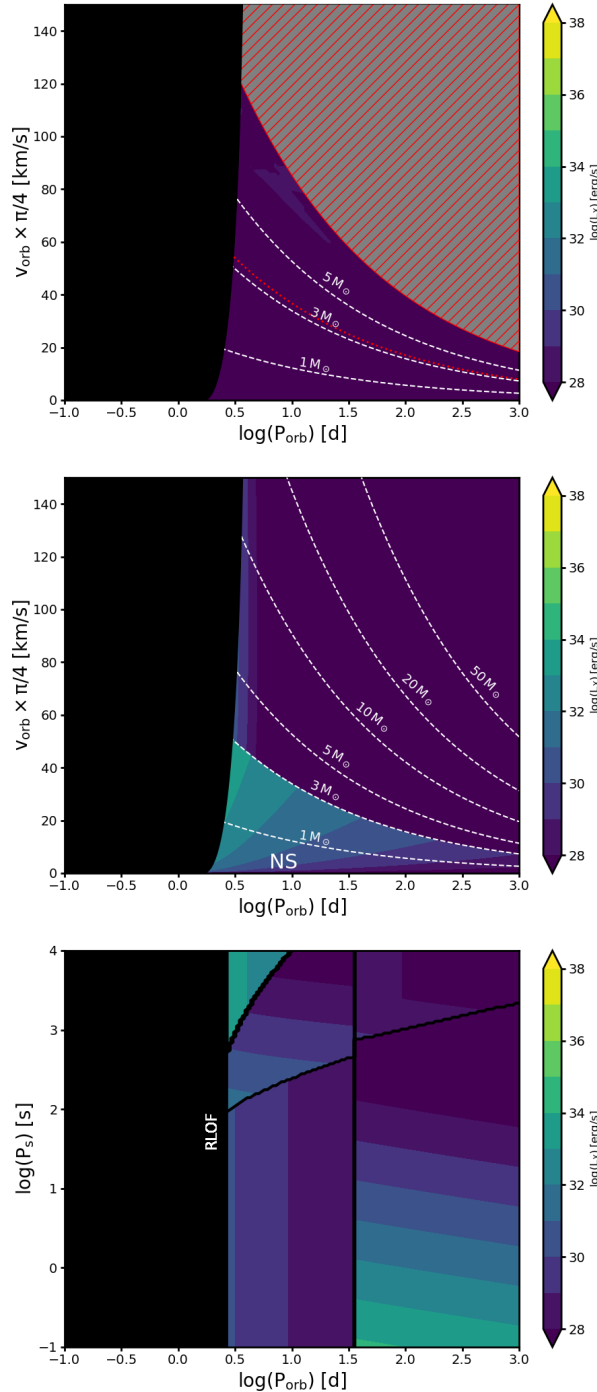


Figure C.48.: Diagnostic diagrams for a star with $T_{\text{eff}} = 25 \text{ kK}$ and $\log(g/\text{cm s}^{-2}) = 3.4$. Assumed stellar parameters can be found in Tab. 4.9.

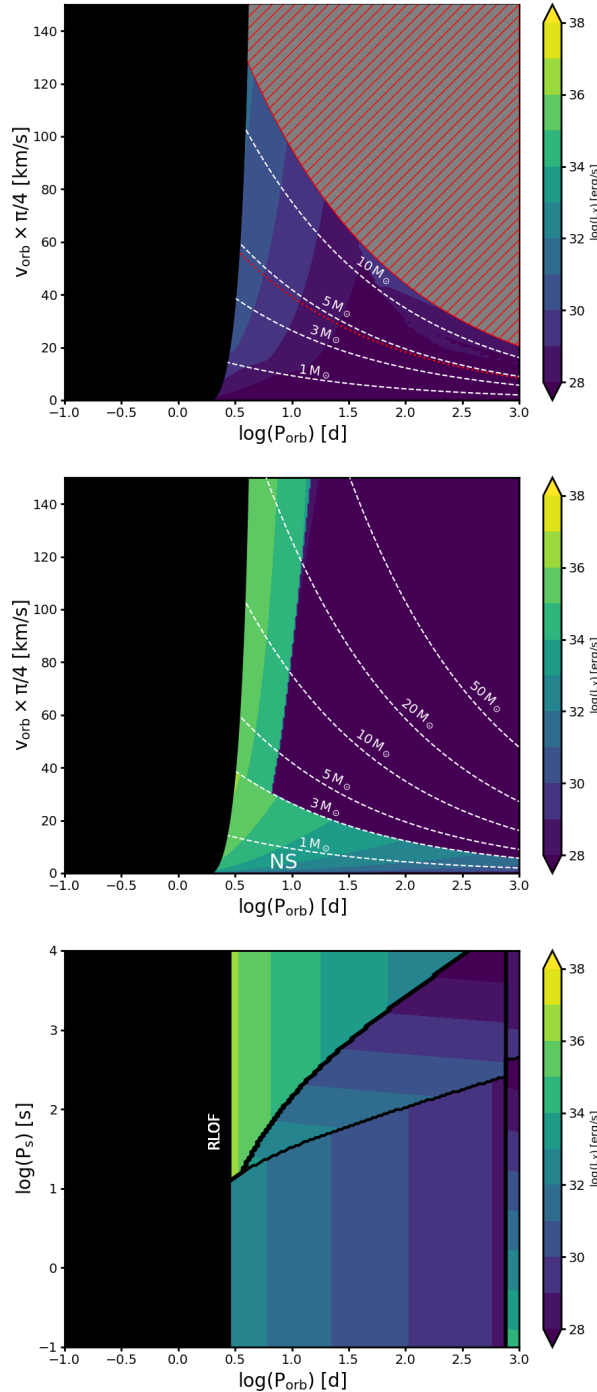


Figure C.49.: Diagnostic diagrams for a star with $T_{\text{eff}} = 30 \text{ kK}$ and $\log(g/\text{cm s}^{-2}) = 3.4$. Assumed stellar parameters can be found in Tab. 4.9.

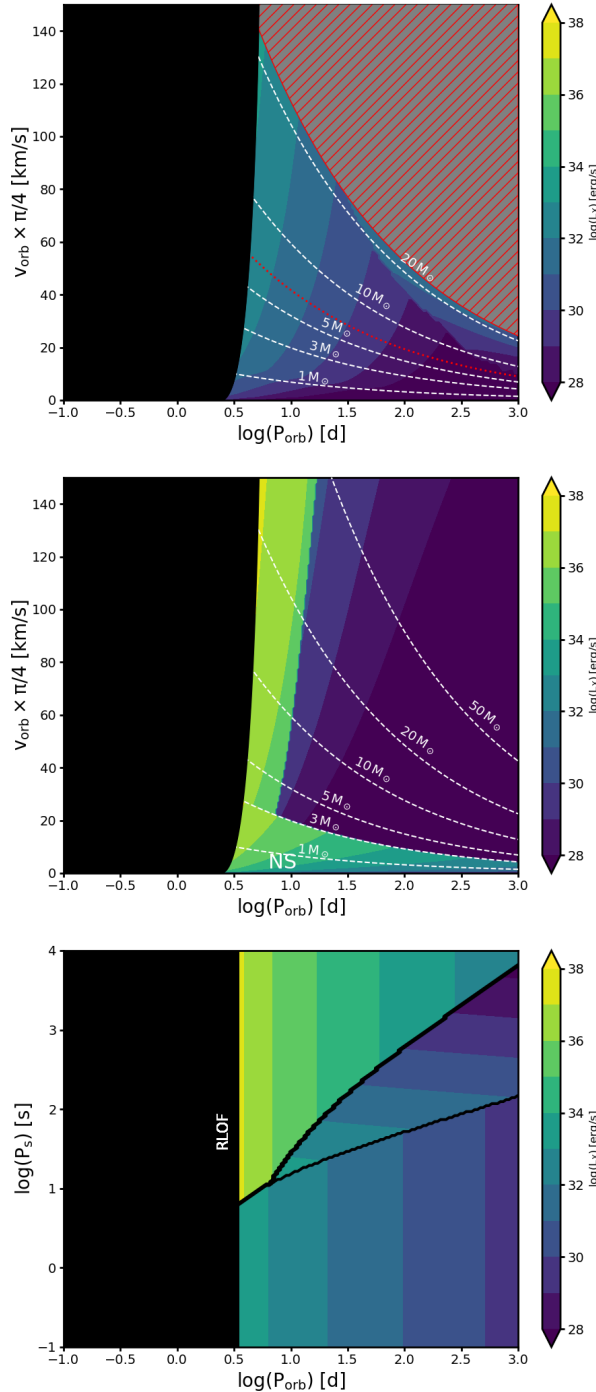


Figure C.50.: Diagnostic diagrams for a star with $T_{\text{eff}} = 35 \text{ kK}$ and $\log(g/\text{cm s}^{-2}) = 3.4$. Assumed stellar parameters can be found in Tab. 4.9.

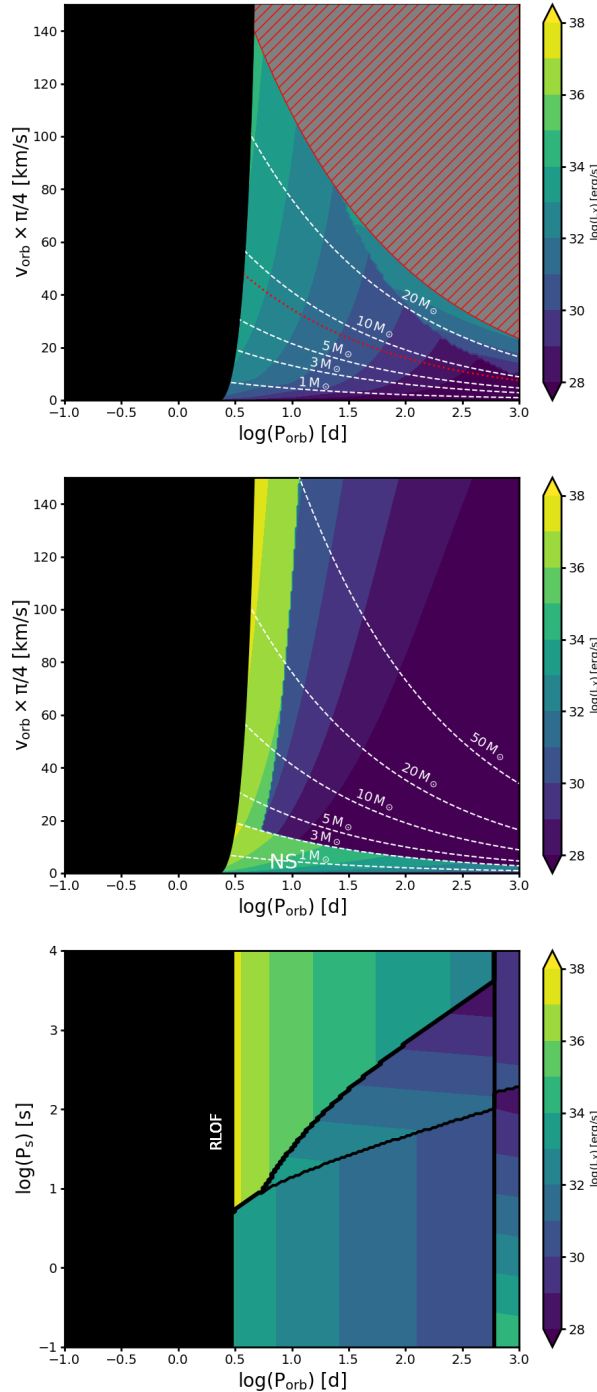


Figure C.51.: Diagnostic diagrams for a star with $T_{\text{eff}} = 40 \text{ kK}$ and $\log(g/\text{cm s}^{-2}) = 3.4$. Assumed stellar parameters can be found in Tab. 4.9.

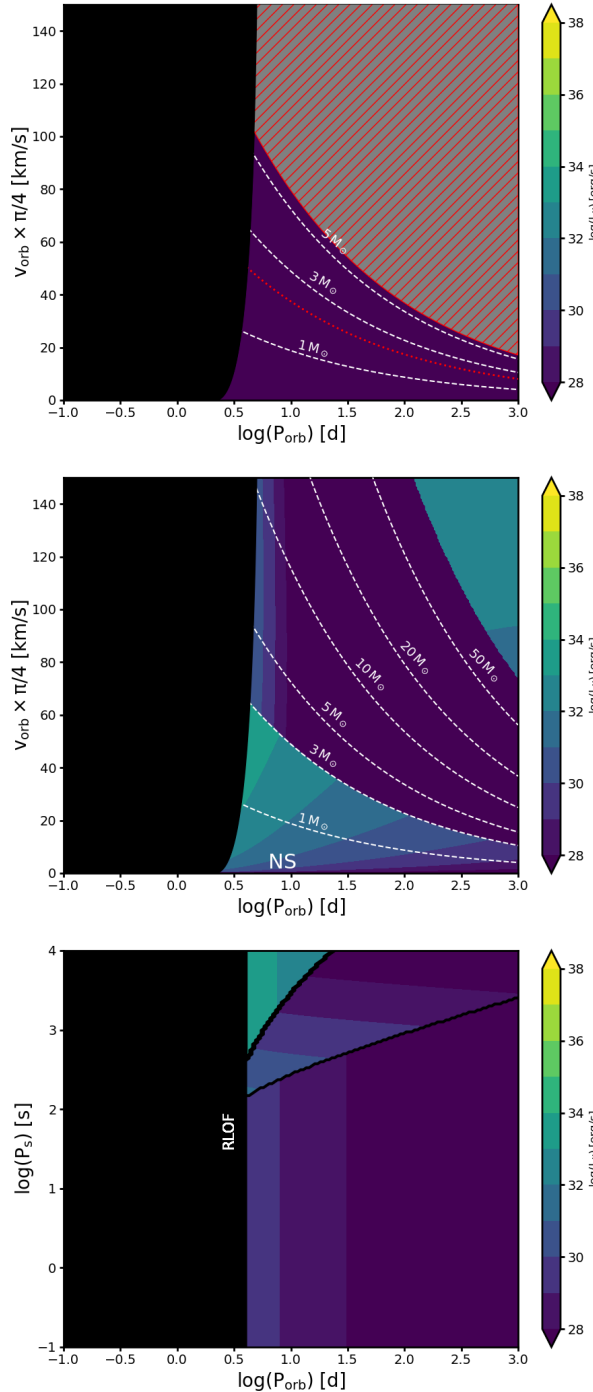


Figure C.52.: Diagnostic diagrams for a star with $T_{\text{eff}} = 15 \text{ kK}$ and $\log(g/\text{cm s}^{-2}) = 3.0$. Assumed stellar parameters can be found in Tab. 4.9.

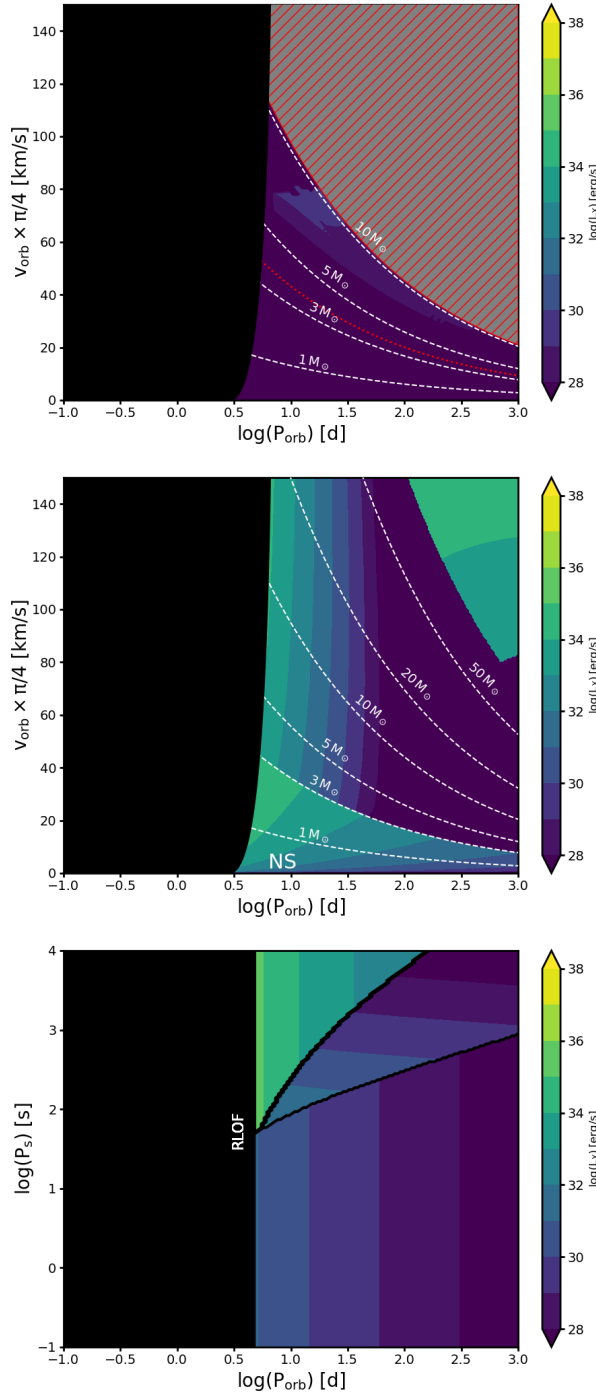


Figure C.53.: Diagnostic diagrams for a star with $T_{\text{eff}} = 20 \text{ kK}$ and $\log(g/\text{cm s}^{-2}) = 3.0$. Assumed stellar parameters can be found in Tab. 4.9.

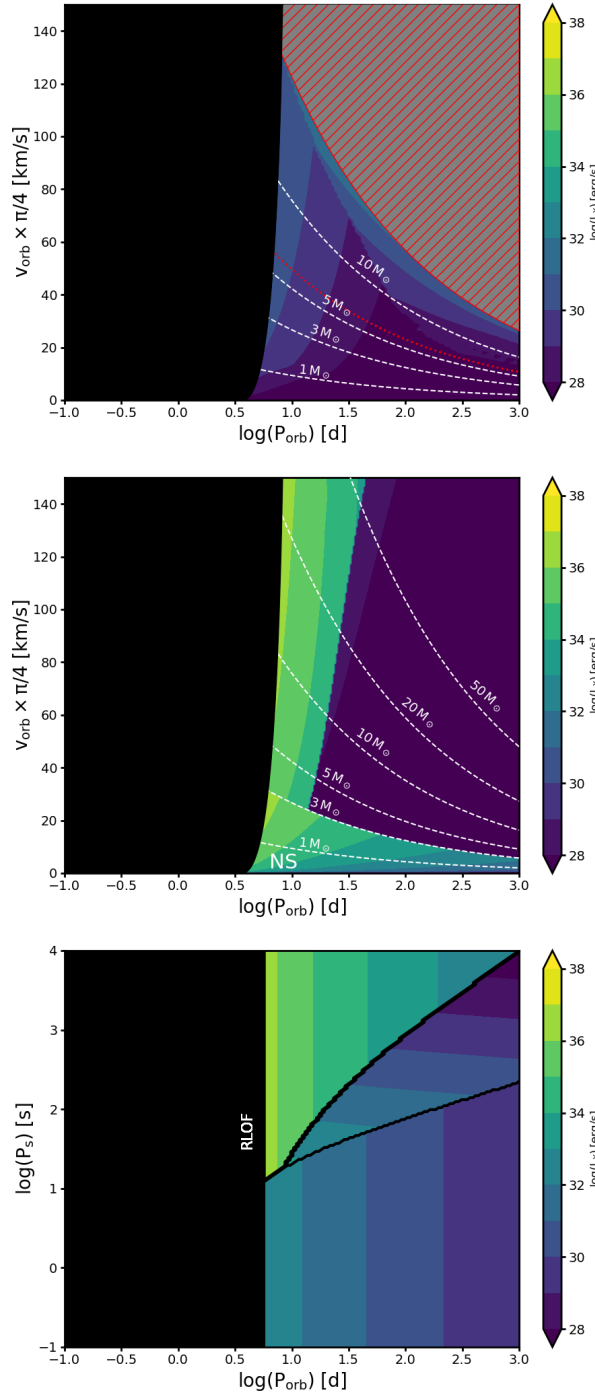


Figure C.54.: Diagnostic diagrams for a star with $T_{\text{eff}} = 25 \text{ kK}$ and $\log(g/\text{cm s}^{-2}) = 3.0$. Assumed stellar parameters can be found in Tab. 4.9.

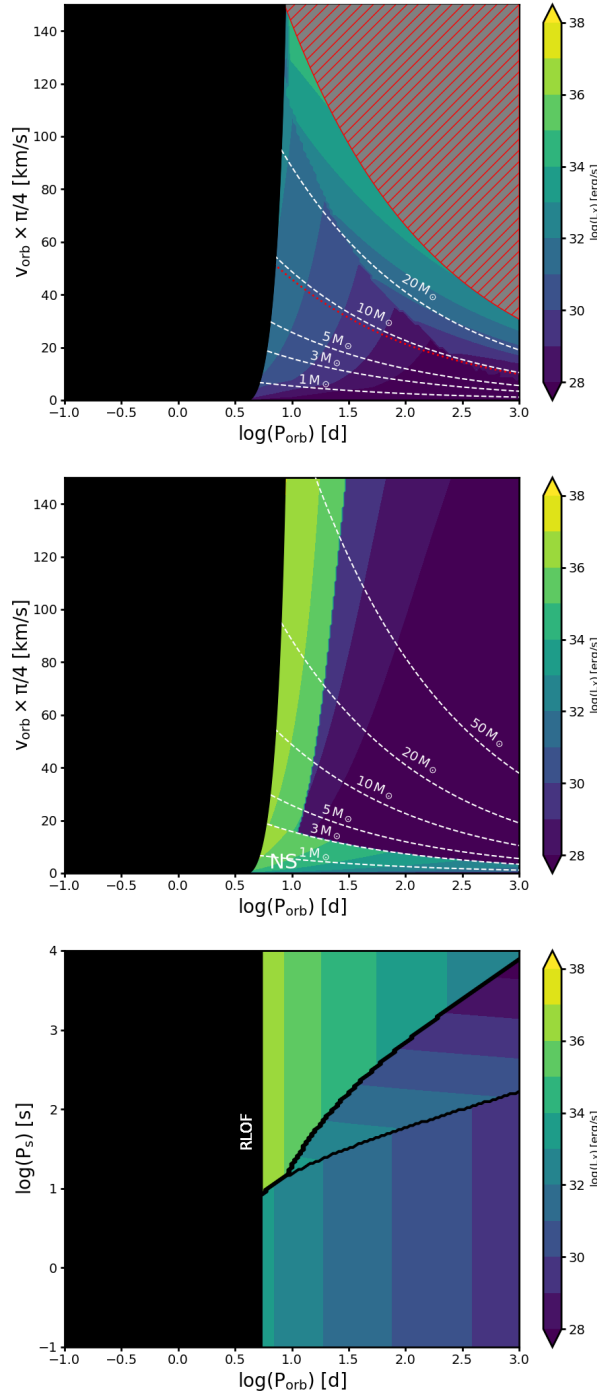


Figure C.55.: Diagnostic diagrams for a star with $T_{\text{eff}} = 30 \text{ kK}$ and $\log(g/\text{cm s}^{-2}) = 3.0$. Assumed stellar parameters can be found in Tab. 4.9.

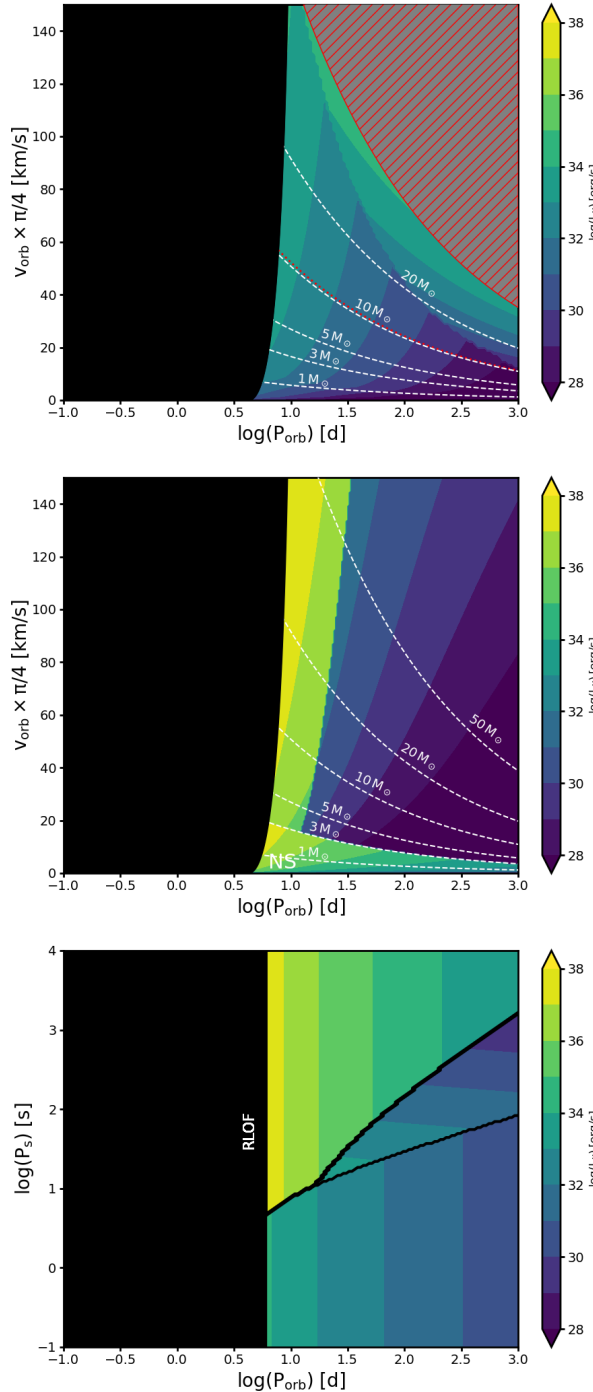


Figure C.56.: Diagnostic diagrams for a star with $T_{\text{eff}} = 35 \text{ kK}$ and $\log(g/\text{cm s}^{-2}) = 3.0$. Assumed stellar parameters can be found in Tab. 4.9.

List of Publications

Refereed Journals

- **Quast, M.** ; Langer, N. ; Tauris, T. M., 2019, A&A, 628, A19:
“Mass transfer on a nuclear timescale in models of supergiant and ultra-luminous X-ray binaries ”
DOI: 10.1051/0004-6361/201935453
- Langer, N. ; Schürmann, C. ; Stoll, K. ; ...; **Quast, M.** , 2020, A&A, 638, A39:
“Properties of OB star-black hole systems derived from detailed binary evolution models”
DOI: 10.1051/0004-6361/201937375
- Sen, K. ; Xu, X. -T. ; Langer, N. ; ...; **Quast, M.** , 2021, A&A, 652, A138 :
“X-ray emission from BH+O star binaries expected to descend from the observed galactic WR+O binaries”
DOI: 10.1051/0004-6361/202141214
- Sen, Koushik ; El Mellah, Ileyk ; Langer, Norbert ; ...; **Quast, M.** , 2024, Accepted for publication in A&A:
“Whispering in the dark: Faint X-ray emission from black holes with OB star companions”
DOI: 10.48550/arXiv.2406.08596

Refereed Journals prepared or submitted

- **Quast, M.** ; Langer, N. ; 2024, Prepared for publication in A&A:
“Constraining unseen companions of massive stars through combined considerations of X-ray and radial velocity signatures”
- Fehlinger, P.; Ertl, B.; **Quast, M.** ; Watzka, B. ; 2024, Submitted for publication in Behavior Research Methods:
“Eye Movement Analysis: A Kernel Density Estimation Approach for Saccade Direction and Length”

Non-Refereed Journals

- **Quast, M.** ; Schulz, A., 2017, Astron. & Raumf. im Unterricht, 55, 3-4:
“Weiße Zwerge im Schulunterricht”
- **Quast, M.** ; Hohmann, S. ; Schulz, A., 2018, Astron. & Raumf. im Unterricht, 56, 6:
“Erhebung astronomischer Lerninhalte in den Lehramtsstudiengängen deutscher Universitäten”

Curriculum Vitae

Personal Details

Name	Martin Quast
Date of Birth	10.11.1990
Email	martin.quast@ovgu.de

Education

2001 – 2009	Abitur, Markgraf-Albrecht-Gymnasium, Osterburg, Germany
2010 – 2015	First Teachers Exam (Erstes Staatsexamen) in Mathematics, Physics, and Astronomy, Martin-Luther-Universität, Halle (Saale), Germany.
2015 – 2024	PhD in Astronomy and Astrophysics, Rheinische Friedrich-Wilhelms-Universität, Bonn, Germany.
2019 – 2020	Second Teachers Exam (Zweites Staatsexamen), GutsMuths-Gymnasium, Quedlinburg, Germany.

Professional Experience

2015 – 2019	Doctoral work at the University of Bonn, Germany.
2015 – 2019	Teaching assistant for the Lab Course Spectroscopy of Stars, University of Bonn, Germany.
2019 – 2020	Teaching Trainee, GutsMuths-Gymnasium, Quedlinburg, Germany.
2020 – 2022	Teacher for Mathematics, Physics, and Astronomy, GutsMuths-Gymnasium, Quedlinburg, Germany.
since 2022	Lecturer for Physics Teacher Education, Otto-von-Guericke-Universität, Magdeburg, Germany.

Languages

German	Mother tongue
English	Fluent
French	Basic

Danksagung

An dieser Stelle möchte ich all denjenigen meinen tiefen Dank aussprechen, die mich während der Entstehung dieser Dissertation unterstützt haben.

Mein besonderer Dank gilt meinem Betreuer Prof. Dr. Norbert Langer, der mich mit wertvollen Anregungen, konstruktiver Kritik und geduldiger Unterstützung durch den gesamten Prozess begleitet hat. Ohne seine fachliche Expertise, die zahlreichen hilfreichen Hinweise und seine Ermutigungen wäre diese Arbeit nicht in ihrer jetzigen Form entstanden. In der Zeit, die ich in seiner Arbeitsgruppe verbringen durfte, habe ich nicht nur viel über Astronomie, sondern auch über wissenschaftliches Arbeiten und persönliche Weiterentwicklung gelernt – Erkenntnisse, die mich auf meinem weiteren Weg begleiten werden.

Darüber hinaus möchte ich auch dem Zweitgutachter dieser Arbeit, PD Dr. Jürgen Kerp, und den weiteren Mitgliedern der Promotionskommission meinen herzlichen Dank aussprechen. Ihre Bereitschaft, sich intensiv mit meiner Arbeit auseinanderzusetzen, und die Zeit, die sie dafür aufbringen, weiß ich sehr zu schätzen.

Ein herzliches Dankeschön gilt auch den Mitgliedern der Arbeitsgruppe Stellar Astrophysics, den Wissenschaftlerinnen und Wissenschaftlern am Argelander-Institut für Astronomie der Universität Bonn sowie allen Forschenden, die mich durch fachlichen Austausch, Diskussionen und freundschaftliche Unterstützung motiviert haben. Mein Dank gilt dabei insbesondere Abel Schootemeijer, Nathan Grin, Patrick Neunteufel, Matthias Kruckow, Chen Wang, Koushik Sen, Pablo Marchant, Debasish Sanyal, Michael Geffert, Carlo Abate, Götz Gräfener, Thomas Tauris, Selma de Mink und Philipp Podsiadlowski, deren wertvolle Ratschläge und Unterstützung für mich von großer Bedeutung waren. Ich danke außerdem Elisabeth und Sabine für die Unterstützung bei allen organisatorischen Angelegenheiten.

Ein ganz besonderer Dank gilt meinem Bürokollegen und guten Freund Christoph Schürmann. Vielen Dank für das Korrekturlesen meiner Arbeit und die vielen hilfreichen Anmerkungen. Danke für die zahlreichen inspirierenden Gespräche und nicht zuletzt für die Abende, an denen wir einfach nur schlechte Filme geschaut haben.

Ebenfalls danke ich Andreas Schulz für das Lesen und Korrigieren meiner Einleitung. Besonders danke ich ihm jedoch dafür, dass ich bei unseren vielen Wanderungen durch die Eifel immer wieder auf neue Gedanken kommen konnte.

Mein herzlicher Dank gilt auch den Kolleginnen und Kollegen der Universität Magdeburg, die mir ermöglicht haben, diese Arbeit zu vollenden. Danke an Bianca, Paula, Michael, Yultuz, Uwe, Sebastian, Yvonne, David und Dieter für eure alltägliche Unterstützung.

Nicht zuletzt möchte ich meiner Familie und meinen Freunden danken. Vielen Dank an Luise, Henrike, Elisabeth, Anne-Marie, Matthias, Juliane, Maria und Benedikt, für eure

stetige Unterstützung, die mir immer wieder neuen Mut gegeben hat – auch in schwierigen Phasen.

Ganz besonders danke ich meinen Eltern Simone und Ralph, die mir den Weg zu den Sternen wiesen, als sie mir vor über 20 Jahren ein kleines Teleskop schenkten. Mein Dank gilt auch ihren Lebenspartnern Markus und Alice. Danke an euch vier, dass ihr mich bei all meinen Entscheidungen unterstützt habt.

Ich danke meiner Partnerin Sandra für ihr Verständnis und ihre Geduld in den letzten Jahren, in denen sie mich viel zu oft entbehren musste. Ohne deine Unterstützung hätte ich diese Arbeit niemals beenden können. Das gilt natürlich auch für unsere zwei Fellkugeln Morty und Merle.

Abschließend möchte ich auch all jenen danken, die in dieser Danksagung ungenannt bleiben, deren Unterstützung jedoch nicht weniger wertvoll war. Vielen Dank!